Institute of Biomedical Engineering &
Department of Engineering Science,
University of Oxford

Multicompartmental Poroelasticity for the Integrative Modelling of Fluid Transport in the Brain

Ioannis C. Vardakis
Keble College

Supervised by:
Professor Yiannis Ventikos

This thesis is submitted to the Department of Engineering Science, University of Oxford, in partial fulfilment of the requirements for the degree of Doctor of Philosophy

Michaelmas Term 2014

Extended Abstract

The world population is expected to increase to approximately 11 billion by 2100. The ageing population (aged 60 and over) is projected to exceed the number of children in 2047. This will be a situation without precedent. The number of citizens with disorders of old age like Dementia will rise to 115 million worldwide by 2050. The estimated cost of Dementia will also increase, from $604 billion in 2010, to $1,117 billion by 2030. At the same time, medical expertise, evidence-driven policymaking and commissioning of services are increasingly evolving the definitive architecture of comprehensive long-term care to account for these changes.

Technological advances, such as those provided by computational science and biomedical engineering, will allow for an expansion in our ability to model and simulate an almost limitless variety of complex problems that have long defied traditional methods of medical practice. Numerical methods and simulation offer the prospect of improved clinically relevant predictive information, and of course optimisation, enabling more efficient use of resources for designing treatment protocols, risk assessment and urgently needed management of a long term care system for a wide spectrum of brain disorders. Within this paradigm, the importance of the relationship of senescence of cerebrospinal fluid transport to dementia in the elderly make the cerebral environment notably worthy of investigation through numerical and computational modelling.

Hydrocephalus can be succinctly described as the abnormal accumulation (imbalance between production and circulation) of cerebrospinal fluid (CSF) within the brain. Using hydrocephalus as a test bed, one is able to account for the necessary mechanisms involved in the interaction between cerebral fluid production, transport and drainage. The current state of knowledge about hydrocephalus, and more broadly integrative cerebral dynamics and its associated constitutive requirements, advocates that poroelastic theory provides a suitable framework to better understand the disease. In this work, Multiple-network poroelastic Theory (MPET) is used to develop a novel spatio-temporal model of fluid regulation and tissue displacement in various scales within the cerebral environment. The model is discretised in a variety of formats, through the established finite difference method, finite difference – finite volume coupling and also the finite element method. Both chronic and acute hydrocephalus was investigated in a variety of settings, and accompanied by emerging surgical techniques where appropriate.

In the coupled finite difference – finite volume model, a key novelty was the amalgamation of anatomically accurate choroid plexuses with their feeding arteries and a simple relationship relaxing the constraint of a unique permeability for the CSF compartment. This was done in order to account for Aquaporin-4 sensitisation. This model is used to demonstrate the impact of aqueductal stenosis and fourth ventricle outlet obstruction. The implications of treating such a clinical condition with the aid of endoscopic third (ETV) and endoscopic fourth ventriculostomy (EFV) are considered. It was observed that CSF velocity in the aqueduct, along with ventricular displacement, CSF pressure, wall shear stress and pressure difference between lateral and fourth ventricles increased with applied stenosis. The application of ETV reduced the aqueductal velocity, ventricular displacement, CSF pressure,

wall shear stress and pressure difference within nominal levels. The greatest reversal of the effects of atresia come by opting for ETV rather than the more complicated procedure of EFV.

For the finite difference model incorporating nonlinear permeability, qualitatively similar results were obtained in comparison to the pertinent literature, however, there was an overall amplification of ventriculomegaly and transparenchymal pressure difference using this model. A quantitative and qualitative assessment is made of hydrocephalus cases involving aqueductal stenosis, along with the effects to CSF reabsorption in the parenchyma and subarachnoid space.

The finite element discretisation template produced for the n^{th}- dimensional transient MPET system allowed for novel insight into hydrocephalus. In the 1D formulation, imposing the breakdown of the blood-CSF barrier responsible for clearance resulted in an increase in ventricular displacement, transparenchymal venous pressure gradient and transparenchymal CSF pressure gradient, whilst altering the compliance proved to markedly alter the rate of change of displacement and CSF pressure gradient. The influence of Poisson's ratio was investigated through the use of the dual-grid solver in order to distinguish between possible over or under prediction of the ventricular displacement. In the 2D model based on linear triangles, the importance of the MPET boundary conditions is acknowledged, along with the quality of the underlying mesh. Interesting results include that the fluid content is highest in the periventricular region and the skull, whilst after longer time scales, the peak CSF content becomes limited to the periventricular region. Venous fluid content is heavily influenced by the Biot-Willis constant, whilst both the venous and CSF/ISF compartments show to be strongly influenced by breakdown in the blood-CSF barrier. Increasing the venous compliance effects the arterial, capillary and venous compartments. Decreasing the venous compliance shows an accumulation of fluid, possibly helping to explain why the ventricles can be induced to compress rather than expand under decreased compliance. Finally, a successful application of the 3D-MPET template is shown for simple geometries.

It is envisaged that future observations into the biology of cerebral fluid flow (such as perivascular CSF-ISF fluid exchange) and its interaction with the surrounding parenchyma, will demand the evolution of the MPET model to reach a level of complexity that could allow for an experimentally guided exploration of areas that would otherwise prove too intricate and intertwined under conventional settings.

Statement of Originality

I hereby declare that this submission is my own work and to the best of my knowledge it contains no materials previously published or written by another person, or substantial proportions of material which have been accepted for the award of any other degree or diploma at the University of Oxford or any other educational institution, except where due acknowledgement is made in the thesis.

Any contribution made to the research by others, with whom I have worked at the University of Oxford or elsewhere, is explicitly acknowledged in the thesis.

I also declare that the intellectual content of this thesis is the product of my own work, except to the extent that assistance from others in the project's design and conception or in style, presentation and linguistic expression is acknowledged.

Ioannis C. Vardakis

October 10, 2014

Acknowledgements

First and foremost, I offer my sincerest gratitude to my supervisor, Professor Yiannis Ventikos, who has supported me throughout my studies with his patience, warm encouragement, thoughtful guidance, critical comments and deep knowledge. I am equally grateful for being afforded the trust, and the independence to work in my own way, in addition to the frequent exposure to the wider scientific interface. I am extremely proud of my academic endeavours in Oxford, and I can only hope to be given an opportunity in sharing the research values instilled in me throughout my supervision.

I would like to take this opportunity to thank Professor Alison Noble, which not only gave me the opportunity to conduct my research through the Centre for Doctoral Training in Healthcare Innovation, but also her support and encouragement on various occasions throughout my first year. I would like to thank Professor Stephen Payne for his instrumental role in paving the way for an inspirational College experience. Professor Peter Dobson and Dr. Marc Ventresca provided a fantastic pedagogical approach and insight into entrepreneurship and market research, in addition to their endless stream of goodwill. Finally, I thank Dr. Piotr Orlowski for his great enthusiasm and willingness to share his deep insights into novel modelling approaches.

In my daily work, I was blessed with a friendly and cheerful group of students. Dean Chou for showing great character, friendship, determination and enthusiasm to proceed within the realm of CSF. Himanshu Kaul is acknowledged for his ability to provoke debates on all levels that could last for a good few hours, and Dr. Chao Wang for his inability to put on a sad face. Dr. Malebogo Ngoepe is acknowledged for her exquisite humour and deep discussions. I would also like to thank Dr. Tom Peach and Dr. Katja Gera for their supremely cheerful approach to CFD, and Dr. Brett Tully, Dr. Paul Watton, Katia Madaltsi, Pedro Aparicio, Jack Hornsby, Nazri Bajuri, Dr. Haoyu Chen and Dr. Alisa Selimovic for their great interaction throughout my time in the IBME and IEB.

Outside the lab, I would like to thank Dr. Antonios Iliopoulos, Kelly Schoina, Dr. Emmanuel Spirakos, Dr. Icel Veronica Souleimanova, Dr. Konstantinos Sakellariou, Dr. Despina Athena Potari, Dr. Berkan Şeşen, Dr. Sarah Rudebeck, Dr. Joseph Sherwood, Dr. Louis Mayaud, Dr. Yee Kai Tee, Dr. Amit Mehndiratta, Dr. Konstantinos Papoutsis, Ersi Lyka, Dr. Sissy Ivi Antoniadou, Eleni Katsouni, Dr. Alexander Breton, Dr. Fahad Dilib, Dr. Elina Vlachodimitropoulou, Zoi Mitsakou and Dr. Panagiotis Polygerinos for showing great spirit, kindness, equanimity and friendship.

I would not have contemplated this road if not for the love and support of my family: my parents Sophia and George; and my brother Theo, who instilled within me a love of curiosity and determination, all of which finds a place in this thesis. To my family, thank you.

The Research Councils UK (RCUK) Digital Economy Programme is acknowledged for its generous support throughout my studies.

Dissemination

Book Chapter (1)

Vardakis J C, Tully B J, Ventikos Y (2013). *Multicompartmental poroelasticity as a platform for the integrative modelling of water transport in the brain*. In: Holzapfel GA, Kuhl E, editors. Computer Models in Biomechanics: from Nano to Macro. Heidelberg: Springer-Verlag. 305–316.

Peer-Reviewed Journal papers (1 published and 4 submitted)

1. Vardakis J C, Tully B J, Ventikos Y (2013). *Exploring the Efficacy of Endoscopic Ventriculostomy for Hydrocephalus Treatment via a Multicompartmental Poroelastic Model of CSF Transport: A Computational Perspective*. PLoS ONE 8(12): e84577. doi:10.1371/journal.pone.0084577.
2. Vardakis J C, Chou D, Tully B, Hung C C, Lee T H., Tsui P-H., Ventikos Y (submitted). *Investigating Cerebral Oedema using Poroelasticity*. Medical Engineering & Physics.
3. Vardakis J C and Ventikos Y (submitted). *A Novel Model of Hydrocephalus using Multicompartmental Poroelasticity*. Journal of Computational Physics.
4. Vardakis J C, Chou D, Tully B, Ventikos Y (submitted). *The impact of nonlinear permeability on a Multicompartmental model of Poroelasticity*. Annals of Biomedical Engineering.
5. Vardakis J C and Ventikos Y (submitted). *A Discontinuous Galerkin Approach to a Multicompartmental Poroelastic Model for Hydrocephalus*. IMA Journal of Applied Mathematics.

Peer-Reviewed conference proceedings (5)

1. Vardakis, J, Chou, D, Tully, B & Ventikos, Y. (2014). *A CFD and FEM Approach to a Multicompartmental Poroelastic Model for CSF Production and Circulation with Applications in Hydrocephalus Treatment and Cerebral Oedema*. 4th Micro and Nano Flows Conference. University College London, UK.
2. Vardakis, J, Tully, B, Chou, D & Ventikos, Y. (2012). *Multicompartmental Poroelasticity for Brain Modelling*. Bioengineering 2012, University of Oxford, UK.
3. Vardakis, J., Tully, B., Byrne, J., & Ventikos, Y. (2011). *Multicompartmental Poroelastic Modelling for CSF Production and Circulation.* 3rd Micro and Nano Flows Conference. Thessaloniki, Greece.
4. Tully, B, Vardakis, J & Ventikos, Y. (2011). *Multicompartmental Poroelasticity as a modelling platform for perfused tissue*. International Union of Theoretical and Applied Mechanics Symposium on Computer Models in Biomechanics. Stanford, California, USA.
5. Vardakis, J, Tully, B & Ventikos, Y. (2010). *Multicompartmental Poroelasticity as a Multiscalar Representation of Living Tissue*. Bioengineering 2010, University of Nottingham, UK.

Conference presentations and posters (5)

1. Vardakis, J C, Chou, D, Tully, B J & Ventikos, Y. (July 2014). *Exploring a Multicompartmental Poroelastic Model for the Integrative Modelling of Fluid Transport*. 7th World Congress of Biomechanics. Boston, Massachusetts, USA.
2. Vardakis, J C, Tully, B J, Chou, D & Ventikos, Y. (January 2013). *Surgical Applications in Endoscopic Ventriculostomy and Aqueductoplasty using Multicompartmental Poroelasticity*. 1st UK National Conference on Patient-Specific Modelling & Translational Research. Cardiff University, UK.
3. Vardakis, J C, Tully, B J, Ventikos, Y. (July 2012). *Multicompartmental Poroelastic Modelling for CSF Production and Circulation: Surgical Applications in Third and Fourth Ventriculostomy*. 6th European Postgraduate Fluid Dynamics Conference. Imperial College London, London, UK.
4. Vardakis, J C, Tully, B J & Ventikos, Y. (July 2011). *Multicompartmental Poroelasticity for the Integrative Modelling of Water Transport in the Brain*. First CSF Hydrodynamics Symposium. Swiss Federal Institute of Technology, Zurich, Switzerland.
5. Vardakis, J C, Tully, B J, Ventikos, Y. (September 2011). *Multicompartmental Poroelasticity for the Multiscalar Modelling of CSF Production and Circulation in the Brain*. 2nd Meeting of the EPSRC Patient-Specific Modelling Network, UK.

Invited Lectures (2)

1. Vardakis, J.C., Tully, B.J., and Ventikos, Y., *Challenges and promise for using multicompartmental poroelasticity as a modelling paradigm for cerebral tissue*. Mathematical and Experimental Models in Mechanobiology Conference, invited lecture: Oxford, UK (2012, March). *Presented by Y. Ventikos*.
2. Vardakis, J.C., Tully, B.J., and Ventikos, Y., *Multicompartmental poroelasticity and the modelling of cerebral tissue.* Biological Flow: A Conference to celebrate the 70th Birthday of Prof. Tim Pedley FRS, invited lecture: Cambridge, UK (2012, April). *Presented by Y. Ventikos*.

Technical meetings (VPH-DARE@IT)

1. Kick off meeting, (2013), University of Sheffield, UK.
2. Cerebral Elastography, (2013), St Thomas' Hospital, King's College London, UK.
3. Lifestyle factors, (2013), University of Oxford, UK.
4. Imaging, (2013), University of Oxford, UK.
5. General Assembly, (2013), VTT Technical Research Centre of Finland. Espoo, Finland.
6. Microvascular-Venous Pathway Meeting, (2014), Klinik Hirslanden, Zürich.
7. Poroelasticiy module development with ESI, IMechE, London, UK
8. General Assembly meeting no. 2, (2014), IRCCS Fondanzione Ospedale San Camillo, Venice.
9. GliaLab (Glio Vascular Imaging), (2014), Centre for Molecular Medicine Norway, Oslo, Norway.
10. VPH-DARE Review Meeting, EU Commission (2014), Brussels, Belgium
11. General Assembly meeting no. 3, (2014), Manchester, UK

FEM related Workshops

London Mathematical Society/EPSRC Course on *Continuum Mechanics in Biology and Medicine*, University College London *(17th -22nd June 2012)*.

Attendance at Multidisciplinary Seminar Series/Workshops (5)

1. Workshop. (2015). Oxford Brain Mechanics Workshop: Carnegie Mellon University-Oxford Alliance, St Hugh's College, Oxford
2. Seminar. (2013). Annual Computational Life and Medical Sciences Network Symposium, UCL.
3. Seminar. (2013). Crick Symposium: Exploring the Cell-Material Interface, Senate House, Univ. of London.
4. Seminar. (2012). Crick Seminar Series - The Brain: Understanding Complexity, King's College London.
5. Seminar. (2012). Crick Seminar Series - Infection and Immunity, UCL Institute of Education.

External Consulting

Computational Fluid Dynamics/ Fluid Structure Interaction (FSI) for Vascular Diagnosis: Department of Radiology at Heidelberg University Hospital, Heidelberg, Germany.

Relevant Certifications

1. Deploying `MATLAB` Based Applications-.NET Edition (MathWorks® Training Certificate).
2. `MATLAB` Programming Techniques (MathWorks® Training Certificate).

Additional Qualifications - Saïd Business School

Diploma in Strategy & Innovation (Science Innovation Plus Initiative), Centre for Entrepreneurship and Innovation, University of Oxford (2011-2012). *Project Title*: "Managing the Transfer of Water within the Cerebral Environment". *Abstract*: This report outlined the technological, marketing and organisational hurdles awaiting a start-up company planning to break through into the drug eluting stent market for endoscopic aqueductoplasty.

Contents

List of figures

List of Tables

Acronyms

AD	*Alzheimer's disease*	**FVOO**	*Fourth ventricle outlet obstruction*
AG	*Arachnoid granulation*	**GMRES**	*Generalised Minimal Residual method*
ALE	*Arbitrary Lagrangian-Eulerian*	**HCP**	*Hydrocephalus*
AMG	*Algebraic Multigrid*	**ICA**	*Inferior cerebellar artery*
AQP	*Aquaporin*	**ICP**	*Intra-cranial pressure*
ASCII	*American Standard Code for Information Interchange*	**IIH**	*Idiopathic intracranial hypertension*
Aβ	*Amyloid β peptide*	**ISF**	*Interstitial fluid*
BBB	*Blood-brain barrier*	**LITP**	*Linear Isotropic Theory of Poroelasticity*
BIH	*Benign intracranial hypertension*	**LPH**	*Low pressure hydrocephalus*
BVP	*Boundary value problem*	**MPET**	*Multiple-Network Poroelastic Theory*
CFD	*Computational fluid dynamics*	**MRE**	*Magnetic Resonance Elastography*
CG	*Conjugate Gradient method*	**MRI**	*Magnetic Resonance Imaging*
CP	*Choroid plexus*	**MS**	*Multiple Sclerosis*
CSF	*Cerebrospinal fluid*	**NMO**	*Neuromyelitis Optica*
CSG	*Constructive solid geometry*	**NPH**	*Normal pressure hydrocephalus*
CT	*Computerized tomography*	**ON**	*Optic Neuritis*
CV	*Control Volume*	**PCA**	*Posterior cerebellar artery*
CVD	*Cerebrovascular Disease*	**PD**	*Parkinson's disease*
dG	*Discontinuous Galerkin*	**PDE**	*Partial differential equation*
DICOM	*Digital Imaging and Communications in Medicine*	**PICA**	*Posterior inferior cerebellar artery*
DLB	*Dementia with Lewy bodies*	**SAS**	*Subarachnoid space*
DTI	*Diffusion tensor imaging*	**SIMPLEC**	*Semi-implicit method for pressure-linked equations – consistent*
DWM	*Deep white matter*	**SPET**	*Single-Network Poroelastic Theory*
EA	*Endoscopic Aqueductoplasty*	**SSS**	*Superior sagittal sinus*
ECF	*Extra-cellular fluid*	**STL**	*Stereo Lithography*
EFV	*Endoscopic Fourth Ventriculostomy*	**SVZ**	*Sub-ventricular zone*
ETV	*Endoscopic Third Ventriculostomy*	**TBI**	*Traumatic brain injury*
EVD	*External ventricular drainage*	**Tet4**	*Four node tetrahedral*
EVOH	*Extraventricular obstructive hydrocephalus*	**TFQMR**	*Transpose-free quasi-minimal residual method*
FDM	*Finite difference method*	**TNT**	*Template numerical toolkit*
FEA	*Finite element approximation*	**UDS**	*User-defined subroutine*
FEM	*Finite element method*	**VaD**	*Vascular dementia*
FT	*Fiber Tractography*	**VPS**	*Ventriculoperitonial shunt*
FTD	*Frontotemporal dementia*	**VRS**	*Virchow Robin space*
FVM	*Finite volume method*	**WSS**	*Wall shear stress*

Nomenclature

A_f	Amplification factor	$1/H$	Poroelastic expansion coefficient
p_{bp}	Arterial blood pressure [Nm^{-2}]	η	Porosity
M	Biot modulus	L	Radial distance between ventricles and skull [m]
a	Biot-Willis constant	r_M	Radius of ventricles [m]
$\boldsymbol{F}$	Body force per unit volume of the bulk material	P_{ref}	Reference pressure [Nm^{-2}]
Γ_s	Boundary conditions at the skull	V	Representative volume of a porous material
Γ_v	Boundary conditions at the ventricles	R	Resistance due to AGs [m^{-3}]
ϱ_B	Bulk density [kgm^{-3}]	$\varkappa_{c\rightarrow vent}$	Resistance of the flow from the capillary network to the ventricles via the choroid plexus [m^5skg^{-1}]
K	Bulk modulus [Nm^{-2}]	G	Shear modulus [Nm^{-2}]
K_p	Bulk modulus of the pore volumetric strain [Nm^{-2}]	Q_Δ	Simplex quality
K'_s	Bulk modulus of the solid phase [Nm^{-2}]	β	Skempton's pore coefficient
V_s	Combined volume of the isolated pores and solid phase	r_v	Skull radius [m]
M'	Constant denoting the dependence of permeability of the ISF/CSF compartment to its deformation	ε	Small strain tensor
ϱ_s	Density of solid phase [kgm^{-3}]	Φ	Source/sink density [s^{-1}]
ϱ_f	Density of the fluid phase [kgm^{-3}]	N_h	Space of all continuous piecewise linears
e_{ij}	Deviatoric strain	$C^0(I)$	Space of continuous functions on the interval I
s_{ij}	Deviatoric stress [Nm^{-2}]	$\wp_1(I_i)$	Space of linear functions on I_i
σ_{kk}	Dilatational stress	$d\varepsilon_{ij}$	Strain increment
Ω	Domain	p_s	Subarachnoid pressures [Nm^{-2}]
$1/K$	Drained material compressibility	σ'	Terzaghi effective stress [Nm^{-2}]
ν	Drained Poisson's ratio	N_i	Test function
n_w	Effective area coefficient	J	Time interval
Q_i	Fluid accumulated in each fluid network i	σ_{ij}	Total stress tensor
$d\zeta$	Fluid content increment	ω_{ij}	Transfer coefficient [$m^2N^{-1}s^{-1}$]
$\boldsymbol{q}$	Fluid flux vector	$1/R$	Unconstrained specific storage
Q_{in}	Flux of fluid entering CV [m^3s^{-1}]	K_u	Undrained bulk modulus [Nm^{-2}]
Q_{out}	Flux of fluid leaving CV [m^3s^{-1}]	ν_u	Undrained Poisson's ratio
g_i	Gravity component in the i^{th} direction	ζ	Variation of fluid content
D_h	Hydraulic diameter [m]	ΔV_f	Variation of fluid volume
$\hat{s}_{ij}$	Interporosity flux	p_{bp}	Venous blood pressure [Nm^{-2}]
k	Intrinsic permeability [m^2]	U_v	Ventricular displacement
σ^*	Isotropic compressive stress [Nm^{-2}]	p_v	Ventricular pressure [Nm^{-2}]
δ_{ij}	Kronecker delta	μ	Viscosity [Nsm^{-2}]
λ	Lamé's first parameter [Nm^{-2}]	v_i	Volume fraction
b_i	Load vector	V_p	Volume of the interconnected pore space
M_{ij}	Mass matrix	dW	Work increment
$\mathcal{J}$	Partition	E	Young's modulus [Nm^{-2}]
Re_p	Peak Reynolds number	p'	Π-pressure
v_p	Peak velocity [m/s]	p	Pore pressure [Nm^{-2}]

Motivation, Physiology, Disease & Modelling History

By 2047, the global population will have increased, and the global ageing population will have exceeded the number of children. The world will be facing a situation without precedent. Currently, 44 million people live with dementia [7], whilst by 2050, this number is expected to triple to 115 million [11]. The estimated cost of Dementia will increase from $604 billion in 2010 to $1,117 billion by 2030 [11]. This chapter will outline the motivation for this research, introduce the cerebral environment and its intricate mechanisms, evaluate various diseases allied to Dementia and provide justification for the modelling framework adopted in this work via a thorough review of the pertinent literature.

1.1 Motivation

The world population is expected to increase from 7.2 billion to 10.9 billion by 2100 [12]. The ageing population (those aged 60 and over) is projected to exceed the number of children in 2047. This will be a situation without precedent [13]. In the two most populous countries, China and India, the numeric surge in those aged over 65 rises from a combined 170 million to 557 million by 2050 [14]. What is even more striking is the percentage of the "oldest old", classified as people over the age of 85, who are anticipated to show a 351 percent increase, whilst the global number of centenarians is also projected to drastically increase by 1004 percent by 2050 [14].

The epidemiologic transition succinctly refers to a process in which infectious, infant and maternal diseases (which are all preventable) are brought under manageable limits courtesy of advances in the healthcare sector, which can to various degrees, be attributed to prolonged social and economic development. At the same time however, the increased mimicking of a 'western' lifestyle and its consequent behavioural model has led to chronic diseases (strongly age associated), taking over as the leading cause of mortality in every region of the world [11].

Brain disorders such as developmental and neurodegenerative diseases represent an enormous disease burden, not only in terms of human distress, but also economic cost. Brain diseases affect approximately 38% (including alcohol use and nicotine addiction) of the European population [15], and make up 13% of global disease prevalence [16], at an estimated cost of €789 billion [17].

Considering the scarce resources available to pursue health research in general, some argue of the unfortunate need to prioritise diseases based on cost-of-illness studies [18]. Ranking of diseases based on economic burden is something policy makers are increasingly

aware of, and important emphasis on calculating indirect costs shows the disproportionate underestimation of the financial impact associated with brain disorders [16]. For the UK, Fineberg *et al.* [19] calculated the 2010 cost of individual disorders of the brain to be in the region of €22 billion for dementia alone (ranked first in order of magnitude). Other notable disorders (for comparison) included stroke (€8.5 billion), multiple sclerosis (€2.7 billion) and Parkinson's disease (€2.4 billion) to name a few.

On a global scale, more than 44 million people live with confirmed and diagnosed dementia [7], whilst by 2050, this number is expected to triple to 115 million [11]. The estimated cost of Dementia will increase from $604 billion in 2010 to $1,117 billion by 2030 [11]. Alzheimer's disease (AD) is known to account for up to 70 percent of all dementia syndromes in the US, whilst vascular dementia (VaD) accounts to around 17 percent [20,21]. Dementias of the elderly, such as AD, VaD and Normal Pressure Hydrocephalus (which are known to present with overlapping features [22,23]) are exerting substantial pressures on society, through greater health expenditure arising from the more specialised medical services (differential diagnosis for instance) required for such complex and overlapping pathologies.

At the same time, medical expertise and evidence-driven policymaking and commissioning of services are increasingly evolving the definitive architecture of comprehensive long-term care, which incorporates diagnostic and medical continuing care services, family care, community care (whilst also taking into account cost containment strategies), relief opportunities and palliative end-of-life care [11].

It is therefore important to embrace technological advances, such as those provided by computational science and biomedical engineering, which will allow for an expansion in our ability to model and simulate an almost limitless variety of complex problems that have long defied traditional methods of medical practice. Numerical methods and simulation offer the prospect of improved clinically relevant predictive information, and of course optimisation, enabling more efficient use of resources for designing treatment protocols, risk assessment and urgently needed management of a long term care system for a wide spectrum of brain disorders. Within this paradigm, the importance of the relationship of senescence of cerebrospinal fluid to dementia in the elderly make the cerebral environment notably worthy of investigation through numerical and computational modelling.

1.2 Cerebral Anatomy & Physiology

1.2.1 Anatomy of the cerebrospinal fluid compartment

Figure 1.1 illustrates the cerebroventricular cavity under consideration. In adults, the CSF volume is estimated to be approximately 65 -170 *ml*, where only around 25 *ml* [24,25] are segregated to the ventricles and the remainder occupies the cranial and spinal spaces [26].

1.2.2 Physiology of cerebrospinal fluid

Throughout evolution, the human brain has been known to expand. CSF has supported this increase in size by minimizing its effective weight and by moderating the effects of trauma to parts of the brain against the base of the skull [27]. CSF also normalises the pressure created by, for instance, a temporary obstruction to venous outflow or an expanding mass lesion, as dictated by the Monro-Kellie doctrine (see §1.4.1).

This compensatory mechanism allows the CSF to maintain a constant intracranial pressure (ICP) in normal conditions [28]. The second critical function compensates for the lack of a lymphatic system in the brain. The problem that arises from such a physiological

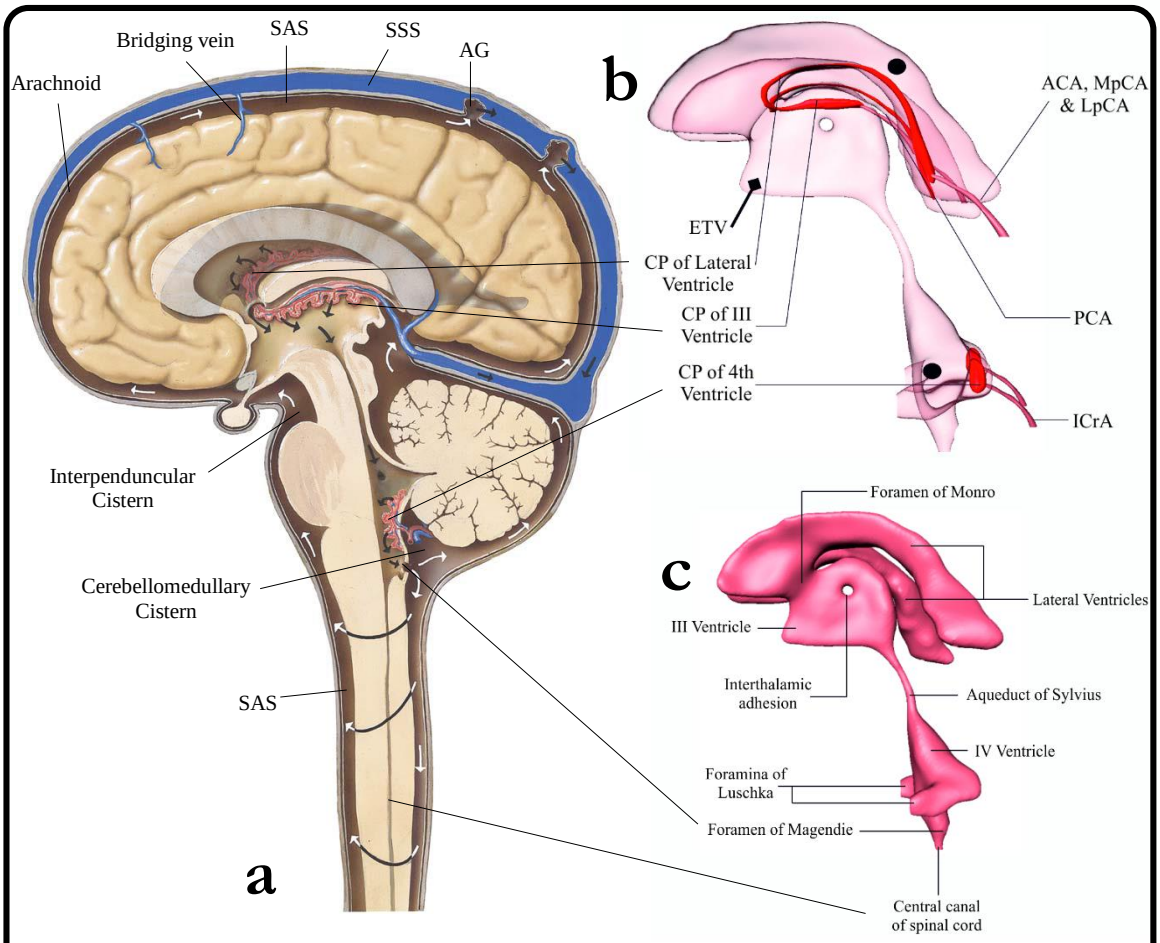

Figure 1.1. *(a) Circulation of CSF according to the classical hypothesis. SSS is the Superior sagittal sinus, SAS is the subarachnoid space and finally AG is an arachnoid granulation. Adapted from Felten DL & Shetty AN, Netter's Atlas of Neuroscience, second edition, Philadelphia: Saunders Company, 2010. (b) CSF circulates through the four brain ventricles and in the subarachnoid space surrounding the brain and spinal cord. (c) View of the ventricular system along with the choroid plexus (CP) of the lateral (LV), 3rd and 4th ventricle. The arteries supplying these plexuses (not all are presented in the figure) are the anterior and lateral posterior choroidal arteries (ACA & LpCA), the P2 segment of the posterior cerebellar artery (PCA) and the medial posterior choroidal artery (MpCA) [6]. The MpCA arises from the PCA (or its branches) and enters the roof of the third ventricle which feeds the CP situated there. Finally, the CP of the fourth ventricle is supplied by the posterior inferior cerebellar artery (PICA), inferior cerebellar artery (ICA) and superior cerebellar artery (SCA) [8-10]. ETV is the location of perforation of the floor of the third ventricle during endoscopic third ventriculostomy. [•] represents the locations of measurement for the deduction of the pressure difference between the lateral and fourth ventricles. Obtained from Vardakis et al. [1]. No permission was required under the CC BY license agreement.*

characteristic is that the extracellular waste products (from the functioning of neuronal and glial cells) must be removed by either collecting in the CSF or passing from the interstitial fluid (ISF) into the venous blood network. A third function is the regulation of the distribution of biologically active substances in the brain [28], as is the case for endocrine actions. For instance it has been shown that a fluctuation in hormone levels in the CSF has an effect on animal physiology [29].

The ratio of CSF production between choroidal and extrachoroidal sources is speculated to be as high as 9:1 [28]. The 10% not arising from the choroid plexuses is assumed to come from the ISF exudate through the pia of the brain. Experiments suggesting the existence of extrachoroidal CSF production include a reduction, but not elimination, of CSF when surgical choroid plexectomy takes place [30]. Recently, the capillary-astrocyte complex in the blood-brain barrier is understood to be an active producer of ISF [31]. Around 600-650 *ml* of CSF is produced each day (with Takahashi *et al.* [32] recording large standard deviations, 510 ± 549 *ml/day*), with a CSF volume turnover of four [26,28,33-35].

CSF formation along the choroid plexus occurs in two stages, utilising a passive filtration mechanism and regulated secretion along its epithelium [36]. The driving force for fluid secretion across the surface of the choroid plexus is primarily thought to be the osmotic gradient arising from the simultaneous movement of water and unidirectional flux of ions from one side of the epithelial layer to the other. The transport of ions is governed by the unequal distribution of ion transporters, co-transporters and ion channels on the apical and basolateral sides of the choroid plexus' epithelial layer. Recent insights by MacAulay and Zeuthen [37] argue that osmotic gradients alone cannot account for water transport across the choroid plexus, and must always be considered with the forcing effects of the membrane transporters. The molecular mechanisms of choroidal CSF secretion are assessed in detail in MacAulay and Zeuthen [37] and Owler *et al.* [38]. Concurrent to the ionic drive, the trans-cellular movement of water into the CSF via Aquaporin-1 (AQP1) channels (situated in high expression on the apical and to a lesser extent the basolateral membrane [36-40]) follows this osmotic gradient [26,28,33,37,41]. There is however, some uncertainty regarding the detailed role of the K^+/Cl cotransporter on the basolateral membrane [37].

1.2.3 The ventricular system

As can be seen from Fig 1.1, the cerebral ventricles are the major CSF containing spaces. When considering adults, the normal CSF circulation proceeds in a consistent and uniform manner since this flow regulation is primarily responsible for cerebral homeostasis [26,28]. The *classical hypothesis* of CSF formulation involves the production of CSF at the choroid plexus of the lateral, third and fourth ventricles (see Fig 1.1). CSF circulation, according to Cushing's concept [42] of the *third circulation*, allows for the transport of CSF from the sites of secretion to the sites of absorption via a unidirectional CSF flow regime within the cerebral ventricles. CSF begins to circulate in the cerebroventricular system by flowing out of the lateral ventricles via the foramen of Monro and into the third ventricle. From there the fluid passes to the fourth ventricle via the aqueduct of Sylvius. The foramen of Magendie and the bilateral foramina of Luschka act as the final outlets of the CSF leading to the subarachnoid space

(SAS). The central canal of the spinal cord also receives CSF from the fourth ventricle; however, in comparison to the foramina of Luschka and foramen of Magendie, this is a minute quantity. Once the CSF has exited from the cerebral ventricular system, it passes through the subarachnoid cisterns surrounding the brainstem (cisterna magna, medullary, pontine, interpenduncular, ambient and suprasellar cistern respectively) before it gets reabsorbed [28].

The form and construction of the lining of cerebral ventricles under normal conditions consists of a single layer of ciliated squamous to columnar ependymal cells [43] which assist the flow through their directional beating. These cells do not regenerate appropriately in response to pathological perturbations, such as numerous modes of ventricular dilatation. Ependymal cell proliferation has been accounted for as part of the overall tissue response, and it has been postulated that the bulk of the deficit is undertaken by sub-ependymal cells [44,45]. The same studies failed to identify a further degree of ependymal differentiation into their corresponding ciliated morphology. Some studies seem to support a novel form of sub-ventricular zone-mediated ependymal repair (SVZ) and astrocyte-mediated regenerative repair of the ependymal lining. However, fully denuded areas do not appear capable of regeneration [46,47]. Ultimately, damaged or altered ependymal cilia can influence the local wall mixing mechanisms, as well as neuroblast migration and even hydrocephalus [448].

1.2.4 The Choroid Plexus (*Plexus choroideus*)

It was Faivre's suggestion [48] and subsequently Dandy's experimental work [49] that showed that CSF was produced within the ventricular cavities by the choroid plexuses. In vertebrates, the choroid plexus (CP) is a highly vascularized structure consisting of granular meningeal protrusions of single layered epithelial cells encapsulating fenestrated capillaries and venules. These have been assumed as the main sites of CSF production, and account for the majority of total CSF production [26,28], however exact production proportions are still in the speculative phase, as it is still unclear as to how extensive both choroidal and extrachoroidal CSF production is [50-53]. Although its total mass is believed to be around 2 *g*, the CSF secretion per *g* is high compared to other epithelial surfaces [28,33,41]. CSF is secreted continuously; however, findings indicate strong circadian variations to its production thought to be due to the finely regulated responsibilities of the autonomic nervous system [26]. Specifically, it has been noted that more (42 ± 2 *ml/h*) CSF is produced around the early morning hours, and less (12 ± 7 *ml/h*) in the early evening [28,34].

In addition to their primary function of producing CSF, the choroid plexuses possess the added impediment of being the most complicated vascular structures in the brain [6]. They can be found in all four ventricular cavities (see Fig 1.1). In the choroid fissures of the lateral ventricles (*Plexus choroideus ventriculi lat*), the choroid plexuses develop from the cisternae of the median walls, whilst in the third ventricle (*Plexus choroideus ventriculi tertii*); they arise from the roof of those entities [28,33,54-57]. In the fourth ventricle (*Plexus choroideus ventriculi quarti*), the corresponding plexus is formed caudally and ventrally of the cerebellum [57].

The macroscopic characteristics of the three types of CP vary in complexity. The CP of the fourth ventricle is extensively lobulated, whereas in the lateral ventricles, it resembles a thin veil. In addition, the CP of the third ventricle is smaller and exhibits an intermediate appearance in comparison to the other two types [54]. A loose connective tissue, experiencing

an external simple cuboidal, or squamous epithelium surrounding a vascular bed embedded within it, is the typical microscopic characteristic of all plexuses in the concluding stages of differentiation [54,58].

The CP is a C-shaped structure and is located at the atrium, temporal horn and the body of the lateral ventricle [6,8]. The CP of the lateral ventricle is split into three main parts, namely: the glomus, the temporal and body portions respectively. The anterior and lateral posterior choroidal arteries (ACA & LpCA) supply the three aforementioned segments, as well as the P2 segment of the posterior cerebellar artery (PCA), the medial posterior choroidal artery (MpCA) and in 10% of witnessed cases [6], the splenothalamic artery. Along the lateral margin of the temporal portion of the choroid plexus runs the inferior choroidal vein. Likewise, for the body portion of the choroid plexus, this is coursed by the large superior choroidal vein [6]. The MpCA arises from the PCA (or its branches) and enters the roof of the third ventricle [8]. The choroid plexus of the fourth ventricle is supplied by the posterior inferior cerebellar artery (PICA) at the point of its midline on its roof, in addition to the medial part of the lateral recess. The anterior inferior cerebellar artery supplies the choroid plexus present in the cerebellopontine angle and simultaneously the adjacent part of the lateral recess. The superior cerebellar artery (SCA) on occasion supplies the floccular (smallest lobe of the cerebellum) portion of the choroid plexus [9]. Venous drainage of the choroid plexus tissue is via the basal, internal cerebral and thalamostriate veins [28].

1.2.5 Aquaporin channels

Water transport in the brain is a profoundly multiscale process. The molecular basis for water transport involves specific cell membrane water channels. These aquaporin (AQP) channels were first discovered by Agre [59,60]. CHIP28 (later coined Aquaporin-1) was the first to be identified. It is a 28 *kDa* protein initially purified from red blood cells and renal proximal tubule membranes [61]. Their affiliation as water channels is assumed to be due to the diameter

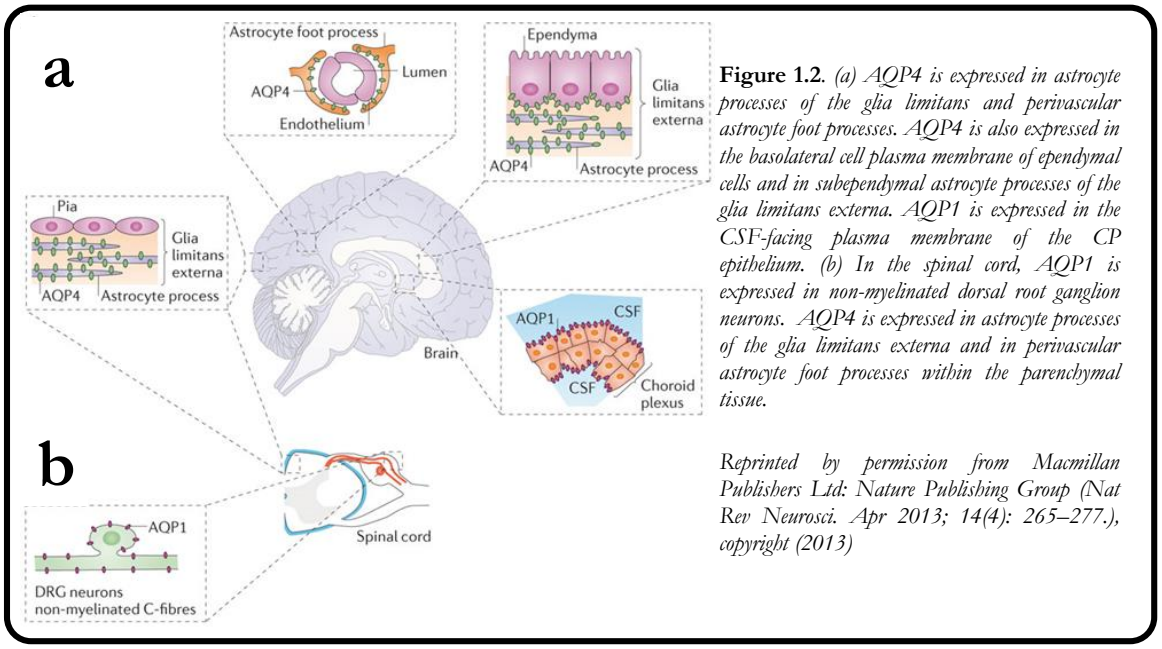

Figure 1.2. *(a) AQP4 is expressed in astrocyte processes of the glia limitans and perivascular astrocyte foot processes. AQP4 is also expressed in the basolateral cell plasma membrane of ependymal cells and in subependymal astrocyte processes of the glia limitans externa. AQP1 is expressed in the CSF-facing plasma membrane of the CP epithelium. (b) In the spinal cord, AQP1 is expressed in non-myelinated dorsal root ganglion neurons. AQP4 is expressed in astrocyte processes of the glia limitans externa and in perivascular astrocyte foot processes within the parenchymal tissue.*

Reprinted by permission from Macmillan Publishers Ltd: Nature Publishing Group (Nat Rev Neurosci. Apr 2013; 14(4): 265–277.), copyright (2013)

of the pores themselves [62]. AQPs are defined as a set of integral membrane transport proteins with a primary function of facilitating water movement across cell membranes in response to osmotic gradients [63]. Diffusion alone cannot account for the rapid passage of water across certain membranes [64], hence the conceptual development that guided the search for and eventual discovery of AQPs [38,59]. The total number of AQPs is growing, however; to date there are 14 distinct family members [36,63,64] identified in humans and rodents (with eight involved in transporting water). These members are split into three subgroups, namely: Aquaporins which are permeable to water, Aquaglyceroporins, which are permeable to water, glycerol and urea and finally unorthodox Aquaporins, whose functions are yet to be fully understood [65-67].

Within the central nervous system (see Figure 1.2), the AQPs (1, 4 and 9) present well-established physiological roles and implications in pathology [68]. AQP1 is mainly situated on the apical membrane of the choroid plexus epithelium and is solely permeable to water, which in turn follows the aforementioned osmotic gradient. This AQP is important in sustaining the osmotic permeability of the apical membrane. The clinical and pharmaceutical importance of investigating AQP1 were highlighted in a recent study where rats with kaolin-induced hydrocephalus presented a regulatory mechanism (CSF secretion) via choroidal AQP1 endocytosis [69]. Some reports indicated sparse populations of AQP1 on the basolateral membrane of the CP epithelium; however these reports are not widespread in the literature [39,70]. It is also believed that AQP1 plays a sensory role in detecting osmolarity fluctuations and orchestrates finely tuned transport rates [68]. A comprehensive review on AQP1 was recently conducted by [71].

AQP4 is the most predominant aquaporin in the brain, and is located on the external and internal glial limiting membranes, the basolateral membrane of ependymal cells and astrocytes [38,63]. In the latter, AQP4 occupies three key locations, namely the perivascular astrocyte end feet, perisynaptic astrocyte processes and in processes that involve K^+ clearance, such as nonmyelinated axons and the nodes of Ranvier [72]. This tactical distribution suggests that AQP4 controls water fluxes into and out of the brain parenchyma. AQP4 has been deemed to possess the essential role of controlling the water balance in the brain [61,63,64,72-75].

AQP9 is the only aquaporin present in neurons of the brain. It is found in ependymal cells and tanacytes (lining the third ventricle) and astrocytes, in glial cells in the pineal gland, as well as brain stem catecholaminergic neurons [72,76]. It is also suggested that AQP 4 and 9 may complement each other by aiding water to traverse between CSF and brain parenchyma [77].

The key roles of AQP1, AQP4 and AQP9 in specific CNS pathologies as discussed by [63,68,74,78-82] include: Brain oedema (AQP4), Brain Trauma (AQP4), Brain Tumours (AQP1, AQP4) [83,84], Stroke (AQP4, AQP9), Dementia (AQP1, AQP4), Autism (AQP4), Migraine (AQP1), Neuromyelitis Optica (AQP4) and Hydrocephalus (AQP4). The latter has also been confirmed by a very recent study which concluded that there was a significant increase in astrocytic AQP4 in the human hydrocephalic cortex [85].

1.2.6 Cerebrospinal Fluid reabsorption

It is understood that CSF absorption is more complex than the existing classical theory, which dictates that CSF flows through the ventricular cavities, out into the SAS and finally resorbed by the arachnoid villi embedded in the dura mater of the superior sagittal sinus (SSS) which mainly lie over the vertex of the pros encephalon [28,31,86]. These villi respond to a positive hydrostatic gradient between CSF and dural venous blood which in turn paves the way for the creation of pores or vacuoles that facilitate the unidirectional transcellular transport of CSF into the venous blood stream [28].

As opposed to the highly orchestrated transport process of CSF secretion, CSF absorption occurs via other outflow mechanisms, such as along the sheaths of major blood vessels and cranial nerves [50]. There has been research outlining a new link between cerebral interstitial fluid, CSF and extra cranial lymph [56,87-89]. In animal experiments by Johnston and colleagues, it was found that there were multiple areas of extracranial lymphatic drainage designated for CSF and in addition, the ratio of CSF-to-lymph clearance to total CSF removed accounted for just below 50% [87]. This functionally intimate association between CSF and extracranial lymph currently provides the view that extracranial lymphatic vessels receive large quantities of CSF (in mammals other than humans, as no human *in vivo* evaluations have taken place). The shift towards CSF drainage via the olfactory route (for instance into the nasal lymphatic system [90]) does not nullify the impact of the classical hypothesis. Instead, it is assumed that under conditions of elevated CSF pressure, CSF clearance may be additionally mediated by the arachnoid villi to facilitate the stabilisation of ICP [31]. Studies have also indicated that CSF reabsorption occurs along the spinal nerves [91] and across capillary aquaporin channels [92-95]. In 2006, Oi and Rocco [96] put forward a theory classifying hydrocephalus with emphasis on the 'minor pathway' present in small mammals and developing immature brains (embryo, foetus and infants) in humans. The authors hypothesise that arachnoid granulations begin their ontogenesis (as part of the classical CSF reabsorption route) later on in life (between 7-20 years of age). It is envisaged that CSF dynamics are maintained by offering a drainage route through perineural spaces into the lymphatic system (perineural lymphatic channels), via transependymal to perivascular spaces in the brain/spinal cord and finally via the choroid plexus epithelium to the fenestrated capillaries and into the galenic venous system (deep venous structures) [96,97].

Iliff *et al.* [98] observed that CSF enters the parenchyma along visible paravascular spaces which surround the penetrating arteries. In addition, they observed that ISF and CSF (there is a functional unity between the two fluids during filtration and reabsorption [99]) moving through the parenchyma are cleared along the same paravenous drainage pathways (in particular, those surrounding the larger calibre medial internal cerebral and caudal rhinal veins). An important conclusion reached by the authors is that astroglial AQP4 support the convective bulk ISF flow (as opposed to diffusion) that ultimately drives the clearance of interstitial solutes from the brain parenchyma. This led them to coining the "glymphatic" pathway to account for the characteristics displayed by this new brain-wide pathway, of possessing both a lymphatic like system (interstitial solute clearance) and the AQP4 dependent astroglial water flux responsible for the clearance of solutes and fluid from the parenchymal

tissue. It is then claimed that the solute and fluid egress is possibly distributed into the subarachnoid CSF which enters the bloodstream via post capillary vasculature or may follow the walls of draining veins to reach the cervical lymphatics. When the aforementioned spinal nerve and arachnoid villi reabsorption mechanisms become saturated by the surplus fluid, it is imagined that the expression of AQPs in the choroid plexus, perivascular membranes and the ependymal cells of the cerebral ventricles may participate in the stabilisation of ICP. In particular, Skjolding *et al.* [100] recorded neuroprotective observations of a decreased abundance of AQP4 in rat brains in periventricular regions two days after hydrocephalus (see §1.3.1). This is in accordance with symptoms observed with acutely raised ICP. The aforementioned authors showed that after two weeks, there was an increased abundance of AQP4 expression in astrocytic processes of the same region, indicative of a near-normal ICP phase. This observation warrants the additional element of pharmacologically regulated AQP expression to regulate the fluid imbalance which is a direct result of improper reabsorption [31,93-95,100]}.

1.2.7 Virchow Robin space

Virchow-Robin spaces (VRS) are pial-lined, interstitial, fluid-filled structures that accompany penetrating arteries and arterioles as they enter the cerebral substance [101]. Important developments are currently taking place in the understanding of the microanatomy of the Virchow Robin space (VRS), accompanied by an ongoing replacement of its previously perceived physiological unimportance. For a detailed understanding of current developments surrounding the VRS, the reader is referred to Brinker *et al.* [36]. The second figure of the aforementioned article succinctly describes the ongoing developments. More specifically, the VRS allows for a bidirectional exchange of fluid between the extracellular space and SAS controlled by the glial and pial membranes. The basement membrane of arteries, arterioles and capillaries are understood to contribute as additional directional pathways to facilitate drainage of ISF and solutes into the lymphatic system. The glymphatic pathway and subpial perivascular spaces are tightly interconnected with ongoing developments [36].

1.3 Diseases of the Cerebral Environment

1.3.1 Hydrocephalus

Hydrocephalus (HCP) can be succinctly described as the abnormal accumulation (imbalance between production and circulation) of CSF within the brain [102-106]. This balance of CSF production and reabsorption normally allows the maintenance of the CSF pressure to lie within the approximate range of 600-2000 Pa [107]. HCP cannot be considered a singular

pathological entity, but instead, a consequence of a variety of congenital and acquired disorders present within the CNS [104]. HCP is classified with regards to whether the point of CSF obstruction or discrete lesion lies within the ventricular system (obstructive) and obstructs the flow before it enters the SAS [25], or not (communicating). Obstructive HCP can also be sub-classified as Hyperacute (obstructive), Progressive acute (obstructive), Chronic obstructive, Extraventricular obstructive (EVOH), Foetal and true congenital HCP [56]. Communicating HCP is described in more detail in §1.3.3.

1.3.2 Obstructive HCP

Hyperacute obstructive HCP is known to develop over a very short period of time, notably a few hours, due to a largely instantaneous obstruction of the CSF pathways. The cerebral cavities are subsequently rounded and various draining veins are compressed, which in turn increases the overall ICP in the brain and may lead to a circulatory arrest [56]. The progressively acute case of obstructive HCP develops due to tumour growth within the ventricular cavities over a period of weeks or months. There is an evident loss of compliance, and the cerebral ventricles (and in some cases the skull) possess an increased pressure and enlarge considerably. The increased ventricular pressure can ultimately lead to an accumulated periventricular oedema since it inhibits the correct drainage of ISF. As in the previous case, a circulatory arrest may arise [56].

A tabulated summary of the various forms of obstructive hydrocephalus discussed is given in Table 1.1. Chronic obstructive HCP represents a rather silent morphology. There are no signs of elevated ICP or oedema; however, signs of visible ventriculomegaly and skull enlargement are evident [56]. EVOH is a form of benign HCP present in the very early stages of infant development, usually before 18 months, as after this the cranial sutures close. It is believed that this is caused by ill-developed arachnoid granulations [56,108] in the vicinity of the frontotemporal region. EVOH is recognised by visible craniomegaly and elevated venous pressure [109]. It has also been suggested that EVOH may develop due to the thrombosis of the superior vena cava (SVC thrombosis) after cardiac surgery in neonates and infants [110].

1.3.3 Normal Pressure Hydrocephalus (NPH)

This form of HCP possesses no radiographically identifiable flow obstruction, however, there is evidence of craniomegaly and ventriculomegaly taking place [56,102,104,106,111-113]. No consensus on the name exists, and several eponyms are used: adult hydrocephalus syndrome, chronic adult hydrocephalus, hydrocephalic dementia, communicating hydrocephalus and occult hydrocephalus [114]. It has been suggested that the primary cause of this form of hydrocephalic disorder which affects the homeostatic features of the Monro-Kelly hypothesis can be attributed to a decreased meningeal and/or cerebral arterial compliance [86,111]. Interestingly, the amplitude of the pulsating arterial flow rate during systole can also be identified with the aid of cine phase-contrast MRI as a measurement medium [115].

Table 1.1 Segregation of obstructive hydrocephalus. '=' denotes no change, 'E' denotes enlargement Adopted from [56].

Type	Time scale	Ventricular Size	Vascular Bed	Interstitial Oedema	Skull	Outcome
Hyperacute	Hours	=	Compressed	No	=	Circulatory arrest
Progressively acute	Weeks/Months	Increases	Compressed	Yes	= / E	Decompensate
Chronic obstructive	Months/Years	Increases	=	No	E	Slowly increases
EVOH	Up to 18 months	Increases	=	No	=	Resolves spontaneously

In addition, systolic pressure pulse waves play an important role in determining the severity of communicating hydrocephalus, since their propagation towards the cerebral capillary bed is increased when there is a decrease in the compliance of the cerebral arteries [86,111].

Idiopathic normal-pressure hydrocephalus (iNPH) is regarded by many as a potentially treatable form of dementia. It is defined by the Hakim triad of symptoms [116], specifically the cardinal features of gait impairment, incontinence, and dementia. It is also most common in adults over the age of 60, and equally common in both sexes [117]. Ventriculomegaly in the absence of elevated ICP is simultaneously attributed to the aforementioned symptoms [117-126]. To complicate matters further, Relkin *et al.* [123] further subdivide the classification of iNPH into probable, possible and unlikely categories.

1.3.3.1 Epidemiology

NPH studies have shown a variation in incidence (most likely due to the inconsistent definition of the disorder), ranging from 2-20 per million per year [127-129]. Brean and Eide [125] found an incidence of 5.5 per 100,000 and a prevalence of 21.9 per 100,000 for suspected iNPH in a Norwegian population study, whilst the Osaki-Tajiri Project in Japan recorded the prevalence of possible iNPH in elderly adults in Japan to be 1.4% [126]. In the US, Maramarou *et al.* [130] reports that at least 21.1% of four nursing homes patients have gait impairment, and where just over 9% have dementia, and nearly 15% have incontinence. A useful review by Conn (a physician who is also a patient), makes the generalisation that 1% of the US population will develop NPH as they approach the age of 80 [131]. Part of the reasoning behind this figure is due to the oversimplified definition of the disease, and some of the overlapping and indistinguishable features of gait disturbance between iNPH and Parkinson's disease (PD) [119,120,123,124,131,132]. Rosseau gives a list (29 items) of comorbidities, which include AD, PD, VaD, HCP disorders (including aqueductal stenosis), neurodegenerative disorders (including Frontotemporal dementia), infectious diseases (including HIV), urological disorders (including bladder/prostate cancer) and even Traumatic Brain Injury (TBI), depression and spinal stenosis [120].

1.3.3.2 Imaging

Neuroimaging is an essential tool in assessing ventriculomegaly (quantification of this is deemed by CT or MR images reflecting an Evan's index of 0.3 or greater [120,123,124,133]).

Important radiographic findings in NPH include: periventricular hyper-intensities, increased CSF flow velocity in the Sylvian aqueduct, thinning and elevation of the corpus callosum on sagittal images, a narrowing of the CSF space at high convexity/midline areas relative to Sylvian fissure size and absence of a visible obstruction to CSF flow [115,123,124,134,135].

1.3.3.3 Pathogenesis and Pathophysiology of iNPH

The exact pathophysiological mechanism is still unknown, however CSF malabsorption (as in secondary NPH) alone is increasingly discounted as the main cause [114]. An association between iNPH and cerebrovascular disease (CVD) is well supported. Neuropathological studies of the brain of hydrocephalic patients depict signs of CVD such as sclerotic arterioles [136,137]. It is postulated that ischemia in the deep white matter (DWM) reduces the tensile strength and elasticity, thus facilitating ventriculomegaly. This is particularly evident in the case of a simultaneous decrease in CSF absorption [114]. Leukoaraiosis of the periventricular and DWM is also common [134]. Recent evidence suggests that a proportion of leukoaraiosis is the consequence of small white matter infarcts in the vulnerable periventricular region in patients with aggressive cerebral small arterial diseases [138]. The contribution of CVD in iNPH is favoured by clinical [139], autopsy [136], biopsy [137], and MRI findings [134] of CVD in patients with iNPH, including those improving after shunt surgery.

The arterial pulse pressure and the arterial pulsations in the ICP curve have gained recent interest. Radford *et al.* [140] conclude that both systolic and pulse pressures contribute to the development of increased ventriculomegaly. In addition, the amplitudes of cardiac-related ICP pulsations have been suggested to be a worthy predictor of good outcome (and possible design of shunt adjustments) after shunting patients with iNPH [141]. Dombroski *et al.* [142] presented results of a clinical trial confirming a change in pulsatility associated with CSF drainage, confirming the role of a coupled CSF-vascular compliance. Experimental results show that normal supratentorial compliance (maintained by cortical veins) results from venous vessel compression and sub-arachnoid CSF flow [143]. Bateman suggests that NPH may give rise to an elevated superficial venous pressure [144]. Treatment methods for NPH are discussed in §1.3.6.

1.3.4 Low Pressure Hydrocephalus

Low and negative pressure hydrocephalus (LPH) possesses a mystifying aetiology [145-147], and it is commonly associated with chronic hydrocephalus. LPH is defined by the presence of very low or negative ICP and ventriculomegaly. An important finding in this disease is increased periventricular fluid at normal or low ICP [148]. LPH patients tend to have enhanced brain permeability in the periventricular region. The parenchyma of LPH patients is also observed to be very compliant. Akins *et al.* [148] make the important consideration that a poroelastic approach is ideally suited in facilitating further understanding of LPH.

When considering small transmantle pressure gradients, Levine [149], through his poroelastic model, argues that if the brain is relatively incompressible (Poisson's ratio ~ 0.5), there is an efficient transmission and high ICP required to maintain a mini transmantle pressure gradient (~ 0.5-1 *mmHg*) resulting in ventriculomegaly. This gradient is dictated by the severity of any

obstruction to CSF and the availability of multiple absorption paths (such as the blood networks and associated porous properties). On the other hand, if the brain is more compressible, the parenchyma attenuates any subsequent increase in ventricular pressure, reducing overall transmission to the skull, therefore negating the need for an increased ICP above normal levels to maintain the mini-transmantle pressure gradient. This latter response is deemed by Levine to lead to NPH, and is better suited to cases where the aforementioned alternative absorption paths have enough time to develop and embrace the additional burden of the pressure gradient. Treatment of LPH includes titrated external ventricular drainage and VPS [146,150].

1.3.5 Stenosis of the Aqueduct of Sylvius

Cinalli *et al.* describe the aqueduct as a curved conduit around 15 *mm* in length and up to 3 *mm* in width, with concavity towards the base of the skull [151] and a highly variable cross section, where there is a shape transition from triangular (cranial orifice), oval in the central area and finally resembles an inverted "U" at the level of the inferior colliculi [152]. The interior lumen of the Sylvian aqueduct is lined with ependymal cells [43]. The cell thickness however, is not confined to being unicellular, and in some cases ependymal cells may even be absent from the lining of the aqueduct. These denuded areas pose a problem since they may lead to the bridging of the canal via an overproduction of glial fibrils. Just shy of the walls of the Sylvian aqueduct, isolated clusters of ependymal cells are also witnessed. The sub-ependymal glial plate possesses similar attributes regarding position and cell density [153].
Histopathological classifications of "nontumoral aqueduct anomalies" have been confirmed as Stenosis, Forking, Septum formation and Gliotic stenosis [151,154,155]. During stenosis, the aqueduct is forced to narrow and the ependymal lining of the lumen remains intact. Forking introduces a splitting of the aqueduct into two or more separate channels that may possess conduits of communication between each other [151]. Septum formation takes place when the aforementioned glial overproduction is confined to the lower end of the aqueduct and slowly forms a thin border of translucent membrane due to the sustained pressure and dilatation of the Sylvian aqueduct [156].

Gliotic stenosis may be considered an acquired condition and is characterised by the occlusion of the aqueduct due to an overproduction of glial fibres or the creation of multiple channels that lack an evident ependymal lining [151].

1.3.6 Approaches to Treatment

The first treatment of HCP was performed in Greece by Hippocrates, in the 5th century B.C [157]. This surgical treatment involved the puncturing of a lateral ventricle in a patient with obstructive HCP. Since then, CSF shunting was (until recently) considered as the preferred method of choice [105]. Stagno *et al.* make an important point in their paper that the management of HCP in general strongly reflects the political, cultural and of course the socioeconomic condition of a country. In developing regions such as East and Central Africa (amongst others) the most common paediatric neurosurgical problem is infant HCP. The burden on society is reflected in the numbers for prevalence and incidence [158]. In developing

countries, there are no reliable estimates of HCP, and it is evident from the ratio of trained neurosurgeons to total population in various countries that it is severely underestimated. In Tanzania the ratio of trained neurosurgeons to total population is as sparse as 1 to 18 million and in Rwanda and Malawi there is none [159]. Warf states that in Uganda, the administration of successful HCP treatment is being hindered by the lack of local understanding of the disease, and it is common to encounter families choosing to acknowledge alternative expensive and simultaneously clinically questionable therapies [159].

Recently, the emergence of endoscopy has allowed for new possibilities, completely changing the landscape for the management of HCP. The plethora of advantages stems from its ability to create alternative CSF pathways or restore existing ones in addition to reducing CSF absorption. Currently, ETV is considered as the treatment of choice for a variety of HCP related disorders [160-162]. Satisfactory endoscopic management is not widespread, and worldwide uniformity remains an ongoing challenge [105].

1.3.6.1 External Ventricular Drainage

External Ventricular Drainage (EVD) is a widely used neurosurgical procedure involving the placement of a silastic catheter in the lateral ventricles. This catheter is led to an external draining system which facilitates the relief (and subsequent monitoring) of raised ICP to nominal levels. EVD is a simple and safe procedure, where the functional accuracy has been documented as being as high as 87% when adapting it to specialised grading systems [163]. At present, it can be considered as a useful emergency treatment for temporary HCP (in addition to its usefulness as a diagnostic procedure), for instance following a subarachnoid haemorrhage. Other reasons for implementing this procedure include cases when CSF is infected, or blood stained [104].

1.3.6.2 Ventricular shunting

A ventricular shunt can be defined as a device that transports CSF from a point of intracranial production to a subsequent site of extracranial absorption. Currently, ventriculoperitoneal shunting (VPS) is the most popular method for treating HCP, as it's considered that the peritoneum is the best site for CSF reabsorption [164]. Ventriculoatrial (VA) shunts are used to transfer CSF from the ventricles to the right atrium of the heart. VA shunts are considered an option for continuous CSF drainage. A notable disadvantage is the need to cannulate a vein in the region o the neck [460]. The main components of a shunt system consist of a silicon rubber proximal catheter, a one way valve (shunt valve, differential pressure valve with anti-siphoning device, flow control valves, gravity-attenuated valves and programmable-adjustable valves) which controls the CSF flow, and finally a silicon distal catheter which transports CSF to either the peritoneal or pleural cavity or the cardiac atrium [164]. As in EVD, the shunt procedure involves placing the proximal catheter into the lateral ventricle via a burr hole. The distal catheter on the other hand is passed subcutaneously with the aid of a tunnelling device such as a trocar [104,164].

As mentioned earlier, shunting is considered a popular surgical procedure, however, this record is marred by the variety of complications that could arise from choosing this

treatment. Various authors describe these complications [104,105,165-171], however, they can all be organised into the following categories: infection [172], blockage, overdrainage (anti-siphon devices limits this effect), shunt ascites/abdominal pseudocyst [173] and disconnection/migration/malposition.

In addition to the possible shunt complications outlined above, it is estimated that between 20-40% of shunt placements are expected to fail after the first year, and this figure rises to 50% after two years. In the USA, the average cost of shunting was estimated (in 2005) to be approximately $35 000 [105,159,174]. An equally controversial statistic is that the cost of a shunt system in the developing world can cost 10-60 times less. Inexpensive shunts have been developed and are currently in use in India and Sub-Saharan Africa, such as the Harare and Chhabra (~ $50) shunts. The Chhabra shunting system was compared to the Codman®-Hakim® Micro Precision shunt system via a randomised prospective trial. The inexpensive system showed an equivalent incidence in terms of complications in comparison to its more established counterpart [105,159].

Very recent studies by Nigim *et al.* [175] compared metrics from 232 patients with and without NPH who underwent VPS via the conventional open surgical approach, to data from patients who had laparoscopic VPS surgery, and subsequently followed these patients longitudinally to observe a significant difference in shunt failure rates and patterns in addition to further recommending the study of laparoscopic techniques. Nakajima *et al.* [176] recently concluded that lumboperitonial shunts (LP) are as effective as VPS in the treatment of iNPH, although they do suffer from high complication rates (see *Table 3* of Nakajima *et al.* [176]).

1.3.6.3 Endoscopic Third Ventriculostomy

As already described, ventricular shunting suffers from various complications, and there are strong incentives for neurosurgeons to find alternative modes of intervention. ETV was initially restricted to patients with triventricular HCP, where a bulging translucent floor of the third ventricle floor was evident, and where a patient's age was greater than two years [177]. In recent years, the list of possible suitable candidates has increased dramatically, especially patients which exhibit a lack of communication between the ventricles and the subarachnoid space. In addition, the patient age constraint has been relaxed [155]. Many recommend that ETV be suggested as a first-line treatment to all patients that require management of HCP [155,177-183].

Advances in endoscope optics, lighting systems, high resolution MRI, 3D CISS sequence, miniaturised CCD cameras, telecontrolled neurosurgery and developments to endovascular techniques to minimise surgical trauma have also played their role in promoting the use of ETV over recent years [177,184-186]. The ETV technique involves passing an endoscope (a good outline of current neuroendoscopic instrumentation and micromanipulator systems can be found in [186,187]) into the (left or right) lateral ventricle via a burr hole in the frontal region. Once various anatomical landmarks of the lateral ventricle of choice have been identified [155], the endoscope trajectory is then aligned towards the foramen of Monro and the tip of the scope is aimed towards the medial canthus of the ipsilateral eye and towards the contralateral external auditory meatus in the anterior/posterior plane. It is this approach that leads to the floor of the third ventricle [188,189] however care must be taken to avoid the

fornix [190]. The enlarged third ventricle will have its thin floor stretched due to HCP, and it will resemble a translucent membrane. Various landmarks are identified, such as the mammillary bodies, basilar artery and infundibular recess [25,104,155,188]. This floor is perforated and enlarged via various means such as a Fogarty, balloon catheter, Grotenhuis perforation and dilation techniques [190] or Decq forceps [191], thus creating an artificial opening into the basal subarachnoid spaces. In both adult and infant cases, the Liliequist's membrane [192] (arachnoid membrane) is penetrated and dilated using a Fogarty or balloon catheter. Atraumatic methods such as saline jet irrigation have also been mentioned in the literature [188]. It is worth noting that recent studies on patients with obstructive hydrocephalus indicate a strong correlation between the degree of enlargement of the third ventricle and the thickness of the third ventricle floor [185]. The final goal of the surgery is to witness the pulsatile nature of the floor of the third ventricle, since this inevitably portrays the flow of CSF through the artificial stoma [155].

Complications surrounding ETV include bradycardia, asystole, hypothalamic damage, vascular damage and stoma occlusion (which can be treated with stenting techniques) to name a few [180,193,194]. When compared to shunts, ETV lacks problems in the domains of disconnection, occlusion overdrainage and valve dysfunction. Since the ETV technique promotes the natural way of draining CSF, there are no over-drainage problems [171]. Other important advantages of ETV over shunts include a low infection rate [155,195]. A recent study by Kandaswamy and Mallucci has attempted to outline the efficacy of ETV, and concluded that ETV has high success rates for primary and secondary (post shunt malfunction) ETV groups present in their study [179,195]. In addition, repeated ETV procedures are also considered to be safe following its favourable complication rate to shunting (5%), and primary and repeat ETV success rates between 60-87.5% [171,182,196]. A very thorough comparative analysis between ETV and shunts was conducted by Kulkarni and colleagues in 2010 [197], which concluded by specifying that ETV possesses an initially higher failure rate than a shunt, but if the threshold of 3 months is surpassed the level of risk drops below that of the shunt. In the same year, a small study by the same group presented a method for predicting the probability of ETV success and failure, however, a drawback was that the sample size for this assessment was small [198]. Earlier studies by [184] showed high (>75%) long term shunt independence due to ETV for a variety of pathologies within the spectrum of noncommunicating HCP. The promising future of ETV is fortified by various other authors echoing their positive assessments of the procedure [180,183,199-202]. A retrospective analysis of a long-term study (average observational period approached 6 years) on VPS and endoscopic ventriculocisternostomy (EV) treatment of HCP (aqueductal stenosis, posthaemorrhagic, tumour, idiopathic and others) was also recently published by Gliemroth *et al.* [182], and concluded that EV outperforms in terms of required revisions (13.89% for EV, 31.15% for VPS) and complications (9.4% for EV compared to 42.7% for VPS).

A recent study by Bonis *et al.* [203] argue that the ETV procedure should also be reconsidered for the treatment of post-traumatic HCP, especially in light of recent success with patients exhibiting elevated ICP.

1.3.6.4 Endoscopic Fourth Ventriculostomy (EFV)

In 2011, a special case of atresia of the foramina of the fourth ventricle was witnessed by Gianetti *et al.*, [204] where prior shunting was unsuccessful and where the size of the foramen of Monro and third ventricle prohibited the planning of an ETV procedure. A burr hole was created as in ETV and the fourth ventricle was approached via the cerebellar hemisphere. Translucent membranes were seen to occlude the aforementioned foramina (atresia). A monopolar cautery and a Fogarty catheter were used to puncture and dilate the openings made in the occluded membrane. As in ETV, CSF was noted to pulsate and the procedure was noted as a success [204].

EFV has the advantage in that all three CSF exits in the fourth ventricle can be opened, which is irrespective of the level of ventricular dilation or contraction of the rest of the ventricular system. Indeed, other methods which proposed opening of an occluded foramen of Magendie via the navigation of an endoscope via the Sylvian aqueduct caused free irrigation to cease since the size of the endoscope completely occludes the aqueduct, posing the threat of bradycardia [205] and increasing pressure in the region. EFV on the other hand does not possess a threat to irrigating solutions.

EFV therefore may prove to be a sound alternative (since ETV is considered as the preferred option for various types of Fourth Ventricular Outlet Obstruction [206] and sequestrated or trapped fourth ventricle [178]) treatment in cases where ETV was not available.

1.3.7 Overlapping diseases of the cerebral environment

1.3.7.1 Cerebral Oedema

Cerebral oedema is the tangible swelling produced by expansion of the interstitial fluid volume or, more simply, an increase in water content (above the normal brain water content of ~ 80%) and a customarily response to primary brain insult [207,208]. Cerebral oedema is usually classified into the major subtypes: cytotoxic, vasogenic, interstitial or combined. Most brain injuries however involve a combination of these subtypes, making overall classification difficult.

- *Cytotoxic oedema* results from intracellular accumulation of the cellular elements (neurons, glia, and endothelial cells) because of derangements in ATP transmembrane pumps, and ultimately affects both grey (affected first due to higher astrocytic density) and white matter. The BBB is known to initially remain intact [207-209].
- *Vasogenic oedema* results from breakdown of the tight endothelial junctions that forms the BBB due to increased vascular permeability, as commonly encountered in traumatic brain injury (TBI), and inflammatory conditions. It predominantly affects white matter (lower density and numerous unconnected parallel axon tracts). It is considered a very common form of oedema [207-209].
- *Interstitial oedema* is considered a consequence of impaired CSF outflow (as in obstructive HCP), leading to increased intraventricular pressure and a compromised ependymal lining. This leads to increases in transependymal CSF flow migration into the parenchyma, and generally into the periventricular regions. The key difference between the resulting CSF compositions and that due to vasogenic oedema is that it is almost devoid of protein [207,208].

- *Combined oedema* is a mixed pattern of both vasogenic and cytotoxic oedema. Causes of this type include trauma, infection or inflammation, hypoxic-ischemic encephalopathy, osmotic oedema (both intra and extra-cellular components are involved) and hydrostatic oedema [208].

It should be noted that AQPs are widely considered as key players in the resolution of oedema, owing to their regionally distinct distribution [209,210]. More specifically, AQP4 is believed to evoke an interrelation between cerebral oedema and neuroinflammation [63,210]. The glymphatic system and its regulation is considered to play an active role in developing key therapies for oedema. Thrane *et al.* [81] suggest that vasogenic oedema is representative of prolonged increase of glymphatic fluid influx that assist in paravascular leukocyte and cytokine delivery.

1.3.7.2 Chiari Malformation

Chiari malformations (CM) are a group of four to six syndromes (Type *0*, *1.5*, *I*, *II*, *III*, *IV*) which describe the protrusion of brain tissue into the spinal canal through the foramen magnum. CM is classified by the severity of the disorder and the anatomical features protruding into the spinal canal:

- *Type I*: Involves the caudal descent of the cerebellar tonsils into the foramen magnum for at least 3–5 *mm*. It is also associated with a stretched fourth ventricle [211,212].
- *Type II (Arnold-Chiari)*: It is the most common form of CM, and involves the caudal descent of the cerebellar vermis, the fourth ventricle, and the lower brain stem, and importantly is intimately associated with a myelomeningocele and HCP (over 90% requires treatment [213]). Ventricular abnormalities include a small, stretched fourth ventricle that is displaced into the cervical canal accompanied with an outward projecting choroid plexus, reduced aqueduct, a 'saw tooth deformity' of the third ventricle [214] and colpocephaly [215]. It is presumed that it may also be linked with spina bifida [211]. An important characteristic is that it is the leading cause of mortality in patients with treated myelomeningocele [211]. It is anticipated that AQPs also play a role in the oedematous areas of Type II CM [216].
- *Type III:* This form is characterized by caudal displacement of the medulla and herniation of the cerebellum into an occipitocervical meningocele. Obstructive HCP (aqueductal stenosis or Dandy-Walker malformation) is present in 50% of cases [211].
- *Type IV:* This is the least frequent form of CM and is defined by hypoplasia/aplasia of the cerebellum in addition to morphological alterations of the pons and brainstem [211].
- *Type 0 & 1.5*: CM-0 involves syringohydromyelia with possible cerebellar tonsillar herniation and is also characterized by an alteration in CSF dynamics at the level of the foramen magnum [211]. CM-1.5 involves a caudal displacement of the brainstem, along with cerebellar tonsil ectopia, in the absence of spina bifida [217]. Markunas *et al.* [218] recently observed that CM-0 and CM-I share a common pathophysiological mechanism, which is possibly underlined by genetic or epigenetic factors.

It has been estimated that the condition occurs in about one in every 1,000 births. The increased use of diagnostic imaging has shown that CM may be much more common. It is also believed that children who are born with the condition may not show symptoms until adolescence or adulthood, if at all. CMs are more common in females than in males, and CM-II malformations are more prevalent in certain groups [219].

Treatment of CM-I involves either bony decompression (BD), BD with duraplasty, tonsil resection and posterior fossa decompression surgery [220,221]. CSF diversion (shunting) and ETV is also used when HCP is observed (as the treatment algorithm is to treat HCP first) [213,222].

In CM-II, a large proportion of patients develop HCP, so the treatment algorithm also involves VPS and ETV (where Guillaume and Menezes [213] recommend additional observation of CSF flow dynamics). VPS has been used with satisfactory outcomes in CM-III [223].

1.3.7.3 Multiple Sclerosis

Multiple sclerosis (MS) is an inflammatory autoimmune disorder of the central nervous system that attacks myelinated axons (the lesions are called plaques) in the CNS and is considered the most common cause of chronic and significant neurologic disability commencing in early to middle adult life [224,225]. It effects more females than males [226,227]. It has no known cure, and the curative diagnostic marker also remains unidentified. MS is believed to express itself through an interaction of both environmental (for instance geography is an important factor [228]) and genetic factors.

The pathophysiology of MS involves breakdown of the BBB during lesion formation. Infiltration of inflammatory cells takes place in the parenchyma, optic nerves (leading to optic neuritis (ON)), spinal cord and brain stem. In the case of ON, sequential involvement of optic nerve involvement in combination with longitudinally extensive myelopathy gives rise to neuromyelitis optica (NMO). The differentiating factor between NMO and MS is AQP4 involvement. This aquaporin is a target for NMO-IgG, and importantly brings in neuroinflammation into its sphere of influence [210].

MRI is the imaging method of choice used for confirming MS and monitoring its progression in the CNS. A useful review of MRI's importance in this disorder is given by Fox *et al.* [229]. Brain parenchymal viscoelasticity is known to reduce in MS patients, and MRE also plays a role in MS, in that it presents possible in vivo markers of neuroinflammation and neurodegenerative pathology [230]. Recent reviews on the novel disease-modifying therapeutics that are used to alleviate the symptoms of MS are given by Damal *et al.* and Koch-Henriksen [231,232].

1.3.7.4 Dementia

Dementia is a general term for a range of progressive, organic brain diseases that are characterized by problems of short-term memory, disturbances in language, psychological changes, psychiatric changes and lifestyle impairments [20,226,227].

On a global scale, 44 million people currently live with dementia [7], whilst by 2050, this number is expected to rise to 115 million [11]. The estimated cost of Dementia will increase from $604 billion in 2010 to $1,117 billion by 2030 [11]. AD is known to account for up to 70 percent of all dementia syndromes in the US, whilst VaD contributes to around 17 percent [20,21]. In England, it was estimated that the total prevalence will increase from 650 000 to 750 000 by 2020 [227].

The most common cause of dementia is AD (in ~70% of cases) [20]. The recognised pathological features of AD are the extracellular deposition of amyloid β peptide (Aβ) into plaques and the formation of intracellular tangles composed of hyperphosphorylated tau protein. Other causes of dementia include VaD [233-235], dementia with Lewy bodies (DLB), Frontotemporal dementia (FTD), MS, PD and NPH. The latter is considered as one of the few potentially treatable causes of dementia [227] and is discussed in §1.3.3. It is apparent that it is necessary to counter these disorders based on an improved mechanistic understanding of their etiopathogenesis. A recent review by Marques *et al.* [236] outlines the possible effects to the BBB and Blood-CSF barriers during aging and AD, and it is highlighted that the permeability (in light of higher protein leakage from blood to CSF) of these barriers would be of definite interest to the overall wider complexity of brain homeostasis. It is postulated that reduced CSF production [237], and hence a lower turnover of CSF (up to a threefold decrease during AD [238]), may lead to a decrease in the clearance of toxic molecules such as Aβ [98] from the ISF space. New findings are beginning to tie AQP4 as a major component in altering the disturbance of Aβ clearance [150,239,240]. Furthermore, it is possible that advanced AD may be connected to either lower or elevated CSF pressure [241,242] with the noteworthy feature of the CP being associated with reversing or slowing down of age-associated cognitive decline [243].

The importance of better understanding diseases of the cerebral environment should be apparent. Appreciating the interaction between different fluid networks in the parenchyma via the utilisation of a clinically relevant setting in hydrocephalus is a promising way to help accelerate understanding of the highly complicated and multifactorial cerebral environment.

1.3.7.5 Pseudotumor Cerebri (PTC) or Idiopathic intracranial hypertension (IIH)

PTC possesses an uncertain aetiology characterized by intracranial hypertension (IH). IIH is defined as increased ICP without a space-occupying lesion or HCP in addition to a normal CSF composition [244]. It is also believed that it may be a result of cerebral oedema [245]. New theories suggests that IIH may also be due to venous outflow obstruction [246].

1.4 Existing Models of Cerebral Transport Phenomena

1.4.1 Scalar models

In 1783, Alexander Monro published a monograph specifying four significant points concerning intracranial dynamics [247]. He outlined that the brain was encapsulated within a rigid skull, substances within the brain could be considered incompressible, the net volume of blood in the cranial cavity was constant, and finally, the net accumulation between venous and arterial blood was naught. Kellie [248] confirmed these finding over a quarter of a century

later, but it still did not convince his contemporaries of the existence of cerebrospinal fluid (CSF). It was not until 1842, that a conceptual revision of the Monro-Kelly hypothesis took place. At this point, Francois Magendie proved that a communication existed between the subarachnoid space and the cerebral ventricles (evident by the foramen bearing his name [249]). In 1846, George Burrows announced a competing relationship between intracranial blood volume and CSF volume, which then amended the Monro-Kelly hypothesis [250]. He observed that CSF was displaced into the spinal space in order to give way to the increasing intracranial blood volume, and subsequently presented a reciprocal relationship between blood and CSF volumes.

The first well documented (the first actual lumped parameter model was that of Agarwal et al. in 1969 [461]) model relying on circuit analysis of CSF hydrodynamics was fronted by Guinane [251], which was described by a differential equation. However, the assumptions supporting this model do not support wide deviations of pressure and volume from equilibrium (it assumes an overall constant compliance). Other deviations of this linear phenomenological model are described in Sivaloganathan *et al.* [252], where a two compartment (two lumped subunits) assumption (incompressible parenchyma tissue and CSF) can be derived from the differential equation governing the work of Guinane, provided that there is suitable use of a viable pressure-volume relationship. Marmarou *et al.* [253] (with slight modifications applied by Sklar [233,234]) were guided by nonlinear relationships of compliance. A similar outlook steered the work of Lim *et al.* [235].

Spertell [254] developed a circuit based viscoelastic spherical shell model of the parenchyma which takes into account available creep compliance. Ventriculomegaly was measured in response to a square-wave intraventricular pressure pulse, and the model possessed the capability to solve for the mechanical parameters of the parenchyma. Karni *et al.* [255] derived a model which was later elaborated by Sorek *et al.* [256], which possessed seven intracranial compartments (also considered by Rekate [239], which led to novel treatments for conditions as diverse as diffuse paediatric head injury and excessive shunt dependency). Stevens and Lakin [241] introduced a model that determines physiologically motivated local compliances in a compartmental model (four compartments) taking into account the physiology of the rest of the body, and essentially recovering a global pressure-volume relationship. An extension to the aforementioned model is presented in Lakin *et al.* [257], with further outlandish applications to microgravity [258]. More recently, a lumped parameter model is utilised to make observations about syringomyelia [259].

Payne [260] predicts the response of the cerebral vasculature to changes in arterial blood pressure, arterial CO_2 concentration and neural stimulation through the use of scalar haemodynamic and metabolic models. Payne and Tarassenko [261] examined the linear dynamic behaviour of cerebral autoregulation, and successfully compared this to experimentally derived data.

Numerous works have assumed the lumped parameter, pressure–volume approach for various modelling objectives, from surgical simulations and investigating cardiac driven pulsations, to simulation of CSF transport [262-264]. High-pressure hydrocephalus has also recently been modelled (via the extension of the work by Ursino [265,266]) through the incorporation of a multicompartmental model that takes into account the influence of the

lymphatic system, and also entertains the prospect of alternative CSF absorption sites [267]. Unfortunately, scalar models do not take into account changes within specific tissue regions and in addition, they are incapable of capturing spatial variations in the mechanical properties of the brain which may dictate the severity and longevity of the hydrocephalic changes taking place [268], and therefore not adequately assisting in possible clinical intervention.

1.4.2 Viscoelastic and Poroelastic models

In the majority of published articles, the main representation of the parenchymal tissue is either poroelastic or viscoelastic. Franceschini *et al.* [269] performed cyclic quasi-static uniaxial stress tests on human brain tissue excised during autopsy, and observed that tissue properties are best described by an augmented Ogden constitutive theory, which includes Mullins effect permanent deformations. Under applied quasi-static uniaxial strain, there was direct and dominating evidence of tissue obeying Terzaghi consolidation theory. Even better correlations between their experimental results and biphasic poroelastic theory was obtained by incorporating the viscous terms in the solid phase, however it remains an open question whether any deviations from pure Terzaghi consolidation theory could be moderated by dwelling on other aspects such as a non-linear variation of porosity or the mere fact that excised tissue was used. The results in this paper directly fortify the use of consolidation theory in assembling a better understanding of HCP, and more specifically NPH, owing to its late onset characteristics (delayed and/or substantial volumetric deformation).

Franceschini *et al.* further observed that the ratio of drained and undrained elastic moduli are the same (practically equal to unity), and this factor helps further clarify possible approaches in the modelling of parenchymal tissue. It is concluded that consolidation theory is suited in cases involving high values of mean stress for prolonged time periods (as in HCP), whilst it acts in a corrective capacity to single phase nonlinear theory when faced with large deviatoric displacements.

A competing argument in favour of alternative mathematical formulations such as transport theory (as opposed to consolidation theory) was experimentally outlined by Dr. Dutta-Roy in the First CSF Hydrodynamics Symposium in ETH Zürich [457], however support for this argument has been subtle.

In the literature, various authors portray their models using viscoelastic or hyperelastic representations of the solid phase. This work will not be reviewed in this report, however the reader is directed to the following papers as a reference [270-276].

1.4.3 Spatial poroelastic models

The limitations of using phenomenological models were exposed when a later class of models that utilize consolidation theory (see §2) [277-282] and the concept of describing brain parenchyma as a sponge appeared [116,283,284]. In the work by Nagashima *et al.* [285], the authors attempted to model non-communicating hydrocephalus. This was done by solving the first representative porous biomechanical model based on Biot's approach with a two dimensional finite-element model. Through the use of computed tomography (CT) scans, they incorporated geometrical attributes within their calculations. They also provided correlative

results to those witnessed in clinical cases of hydrocephalus and vasogenic brain oedema [285]. This model however, was criticised by Drake *et al.* [286] since it used a Poisson ratio of 0.499 (nearly incompressible) for the brain parenchyma, rendering the results physically inconsistent [287]. Kaczmarek *et al.* [287] give an account of an analytical steady-state solution of a poroelastic model of both the brain and ventricles. In this cylindrical model the CSF and the solid matrix of the porous medium are in communication. The aim was to reproduce the features of ventricular dilatation and oedema when under the influence of obstructive hydrocephalus (occlusion of the aqueduct), whilst utilising a two-phase poroelastic representation of the parenchyma. The work exploited an ependymal permeability which is dependent on ventricular dilation and a numerical scheme based on a small-strain approximation (a comparison of the overestimation of displacement is given). Finite deformation is globally acknowledged via the superposition of the small-strain solutions.

In 1999, Levine used a one dimensional, spherical poroelastic model to show how NPH exists with nominal levels of ventricular CSF pressure [288]. This was done by assessing the role of CSF absorption within brain parenchyma. Levine describes the transcapillary exchange between interstitial fluid and blood networks using Starling's law, and in doing so takes into account the net colloid osmotic and hydrostatic pressures. The parenchyma is modelled as a tri-phasic linear poroelastic structure, namely incorporating a single solid network (representing cytoskeletal and other connective tissue elements) and two fluid networks representing interstitial fluid and compressible capillary and venous channels. Levine's model was used to test three theories relating to the physiology of CSF, namely (i) ventricular walls being impermeable to CSF; (ii) the efficient absorption of ventricular CSF seeping into the parenchyma; and (iii) inefficient absorption of ventricular CSF seeping into the parenchyma. The model concluded in outlining that only case (ii) accounts for the clinical observations of NPH. In 2000, Levine [289] outlined a study where he investigated the relationship between ventricular size and impaired CSF absorption in psuedotumor cerebri, using a similar representation of the parenchyma, as mentioned earlier.

Peña *et al.* [290] investigated the biomechanics of acute obstructive HCP and periventricular lucency (PVL) through the use of a 2D biphasic poroelastic model solved using finite element analysis. This model was later refined to accommodate observations in communicating HCP [291].

In 2005, Smillie *et al.* [292] developed a model for investigating HCP and the effect of shunting. Using this poroelastic model, they utilised a simplified yet accurate (white and grey matter) representation of the brain whilst simultaneously introducing flow through the aqueduct. This was in addition to flow already taking place through the porous parenchyma. A robust set of boundary conditions incorporating effects such as resistance of drainage pathways and possible deformation of the skull is also introduced here, along with a quasi-steady assumption dictating time dependence. Sivaloganathan *et al.* [293] defined a single parabolic equation governing unidirectional biphasic displacement and flow which is able to describe consolidation with a constant and deformation dependent permeability. Sivaloganathan [294] also counter their poroelastic model with a viscoelastic analogy, and present the parenchyma as an impermeable, viscoelastic solid. Considering these two models

by the same author, the argument tends towards the use of a poroelastic model when considering interactions between CSF and parenchymal tissue.

In the same volume of *Mathematical Medicine and Biology*, With and Sobey [295,296] observed the effect of a nonlinear permeability (a function of ventricular dilation) in the CSF compartment of their spherically symmetric poroelastic model. A finite difference template was utilised for their work, and inferences could be made on the slow blockage of the Sylvian aqueduct during acute HCP, whilst a more detailed argument is made on their work covering NPH, as it includes a mechanism on parenchymal absorption of CSF. An altered compliance is theorized to influence idiopathic intracranial hypertension. In their other paper, they develop a 2D cylindrically symmetric poroelastic extension of their spherically symmetric work, with the key difference being that the fluid phase is discretised using the finite element method. The solid phase utilised the finite difference method, as in the 1D case. They explore similar concepts as their 1D model, with the addition of observing the effects of gravity in acute hydrocephalus. In addition to their 2D model, they develop a simple 3D model based on solving the same poroelasticity equations as in the 2D case, but for an axisymmetric geometry. Acute HCP was investigated, and ventricular expansion pictorially portrayed.

Clatz *et al.* [263] couple a three-dimensional patient specific ventricular representation of the biphasic (CSF and parenchyma) parenchyma with a scalar description of CSF production and resorption to model communicating HCP. A limitation is their quashing of the pressure gradient in Darcy's law to account for the supposedly limited flow of CSF (through the parenchyma during communicating HCP), even though they claim that a transparenchymal pressure boundary condition is imposed to induce a CSF flux. In the same year, Song *et al.* [297] published a paper of an analytical model of blood flow model in capillaries, utilising Casson's constitutive equation.

In 2008, Wirth and Sobey published a detailed analysis of a multiple-network poroelastic model (however, without considering interaction between the various fluid compartments) based on their previously described methodology that was used to model the infusion test. Momjian and Bichsel [298] developed a model that was able to capture the magnitude, as well as the geometrical attributes of ventriculomegaly (using a quality factor) in acute and chronic HCP (from CT images). This model utilised a nonlinear poroelastic framework, since the hydraulic permeability of the fluid phase was a function of void ratio. It was discretised using the finite-element method and was coupled with `COMSOL Multiphysics®` (COMSOL Ltd, Cambridge, UK). In a similar fashion, Narsilio *et al.* [299] used an overly simplified porous (not poroelastic) model for acute HCP, with the incorporation of patient-specific MRI. These were discretised and solved using the FEM within a `COMSOL` environment. The white and grey matter were treated as separate entities, with different values attributed to their permeability.

Linninger *et al.* [300] compared their coupled poroelastic model for the parenchymal tissue which utilised both Navier-Stokes and Darcy equations for fluid-tissue interaction (to deduce pressure and velocity fields), with in vivo CINE-MRI measurements of CSF flow for normal and diseased patients (communicating HCP). Liu *et al.* [301] describe a poroelastic model that is able to describe the ventriculomegaly in five felines with kaolin-induced HCP. A key addition to this model is the incorporation of intraoperative measurements. Both FEM

and the Adjoint equations method (AEM) are used in this study. In the same year, Tully and Ventikos [302] adapted Smillie's poroelastic model by coupling it with multidimensional representations of the aqueduct of Sylvius in order to investigate the impact of relevant degrees of stenosis, in addition to the influence of pulsatile boundary conditions. Penn and Linninger [303] give a good interpretation of their previous work on acquiring CSF flow, pressure and brain tissue displacement based on fluid dynamics and poroelasticity theory. They specify that only small pressure gradients are needed to induce ventriculomegaly and indicate that ETV is a sound procedure for patients with proximal obstructions.

In 2010, Shahim *et al.* [304] published a paper on a poroelastic model of the parenchyma that was used in combination with MRI and DTI (to account for microstructure characteristics) data for the computational domain, CSF content and CSF permeability. This allowed for a description using non-uniform CSF content and non-isotropic permeability (using Westhuizen and Du Plessis formulas). The FEM was used to discretise the poroelastic system. There were noticeable changes in ventriculomegaly, pressure distribution and CSF streamlines when considering inhomogeneous CSF content and anisotropic permeability.
In 2011, Tully and Ventikos [102], introduced a novel representation of Multiple-Network Poroelastic theory. This allowed for the first time, the individual investigation of the multiscalar and spatio-temporal properties dictating the transfer of fluid between the cerebral blood network, CSF and brain parenchyma. The MPET extension was specifically used to interrogate the clinical markers of NPH.

The year 2012 was rather productive for the field, yielding numerous papers of varying importance. Shahim *et al.* [305] derived a 1D analytical poroelastic model to predict the onset of NPH. The model was based on a spherical representation of skull and ventricles, which echoed literature in its recent history. The model solved a large deformation problem in a similar manner to that of Kaczmarek *et al.* [287], however the main focus of the paper was CSF seepage towards brain parenchyma and equilibrium position of the ventricular wall, as opposed to CSF pressure. Sobey *et al.* [306] use a spherically symmetric biphasic (CSF and conflated blood compartment) poroelastic model to simulate an infusion test. The authors also analysed the impact of incorporating the blood pressure fluctuations and also assess the importance of the spatial dependence of their model. A notable limitation of this model is the lack of exchange between the compartments. Wilkie *et al.* [307] once again utilise the spherical representation of the brain geometry, and solve a 1D poroelastic problem, with the inclusion of antibody concentration in the parenchyma through a convection-diffusion equation in order to simulate the effects of anti β_1 antibodies on brain tissue and therefore HCP development. Such a framework speculates on the required incorporation of capillary absorption of water, and the influence of an AQP4-β_1 integrin relationship would need to be further investigated.

A 3D linear poroelastic model developed by Li *et al.* [308] was recently solved using FEM in order to compare experimental results of constant-rate infusion. The transient nature of the field equations was used to conduct the modelling. An important aspect of the work was that the main poroelastic constants underwent a parametric study to observe their influence on the mean ICP infusion curve. The specific storage of the fluid phases along with the drained Young's modulus stood out as important candidates for future consideration.

Further optimisation of the poroelastic parameters took place through the use of an artificial neural network.

Very recently, Wirth *et al.* [309] investigate the breakdown of a steady poroelastic problem for combinations of elastic model and permeability-strain relation (as there are relations of permeability and strain where permeability tends to zero provided there is sufficient solid matrix compression, giving rise to choking). Conditions under which choking can occur are given for different hyperelastic-permeability (volume dependent) pairings.

1.4.4 Other pertinent models

Fin and Grebe [310] outline a CFD based model of the Sylvian aqueduct, whilst Kurtcuoglu *et al.* [311]outlined a computational fluid dynamics (CFD) model to elucidate the behaviour of the CSF containing space (simplified, but unified ventricular system). They obtained pressure and flow patterns within the ventricular system through the use of appropriate boundary conditions (sinusoidal oscillatory motion) on the third ventricle lateral walls. Peak pressures in the lateral ventricles were observed, and corresponded to a peak rate of displacement at the third ventricle. In addition, it was found that aqueductal stenosis gave rise to a higher intraventricular pressure in the lateral ventricles.

Linninger *et al.* [312] observed (via their fluid-mechanical model for the pulsatile CSF flow) that large transmural pressure gradients were not found (it is a possibility that the sensitivity (133-266 *Pa*) of the equipment was not adequate) in kaolin induced communicating hydrocephalus in canines. Modelling of the pulsatile CSF dynamics took place with the aid of a simple hydrodynamic model, utilizing the use of a forcing function to depict the existence of the choroid plexus undergoing cyclic motion and the assumption that the periventricular tissue lining the ventricles is modelled by linear elastic springs. This computational model also allowed for an explanation regarding CSF flow reversal, and showed that increased ICP is a result of increased fluid due to lowered absorption of CSF.

Kurtcuoglu *et al.* [313] used MRI scans to acquire the patient-specific geometries of the aqueduct of Sylvius and third ventricle. These geometries were used in combination with MRI obtained boundary conditions (brain motion scans and CSF flow velocity via volicimetric MRI scans) for conducting CFD simulations. Reference was made to a lack of resolution in MRI scans for the acquisition of the choroid plexus geometries, and importantly, stating that these structures would have limited influence in the flow field. This work also outlined the various flow features witnessed in the third ventricle and aqueduct, such as jets and recirculation zones.

Linninger *et al.* [51] use a homogenous isotropic porous medium to represent brain tissue and bulk CSF flow boundary conditions (where diffuse CSF generation is assumed to occur in the choroid plexus of the lateral ventricles). The choroid plexus is assumed to constantly generate CSF as well as to produce the pulsating flow of CSF during the cardiac cycle. The goal of the work was to integrate patient-specific ventricular and subarachnoid space geometries of normal and hydrocephalic patients and compare experimentally obtained results of flow velocities and flow patterns to two and three dimensional CFD results in the normal and hydrocephalic states. Small transmantle pressure differences were accounted for in this

model, however, large ICP variations in amplitude between normal and diseased states were also witnessed.

Howden *et al.* [314] perform CFD simulations in order to determine CSF flow of a unified, patient-specific ventricular system. They utilized a nesting approach to account for the pressure boundary conditions at the outlets. For the inlets, pulsating velocity conditions were applied at the choroid plexus regions (represented by 6 *mm* diameter holes indented 2 *mm* in the lateral ventricles) of the lateral ventricles. They note that CSF follows a transient creeping flow in most of the regions of the ventricular system. A hyperelastic constitutive model for the brain parenchyma was used by Dutta-Roy *et al.* [272] to investigate the notion that a transmantle pressure gradient of no more than 1 *mmHg* is associated with NPH. The parenchyma was treated as a single and biphasic continuum respectively. Their results indicated that a minimum transmantle pressure gradient of ~1.8 *mmHg* is required to produce NPH.

Gupta and colleagues [52] present a 3D patient-specific model of a healthy patient to assess the CSF dynamics in the inferior cranial SAS, superior spinal SAS and fourth ventricle through the use of an anisotropic porous media model. This has the benefit of taking directional variations in permeability within the trabecular SAS into consideration. CSF was assumed to be produced in the fourth ventricle. The choroid plexuses in the third and lateral ventricles were not independently considered. For the boundary conditions, velocity profiles were obtained through volicimetric MRI.

In 2011, Sweetman *et al.* [315] presented a 3D flow model of the intracranial space and used it to predict CSF flow patterns and ICP as a consequence of brain tissue displacement in normal and hydrocephalic cases. They included the ventricular system and the entire cranial SAS. Arterial expansion and contraction are represented by volumetric expansion terms (source terms). Importantly they propose to treat brain tissue as poroelastic in order to foster a better understanding of pathological brain dynamics as part of their future model refinement.

A review of CFD to model CSF flow is given by Kurtcuoglu [316]. The use of CFD models in the SAS, ventricles and perivascular space are mentioned. The same author also describes the flow features in the SAS of a healthy volunteer [317]. Finally, Bottan *et al.* [318] recently developed a phantom model of the intracranial cavity that is able to replicate CSF and pressure dynamics, under the auspice of constant compliance.

This chapter outlined the need for society to embrace technological advances that offer the prospect of improved clinically relevant predictive information for diseases of old age. This is justified by the mere fact that the ageing population will exceed that of children in just over a generation. Brain diseases in general occupy around 13% of global disease prevalence. More specifically, the numbers of individuals that live with dementia will increase by around 90% in just over 3 decades, which will undoubtedly exert strain on policy makers in the years to come. The importance of understanding the cerebral environment in detail has never been more opportune, and in this chapter effort was made to outline the multitude and overlapping state of diseases of the cerebral environment, in addition to the simultaneous need to better understand the intertwined and complicated nature of cerebrospinal fluid transport and its modelling through a poroelastic framework.

CHAPTER 2

Multiple-Network Poroelastic Theory

As described in the latter sections of the last chapter, human tissue is well described by a porous medium. A sound understanding of poromechanics provides a powerful tool in understanding the aetiology of hydrocephalus. The theory in this chapter is mainly augmented from the work conducted by Detournay & Cheng [3]. The aforementioned work was deemed optimal in describing the transition from the micromechanical observations to the required multiple-network linear isotropic poroelastic theory and its adaptation to the cerebral environment.

Poroelastic behaviour is best described by two phenomena, namely solid-to-fluid coupling and vice-versa. Considering the pore network as a closed one (for both cases), the latter, fluid-to-solid coupling occurs when a change in the pressure of the fluid (or fluid mass) produces a change in the volume of the porous medium under consideration. The prior takes place when a change in fluid pressure (or fluid mass) is the consequence of a change in the applied stress (compression) [319]. The aforementioned mechanisms present a time-dependent character to the mechanical properties of the solid matrix. A good example is that if additional pore pressure (as for instance when considering changes in applied stress) is allowed to dissipate through diffusive fluid mass transport, a consequent deformation of the solid matrix gradually takes place [3].

The Biot model of a porous material obeys the conceptual model of a solid skeleton percolated with a freely moving pore fluid (see Figure 2.1). This concept dictates the choice of the kinematic quantities: a solid displacement vector u_i which tracks the movement of the porous solid with respect to a reference configuration, and a specific discharge vector q_i for the motion of fluid relative to the solid matrix. Two *strain quantities* are also introduced to follow the deformation and the change of fluid content of the porous solid with respect to an initial state: ε and ζ, namely the small strain tensor and variation of fluid content. The latter is defined as the variation of fluid volume per unit volume of porous material [3].
$\varepsilon > 0$ is conventionally an extension, whilst a $\zeta > 0$ corresponds to a gain of fluid by the porous solid, and can be generically thought of as oedema. ε and ζ are related to the original kinematic variables u_i and q_i via the compatibility expression:

$$\boldsymbol{\varepsilon} = \frac{1}{2}\left(\nabla \mathbf{u} + \nabla \mathbf{u}^T\right) \tag{2.1}$$

and fluid mass balance relation:

$$\frac{\partial \zeta}{\partial t} = -\frac{\partial q_i}{\partial x_i} \tag{2.2}$$

where t represents time.

The total stress tensor σ_{ij}, and the pore pressure p (scalar) represent the dynamic variables. As per normal convention, a positive normal stress implies tension, whilst the pore pressure in a material element is defined as the pressure in a hypothetical reservoir where no fluid exchange takes place between the reservoir and the material element.

The work increment associated with the strain increment $d\varepsilon_{ij}$ and $d\zeta$, in the presence of the stress σ_{ij} and p, is

$$dW = \sigma_{ij} d\varepsilon_{ij} + p d\zeta \tag{2.3}$$

Under the auspice of the Biot model, σ and ε is isolated to their isotropic component. Shear stresses at the contact between fluid phase and solid matrix associated with a local velocity gradient in the fluid are not taken into account, whilst the definition of p induces constraints on the time scale at which the coupled diffusion-deformation processes can be analysed. Modelling quasi-static problems (also extendable to the dynamic range of problems) allows full use of the Biot formulation, since the pore pressure must be locally equilibrated between neighbouring pores, over the length scale. The viscosity of the interstitial fluid allows both the time scale and length scale to be associated through diffusivity coefficients [3].

2.1 Constitutive equations

2.1.1 Lumped continuum model

In this section the bulk response to the bulk material properties of a poroelastic medium are discussed. The Biot formulation relies upon the following basic properties of the porous medium: (i) Isotropy of the material (ii) Reversibility of the stress-strain relations under final equilibrium conditions (iii) linearity between the stress (σ_{ij}, p) and the strain (ε_{ij}, ζ); (iv) small strain approximation; (v) fluid present in the pores is incompressible, and; (vi) may contain air bubbles, and finally; (vii) The fluid moves through the porous skeleton according to Darcy's Law [277]. The most general form for isotropic material response as given by Detournay & Cheng [3] is given by:

$$\begin{aligned} \varepsilon_{ij} &= \frac{\sigma_{ij}}{2G} - \left(\frac{1}{6G} - \frac{1}{9K} \right) \delta_{ij} \sigma_{kk} + \frac{1}{3H} \delta_{ij} p \\ \zeta &= \frac{\sigma_{kk}}{3H^*} + \frac{p}{R} \end{aligned} \tag{2.4a-b}$$

The parameters K and G are the bulk and shear modulus of the drained elastic solid, whilst the coupling between solid and fluid phase stress-strain is represented by the additional constants, H, H^* and R. σ_{kk} defines the dilatational stress and δ_{ij} is the Kronecker delta. From the above, $H=H^*$ due to the reversibility condition. Specifically, the assumption of potential energy in the porous medium is assumed, and extends to the notion that work done in order to bring the porous medium from its initial condition to final state (ε_{ij}, ζ) is independent of the manner

taken to reach this final state [277]. Equation (2.4a-b) may also be separated into a deviatoric and volumetric response:

$$\begin{aligned} e_{ij} &= (2G)^{-1} s_{ij} \\ \varepsilon &= \frac{1}{H} p - \frac{1}{K} \sigma^* \\ \zeta &= \frac{1}{R} p - \frac{1}{H} \sigma^* \end{aligned} \tag{2.5a-c}$$

In equation (2.5a-c), e_{ij} and s_{ij} represent deviatoric strain and stress, whilst ε is the volumetric strain and σ^* is the isotropic compressive stress (mean pressure). $1/H$ is the poroelastic expansion coefficient, and it describes how much a change of pore pressure consequently changes the bulk volume whilst the applied stress is held constant. $1/K$ is the drained material compressibility, and $1/R$ is the unconstrained specific storage. In more detail:

$$\begin{aligned} e_{ij} &= \varepsilon_{ij} - \left(\frac{\varepsilon}{3}\right)\delta_{ij} \\ s_{ij} &= \sigma_{ij} - p^* \delta_{ij} \\ \sigma^* &= -\frac{\sigma_{kk}}{3} \\ \varepsilon &= \varepsilon_{kk} \end{aligned} \tag{2.5d-g}$$

2.1.2 Volumetric response

Two of the characteristic modes of response of a porous medium consisting of fluid-filled pores is the different deformation under drained and undrained conditions. It is important to consider the volumetric response in this instant as it will help decipher the physical meaning to certain volumetric constitutive constants.

The drained response corresponds to pore pressure of naught ($p = 0$) whilst the undrained response encapsulates the description of when fluid is trapped within the porous solid ($\zeta = 0$). For the drained condition, the volumetric strain is directly proportional to the total pressure σ^*, by allowing $p = 0$, hence from (2.5b) we have:

$$\varepsilon = -\frac{\sigma^*}{K} \tag{2.6}$$

Substituting equation (2.6) into (2.5c) and letting $p=0$ gives:

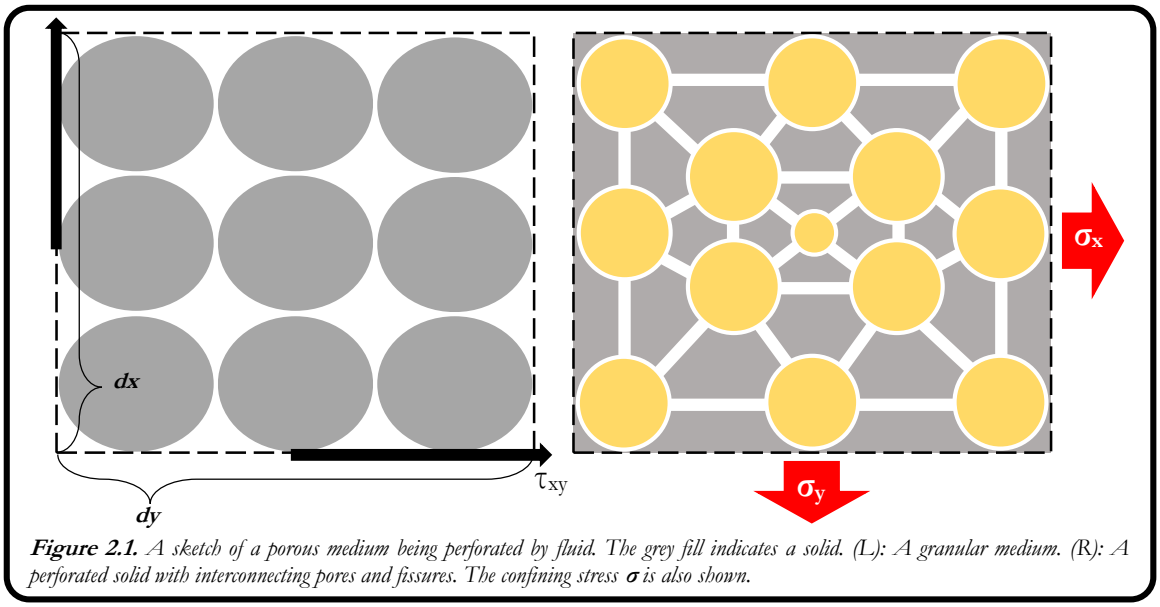

Figure 2.1. *A sketch of a porous medium being perforated by fluid. The grey fill indicates a solid. (L): A granular medium. (R): A perforated solid with interconnecting pores and fissures. The confining stress* σ *is also shown.*

$$\zeta = \alpha\varepsilon \tag{2.7}$$

For the undrained condition:

$$p = \beta\sigma^{*} \tag{2.8}$$

by letting $\zeta=0$ in equation (2.5c). Substituting (2.8) into (2.5b) for p yields:

$$\varepsilon = -\frac{\sigma^{*}}{K_u}, \text{ where } K_u = K\left(1+\frac{KR}{H^2-KR}\right) \tag{2.9}$$

In the above equations, β is Skempton's pore coefficient, K_u is the undrained bulk modulus of the porous material and α is the ratio of fluid volume gained (or lost) in a material element to the volume change of that element provided the intermatrix pore pressure is allowed to return to its initial condition, and is usually defined as $\alpha = K/H$. The range of the constants α and K_u is $[0, 1]$ and $[K, \infty]$, where the latter bound implies existence provided $H^2 \gg KR$ and $H^2 = KR$ respectively. It should be noted that under the linearized approximation (iii) in §2.1, $\alpha < 1$ since the representative volume gained/lost cannot be greater than the total change in volume of that specific element. In addition, the short term volumetric deformation response of the porous matrix is given by equation (2.9) (not enough time for diffusive mass transport to allow the movement of fluid between elements), whilst we expect the porous material to achieve the deformation response represented by equations (2.6) in the longer term (when pore pressure reaches its initial value). This is due to the difference in stiffness (K_u and K) between the two responses.

In order to facilitate the understanding of the form of the constitutive equations used, the volumetric response is presented in an alternative form:

$$\varepsilon = -\frac{1}{K}(\sigma^{*} - \alpha p)$$
$$\zeta = -\frac{\alpha}{K}(\sigma^{*} - \frac{p}{\beta}) \tag{2.11a-b}$$

In the above equation (2.11b), β is defined as:

$$\beta = \frac{K_u - K}{\alpha K_u} \tag{2.12a}$$

Rearranging (2.11a-b) and solving for (σ^*, p) as $f(\varepsilon)$, one is also able to obtain the Biot modulus, M, defined as:

$$\left.\frac{\partial \zeta}{\partial p}\right|_{\varepsilon} = \frac{1}{M} = \frac{\alpha^2}{K_u - K} \tag{2.12b}$$

The Biot modulus is defined as the increase in the amount of fluid due to a unit increase of pore pressure, under an assumed constant volumetric strain ($|_{\varepsilon}$).

2.2 Micromechanical aspects of a porous medium

In order to obtain a more detailed understanding of the constituents underlying the previous chapter, one needs to observe the interaction between the bulk parameters outlined previously with the micromechanical ones in this section. In order to explain certain aspects of the volumetric response of fluid infiltrated pores from a micromechanical perspective, it is important to define a different loading decomposition to that which was used until now (σ, p). We define "Π-loading" as the components of (σ, p), namely (σ', p'), where σ' is the Terzaghi effective stress (defined as: $\sigma_{ij}' = \sigma_{ij} + n_w \delta_{ij} p$) and p' is the Π-pressure which has the same magnitude as p. σ_{ij}' is the stress in the solid skeleton, n_w is the effective area coefficient ($n_w \approx 1$) and δ_{ij} is the Kronecker delta [3,320,321].

2.2.1 Porous medium with interconnected pore space

We define a representative volume of a porous material as $V = V_p + V_s$, where V_p is the volume of the interconnected pore space and V_s is the combined volume of the isolated pores and solid phase. The porosity is now conveniently given as $\eta = V_p / V$. This convention allows one to use the linearity between stress and strain to define the volumetric response of the porous material in terms of volumetric strain of the bulk material and pore space, per applied load (σ, p) as:

$$\begin{aligned} \Delta V / V &= -\left(1/K\right)\left(\sigma' - \alpha^* p'\right) \\ \Delta V_p / V_p &= -\left(1/K_p\right)\left(\sigma' - \beta^* p'\right) \end{aligned} \tag{2.13a-b}$$

where:

$$\begin{aligned} \alpha^* &= 1 - \left(K / K_s'\right) \\ \beta^* &= 1 - \left(K_p / K_s''\right) \end{aligned} \tag{2.14a-b}$$

In the above equations, K'_s and K''_s are bulk moduli of the solid phase (they are described in §2.2.4), whilst K_p is defined as the bulk modulus of the pore volumetric strain ($K_p=\eta/\alpha^*K$, where the Betti - Maxwell reciprocal theorem is utilised [3]). α^* and β^* are dimensionaless effective stress coefficients.

2.2.2 Solid constituent and porosity

Here we utilise Π-loading, and in this way we are able to define

$$\begin{aligned} \Delta V/V &= \Delta V_s/V_s + \Delta\eta/(1-\eta) \\ \Delta V_p/V_p &= \Delta V_s/V_s + \Delta\eta/\eta(1-\eta) \end{aligned} \tag{2.15a-b}$$

In equations (2.15a-b), $\Delta V_s/V_s$ is the volumetric deformation of the solid phase, and $\Delta\eta/(1-\eta)$ measures the relative deformation of the pore space and porous solid. Utilising equations (2.13a-b) and the above decomposition, the following constitutive relations for the solid phase and porosity are obtained:

$$\begin{aligned} \Delta V_s/V_s &= -\left(1/(1-\eta)K'_s\right)(\sigma') - \left(1/(1-\eta)\right)\left(1/K'_s - \eta/K''_s\right)p' \\ \Delta\eta/(1-\eta) &= -\left(1/K'_\eta\right)(\sigma') + \left(\eta/(1-\eta)\right)\left(1/K'_s - 1/K''_s\right)p' \end{aligned} \tag{2.16a-b}$$

In equation (2.16b), we introduce:

$$1/K'_\eta = 1/K - 1/K'_s(1-\eta) \tag{2.17}$$

2.2.3 Volumetric response for fluid

The variation of fluid volume, ΔV_f, is defined as:

$$\Delta V_f = \Delta V_f^a + \Delta V_f^b \tag{2.18}$$

where the component with superscript (a) denotes compression/dilation of the interstitial fluid and the component with superscript (b) denotes fluid exchange between porous medium and the external surroundings. We now express the elements of (2.18) as:

$$\begin{aligned} \frac{\Delta V_f^a}{V_f} &= \frac{-p}{K_f} \\ \zeta = \frac{\Delta V_f^b}{V} &= \eta\frac{\Delta V_f^b}{V_f} \end{aligned} \tag{2.19a-b}$$

Amalgamating (2.15b) and (2.19a-b), one may represent the variation in fluid content, ζ, as:

$$\zeta = \frac{-\eta}{K_p}\left(\sigma^* - \gamma p\right) \tag{2.20}$$

where $\gamma = \left(1 - \frac{K_p}{K''_s} + \frac{K_p}{K_f}\right)^{-1}$.

2.2.4 Invariance of porosity (η) under Π-loading

As described by Detournay & Cheng [3], the reason for considering the invariance of η under Π-loading is to try and bring the bulk parameters closer to the ones defined in the micromechanical approach. To do this an ideal porous medium is considered. This medium possesses a homogenous and isotropic matrix with a fully connected pore space. Under a Π-load, the matrix and solid phase are under the influence of a uniform volumetric strain with no shape change (no change in porosity), hence:

$$\Delta V/V = \Delta V_s/V_s = \Delta V_p/V_p \tag{2.21}$$

Applying the above relationship to (2.13) with $\sigma' = 0$, the solid moduli simplify to [322]:

$$K_s' = K_s'' = K_s \tag{2.22}$$

The above equality along with equations (2.16a-b) yields [323]:

$$\begin{aligned} \Delta V_s/V_s &= -1/K_s\left(1-\eta\right)\left(\sigma-\eta p\right) \\ \Delta\eta/\left(1-\eta\right) &= \sigma'/K_\eta \end{aligned} \tag{2.23a-b}$$

The latter equation (2.23b) possesses the Terzaghi effective stress, whilst the prior equation reveals that the isotropic component of the compressive stress averaged over the solid phase is proportional to the volumetric strain, $\Delta V_s / V_s$. The relationships in this section allow us to express a, K_u, β and $1/M$ as [3]:

$$\begin{aligned} \alpha &= 1-K/K_s \\ K_u &= K\left[1+\alpha^2 K_f/(K_f\left(\alpha-\eta\right)\left(1-\alpha\right)+\eta K)\right] \\ \beta &= \alpha K_f/[K_f\left(\alpha-\eta(1-\eta)\right)+\eta K] \\ 1/M &= \eta/K_f+\left(\alpha-\eta\right)/K_s \end{aligned} \tag{2.24a-d}$$

2.3 Governing equations

In this section, an outline of the governing equations of the theory of poroelasticity are sought. What ultimately prevails from this section are the field equations which define the characteristic nature of the system that forms the basis of the MPET framework. The transition from the Linear Isotropic Theory of Poroelasticity (LITP) to MPET is smooth, as will be shown in adequate detail here.

2.3.1 Constitutive equations for a fluid and porous solid

The following constants are defined [3] which relate drained (ν) and undrained (ν_u) Poisson ratios to the previously described moduli K, K_u and G:

$$v = \left(3K - 2G\right)/2(3K + G)$$
$$v_u = \left(3K_u - 2G\right)/2(3K_u + G) \tag{2.25a-b}$$

The above equations can be used to describe the Biot modulus and Skempton's coefficient [3]:

$$M = 2G\left(v_u - v\right)/\alpha^2\left(1-2v_u\right)\left(1-2v\right)$$
$$\beta = 3\left(v_u - v\right)/\alpha\left(1-2v\right)\left(1+v_u\right) \tag{2.26a-b}$$

It is always useful to know the ranges of these important coefficients, and these are: $\alpha[0,1]$, $v_u[v, 0.5]$, $\beta[0, 1]$ and $M[0, \infty]$. We now use the aforementioned constants to rewrite the stress-strain relationship for the solid (equation (2.4a)) utilising the pore pressure as the coupling term as:

$$\sigma_{ij} + \alpha p\delta_{ij} = 2G\varepsilon_{ij} + \left(\frac{2Gv}{1-2v}\right)\varepsilon\delta_{ij} \tag{2.27}$$

For the pore fluid (Eq. 2.4b), we utilise the volumetric strain as the coupling term and obtain:

$$p = M\left(\zeta - \alpha\varepsilon\right) \tag{2.28}$$

2.3.2 Transport and Balance Laws

2.3.2.1 Transport Law

Darcy's Law is used to describe the transport of percolating fluid (interstitial fluid, arterial blood, capillary blood and venous blood) within the solid matrix:

$$\boldsymbol{q} = -\frac{k}{\mu}\left(\nabla p - \rho_f g_i\right) \tag{2.29}$$

In the above equation, it is assumed that ϱ_f is the density of the fluid phase, g_i is the gravity component in the i^{th} direction and since this is an isotropic porous medium, the intrinsic permeability tensor is the same for all diagonal elements ($k_{ij} = 0, i \neq j$). μ is the viscosity.

2.3.2.2 Equilibrium equation

The linear momentum balance in terms of Cauchy stress distribution within a deformed solid is a standard consideration, where $\boldsymbol{u}$ is the matrix displacement (ignoring acceleration of fluid through the matrix):

$$\nabla \cdot \boldsymbol{\sigma} + \rho_B g_i = \rho_B \frac{\partial^2 u}{\partial t^2} \tag{2.30}$$

In the above, ϱ_B is the bulk density, defined by incorporating the density of the fluid and solid phase (ϱ_s) as:

$$\rho_B = \eta\rho_f + \left(1-\eta\right)\rho_s \tag{2.31}$$

2.3.2.3 Fluid phase continuity equation

$$\frac{\partial \zeta}{\partial t} + \nabla \cdot \boldsymbol{q} = \Phi \tag{2.32}$$

In the above, ζ is the amount of fluid $\boldsymbol{q}$ per unit volume (fluid mass increment caused by either the dilation of the solid skeleton or by the compressibility of fluids in the inter-matrix pores due to pressure changes) and Φ are source ($\Phi > 0$) or sink ($\Phi < 0$) densities and $\boldsymbol{q}$ represents the fluid flux vector.

2.3.3 Field Equations for a Linear Isotropic Medium

It has been seen in this section that a linear isotropic poroelastic material requires the definition of constitutive equations for a porous solid that of the fluid phase, along with transport and balance laws. Substituting the constitutive relation equation (2.27) into the equilibrium equation (2.30) and using equation (2.1) for ε_{ij}, yields the Navier equation:

$$G\nabla^2 \boldsymbol{u} + \left(\frac{G}{1-2\nu}\right)\nabla\left(\nabla \cdot \boldsymbol{u}\right) = \alpha \nabla p - \boldsymbol{F} \tag{2.33a}$$

In the above equation, $\boldsymbol{F}$ is defined as the body force per unit volume of the bulk material. We next define a diffusion equation for the pore pressure, p. Inserting equation (2.29) and equation (2.32) into the constitutive relation represented by equation (2.28) gives rise to:

$$\frac{\partial p}{\partial t} + \alpha M \frac{\partial \varepsilon}{\partial t} = \frac{kM}{\mu}\nabla^2 p + M\left(\Phi - \frac{k}{\mu}\nabla \cdot \boldsymbol{F}\right) \tag{2.33b}$$

2.4 Multiple-Network Linear Isotropic Poroelastic Theory

2.4.1 Constitutive equations for multiple fluids and porous solid

It was mentioned in various places within §2.3 that the form of the constitutive relations take the form:

$$\begin{pmatrix} \varepsilon \\ \zeta \end{pmatrix} = \begin{pmatrix} a_{11} & a_{12} \\ a_{21} & a_{22} \end{pmatrix}\begin{pmatrix} \sigma \\ p \end{pmatrix} \tag{2.34}$$

In the above equation, $a_{11} = 1/K$, $a_{12} = a_{21} = a/K$, $a_{22} = a/\beta K$. A generalised form of equation (2.34) which takes into account n distinct porous continuum networks is thus:

$$\begin{pmatrix} \varepsilon \\ \zeta_1 \\ \vdots \\ \zeta_n \end{pmatrix} = \begin{pmatrix} a_{11} & \cdots & a_{1(n+1)} \\ \vdots & \ddots & \vdots \\ a_{(n+1)1} & \cdots & a_{(n+1)(n+1)} \end{pmatrix} \begin{pmatrix} \sigma \\ p_1 \\ \vdots \\ p_n \end{pmatrix} \tag{2.35}$$

Equation (2.35) represents a porous medium with n distinct porous continuum networks, with the solid phase being depicted by material properties [a_1, K_1, β_1] and volume fraction [$v_1 = V_1/V$] whilst the (n - 1) intertwined fluid phases are embedded within the same solid porous matrix, with material properties [a_i, K_i, β_i] and (n - 1) volume fractions of [$v_i = V_i/V$]. The total normal stress (σ), volumetric strain (ε), excess pore pressure (p_i) and fluid increment content (ζ_i) are defined in the same manner as before, however the latter two variables are representative of i porosity networks (i = 1,..,n). The coefficients in equation (2.35) are given as in Mehrabian and Abousleiman [324]:

$$\begin{aligned} a_{11} &= \sum_{i=1}^{n} v_i / K_i \\ a_{1i} &= -\alpha_i \left(v_i / K_i \right), \quad i = 2,...,n \\ a_{ij} &= 0, \quad i > 2, i \neq j \\ a_{ii} &= \alpha_i v_i / \beta_i K_i, \quad i = 2,...,n+1 \end{aligned} \tag{2.36a-d}$$

The aforementioned coefficients require interpretation. a_{11} is the effective compressibility (weighted average of the components' compressibilities), a_{1i} are the generalised Biot-Willis coefficients.

Equation (2.27) which relates the stress-strain relationship for the solid is re-written in the form reminiscent of Rice and Cleary [325], which makes use of Lamé's constants (G, λ), and subsequently extended to multiple-porosity poroelasticity:

$$\sigma_{ij} = 2G\varepsilon_{ij} + \lambda\varepsilon_{kk}\delta_{ij} - \sum_{i=1}^{n} \alpha_i p_i \delta_{ij} \tag{2.38}$$

In the above equation, the Biot-Willis coefficient α_i can be interpreted from both a microscopic and macroscopic perspective. In the prior, each porosity network has a porosity equivalent to $\alpha_i = \alpha_i(v_i/K_i)$, whereas the latter perspective gives rise to a global coefficient for the entire fluid-percolated solid matrix. This global version of the Biot-Willis parameter allows for equation (2.38) to be interpreted as the weighted average contribution of each fluid network to the constitutive effective stress of multiple network system. According to the literature [319,324], the range of values for the global Biot-Willis coefficient is α_i [0, 1].

2.4.2 Transport and Balance Laws

2.4.2.1 Transport Law

Darcy's Law is extended to take into account all of the fluid networks, hence:

$$\boldsymbol{q}_i = -\frac{k_i}{\mu_i}\left(\nabla p_i\right), \quad i = 1,\ldots,n \tag{2.39}$$

2.4.2.2 Equilibrium equation

From equation (2.30), the static equilibrium equation for a poroelastic medium can be written as:

$$\sum_{j=1}^{n} \frac{\partial \sigma_{ij}}{\partial x_j} = F_i \quad i, j = 1,2,3 \tag{2.40}$$

2.4.2.3 Fluid phase continuity equation

$$\frac{\partial \zeta_i}{\partial t} + \nabla \cdot \boldsymbol{q}_i = \sum_{j=1}^{n} \overbrace{\omega_{ij}\left(p^j - p^i\right)}^{\hat{s}_{ij}} \quad i = 1,\ldots,n \tag{2.41}$$

From equation (2.41), the fluid phase continuity equations include the sum of all interporosity fluxes ($\hat{s}_{ij}$), from network j to i. Here, the transfer is considered to be driven by a hydrostatic pressure gradient, whilst ω_{ij} is the transfer coefficient scaling the flow from network j to network i.

2.4.3 Field Equations

The Navier equation is extended to:

$$G\nabla^2 \boldsymbol{u} + \left(G + \lambda\right)\nabla\left(\nabla \cdot \boldsymbol{u}\right) = \sum_{i=1}^{n} \alpha_i \nabla p_i - \boldsymbol{F} \tag{2.42}$$

In equation (2.42), we use the fact that the strain tensor ε_{ij} is equivalent to $\varepsilon = \nabla \cdot \boldsymbol{u}$ (total strain or dilatation), and λ is Lamé's first parameter. From Eq. (2.33b), we see the extension to the MPET framework:

$$\sum_{j=1}^{n} \frac{\partial p_j}{\partial t} + \alpha_j M_j \frac{\partial\left(\nabla \cdot \boldsymbol{u}\right)}{\partial t} = \frac{k_j M_j}{\mu_i} \nabla^2 p_j + M_j \left(\sum_{j=1}^{n} \omega_{ij}\left(p^j - p^i\right) \right) \tag{2.43}$$

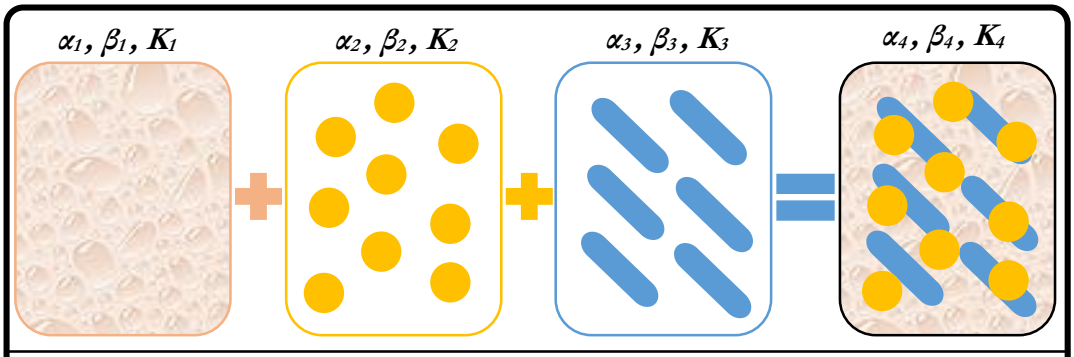

Figure 2.2. *Description of a typical triple MPET system. In this instance, the material is considered to be comprised of a solid matrix permeated by a network of low porosity pores and two network of high porosity pores. Fluid transport can occur between the three fluid domains, each with a unique pore pressure, Skempton's pore pressure coefficient, porosity and permeability.*

2.5 Adaptation to the Cerebral Environment

Sections 2.1 through to 2.4 describe the theoretical evolution of multiple fluid phases permeating a solid porous matrix (MPET model). The first stage of adapting an MPET modelling framework to describe the transfer of fluid through the brain parenchyma, is to postulate the overall formation of the MPET network. In this work, the solid porous matrix represents brain parenchyma, whilst the communicating fluid phases that will be taken into account are: arterial blood (*a*), arteriole/capillary blood (*c*), venous blood (*v*) and the CSF/ISF (*e*) space, i.e. four networks.

2.5.1 Field equations for four network MPET model

Representing the $\boldsymbol{\Sigma}\omega_{ij}(p^j\text{-}p^j)$ terms on the right hand side of equation (2.43) as $\hat{s}_{ij}$ (as shown in §2.4.2), the field equations (2.42 - 2.43) for the four compartment MPET model are as follows:

$$
\begin{aligned}
&G\nabla^2\boldsymbol{u}+(G+\lambda)\nabla\varepsilon=(\alpha_a\nabla p_a+\alpha_c\nabla p_c+\alpha_e\nabla p_e+\alpha_v\nabla p_v)-\boldsymbol{F}\\
&\frac{1}{M_a}\frac{\partial p_a}{\partial t}+\alpha_a\frac{\partial\varepsilon}{\partial t}=\frac{k_a}{\mu_a}\nabla^2 p_a+(\hat{s}_{c\to a}+\hat{s}_{e\to a}+\hat{s}_{v\to a})\\
&\frac{1}{M_c}\frac{\partial p_c}{\partial t}+\alpha_c\frac{\partial\varepsilon}{\partial t}=\frac{k_c}{\mu_c}\nabla^2 p_c+(\hat{s}_{a\to c}+\hat{s}_{e\to c}+\hat{s}_{v\to c})\\
&\frac{1}{M_e}\frac{\partial p_e}{\partial t}+\alpha_e\frac{\partial\varepsilon}{\partial t}=\frac{k_e}{\mu_e}\nabla^2 p_e+(\hat{s}_{a\to e}+\hat{s}_{c\to e}+\hat{s}_{v\to e})\\
&\frac{1}{M_v}\frac{\partial p_v}{\partial t}+\alpha_v\frac{\partial\varepsilon}{\partial t}=\frac{k_v}{\mu_v}\nabla^2 p_v+(\hat{s}_{a\to v}+\hat{s}_{c\to v}+\hat{s}_{e\to v})
\end{aligned}
\qquad (2.44a\text{-}e)
$$

2.5.2 Continuity and Directional Fluid Transfer

The transfer of fluid between four fluid networks is required to obey the law of continuity for the entire system, and so directionality between fluid compartments must be accurately specified. Figure 2.3 below provides a summary of the directional fluid restrictions placed. From this figure, the following constraints are deduced:

$$
\begin{aligned}
&Q_{acc}=Q_a+Q_c+Q_e+Q_v\\
&Q_{in}=Q_{acc}+Q_{out},\ \text{where:}\\
&Q_a=Q_{in}-\hat{s}_{a\to c}\\
&Q_c=\hat{s}_{a\to c}-\hat{s}_{c\to e}-\hat{s}_{c\to v}\\
&Q_e=\hat{s}_{c\to e}-\hat{s}_{e\to v}\\
&Q_v=\hat{s}_{c\to v}+\hat{s}_{e\to v}-Q_{out}
\end{aligned}
\qquad (2.45a\text{-}f)
$$

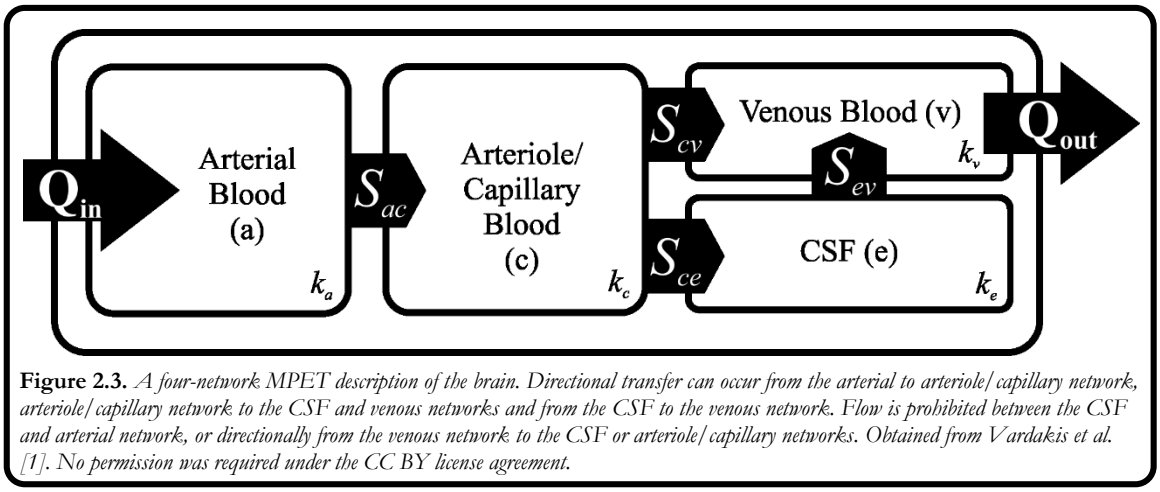

Figure 2.3. *A four-network MPET description of the brain. Directional transfer can occur from the arterial to arteriole/capillary network, arteriole/capillary network to the CSF and venous networks and from the CSF to the venous network. Flow is prohibited between the CSF and arterial network, or directionally from the venous network to the CSF or arteriole/capillary networks. Obtained from Vardakis et al. [1]. No permission was required under the CC BY license agreement.*

In equations (2.45a-f) above, the flux of fluid entering and leaving the control volume is represented by Q_{in} and Q_{out}, whilst Q_{acc} is the fluid accumulated in the control volume as a whole, and finally, Q_a, Q_c, Q_e, Q_v represent the fluid accumulated in each individual fluid network, namely: arterial blood *(a)*, arteriole/capillary blood *(c)*, venous blood *(v)* and the CSF/ISF *(e)* network. As described in §2.4.2, $\hat{s}_{ij}$ represents the interporosity fluxes (which can be both positive and negative), from network j to i. The transfer is considered to be driven by a hydrostatic pressure gradient, whilst ω_{ij} is the transfer coefficient scaling the flow from network j to network i. In a normal brain, Q_{acc} should equal zero when averaged over time. In the symptomatic brain, fluid accumulates in the CSF and ISF space or in the individual blood networks. More specifically ($|\hat{s}| > 0$ represents a loss of fluid from the network and $|\hat{s}| < 0$ indicates that fluid is added to the network):

1. Directional Fluid transport always occurs from the arterial network *(a)* to the arteriole/capillary network *(c)*:

$$\hat{S}_{a\to c} = -\hat{S}_{c\to a} = \left|\hat{S}_{a\to c}\right| \geq 0 \tag{2.46a}$$

2. Fluid transport from the arteriole/capillary network will enter the CSF/ISF network or the venous network, so:

$$\begin{aligned} \hat{S}_{c\to e} &= -\hat{S}_{c\to e} = \left|\hat{S}_{e\to c}\right| \geq 0 \\ \hat{S}_{c\to v} &= -\hat{S}_{c\to v} = \left|\hat{S}_{v\to c}\right| \geq 0 \end{aligned} \tag{2.46b-c}$$

3. CSF egress flows into the venous compartment, hence:

$$\hat{S}_{e\to v} = -\hat{S}_{e\to v} = \left|\hat{S}_{e\to v}\right| \geq 0 \tag{2.46d}$$

The four-network MPET model in a specified domain, Ω over a time interval $t \in J = [0, T]$:

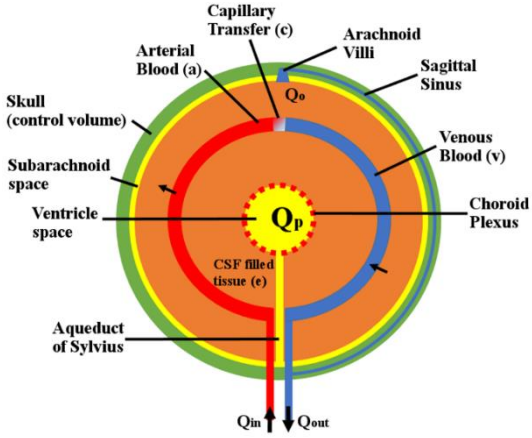

Figure 2.4. *The parenchyma of the brain is simplified to a spherical shell with physically relevant values for the ventricle and tissue radii of a healthy adult. In our 1D MPET model, the ventricles are connected to the subarachnoid space via an anatomically accurate representation of the ventricular system. In the 3D MPET model, lateral, third and fourth ventricles are amalgamated into idealised primitive spheres. The two arrows in the figure denote directional transfer between arterial blood and CSF filled tissue ($\hat{s}_{a}$), and finally CSF filled tissue and venous blood ($\hat{s}_{ev}$). Obtained from Vardakis et al. [1]. No permission was required under the CC BY license agreement.*

$$
\begin{aligned}
&G\nabla^2\boldsymbol{u}+\left(G+\lambda\right)\nabla\varepsilon=\left(\alpha_a\nabla p_a+\alpha_c\nabla p_c+\alpha_e\nabla p_e+\alpha_v\nabla p_v\right)-\boldsymbol{F} \quad \text{in} \quad \Omega\times J\\
&\frac{1}{M_a}\frac{\partial p_a}{\partial t}+\alpha_a\frac{\partial\varepsilon}{\partial t}=\frac{k_a}{\mu_a}\nabla^2 p_a-\left|\hat{s}_{a\to c}\right| \quad \text{in} \quad \Omega\times J\\
&\frac{1}{M_c}\frac{\partial p_c}{\partial t}+\alpha_c\frac{\partial\varepsilon}{\partial t}=\frac{k_c}{\mu_c}\nabla^2 p_c+\left|\hat{s}_{a\to c}\right|-\left|\hat{s}_{c\to e}\right|-\left|\hat{s}_{c\to v}\right| \quad \text{in} \quad \Omega\times J\\
&\frac{1}{M_e}\frac{\partial p_e}{\partial t}+\alpha_e\frac{\partial\varepsilon}{\partial t}=\frac{k_e}{\mu_e}\nabla^2 p_e+\left|\hat{s}_{c\to e}\right|-\left|\hat{s}_{e\to v}\right| \quad \text{in} \quad \Omega\times J\\
&\frac{1}{M_v}\frac{\partial p_v}{\partial t}+\alpha_v\frac{\partial\varepsilon}{\partial t}=\frac{k_v}{\mu_v}\nabla^2 p_v+\left|\hat{s}_{c\to v}\right|+\left|\hat{s}_{e\to v}\right| \quad \text{in} \quad \Omega\times J
\end{aligned}
\tag{2.47a-e}
$$

The latter four equations are applied to the pressure gradients of the deformed brain configuration, whereas the stress equilibrium equation (2.47a) catalyses the pressure derivatives from the undeformed configuration. This adaptation is driven by the overall need to visualise the displacements obtained from the deformed brain configuration under the auspice of small-strain based linear elasticity.

2.5.3 General assumptions

The MPET framework has been described independently of coordinate system. For this thesis, we use a spherical representation of the geometry (see Figure 2.4) of the brain when developing the boundary conditions and applying this direct representation to the 1D system described in the next chapter. The finite element based extension in the subsequent chapter allows for some flexibility when morphing the boundary conditions to suit more specific needs.

2.5.4 Boundary conditions

The MPET system is completed with boundary conditions for each of the four compartments *(a, e, c, v)*, in which $\partial\Omega=\Gamma_s\cup\Gamma_v$, where Γ_s and Γ_v are boundary conditions at the skull and ventricles respectively and $\Gamma_s\cap\Gamma_v\neq\boldsymbol{0}$. The skull is assumed rigid, since the model is assumed to apply for adult cases[1,106,296], hence:

$$\mathbf{u} = 0 \quad \text{on} \quad \Gamma_S \times J \tag{2.48}$$

For continuity of stresses, the poroelastic stress present in the brain's tissue must balance the ventricular pressure exerted by the CSF within the inner ventricular wall, hence:

$$-p_v \mathbf{n} = \sigma \cdot \mathbf{n} \quad \text{on} \quad \Gamma_V \times J \tag{2.49}$$

CSF secretion is assumed to take place in the cerebral ventricles, and is of the order of $Q_p \approx$ 500 *ml/day* [1,106,292,296].

Darcy flow is assumed to govern the flow through the brain tissue (Equation 2.39), and the permeability k_i may take the form of a constant, or the strain-dependent form:

$$k_i = k_0 e^{M'\varepsilon} \tag{2.50}$$

The use of equation (2.50) is investigated in §3.4.2. The parameter *M'*, denotes the dependence of permeability of the ISF/CSF compartment to its deformation. It has a value of 4.3, in line with Kaczmarek *et al.* (1997) and Smillie *et al.* (2005).

We assume an open aqueduct and unobstructed fourth ventricle in order for CSF to run through them. This assumption is fortified by the steady Hagen–Poiseuille relationship for the flow rate:

$$Q_{HP} = \frac{\pi d^4}{128 \mu_e L} \left(p_v - p_s \right) \tag{2.51}$$

In the above equation, p_v and p_s denote the ventricular and subarachnoid pressures, whilst L denotes the radial distance between ventricles and skull.

The absorption of CSF is assumed to take place in the bloodstream near the skull (in line with the classical hypothesis of CSF), where the rate of absorption is described by:

$$Q_{abs} = \frac{p_s - p_{pb}}{\mu_e R} \tag{2.52}$$

where p_{bp} denotes the venous blood pressure and R is a resistance due to the arachnoid granulations.

Next there is a balance of flow rates directed at the skull. The amount of fluid absorbed into the blood stream must be equal to the amount of fluid flowing to the skull via the aqueduct in addition to the amount of fluid passing through the brain parenchyma:

$$Q_{abs} = Q_{HP} + \oint_S \left(-\frac{k_e}{\mu_e} \nabla p^e \right) \mathbf{n} ds \quad \text{on} \quad \Gamma_S \times J \tag{2.53}$$

The surface integral is over the brains outer surface, S, with corresponding unit outward normal, **n**. The surface integral that will be described below is that of the outer ventricular wall, V. The Hagen–Poiseuille relationship for the flow rate (equation 2.51) which is incorporated in the equation above makes use of Dirichlet conditions for both the ventricular and subarachnoid pressures on S and V.

The relationship between the rate of change of ventricular volume (dV/dt) to that of CSF production (Q_p), flow through the aqueduct (Q_{HP}) , flow rate through the brain parenchyma and any additional surgical technique which drains CSF (shunts, ETV or EFV for instance), Q_s:

$$\frac{dV}{dt} = Q_p - Q_{HP} - Q_s - \oint_V \left(-\frac{k_e}{\mu_e} \nabla p^e \right) \mathbf{n} ds \quad \text{on} \quad \Gamma_V \times J \tag{2.54}$$

Equation (2.54) introduces a time dependence into the boundary conditions. CSF being produced from the blood results in a pressure drop (in Neumann form) in the arteriole/capillary blood network *(c)*:

$$\nabla p^c \mathbf{n}|_{\Gamma_V} = \frac{-Q_p}{-\kappa_{c-vent}} \quad \text{on} \quad \Gamma_V \times J \tag{2.55}$$

where $\kappa_{c \to vent}$ is the resistance of the flow from the capillary network to the ventricles via the choroid plexus.

Based on vascular wall-thickness arguments, there is no flow into or out of the arterial and venous blood networks, hence, in Neumann form:

$$\begin{aligned} \nabla p^a \mathbf{n}|_{\Gamma_V} &= 0 \quad \text{on} \quad \Gamma_V \times J \\ \nabla p^v \mathbf{n}|_{\Gamma_V} &= 0 \quad \text{on} \quad \Gamma_V \times J \end{aligned} \tag{2.56a-b}$$

The blood pressures are given by arterial and venous blood pressures in Dirichlet form:

$$\begin{aligned} p^a|_{\Gamma_S} &= p_{bpA} \quad \text{on} \quad \Gamma_S \times J \\ p^v|_{\Gamma_S} &= p_{bp} \quad \text{on} \quad \Gamma_S \times J \end{aligned} \tag{2.57a-b}$$

It is assumed that there is no flow into or out of the arteriole/capillary blood network at the skull, hence in Neumann form:

$$\nabla p^c \mathbf{n}|_{\Gamma_S} = 0 \quad \text{on} \quad \Gamma_S \times J \tag{2.58}$$

At the skull, CSF absorption causes a pressure rise dependent on the resistance to absorption via the arachnoid granulation, R, and the rate of CSF egress at the skull, Q_o:

$$p_S^e|_{\Gamma_S} = p^v|_{\Gamma_S} + \mu^e R Q_o \quad \text{on} \quad \Gamma_S \times J \tag{2.59}$$

2.6 Parameter Estimation

In this section, we evaluate various parameters (listed in Table 2.1) used in the MPET framework. All of the parameters used (unless already specified), are shown in Table 2.1.

2.6.1 Geometry of the brain

The radii of the skull (r_v and r_M) and amalgamated ventricles in Figure 2.4 are chosen to correspond to the measurements used by various authors [102,287,292,296,302], and roughly correspond to values expected from the adult human brain. The parameter L, which denotes the radial distance between ventricles and skull (transparenchymal region), is merely the difference between the two aforementioned radii.

2.6.2 Poroelastic Constants

For the Young's modulus, E, the same value (584 Pa) as Taylor and Miller is used [275], since they treated brain parenchyma as a strain-rate dependent material, and is directed at hydrocephalus simulations. The section of brain that was used composed mainly of white matter, and the assumption made here is that both white and grey matter possess the same value of E.

A Poisson's ratio *(v)* of 0.35 is again adopted from Kaczmarek *et al.* [287] and Taylor and Miller [275], since this value conceptualises the relative compressibility of a biphasic mediums solid phase, and allows for fluid to be absorbed or relieved from the solid matrix. A value of 0.5 would imply incompressibility, and is thus the upper limit. From the elastic modulus and Poisson's ratio, the remaining elastic moduli (for homogenous isotropic materials) are obtained, namely the Bulk modulus (K), Lame's first parameter (λ) and shear modulus (G). The values can be seen in Table 2.1. The same values as those in the pertinent literature are used, especially since it is known that observable differences between white and grey matter exist, however without concrete approval for a range of values from the scientific community. The pertinent literature all treats the parenchyma as a homogenous tissue for this reason [102,292,296,302]. It is worth noting that Magnetic Resonance Elastography (MRE) is an accurate and non-invasive technique that is used to provide the mechanical properties (shear stiffness) of the human brain *in vivo* [326]. The viscoelastic properties of the human brain in various disorders and aging are investigated in NPH, MS and Alzheimer's [230,327-331]. Although studies in this field look promising, consistent and agreeable values are not yet established (orders of magnitude differences exist [332,333]).

The use of diffusion tensor imaging (DTI) also allows for the investigation of brain matter microstructure in a non-invasive manner. White matter fibres for example can be juxtaposed with the storage modulus *(G')* obtained from MRE in order to observe the more intricate spatial variation in mechanical properties [334].

The poroelastic constants (Biot-Willis parameters, network transfer coefficients (Equation 2.47a-e), network permeabilities) are assumed to represent almost saturated

conditions, and are identical to Tully and Ventikos (2011), who performed a careful large scale parametric estimation study on a high performance computing (HPC) facility. The values for the MPET 'mixture' are given in Table 2.1, and follow from the pertinent literature [102,292,296,302]. We investigate alternatives to the values proposed in Table 2.1 in the relevant sections of this thesis.

This chapter outlined the origins of the MPET method that will be used in the next chapter to model hydrocephalus. The governing equations of this template were broken down to include the constitutive, transport and balance laws in order to satisfy the reader of their origin. The importance of the micromechanical interactions was also highlighted in order to provide further insight and justification into the corresponding macromechanical constituents. The adaptation of the generic MPET framework to the cerebral environment occupied the latter section of the chapter, where adequate consideration on the importance of directionality of fluid transfer between compartments was given, along with a description of the underlying boundary conditions. The parameters used throughout this study were outlined, and referece were given linking these to the relevant literature. It should be noted that these parameters are analysed in a critical manner in §2.6, however further insight into specific parameters is provided in the relevant sections throughout the thesis.

Table 2.1. *List of the parameter values used in the MPET framework. For the diameter, **d**, the values 3, 1.25 and 0.8 mm correspond to the values used in the CFD simulations in the next chapter. References linking the parameters to the literature are also provided.*

	Value	***Units***	***Reference***		***Value***	***Units***	***Reference***
r_v	30×10^{-3}	m	[102,292,296,302]	ω_{ac}	1.5×10^{-19}	$m^2N^{-1}s^{-1}$	[102]
r_M	100×10^{-3}	m	[102,292,296,302]	ω_{cv}	1.5×10^{-19}	$m^2N^{-1}s^{-1}$	[102]
L	70×10^{-3}	m	[102,292,296,302]	ω_{ev}	1.0×10^{-13}	$m^2N^{-1}s^{-1}$	[102]
d	$[3, 1.25, 0.8]\times10^{-3}$	m	[102,292,296,302]	ω_{ce}	2.0×10^{-19}	$m^2N^{-1}s^{-1}$	[102]
E	584	Nm^{-2}	[102,275,292,296,302]	$k^{a,c,v}$	1.0×10^{-10}	m^2	[102]
p_{bp}	650	Nm^{-2}	[102,292,295-96]]	k^e	1.4×10^{-14}	m^2	[102,292,296,302]
p_{bpA}	13.3×10^{3}	Nm^{-2}	[102,292,295-96]	K	649	Nm^{-2}	[292.296]
R	8.5×10^{13}	m^{-3}	[102,292,295-96]	λ	524	Nm^{-2}	[296]
Q_p	5.8×10^{-9}	m^3s^{-1}	[102,292,295-96]	G	216	Nm^{-2}	[296]
Q_o	5.8×10^{-9}	m^3s^{-1}	[102,292,295-96]	$\alpha^{a,e,c,v}$	1.0		[102,292,296]
μ^e	8.9×10^{-4}	Nsm^{-2}	[102,292,295]	ν	0.35		[102,106,263,272,274, 287-8,292,295-6, 302,350]
$\mu^{a,c,v}$	2.67×10^{-3}	Nsm^{-2}	[102]	β	0.99		[102,292,302]
ϱ^e	997	kgm^{-3}	[102,292,296]	M'	4.3		[295]

CHAPTER 3

Creating the Numerical Templates

The aim of this chapter is to show the numerical templates by which HCP can be modelled. The discretisation of the MPET system is shown through a variety of formats. Firslty, a one dimensional, spherically symmetric finite difference method based discretisation is coupled with a finite volume based multiphysics suite to investigate pathologies associated with acute HCP and the implementation of two surgical techniques, namely endoscopic third and fourth ventriculostomy. Subsequently, a one dimensional, spherically symmetric MATLAB based standalone FDM discretisation template to account for a nonlinear CSF permeability of the MPET sytem.

A genral n^{th} dimensional discretisation of the MPET equations is constructed (relaxing the constraint of spherical symmetry) using the FEM by obtaining the varational formulations in one, two and three dimensions. The spatial semi-discretisation is also described through the one-dimensional formulation, however its true application finds use in two and three dimensions. A simple Newton-Galerkin setup is also described and implemented in two dimensions in order to provide an example of how it's one dimensional FDM analog can be extended in higher dimensions. A multigrid solver is also presented for the one dimensional FEM discretisation as linear elements can display wildly oscillating results for general elasticity problems. Finally, a note on the choice of iterative method used in the FEM simulations is given, on account of the presence of very sparse matrices when using the FEM.

3.1 Anatomy acquisition for the 1D FDM-CFD model

3.1.1 Segmentation

Imaging was performed on a 1.5*T* GE Signa system (General Electric, WI, USA) and a T2 weighted imaging sequence was used for obtaining the brain anatomy data (Figure 3.1a). Images were acquired axially covering the whole brain at a voxel size of $1\times0.5\times2$ mm^3. These were then interpolated to 0.5 *mm* isotropic voxel size volume data which was used as an input for further processing.

The segmentation was mostly discontinuous between the slices. To increase the continuity of the computational domains (ventricular system and choroid plexuses), various

"Segmentation" and "Selection" menu tools were used to fill holes, remove islands or smooth the selection on either the current slice, all slices, or the three-dimensional volume. The acquired voxels were manually segmented for the ventricular system and choroid plexus using `Amira` (Mercury Computer Systems, San Diego, CA, USA) and the raw segmented geometries from this process were converted to Stereo Lithography *(STL)* files (Figure 3.1b).

3.1.2 Smoothing of the geometry and applying aqueductal stenosis

In order to preserve key anatomical features such as the Sylvian aqueduct and features of the choroid plexus, subsequent smoothing of the *STL* files was done using the open-source modelling software, `Blender` (The Blender Foundation, www.blender.org). This software provides the user with powerful wireframe, node-by-node, editing capabilities and in the process improves the general continuity of the required domains. Smoothing is an iterative process, and good judgement was required to ensure that the surface was sufficiently smooth for the final CFD computations, while maintaining all of the anatomical features. In order to maximise the clinical resemblance to the original segmented geometry, the surface triangles on both domains were subdivided numerous times in the more delicate features such as the aqueduct, fourth ventricle outlets and the feeding arteries of the choroid plexus. The final *STL* geometry for a healthy volunteer (open aqueduct) is used in the CFD simulations is shown in Figure 3.2a.

The current standard voxel size produced from clinical imaging does not permit the accurate differentiation of different degrees of aqueductal stenosis. `Blender` was therefore also used to apply the local stenosis for the mild and severely stenosed aqueducts (see Figure 3.2c-d). Nodal manipulations of the region of interest (see Figure 3.2b) involved proportional scaling inwards towards the centre of the aqueduct. The use of proportional scaling allowed the subsequent inward oriented scaling of vertices further afield (for a specified radius), to harmonise the smoothing of the region of interest on the aqueduct.

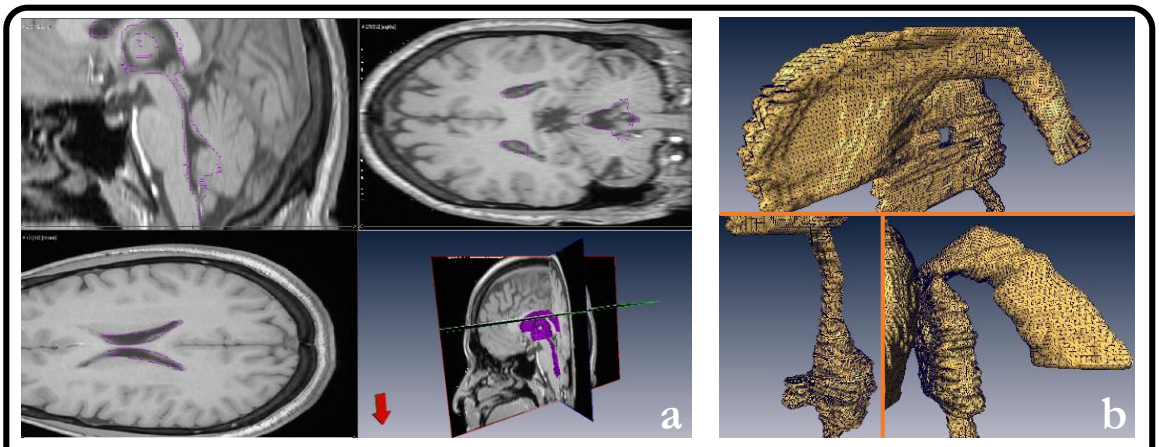

Figure 3.1. *(a) The MRI segmentation process. The software used for this purpose was* `Amira`. *The raw data in the form of multiple* `DICOM` *files is imported into the software and regions of interest (ventricular system and choroid plexuses) are manually segmented (in purple). The choroid plexuses are conceptually picked out within the ventricles to geometrically follow their expected shape. (b) Multiple views of the iso-surface created by* `Amira` *prior to additional smoothing by* `Blender`. *This surface is saved as an STL file.*

3.1.3 Creating the inlets and outlets of the STL geometries

3.1.3.1 Cases for stenosis of Sylvian Aqueduct

Inlets and outlet boundaries were created using `CFD-VisCART` (ESI Group, Paris, France). Cuts at the required inlets of the feeding arteries of the 5 choroid plexuses (Left Lateral Ventricle, Right Lateral Ventricle, Third Ventricle, Left fourth ventricle, Right fourth ventricle) were made by splitting the geometry at the required planes. The four outlets (Foramen of Magendie, Foramina of Luschka and Central canal were created in the same way.

3.1.3.2 Additional outlet due to ETV

As can be seen in Figure 1.1b, ETV is the location of perforation of the floor of the third ventricle during endoscopic third ventriculostomy. This cut in the geometry was performed in `Blender`, and defined as an additional outlet in `CFD-VisCART`. The approximate diameter of the hole was 1 *cm* (as also in Figure 3.2e).

3.1.3.3 Additional occlusions and outlets due to EFV

There were three occlusion (atresia) possibilities taken into consideration. The atresia of the bilateral foramina of Luschka was investigated, then the sole atresia of the foramen of Magendie, and finally the occlusion of both of the aforementioned outlets. Atresia was simulated as a blocked outlet, whilst the application of EFV was to apply a concentric oval shaped hole within the blocked outlet (of similar size to the ETV case), which was created in `Blender`. These can be seen in Figure 3.2e-f.

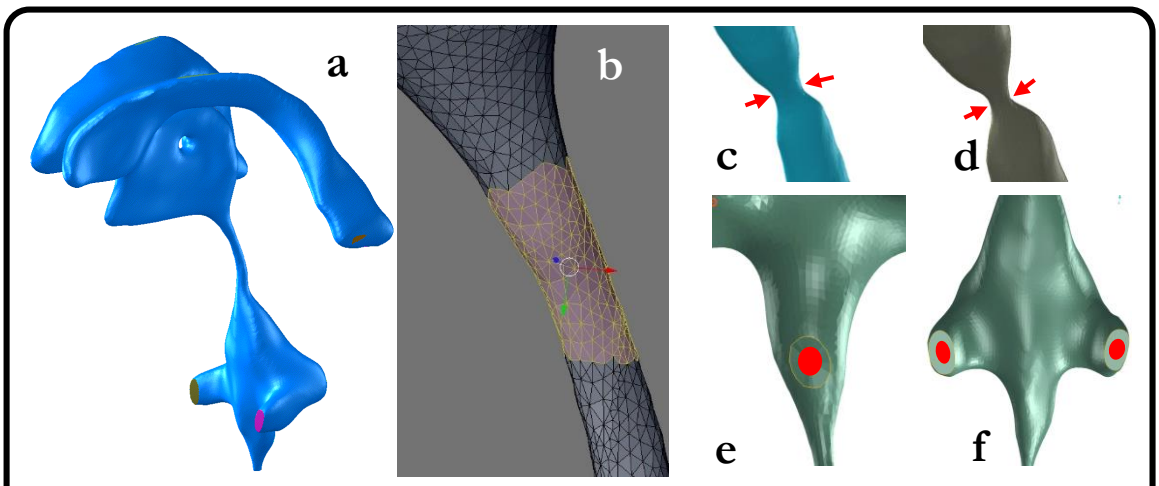

Figure 3.2. *(a) The final ventricular geometry used for the CFD simulations. (b) Application of local stenosis using* `Blender` *(c) The resulting mildly stenosed aqueduct. (d) The resulting severely stenosed aqueduct. The red arrows in the figure denote inward proportional scaling. (e) Location and approximate size of outlet (red circle) created to mimic EFV at the Foramen of Magendie. (f) Location and approximate size of outlets (red ovals) created to mimic EFV at the bilateral Foramina of Luschka situated in the fourth ventricle.*

3.2 Biological MPET assumptions: 1D FDM-CFD

The final system of Equations (2.47a-e) utilise a one-dimensional, spherically symmetric geometrical representation, which is provided by the transformation of the nabla (∇) operator in spherical coordinates.

Additional assumptions include the notion that HCP has a long time scale for development, of the order of days, weeks or even years (if one considers the chronic case). It is therefore evident that an assumption of a quasi-steady ($\partial^2/\partial t^2$, $\partial/\partial t \rightarrow 0$) system is not unrealistic. It should be noted that the MPET model does not take pulsatile effects into account for this specific study. The equations that will be solved are displayed below, along with the new adjustments just described:

$$\frac{\partial^2 u}{\partial r^2}+\frac{2}{r}\frac{\partial u}{\partial r}-\frac{2}{r^2}u=\frac{1-2\nu}{2G(1-\nu)}\left[\alpha^a\frac{\partial p^a}{\partial r}+\alpha^e\frac{\partial p^e}{\partial r}+\alpha^c\frac{\partial p^c}{\partial r}+\alpha^v\frac{\partial p^v}{\partial r}\right]$$

$$-k^a\left(\frac{\partial^2 p^a}{\partial r^2}+\frac{2}{r}\frac{\partial p^a}{\partial r}\right)+\left|\hat{s}_{a\rightarrow c}\right|=0$$

$$-k^e\left(\frac{\partial^2 p^e}{\partial r^2}+\frac{2}{r}\frac{\partial p^e}{\partial r}\right)-\left|\hat{s}_{c\rightarrow e}\right|+\left|\hat{s}_{e\rightarrow v}\right|=0 \qquad (3.1a\text{-}e)$$

$$-k^c\left(\frac{\partial^2 p^c}{\partial r^2}+\frac{2}{r}\frac{\partial p^c}{\partial r}\right)-\left|\hat{s}_{a\rightarrow c}\right|+\left|\hat{s}_{c\rightarrow e}\right|+\left|\hat{s}_{c\rightarrow v}\right|=0$$

$$-k^v\left(\frac{\partial^2 p^v}{\partial r^2}+\frac{2}{r}\frac{\partial p^v}{\partial r}\right)-\left|\hat{s}_{e\rightarrow v}\right|-\left|\hat{s}_{c\rightarrow v}\right|=0$$

The following relationship was proposed to alleviate the constraint of a unique permeability for the CSF compartment in order to account for AQP4's swelling characteristics:

$$k_e/\mu_e=\left(k_e/\mu_e\right)\left[1-\left(\frac{P_e-P_{ref}}{P_{ref}}\right)\right](A_f) \qquad (3.2)$$

From equation 3.2, k_e and μ_e have already been described, P_e is the CSF pressure, P_{ref} is a reference pressure and finally A_f is an amplification factor, and here it has a value of unity. The permeability was made to vary between the interval: $1.4\cdot10^{-14} \leq k_e\,[m^2] \leq 9.9\cdot10^{-14}$, and coupled with the varying CSF pressure P_e. P_{ref} was chosen to possess a value $P_{ref} = 1$ *kPa*. Due to insufficient experimental data, AQP4 expression is not accounted for in equation 3.2. More detail can be assigned to this boundary condition (when sufficient data become available) by including the swelling characteristics as a function of pressure and aquaporin expression. This can also be done by additionally altering the relevant transfer coefficient $\hat{s}_{c\rightarrow e}$ in equations 3.1c and 3.1d.

Finally, we define a useful parameter, namely the increment of fluid content, ζ, in terms of strain, ε as [292]:

$$\zeta = \alpha\varepsilon + \frac{(1-\alpha\beta)\alpha}{K\beta}\, p \tag{3.3}$$

In Equation 3.3, ε, the dilation, is given by $\varepsilon = (\partial u/\partial r) + 2(u/r)$, β is Skempton's coefficient and K, the bulk modulus. β denotes the measure of the distribution of the applied stress between the solid matrix and CSF. A value of $\beta = 0.99$ represents a saturated mixture where the applied load is nearly entirely supported by the CSF fluid.

3.3 Boundary conditions: 1D FDM-CFD

3.3.1 Boundary conditions for the skull

As discussed earlier, the shell responsible for outlining the skull lies at $r = r_M$, and here the displacement is deemed to be zero, as we are taking into account a rigid, adult skull:

$$u\left(r_M, t\right) = 0 \tag{3.4}$$

The blood pressures in the arterial and venous compartments are assigned physical values:

$$p^a\left(r_M, t\right) = p_{bpA} \text{ and } p^v\left(r_M, t\right) = p_{bp} \tag{3.5a-b}$$

In addition to the above boundary conditions, there is a restraint on the flow both into and out of the capillary network *(c)* at the skull and the resulting accumulation of CSF into the venous network ultimately results in a pressure rise, hence:

$$\frac{\partial p^c(r_M, t)}{\partial r} = 0 \text{ and } p^e\left(r_M, t\right) = p^v\left(r_M, t\right) + \mu^e R Q_0 \tag{3.6a-b}$$

3.3.2 Boundary conditions at the ventricular wall

Stress is assumed continuous across the wall, Hence at $r = r_v$,

$$(1-\nu)\frac{\partial u\left(r_v, t\right)}{\partial r} + 2\nu\frac{u\left(r_v, t\right)}{r_v} - \sum_{i=a,e,c,v} \frac{\left(\alpha^i - 1\right)(1-2\nu)}{2G}\, p^i\left(r_v, t\right) = 0 \tag{3.7}$$

A pressure drop exists in the capillary compartment due to the production of CSF from the blood, hence:

$$-\kappa_{c\to ven}\frac{\partial p^c\left(r_v, t\right)}{\partial r} = -Q_p \tag{3.8}$$

There is no flow into or out of the arterial and venous networks, hence:

$$\frac{\partial p^a\left(r_v, t\right)}{\partial r} = \frac{\partial p^v\left(r_v, t\right)}{\partial r} = 0 \tag{3.9a-b}$$

The final boundary condition involves the conservation of mass of fluid within the ventricular system:

$$Q_p = \frac{\pi d^4}{128\mu^e L}\left[p^e\left(r_v,t\right) - p^e\left(r_M,t\right)\right] - 4\pi k^e\left(r_1+u_1^n\right)^2\frac{\partial p^e\left(r_v,t\right)}{\partial r} + 4\pi\left(r_1+u_1^n\right)^2\frac{\partial u\left(r_v,t\right)}{\partial t} \quad (3.10)$$

3.3.3 Boundary conditions at the choroid plexuses and outlets

The porosity of the choroid plexus was varied according to the constant initial inlet pressure of 2000 *Pa*. An outlet pressure of 0 *Pa* was assigned to all exits from the fourth ventricle. The same boundary condition of 0 *Pa* was also assigned to the outlets when considering EFV and ETV. In addition, this surface was assumed isotropic, with a permeability of 10^{-10} m^2. The choroid plexuses shown in Figure 1.1c are supplied by the aforementioned unified initial inlet pressure boundary condition representing the feeding arteries at the different choroid plexus locations that ultimately produce CSF filtrate. The CSF produced in the plexuses passes through the choroid plexus surface (which encapsulates both the basolateral and apical membranes) of varying porosity and aforementioned permeability.

These conditions are assigned to the surface. In addition, the capillary network resistance given by $\varkappa_{c\rightarrow ventricle}$, is included in the framework of the choroid plexuses producing CSF filtrate via the inlet blood supplies.

When running the CFD simulations to determine the CSF flow dynamics through the ventricular system, the flux of CSF exiting the outlets is used to replace the Poiseuille assumption in equation 3.10.

3.3.4 Reynolds number and Wall Shear Stress (WSS)

The peak velocity in the aqueduct was noted, along with the peak Reynolds number, Wall Shear Stress (WSS) and pressure difference between isolated points in the lateral ventricle and fourth ventricle (see Figure 3.1b for location of measurement), ΔP. The peak Reynolds number, Re_p, is based on the peak velocity v_p and hydraulic diameter D_h. D_h is given by $D_h = 4A/P_e$, where A and P_e are the area and perimeter respectively. In this work, all cross sectional areas resembled an ellipse as $Axis_{major}(a)/Axis_{minor}(b) > 1$ for all concerned cross sections. The perimeter of an ellipse was therefore used, and this is approximately given by: $P_e = 2\pi(a^2/2+b^2/2)^{1/2}$. Re_p is therefore defined as $Re_p = (\rho^e v_p D_h)/\mu^e$, where ρ^e and μ^e are the density and dynamic viscosity of CSF. Finally, the wall shear stress is defined by $\tau = \mu^e(\partial u/\partial y)|_{y=0}$. Here, μ^e has already been defined and u is the flow velocity parallel to the wall and y is the distance from the wall.

3.4 Solution Method: 1D FDM-CFD

The governing multicompartmental poroelastic equations are solved with an implicit (necessary to overcome the stiffness of the multi-scalar MPET system) second-order central finite differences scheme on the midpoints and forward/backward Euler used on the boundary nodes. The implicit method is unconditionally stable for all values of grid spacing. The quasi-steady time discretization (for the temporally dependent terms in the boundary conditions) is performed via a first-order Euler approach. The final discretised system is of the form $\boldsymbol{Ax} = \boldsymbol{b}$.

3.4.1 Discretisation of the MPET system

The system Equations 3.1a-e, adaptive permeability (Equation 3.2) and the boundary condition equations 3.4-3.10 are holistically specified as a boundary value problem (BVP), and are discretised using the Finite Difference Method (FDM).

The derivative of $c(x)$ with respect to x is given by the difference quotients for forward, backward and central difference as:

$$\begin{aligned} c_x|_i &= c_x(x_i) \\ &= \lim_{\Delta x \to 0} \frac{c_x(x_i + \Delta x) - c_x(x_i)}{\Delta x} \\ &= \lim_{\Delta x \to 0} \frac{c_x(x_i) - c_x(x_i - \Delta x)}{\Delta x} \\ &= \lim_{\Delta x \to 0} \frac{c_x(x_i + \Delta x) - c_x(x_i - \Delta x)}{2\Delta x} \end{aligned} \tag{3.11a-c}$$

If Δx is small but finite, once can therefore obtain approximations of the derivative $c(x)$ in the form of the explicit forward difference:

$$c_x|_i \approx \frac{c_{i+1} - c_i}{\Delta x} \tag{3.11d}$$

Implicit backward difference,

$$c_x|_i \approx \frac{c_i - c_{i-1}}{\Delta x} \tag{3.11e}$$

and finally the central difference,

$$c_x|_i \approx \frac{c_{i+1} - c_{i-1}}{2\Delta x} \tag{3.11f}$$

The analysis of the aforementioned approximations of the derivatives is conducted using Taylor expansion around the point x_i. The truncation error (err) is defined as the difference between the exact value and its numerical approximation. The order of the forward and backward finite difference approximations is $err = O(\Delta x)$ and is therefore first order accurate, whilst the central difference is second order accurate.

As already mentioned, the central difference scheme is used for spatial discretization (equations of motion), forward difference scheme for the temporal discretisation and forward/backward difference schemes for the spatial portions of the boundary conditions. Hence:

$$\frac{\partial^2 c}{\partial r^2} = \frac{c_{i+1}^{n+1} - 2c_i^{n+1} + c_{i-1}^{n+1}}{\Delta r^2} \qquad r_i = r_A + i\Delta r \quad i = 0,...,M$$

$$\frac{\partial c}{\partial r} = \frac{c_{i+1}^{n+1} - c_{i-1}^{n+1}}{2\Delta r} \qquad t^n = n\Delta t \qquad n = 0,...,N$$

$$\frac{\partial c}{\partial t} = \frac{c_i^{n+1} - c_i^n}{\Delta t} \qquad c_i^n = c\left(r_i, t^n\right)$$

$$\frac{\partial}{\partial t}\left(\frac{\partial c}{\partial r}\right) = \frac{c_{i+1}^{n+1} + c_{i-1}^n - c_{i-1}^{n+1} + c_{i+1}^n}{2\Delta r \Delta t}$$

Applying the above discretisation to the MPET system already outlined, we obtain:

3.4.1.1 Displacement equation (Equation 3.1a)

$$\begin{aligned} &a_i u_{i-1}^{n+1} + b_i u_i^{n+1} + c_i u_{i+1}^{n+1} + d_i p_{i-1}^{a,n+1} - d_i p_{i+1}^{a,n+1} + e_i p_{i-1}^{c,n+1} - e_i p_{i+1}^{c,n+1} + ... \\ &...+ f_i p_{i-1}^{e,n+1} - f_i p_{i+1}^{e,n+1} + g_i p_{i-1}^{v,n+1} - g_i p_{i+1}^{v,n+1} = 0 \end{aligned} \tag{3.12}$$

3.4.1.2 Pressure equations (Equation 3.1b-e)

$$\begin{aligned} a_i p_{i-1}^{a,n+1} + h_i p_i^{a,n+1} + c_i p_{i+1}^{a,n+1} &= J_A \\ a_i p_{i-1}^{c,n+1} + h_i p_i^{c,n+1} + c_i p_{i+1}^{c,n+1} &= J_C \\ a_i p_{i-1}^{e,n+1} + h_i p_i^{e,n+1} + c_i p_{i+1}^{e,n+1} &= J_E \\ a_i p_{i-1}^{v,n+1} + h_i p_i^{v,n+1} + c_i p_{i+1}^{v,n+1} &= J_V \end{aligned} \tag{3.13a-d}$$

3.4.1.3 Boundary conditions for the skull (Equations 3.4-3.6)

$$\begin{aligned} u_M^{n+1} &= 0 \\ p_M^{a,n+1} &= p_{bpA} \\ p_M^{v,n+1} &= p_{bp} \\ p_M^{c,n+1} &= p_{M-1}^{c,n+1} \\ p_M^{e,n+1} &= p_M^{v,n+1} + P^* \end{aligned} \tag{3.14a-e}$$

3.4.1.4 Boundary conditions for the ventricle wall (Equations 3.7-3.10)

$$\begin{aligned} Au_1^{n+1} + Bu_2^{n+1} + C_A p_1^{a,n+1} + C_C p_1^{c,n+1} + C_E p_1^{e,n+1} + C_V p_1^{v,n+1} &= 0 \\ p_1^{c,n+1} - p_2^{c,n+1} &= D \\ p_1^{a,n+1} &= p_2^{a,n+1} \\ p_1^{v,n+1} &= p_2^{v,n+1} \\ Hu_1^{n+1} + Jp_1^{e,n+1} + L^* p_2^{e,n+1} + Np_M^{e,n+1} &= F^* \end{aligned} \tag{3.15a-e}$$

The numerical template of the MPET system is shown below (in the form $\boldsymbol{Ax} = \boldsymbol{b}$). This template is coupled with CFD-ACE+ (ESI Group, Paris, France) as a user-defined subroutine (UDS). For $M = 4$, we obtain:

$$
\left[\begin{array}{cccccccccccccccc|c}
A & B & & & C_A & & & & C_C & & & & C_E & & & & C_V & & & & \\
a_2 & b_2 & c_2 & & d_2 & & -d_2 & & e_2 & & -e_2 & & f_2 & & -f_2 & & g_2 & & -g_2 & & \\
 & a_3 & b_3 & c_3 & & d_3 & & -d_3 & & e_3 & & -e_3 & & f_3 & & -f_3 & & g_3 & & -g_3 & \\
 & & & 1 & & & & & & & & & & & & & & & & & \\
\hline
 & & & & 1 & -1 & & & & & & & & & & & & & & & \\
 & & & & a_2 & h_2 & c_2 & & & & & & & & & & & & & & \\
 & & & & & a_3 & h_3 & c_3 & & & & & & & & & & & & & \\
 & & & & & & & 1 & & & & & & & & & & & & & \\
\hline
 & & & & & & & & 1 & -1 & & & & & & & & & & & \\
 & & & & & & & & a_2 & h_2 & c_2 & & & & & & & & & & \\
 & & & & & & & & & a_3 & h_3 & c_3 & & & & & & & & & \\
 & & & & & & & & & & -1 & 1 & & & & & & & & & \\
\hline
H & & & & & & & & & & & & J & L^* & & N & & & & & \\
 & & & & & & & & & & & & a_2 & h_2 & c_2 & & & & & & \\
 & & & & & & & & & & & & & a_3 & h_3 & c_3 & & & & & \\
 & & & & & & & & & & & & & & & 1 & & & & 1 & \\
\hline
 & & & & & & & & & & & & & & & & 1 & -1 & & & \\
 & & & & & & & & & & & & & & & & a_2 & h_2 & c_2 & & \\
 & & & & & & & & & & & & & & & & & a_3 & h_3 & c_3 & \\
 & & & & & & & & & & & & & & & & & & & 1 &
\end{array}\right]
\left[\begin{array}{c}
u_1 \\ \vdots \\ \vdots \\ u_4 \\ \hline
p_1^a \\ \vdots \\ \vdots \\ p_4^a \\ \hline
p_1^c \\ \vdots \\ \vdots \\ p_4^c \\ \hline
p_1^e \\ \vdots \\ \vdots \\ p_4^e \\ \hline
p_1^v \\ \vdots \\ \vdots \\ p_4^v
\end{array}\right]
=
\left[\begin{array}{c}
0 \\ \vdots \\ \vdots \\ 0 \\ \hline
0 \\ J_A \\ J_A \\ 0 \\ \hline
D \\ J_C \\ J_C \\ p_{bpA} \\ \hline
F^* \\ J_E \\ J_E \\ P^* \\ \hline
0 \\ J_V \\ J_V \\ p_{bp}
\end{array}\right]
\tag{3.16}
$$

In the MPET template shown in Equation (3.16), the parameters/coefficients are given by:

$$
\begin{aligned}
a_i &= \left(1/\Delta r^2\right) - \left(1/r_i \Delta r\right) \\
b_i &= \left(-2/\Delta r^2\right) - \left(2/r_i^2\right) \\
c_i &= \left(1/\Delta r^2\right) + \left(1/r_i \Delta r\right) \\
d_i &= \alpha^a \left(1-2\nu\right)/4G\left(1-\nu\right)\Delta r \\
e_i &= \alpha^c \left(1-2\nu\right)/4G\left(1-\nu\right)\Delta r \\
f_i &= \alpha^e \left(1-2\nu\right)/4G\left(1-\nu\right)\Delta r \\
g_i &= \alpha^v \left(1-2\nu\right)/4G\left(1-\nu\right)\Delta r \\
h_i &= \left(-2/\Delta r^2\right)
\end{aligned}
\qquad
\begin{aligned}
J_A &= \left|\hat{s}_{a\to c}\right|/k^a \\
J_C &= -\left|\hat{s}_{a\to c}\right|/k^c + \left|\hat{s}_{c\to e}\right|/k^c + \left|\hat{s}_{c\to v}\right|/k^c \\
J_E &= -\left|\hat{s}_{c\to e}\right|/k^e + \left|\hat{s}_{e\to v}\right|/k^e \\
J_V &= -\left|\hat{s}_{c\to v}\right|/k^v - \left|\hat{s}_{e\to v}\right|/k^v \\
C_A &= \left(1-\alpha^a\right)\left(1-2\nu\right)/2G \\
C_C &= \left(1-\alpha^c\right)\left(1-2\nu\right)/2G \\
C_E &= \left(1-\alpha^e\right)\left(1-2\nu\right)/2G \\
C_V &= \left(1-\alpha^v\right)\left(1-2\nu\right)/2G
\end{aligned}
\qquad
\begin{aligned}
A &= 2\nu/r_1 - \left(1-\nu\right)/\Delta r \\
B &= \left(1-\nu\right)/\Delta r \\
D &= Q_p \Delta r/\kappa_{c\to ven} \\
F^* &= Q_p + 4\pi u_1^n \left(r_1 + u_1^n\right)^2/\Delta t \\
H &= 4\pi \left(r_1 + u_1^n\right)^2/\Delta t \\
J &= \pi d^4/128\,\mu^e L + 4\pi k^e \left(r_1 + u_1^n\right)^2/\Delta r \\
L^* &= -4\pi k^e \left(r_1 + u_1^n\right)^2/\Delta r \\
N &= -\pi d^4/128\,\mu^e L \\
P^* &= \mu^e R Q_o
\end{aligned}
$$

3.4.2 Discretisation of the nonlinear CSF permeability MPET system

As was mentioned in §2.5.4, and represented by Equation (2.50), this work also incorporates an assessment of a strain-dependent permeability for the ISF/CSF compartment. The transport law in §2.4.2 is amended to include the nonlinear permeability, and subsequently inserted into the fluid phase continuity equation (for the CSF compartment), namely, Equation (2.41). The governing equations are amended to:

$$\frac{\partial^2 u}{\partial r^2}+\frac{2}{r}\frac{\partial u}{\partial r}-\frac{2}{r^2}u-\frac{1-2\nu}{2G(1-\nu)}\left[\alpha^a\frac{\partial p^a}{\partial r}+\alpha^e\frac{\partial p^e}{\partial r}+\alpha^c\frac{\partial p^c}{\partial r}+\alpha^v\frac{\partial p^v}{\partial r}\right]=0$$

$$-k^a\left(\frac{\partial^2 p^a}{\partial r^2}+\frac{2}{r}\frac{\partial p^a}{\partial r}\right)+\left|\dot{s}_{a\to c}\right|=0$$

$$-k^c\left(\frac{\partial^2 p^c}{\partial r^2}+\frac{2}{r}\frac{\partial p^c}{\partial r}\right)-\left|\dot{s}_{a\to c}\right|+\left|\dot{s}_{c\to e}\right|-\left|\dot{s}_{c\to v}\right|=0 \qquad (3.17a\text{-}e)$$

$$\frac{1}{r^2}\frac{\partial}{\partial r}\left(r^2k^e e^{M\varepsilon}\frac{\partial p^e}{\partial r}\right)-\left|\dot{s}_{c\to e}\right|+\left|\dot{s}_{e\to v}\right|=0$$

$$-k^v\left(\frac{\partial^2 p^v}{\partial r^2}+\frac{2}{r}\frac{\partial p^v}{\partial r}\right)-\left|\dot{s}_{e\to v}\right|-\left|\dot{s}_{c\to v}\right|=0$$

The boundary condition that is amended to accommodate the non-linear permeability for the CSF compartment is Equation (3.10):

$$Q_p=\frac{\pi d^4}{128\mu^e L}\left[p^e\left(r_v,t\right)-p^e\left(r_M,t\right)\right]-4\pi k^e e^{M'\varepsilon}\left(r_1+u_1^n\right)^2\frac{\partial p^e\left(r_v,t\right)}{\partial r}+4\pi\left(r_1+u_1^n\right)^2\frac{\partial u\left(r_v,t\right)}{\partial t} \qquad (3.18)$$

The new system to be solved (equations (3.17a-e) with relevant boundary conditions) uses once again a Finite Difference scheme. The displacement interval $[r_a, r_M]$ is subdivided into $m = (r_M - r_a)/\Delta r$ equispaced points, where $r_i = r_a + i\Delta r$, $i=0,\ldots,m$. Central differences are used for the derivatives. Defining the nodal approximations $U_i \approx u(r_i)$ and $P_i \approx p(r_i + u(r_i))$, Equation 3.16a discretizes to:

$$\frac{U_{i-1}-2U_i+U_{i+1}}{(\Delta r)^2}+\frac{2}{r_i}\frac{U_{i+1}-U_{i-1}}{2(\Delta r)}-\frac{2U_i}{r_i^2}=\frac{1-2\nu}{2G(1-\nu)}\left[\alpha^a\frac{P_{i+1}-P_{i-1}}{2(\Delta r)}+\alpha^c\frac{P_{i+1}-P_{i-1}}{2(\Delta r)}+\alpha^e\frac{P_{i+1}-P_{i-1}}{2(\Delta r)}+\alpha^v\frac{P_{i+1}-P_{i-1}}{2(\Delta r)}\right] \qquad (3.19)$$

The strain, which is defined as $\varepsilon = \partial u/\partial r + 2u/r$, is calculated using one-sided differences on the boundaries and central differences everywhere else.

For the pressure, the domain of computation is classified as $[r_0 + U_0, r_M + U_M]$, and discretised into $m = (r_M + U_M - r_0 - U_0)/\Delta r$ points, where $\breve{r}_j = r_0 + U_0 + j\Delta\breve{r}$, $j = 0,\ldots,m$. The strain is interpolated at each node in the manner: $\breve{r}_{j+1/2} = \breve{r}_j + \Delta\breve{r}/2$. Equation (3.17c) is therefore discretised as the displacement equation, namely using central differences, hence:

$$\left[\breve{r}_{j+1/2}^2 k^e e^{M'\varepsilon_{j+1/2}}\left(P_{j+1}-P_j/\Delta\breve{r}\right)-\breve{r}_{j-1/2}^2 k^e e^{M'\varepsilon_{j-1/2}}\left(P_j-P_{j-1}/\Delta\breve{r}\right)\right]=\left(\left|\dot{s}_{c\to e}\right|-\left|\dot{s}_{e\to v}\right|\right)\Delta\breve{r} \qquad (3.20)$$

The full discretisation template is similar to that in Equation (3.16), with adjustments to the coefficients in the CSF pressure compartment of the matrix, along with the relevant boundary conditions. Figure 3.4 gives an outline of the operations involved.

3.4.3 Implementation

The numerical template in equation (3.16) was implemented in `C++` to allow for coupling with `FORTRAN` and therefore by default `CFD-ACE+` in the form of a UDS. This series is essential for the coupling of the 1D MPET solver and the use of patient specific ventricular geometries. Template Numerical Toolkit (`TNT`) is a collection of interfaces and reference implementations of numerical objects useful for scientific computing in `C++`. The toolkit defines interfaces for basic data structures, such as multidimensional arrays and sparse matrices, commonly used in numerical applications. In this work, the MPET solver written in `C++` makes use of

TNT::Array1D, which incorporates the MPET discretization template (including boundary conditions), the grid domain and of course the solution vectors. The linear system ($\boldsymbol{Ax} = \boldsymbol{b}$) is solved using the incorporated (JAMA::LU) *LU* decomposition framework, as pivoting is always applied and therefore minimising the chances of the constructor failing when presented with determinants close to zero. The system in equation (3.16) with all the relevant boundary conditions is solved using MATLAB (*R2013a*). Figure 3.5 depicts a flowchart summarising the solution process.

3.4.4 Mesh Generation

Mesh generation (see Figure 3.3) for the 3D volumes was achieved via the use of CFD-VisCART (ESI Group, Paris, France). CFD-VisCART is a 3D viscous, unstructured adaptive Cartesian mesh grid generation system for use with the CFD-ACE+ and CFD-FASTRAN flow solvers. CFD-VisCART is ideally suited for extremely complex geometries found in biomedical engineering applications (the cerebral ventricles and choroid plexuses for instance). It handles imperfect geometries with holes, overlaps, and cracks. It also offers solution-based adaptive mesh refinement for obtaining optimal mesh resolution. In CFD analysis, the grid generation process is considered the most serious bottleneck. The most demanding part within that process is the handling of complex geometries and generating a computational grid.

CFD-VisCART offers a tree-based data structure to generate a Cartesian-based grid. One of the most appealing properties of a Cartesian grid is its efficiency in filling space with a minimum number of cells and faces, given a certain grid resolution. CFD-VisCART supports both *Octree* and *Omnitree* data structures. The *Omnitree* data structure supports anisotropic grid adaptations of Cartesian cells in natural manner [335], and is the chosen method for this work.

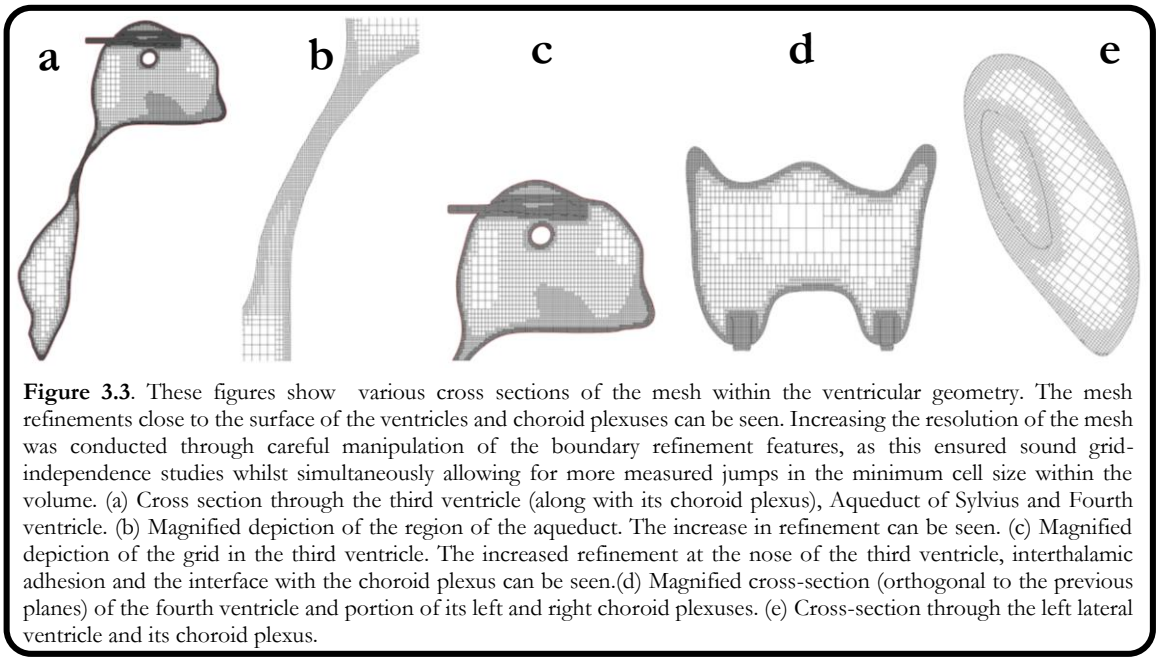

Figure 3.3. These figures show various cross sections of the mesh within the ventricular geometry. The mesh refinements close to the surface of the ventricles and choroid plexuses can be seen. Increasing the resolution of the mesh was conducted through careful manipulation of the boundary refinement features, as this ensured sound grid-independence studies whilst simultaneously allowing for more measured jumps in the minimum cell size within the volume. (a) Cross section through the third ventricle (along with its choroid plexus), Aqueduct of Sylvius and Fourth ventricle. (b) Magnified depiction of the region of the aqueduct. The increase in refinement can be seen. (c) Magnified depiction of the grid in the third ventricle. The increased refinement at the nose of the third ventricle, interthalamic adhesion and the interface with the choroid plexus can be seen.(d) Magnified cross-section (orthogonal to the previous planes) of the fourth ventricle and portion of its left and right choroid plexuses. (e) Cross-section through the left lateral ventricle and its choroid plexus.

The use of anisotropic solution adaptation allows for a substantial reduction in the total number of cells to achieve a given level of solution accuracy. *Octree* will always split the cell into eight sub-cells along *X*, *Y* and *Z* dimension (high possibility of creating skinny cells), while *Omnitree* can split the cell along *X*, or *Y*, or *Z*, or *XY*, or *XZ*, or *YZ* or *XYZ* as necessary so that one can obtain fewer cell numbers with the same bounding box setting. CFD-VisCART also possesses a Grid Quality Panel which enables the detection of various cell types in a viscous grid and repairs them. The following types of bad cells can be detected and removed: negative volume cells, small volume cells, degenerated faces, skewed cells and jump cells.

3.4.5 Base discretization of MPET model

The base discretisation for the spherically symmetric poroelastic models (both strain dependent and independent permeability) involved $M = 81$ nodes, as this yielded results within a 5% band from what we considered as the fully converged solution. Full grid independence was achieved at $M = 200$ nodes.

Flow through the multidimensional ventricles is solved using the multiphysics software CFD-ACE+ (ESI Group, Paris, France) which is based on the finite volume method (FVM), along with central spatial differencing, algebraic multigrid scheme and the SIMPLEC pressure–velocity coupling (See Appendix A). The coupling between the poroelastic solver and the flow solver is achieved through appropriate CFD-ACE+ UDS. Similarly, adequate discretization of the 3D ventricular domain is required in order to acquire fully resolved results. Similar grid independence analysis resulted in meshes of over 2 million cells for that domain.

The coupling between the poroelastic solver and the flow solver is achieved through the use of CFD-ACE+s' UDS. After an initial assumption of the aqueductal flow, the pressures at the skull and inside the ventricles are passed to the UDS as pressure boundary conditions (after each time step of the poroelastic solver). Following the finite volume solution of the ventricular and therefore aqueductal flow, the mass flux is calculated in the UDS and passed to the poroelastic solver for the next iteration. CFD-VIEW (ESI Group, Paris, France) is used as the post processing tool to analyse the flow physics. This tool also interacts with the CFD solver used in this work (CFD-ACE+). Figure 3.5 shows a schematic of the coupling involved.

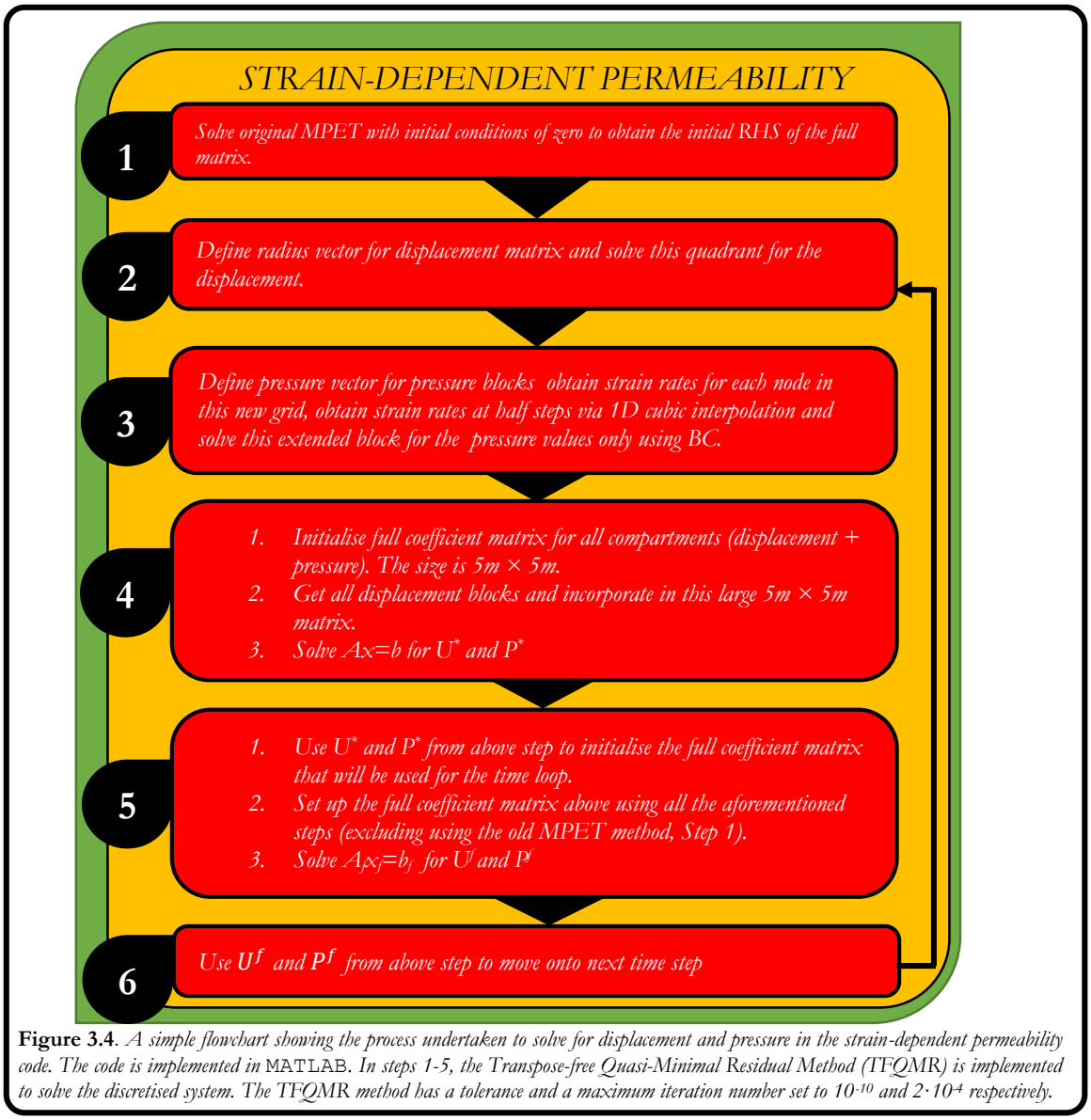

Figure 3.4. *A simple flowchart showing the process undertaken to solve for displacement and pressure in the strain-dependent permeability code. The code is implemented in* MATLAB. *In steps 1-5, the Transpose-free Quasi-Minimal Residual Method (TFQMR) is implemented to solve the discretised system. The TFQMR method has a tolerance and a maximum iteration number set to* 10^{-10} *and* $2 \cdot 10^{-4}$ *respectively.*

3.4.6 Simulations setup

3.4.6.1 Parallel decomposition

In CFD-ACE+, the solver can be run in parallel mode by utilising domain decomposition. This involves the division of the data amongst multiple processors. Each processor solves for a single zone of the overall mesh. CFD-ACE+ provides several methods and options for decomposition of the domain, such as metis, cell_groups, orig_topo, material, wavefront and *x*, *y*, *z* decomposition. The manner of decomposition influences the parallel efficiency and speed. It is important that all the processors get nearly equal numbers of cells (workload balancing). In this work, the metis scheme was used, along with the recursive bisection partition method since the geometries were decomposed into 6 zones. *Metis* (Serial Graph Partitioning and Fill-reducing Matrix Ordering) is a set of serial programs for partitioning graphs, partitioning finite element meshes, and producing fill reducing orderings for sparse

matrices. The algorithms implemented in metis are based on the multilevel recursive-bisection, multilevel k-way, and multi-constraint partitioning schemes [458-459] developed by the Karypis Lab (George Karypis, a Professor at the Department of Computer Science & Engineering at the University of Minnesota in the Twin Cities of Minneapolis and Saint Paul). metis' features include providing high quality partitions, between 10% - 50% better than those produced by analogous spectral partitioning algorithms. The algorithm is fast (one to two orders of magnitude faster than other widely used partitioning algorithms) and finally, it produces low fill orderings (able to reduce the storage and computational requirements of sparse matrix factorisation, by up to an order of magnitude) [336].

3.4.6.2 CFD-ACE+ Simulation setup

The iterative coupling between the poroelastic solver and CFD-ACE+ inherently results in a very stiff system. The initial conditions therefore play a pivotal role in the evolution of the simulation. To cater correctly for this stiffness, a steady-state solution is computed based on a set of boundary conditions ascertained from the model in §3.4. This steady-state model is then used as the initial conditions for the transient model, and the steady-state CSF flux is used in the first call to the poroelastic C++ solver.

The steady-state solver is defined using the steady flow solver module (see Appendix *A*) with a single fluid ($\varrho^e = 997\ kg/m^3$, $\mu^e = 8.9 \cdot 10^{-4}\ kg/ms$) and reference pressure of 100 *kPa* or approximately 1 *atm*. The outlet pressures is specified as 0 *Pa* and the inlet pressures (see §3.1.3) are 2000 *Pa*, the flow domain is initialized to the outlet pressure, and all velocities are set as zero. Central differences are used for the spatial differencing method, with a blending of 0.3, both the velocity and pressure correction solvers use the AMG method, and the maximum number of iterations is 250 with a convergence criterion and minimum residual of 10^{-18}. No pre-conditioners were used for the AMG velocity and pressure solver, whilst the number of Sweeps was set at 500, along with a criterion of 0.001. The inertial relaxation for the velocity was set at 0.2, whilst it a value of unity was assigned for the linear relaxation of the pressure, density and viscosity. Limits are placed on the velocity and pressure solver such that p, $\boldsymbol{v}(u,v,w) \in [-10^5, 10^5]$. The density was set as $\varrho^e \in [10^{-6}, 10^{20}]$ and the viscosity as $\mu \in [10^{-10}, 10^2]$. Finally, the Gradient and Divergence Calculation Method was the *Green-Gauss Methodology*, using the *Cell-To-Face* interpolation method.

Once the steady-state simulation is completed, a copy of the file can be transferred into the transient model. To make this change, the transient flow module is used with a user defined time step size, and the inlet pressure is specified by a UDS. The steady-state solution is used as the initial condition for the solver, the maximum number of iterations here is 500 and the convergence criteria was the same as before. The CFD-ACE+ simulation is linked with the poroelastic C++ solver through the *uout* UDS.

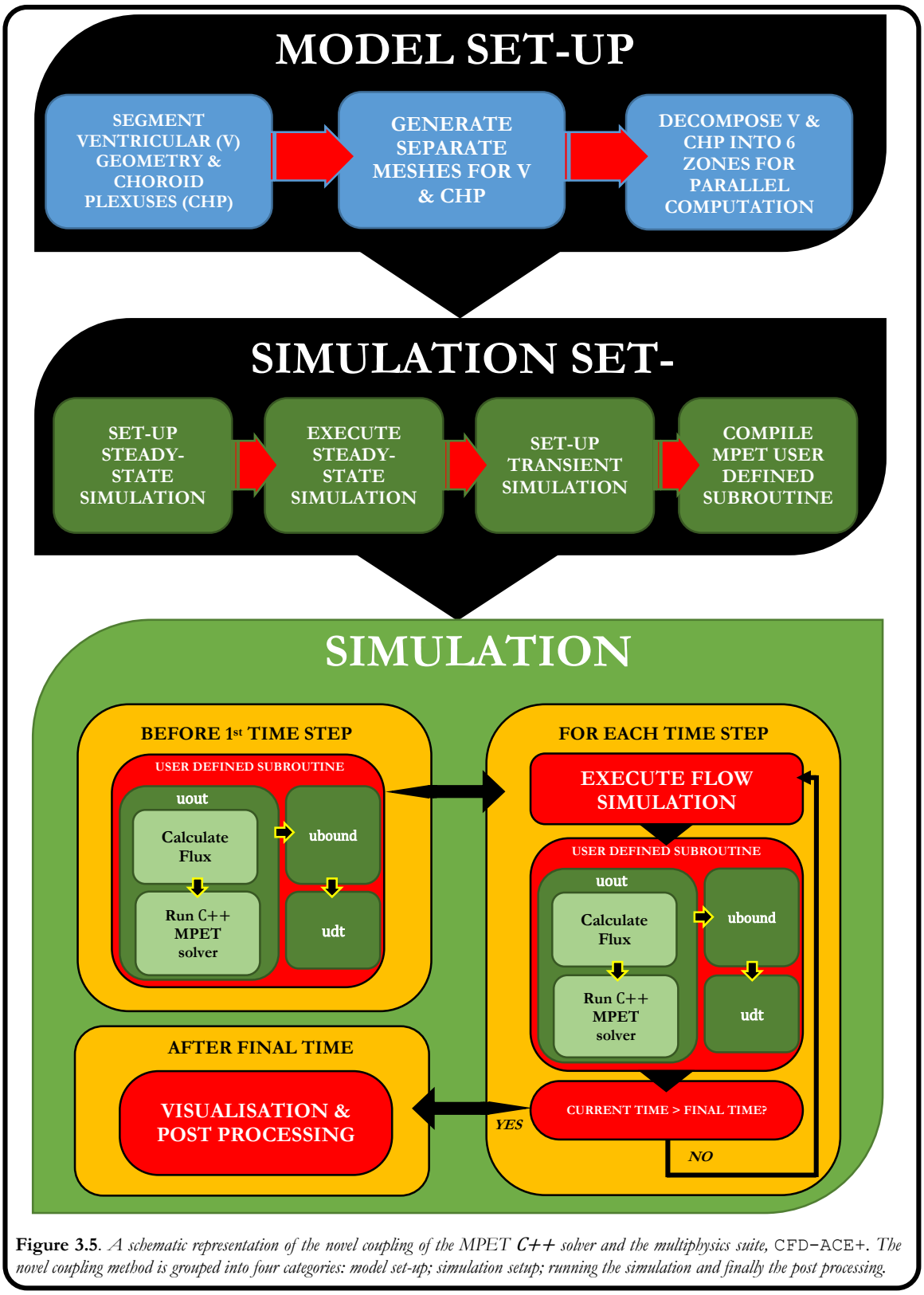

Figure 3.5. *A schematic representation of the novel coupling of the MPET C++ solver and the multiphysics suite,* `CFD-ACE+`. *The novel coupling method is grouped into four categories: model set-up; simulation setup; running the simulation and finally the post processing.*

3.5 MPET discretisation using the FEM

The previous section showed the development of FDM based MPET schemes. The purpose of this section is to devise a discretisation template for an n^{th}-dimensional transient MPET system. In this section, the MPET equations (2.47a-e) and relevant boundary conditions (2.48-2.59) are discretised using the continuous Galerkin (cG) Finite Element Method (FEM). Development of the MPET methodology includes the first simulations of a transient, four-network MPET model. The MPET methodology has been developed and harnessed in one, two and three dimensions.

3.5.1 Domain discretization for FDM and FVM

In the FDM method, the domain Ω is represented by a finite subset of nodal points, $\{x_i\} = \Omega_h \subset \Omega$. The grid is usually arranged in a uniform or non-uniform rectangular manner. The functions $\boldsymbol{u}$ and p are represented by a set of function values $\mathbf{u}_i$ and p_i that approximate $\mathbf{u}(x_i)$ and $p(x_i)$. The discrete equations are obtained by replacing the differentials in the PDEs by finite differences in the discrete equations, as seen in the previous section.

In the finite volume method, the domain Ω is partitioned into a finite set of volumes so that $\Omega_i \cap \Omega_j = \emptyset$, for $i \neq j$, and $\cup\bar{\Omega}_i = \bar{\Omega}$. In the cell centres (FVM described in Appendix A and used throughout the MPET-CFD simulations), the functions $\boldsymbol{u}$ are approximated by:

$$u_h = \sum_i a_i \varphi_i(x), \;\; i = 1, \ldots, n_{elements} \tag{3.21}$$

A similar result holds for p. In the above equation, the functions $\varphi(x_i)$ are defined on a single volume, or its boundaries. If there is a single location where the coefficient a_i is associated with each volume, the grid is termed cell centred (see Appendix A on FVM used in `CFD-ACE+`). If this coefficient is associated with each vertex, then this method is termed cell vertex. If on the other hand, the discretisation is constructed on cells located in the surrounding vertices of a grid, the mesh is referred to as vertex centred.

In order to prove the existence and uniqueness of solutions of the MPET PDEs, one must get acquainted with the Babuška-Lax-Milgram theorem which is an invariant of the Riesz Representation Theorem. In order to reach this stage one must first have an appreciation of some basic notions arising from Functional Analysis. The reader is referred to the book by Brezis [356] for a more thorough discussion, as their inclusion in the body of this text would sway the discussion towards a more theoretical treatment of Functional Analysis. In this chapter, the development of the FEM template for the MPET system will ensue in a step by step manner, inherently utilising these important theoretical concepts.

3.5.2 The MPET equations used in the FEM method

The quadruple-MPET system in a specified domain, Ω over a time interval $t \in J = [0, T]$, $T > 0$ reads:

$$
\begin{aligned}
& G\nabla^2 \boldsymbol{u} + (G+\lambda)\nabla\varepsilon = \left(\alpha^a \nabla p_a + \alpha^c \nabla p_c + \alpha^e \nabla p_e + \alpha^v \nabla p_v\right) \quad \text{in} \quad \Omega \times J \\
& \frac{\partial}{\partial t}(S^a p^a + \alpha^a \varepsilon) = \left(\frac{k_a}{\mu_a}\right)\nabla^2 p_a - \left|\hat{s}_{a\to c}\right| \quad \text{in} \quad \Omega \times J \\
& \frac{\partial}{\partial t}(S^c p^c + \alpha^c \varepsilon) = \left(\frac{k_c}{\mu_c}\right)\nabla^2 p_c + \left|\hat{s}_{a\to c}\right| - \left|\hat{s}_{c\to e}\right| - \left|\hat{s}_{c\to v}\right| \quad \text{in} \quad \Omega \times J \qquad (3.22\text{a-e}) \\
& \frac{\partial}{\partial t}(S^e p^e + \alpha^e \varepsilon) = \left(\frac{k_e}{\mu_e}\right)\nabla^2 p_e + \left|\hat{s}_{c\to e}\right| - \left|\hat{s}_{e\to v}\right| \quad \text{in} \quad \Omega \times J \\
& \frac{\partial}{\partial t}(S^v p^v + \alpha^v \varepsilon) = \left(\frac{k_v}{\mu_v}\right)\nabla^2 p_v + \left|\hat{s}_{c\to v}\right| + \left|\hat{s}_{e\to v}\right| \quad \text{in} \quad \Omega \times J
\end{aligned}
$$

The MPET system is completed with the following boundary conditions for each of the four compartments (Arterial blood, Arteriole/Capillary blood, Venous blood and CSF/ISF), in which $\partial\Omega = \Gamma_S \cup \Gamma_V$, where Γ_S and Γ_V are boundary conditions at the skull and ventricles respectively.

In equations (3.22a-e) above, $S^j(>0) = 1/M_j$ was defined in equation 2.44, where $j = [a, e, c, v]$ and S^j is deemed as the amalgamated compressibility of both fluid and solid phases (it is related to the bulk moduli) at the relevant compartment. $\mathbf{u}(\mathbf{x},t)$ is the displacement of the porous medium (describes the mean displacement of particles forming the solid matrix) and $p^{\phi}(\mathbf{x},t)$ is the fluid pressure of each compartment.

In this chapter, the focus will be on chronic HCP and oedema. Acute HCP will be revisited, however, this will be isolated to the 1D case. This is the first application of MPET to the cerebral environment in a higher (2nd and 3rd) spatial dimension. In addition, this will also be the first time that the transient effects of the fluid compartments are inherently included in such a methodology.

The use of the MPET framework is in itself a very recent development [102,106], and has been limited to a one dimensional finite difference formulation. The applicability of the method in higher spatial dimensions has never been investigated. The increase in spatial dimension, but also the addition of temporal variation in the pressure compartments under the guidance of the more rigorous FEM framework is presented. Of course, the problem occupying the developments of such methodologies is the availability of experimental data. This is an ongoing process, however, the final section of this chapter outlines the steps that are being taken to ascertain these specific parameters within a clinical setting, namely the EU project, `VPH-DARE@IT` (www.vph-dare.eu). The implications of the framework presented here, along with the development in experimental techniques that are discussed, will help shed light not only on the pathology of HCP development, but also on Vascular Dementia (VaD), Alzheimer's Disease (AD), Multiple Sclerosis (MS), Neuromyelitis optica (NMO), Neuroinflammation, Chiari Malformation (CM) and Glaucoma to name a few.

3.5.3 Variational formulation in 1D

In the formal derivation of any FEM, one has to approach this process by acquiring the variational formulation. This is done by multiplying the MPET equations (3.22a-e) with test functions and subsequently integrating by parts. This process is very important, and so it is appropriate to split the solid and liquid phases separately, for clarity's sake. This theme will persist for the higher dimensional ***u-p*** MPET formulations.

3.5.3.1 Variational formulation of the solid phase

From 4.2a, we have in the one dimensional case:

$$G\nabla^2\boldsymbol{u}+(G+\lambda)\nabla\varepsilon=\left(\alpha^a\nabla p_a+\alpha^c\nabla p_c+\alpha^e\nabla p_e+\alpha^v\nabla p_v\right)$$

$$G\nabla^2\boldsymbol{u}+(G+\lambda)\nabla(\nabla\cdot\boldsymbol{u})=\left(\alpha^a\nabla p_a+\alpha^c\nabla p_c+\alpha^e\nabla p_e+\alpha^v\nabla p_v\right),\quad x\in I \tag{3.23}$$

$$\text{where:}\quad \nabla^2\boldsymbol{u}=\frac{\partial^2 u}{\partial x^2}\ \left(\text{Cartesian coordinates}\right)$$

In the above equation, $G > 0$ and $\lambda > 0$ which assist in establishing uniqueness and existence of the solution for displacement $u = \mathbf{u}(x)$. Considering $I \in [x_v, x_s]$, where x_v and x_s are the radial Cartesian distances corresponding to the ventricles and skull respectively, one may multiply by a test function $N^{p,u}$ and integrate by parts:

$$\int_I\left[\nabla(\nabla u)N_i^u-\frac{1}{(2G+\lambda)}\sum_{j=a,e,c,v}\left(\alpha^j\nabla p_j\right)N_i^p\right]dx=0\ \therefore$$

$$\int_I\left(\nabla^2 uN_i^u-D_a\nabla p^aN_i^p-D_e\nabla p^eN_i^p-D_c\nabla p^cN_i^p-D_v\nabla p^vN_i^p\right)dx=0\quad\therefore$$

$$\int_I\left(\nabla^2u\right)N_i^u dx=N_i^u\frac{du}{dx}\bigg|_{x_v}^{x_s}-\int_I\frac{du}{dx}\frac{dN_i^u}{dx}dx\quad\text{and} \tag{3.24}$$

$$\int_I D_k\left(\nabla p^q\right)N_i^p dx=N_i^pD_k\ p^q\big|_{x_v}^{x_s}-D_k\int_I p^q\frac{dN_i^p}{dx}dx\quad\text{where}$$

$$k,q=a,e,c,v\quad\text{and}\quad D_k=\frac{\alpha^q}{(2G+\lambda)}$$

Hence, the combined formulation is:

$$\int_I\nabla^2uN_i^u-D_a\nabla p^aN_i^p-D_e\nabla p^eN_i^p-D_c\nabla p^cN_i^p-D_v\nabla p^vN_i^pdx=0\quad\therefore$$

$$N_i^u\frac{du}{dx}\bigg|_{x_v}^{x_s}-N_i^pD_a\ p^q\big|_{x_v}^{x_s}-N_i^pD_c\ p^c\big|_{x_v}^{x_s}-N_i^pD_e\ p^e\big|_{x_v}^{x_s}-N_i^pD_v\ p^v\big|_{x_v}^{x_s}-\int_I\frac{du}{dx}\frac{dN_i^u}{dx}dx+\ldots \tag{3.25}$$

$$\ldots+D_a\int_I p^a\frac{dN_i^p}{dx}dx+D_c\int_I p^c\frac{dN_i^p}{dx}dx+D_e\int_I p^e\frac{dN_i^p}{dx}dx+D_v\int_I p^v\frac{dN_i^p}{dx}dx=0$$

The distinction between N^u and N^p is made when considering the liquid phases later on. In this section (solid phase), the apex is dropped for the remainder of this section to ease the

analysis. The distinction between the two however, will become clear when considering the liquid phase. For the variational formulation to make sense, one has to make sure that the test function N_i is well behaved to the degree that the integrals in Equation 3.25 exist. We specifically require that N_i and its derivative N_i' are square integrable on the interval defined as *I*. In addition, the boundary condition on the skull is $u = 0$. Hence, the largest collection of admissible functions for the aforementioned properties is succinctly given by the space:

$$N_0 = \{N : \|N'\|_{L^2(\mathrm{I})} < \infty, \|N\|_{L^2(\mathrm{I})} < \infty, N(x_s) = 0\} \tag{3.26}$$

N_0 has infinite dimension, as there are an infinite number of functions that may be used as test functions. In addition, $\boldsymbol{u}$ is also a member of the aforementioned space, as it may be differentiated twice (smoothness) and also satisfies the fixed Dirichlet boundary condition at the skull. Hence, the variational formulation becomes: Find $u \in N_0$, such that:

$$\begin{aligned}
&\int_I \left(\nabla^2 u - D_a \nabla p^a - D_e \nabla p^e - D_c \nabla p^c - D_v \nabla p^v\right) N_i dx = 0 \quad \therefore \\
&N_i \left.\frac{du}{dx}\right|_{x_v}^{x_s} - N_i D_a \left. p^q \right|_{x_v}^{x_s} - N_i D_c \left. p^c \right|_{x_v}^{x_s} - N_i D_e \left. p^e \right|_{x_v}^{x_s} - N_i D_v \left. p^v \right|_{x_v}^{x_s} - \int_I \frac{du}{dx}\frac{dN_i}{dx} dx + \ldots \\
&\ldots + D_a \int_I p^a \frac{dN_i}{dx} dx + D_c \int_I p^c \frac{dN_i}{dx} dx + D_e \int_I p^e \frac{dN_i}{dx} dx + D_v \int_I p^v \frac{dN_i}{dx} dx = 0, \quad \forall N \in N_0
\end{aligned} \tag{3.27}$$

3.5.3.2 Finite Element Approximation (FEA) of the solid phase

The displacement now needs to be approximated by a continuous piecewise linear function via the introduction of a mesh in the interval *I*. The mesh possesses *n* subintervals. The space of all continuous piecewise linears is N_h. Since there is a function vanishing at the skull, a subspace of N_h is also required to satisfy this boundary condition, and in the process, contain all possible piecewise linears that satisfy the Dirichlet boundary condition. This is introduced as $N_{h,0}$:

$$N_{h,0} = \{N \in N_h : N(x_s) = 0\} \tag{3.28}$$

The space in Equation 3.28 is a smaller subspace than the large space N_0, hence, the Galerkin FEM utilising $N_{h,0} \subset N_0$ is sought: Find $u_h \in N_{h,0}$, such that:

$$\begin{aligned}
&-N_i \left.\frac{du_h}{dx}\right|_{x_v} + N_i D_a \left. p^a \right|_{x_v} + N_i D_c \left. p^c \right|_{x_v} + N_i D_e \left. p^e \right|_{x_v} + N_i D_v \left. p^v \right|_{x_v} - \int_I \frac{du_h}{dx}\frac{dN_i}{dx} dx + \ldots \\
&\ldots + D_a \int_I p^a \frac{dN_i}{dx} dx + D_c \int_I p^c \frac{dN_i}{dx} dx + D_e \int_I p^e \frac{dN_i}{dx} dx + D_v \int_I p^v \frac{dN_i}{dx} dx = 0, \quad \forall N \in N_{h,0}
\end{aligned} \tag{3.29}$$

3.5.3.3 The space of continuous piecewise linear polynomials

Piecewise linear functions are an organic extension of linear functions. The concept behind the construction of a piecewise linear function, *N*, is to partition the domain of *N* into smaller

subintervals. A linear function defines N on that subinterval. Placing the degrees of freedom at the common points between corresponding subintervals ensures that continuity of N is maintained between adjacent segments.

If $I = [x_0, x_n]$ is the interval of interest in the 1D MPET framework, $n+1$ node points $\{x_i\}^n_{i=0}$ define a partition $\mathcal{J}$: $\boldsymbol{x_v} = x_0 < x_1 < \ldots < x_n = \boldsymbol{x_s}$ of this interval into n subintervals $I_i = [x_{i-1}, x_i]$, $i=1,\ldots,n$ of length $h_i = x_{i-1} - x_i$, which in essence is the one dimensional mesh. On this mesh, $\mathcal{J}$, one may define the space N_h of continuous linear functions by: $N_h = \{N: N \in C^0(I), N|_{I_i} \in \wp_1(I_i)\}$, where $C^0(I)$ denotes the space of continuous functions on the interval I, and $\wp_1(I_i)$ denotes the space of linear functions on I_i. The functions in N_h are linear on each subinterval I_i and in the process continuous on the whole interval I. Any function N in N_h is therefore uniquely determined by its nodal values $\{N(x_i)\}^n_{i=0}$. This allows for the formal use of basis functions (hat functions) N_h for the nodes:

$$\theta_i = \begin{cases} (x_{i+1} - x)/h_i, & \text{if} \quad x \in I_i \\ (x - x_{i-1})/h_{i+1}, & \text{if} \quad x \in I_{i+1} \\ 0, & \text{otherwise} \end{cases} \tag{3.30}$$

The nodal values define the DOF, and an important property of the linearly independent combination of basis functions of monomials in 1D space (from Pascal's Triangle), and the coefficients $\{\vartheta_i\}^n_{i=0}$ allow for any function N in N_h, where $\vartheta_i = N(x_i)$, $i=0,\ldots,n$. In the latter, i represents the nodal values of N. One may therefore write:

$$N(x) = \sum_{i=0}^{n} \vartheta_i N_i(x) \tag{3.31}$$

An important property of the relationship in Equation 3.31 is the Kronecker delta function property:

$$N_i(x_j) = \delta_{ij} = \begin{cases} 1, & i = j, \quad j = 0,\ldots,n \\ 0, & i \neq j, \quad i, j = 0,\ldots,n \end{cases} \tag{3.32}$$

This function implies that the function N should be equal to unity at its home node i, whilst vanishing at the remote nodes $(i \neq j)$ of the element. Other additional properties that are generally overlooked in constructing FEM templates are: (i) Reproduction property and consistency; (ii) Linear independence; (iii) Partitions of Unity and (iv) Linear field reproduction. The importance of (iii) is that it allows a constant field or rigid body movement to be reproduced, whilst (iii) and (iv) are required to validate the elements in a standard patch test [357].

3.5.3.4 L^2- Projection

In general, the orthogonal approximation, or L^2-projection, is the best approximation to a function f when calculating the error in the L^2-norm (see Figure 3.6). As opposed to interpolation which approximates the continuous functions exactly at the nodes, the L^2-

projection is better on average, in addition to the added benefit of not requiring the function to be approximated to be continuous or have strictly defined nodal values [358]. The formal definition is given as:

Given a function $f \in L^2(I)$ the L^2-projection $P_h f \in N_h$ of f is given by:

$$\int_I (f - P_h f) N dx = 0, \quad \forall N \in N_h \tag{3.33}$$

A depiction of the orthogonal projection is shown in Figure 4.1a. Equation 4.13 is equivalent to:

$$\int_I (f - P_h f) N_i dx = 0, \qquad i = 0,1,...,n \tag{3.34}$$

where N_i represents the hat functions described earlier (see Figure 3.6b). Since $P_h f \in N_h$, it can be written in the linear combination: $P_h f = \sum_{j=0}^{n} \vartheta_j N_j$, with $n + 1$ unknown coefficients ϑ_j, $j = 0, 1\ldots, n$ to be determined. Inserting this ansatz into the original definition of the orthogonal projection one obtains:

$$\begin{aligned} \int_I f N_i dx &= \int_I \left(\sum_{j=0}^{n} \vartheta_j N_j \right) N_i dx \\ &= \sum_{j=0}^{n} \vartheta_j \int_I N_j N_i dx \quad \therefore \\ M_{ij} &= \int_I N_j N_i dx, \quad i, j = 0,1,...,n \\ b_i &= \int_I f N_i dx = \sum_{j=0}^{n} M_{ij} \vartheta_j, \quad i = 0,1,...,n \end{aligned} \tag{3.35a-b}$$

The coefficients ϑ_j, $j = 0, 1\ldots, n$ in the ansatz satisfy a linear system, which is solved to obtain the orthogonal projection. M_{ij} and b_i in this example are the traditional mass matrix and load vector.

3.5.3.5 Stiffness Matrix and Load Vector Assembly for solid phase

A basis for N_h is given by the aforementioned hat functions, defined in Equation 3.30. One may proceed by inserting the following ansatz into equation (3.29):

$$u_h = \sum_{j=0}^{n} \vartheta_j \theta_j \tag{3.36}$$

In addition, one must also incorporate $N=\theta_i$, $i=0,\ldots,n$ into equation (3.29). It should be noted that half-hat functions are also incorporated into this methodology. The final linear system is of the form:

$$(U + D)\vartheta = \eta + d \tag{3.37}$$

The matrices (*U, D*) and vectors *(f, d)* are defined together with the liquid phases in the next section for the sake of unified completeness and assimilation of all the boundary conditions. The size of the matrices is *(n+1)* × *4(n+1)* whilst that of the vectors is *(n+1)*.

3.5.3.6 Variational Formulation of the Liquid Phases

It should be noted that in this section, the quasi-steady ($\partial/\partial t \to 0$) derivation will be shown. Further details outlining the transient terms will follow. Hence, focusing on the right hand side of Equations (3.22b-e):

$$\begin{aligned}
(k_a/\mu_a)\nabla^2 p_a &= -|\hat{s}_{a\to c}| \\
(k_c/\mu_c)\nabla^2 p_c &= |\hat{s}_{a\to c}| - |\hat{s}_{c\to e}| - |\hat{s}_{c\to v}| \\
(k_e/\mu_e)\nabla^2 p_e &= |\hat{s}_{c\to e}| - |\hat{s}_{e\to v}| \\
(k_v/\mu_v)\nabla^2 p_v &= |\hat{s}_{c\to v}| + |\hat{s}_{e\to v}|
\end{aligned} \qquad (3.38a\text{-}d)$$

Improving the representation of 3.38a-d:

$$\nabla^2 p^a = \eta_1,\ \nabla^2 p^c = \eta_2,\ \nabla^2 p^e = \eta_3,\ \nabla^2 p^v = \eta_4\} \qquad x \in I = (x_v, x_s)$$

where, (3.39a-d)

$$\eta_1 = \frac{-|\dot{s}_{a\to c}|}{(k_a/\mu_a)},\ \eta_2 = \frac{|\dot{s}_{a\to c}| - |\dot{s}_{c\to e}| - |\dot{s}_{c\to v}|}{(k_c/\mu_c)},\ \eta_3 = \frac{|\dot{s}_{c\to e}| - |\dot{s}_{e\to v}|}{(k_e/\mu_e)},\ \eta_4 = \frac{|\dot{s}_{e\to v}| + |\dot{s}_{c\to v}|}{(k_v/\mu_v)}$$

Once again, as in the displacement equation ***(u)***, one has to multiply each pressure compartment, *i*, by a test function, and integrate by parts:

$$\begin{aligned}
\int_I \eta_i N^{pi} dx &= \int_I \nabla^2 p^i N^{pi} dx \\
&= \left[\left(p^{i'}(x) N^{pi}(x)\right)\right]_{x_s}^{x_v} - \int_I \nabla p^i \nabla N^{pi}(x) dx
\end{aligned} \qquad (3.40)$$

where $i = a, c, e, v$

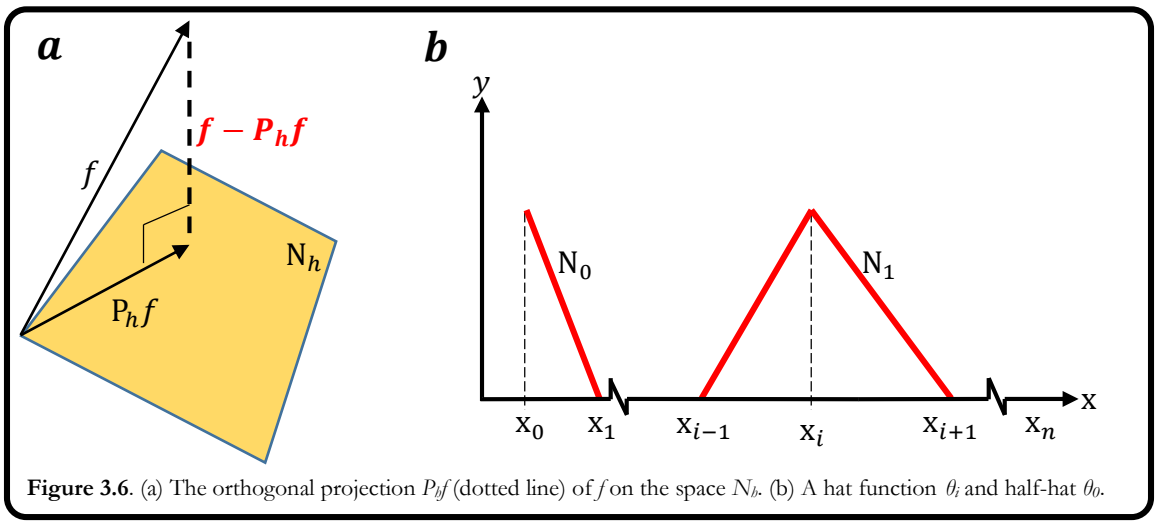

Figure 3.6. (a) The orthogonal projection $P_h f$ (dotted line) of f on the space N_h. (b) A hat function θ_i and half-hat θ_0.

In this description, there will be four separate test functions, namely N^{pa}, N^{pc}, N^{pe} and N^{pv}. The appropriate test and trial space of each compartment (*a*, *c*, *e* and *v*) is:

$$\begin{aligned}
N_0^{pa} &= \{N^{pa} : \left\|N^{pa'}\right\|_{L^2(\mathrm{I})} < \infty, \left\|N^{pa}\right\|_{L^2(\mathrm{I})} < \infty, N^{pa}(x_s) = p_{bpa}\} \\
N^{pc} &= \{N^{pc} : \left\|N^{pc'}\right\|_{L^2(\mathrm{I})} < \infty, \left\|N^{pc}\right\|_{L^2(\mathrm{I})} < \infty\} \\
N_0^{pe} &= \{N^{pe} : \left\|N^{pe'}\right\|_{L^2(\mathrm{I})} < \infty, \left\|N^{pe}\right\|_{L^2(\mathrm{I})} < \infty, N^{pe}(x_s) = p_{bp} + \mu^e RQ_0\} \\
N_0^{pv} &= \{N^{pv} : \left\|N^{pv'}\right\|_{L^2(\mathrm{I})} < \infty, \left\|N^{pv}\right\|_{L^2(\mathrm{I})} < \infty, N^{pv}(x_s) = p_{bp}\}
\end{aligned} \tag{3.41a-d}$$

As can be seen from the spaces above, N^{pc} seems distinct. All of the compartments apart from the capillary compartment possess a Dirichlet boundary condition. This implies that specific values have to be assumed for N^{pa}, N^{pe}, N^{pv} and p^a, p^e, p^v at the skull (x_s). The capillary compartment on the other hand, possesses Neumann boundary conditions at the skull and ventricles. The variational formulation is therefore:

Find $p^a, p^c, p^e, p^v \in \left[N^{pa}, N_0^{pc}, N^{pe}, N^{pv}\right]$ such that:

$$\int_I \eta_i N^{pi} dx = \left[\left(p^i{}'(x) N^{pi}(x)\right)\right]_{x_s}^{x_v} - \int_I \nabla p^i \nabla N^{pi} dx \tag{3.42}$$

3.5.3.7 Finite Element Approximation (FEA) of the liquid phases in 1D

In the same spirit as before when approximating the displacement equation, the Galerkin approximation is sought for the pressure compartments:

Find $p_h^a, p_h^c, p_h^e, p_h^v \in \left[N_h^{pa}, N_{h,0}^{pc}, N_h^{pe}, N_h^{pv}\right]$ such that:

$$\begin{aligned}
\int_I \eta_i N^{pi} dx &= \int_I \nabla^2 p_h^i N^{pi} dx \\
&= \left[\left(p_h^i{}'(x) N^{pi}(x)\right)\right]_{x_s}^{x_v} - \int_I \nabla p_h^i \nabla N^{pi} dx
\end{aligned} \tag{3.43}$$

where $i = a, c, e, v$

3.5.3.8 Stiffness Matrix and Load Vector for liquid phases in 1D

As in the displacement equation, N^{pi} are the hat functions spanning $\left[N_h^{pa}, N_{h,0}^{pc}, N_h^{pe}, N_h^{pv}\right]$, and since $p_h^a, p_h^c, p_h^e, p_h^v \in \left[N_h^{pa}, N_{h,0}^{pc}, N_h^{pe}, N_h^{pv}\right]$, they can be written in the following linear combination:

$$p_h^i = \sum_{j=0}^{n} \bar{\vartheta}_j N^{pi} \tag{3.44}$$

where $\bar{\vartheta}_j$ are *(n-1)* unknown coefficients to be determined. Inserting the ansatz in 3.44 into the FEM for the pressure compartments in 3.43, one obtains:

$$\begin{aligned}\int_I \eta_i N_i^{pi} dx &= \int_I \left(\sum_{j=1}^{n-1} \bar{\vartheta}_j \nabla N_j^{pi} \right) \nabla N_i^{pi} dx \\ &= \sum_{j=1}^{n-1} \bar{\vartheta}_j \int_I \nabla N_j^{pi} \nabla N_i^{pi} dx \quad i = 1, 2, ..., n-1\end{aligned} \tag{3.45}$$

Hence, the following notation is obtained:

$$\begin{aligned}P_{ij} &= \int_I \nabla N_j^{pi} \nabla N_i^{pi} dx \quad i = 1, 2, ..., n-1 \\ p_i &= \int_I f_i N_i^{pi} dx \quad i = 1, 2, ..., n-1 \quad \therefore \\ p_i &= \sum_{j=1}^{n-1} P_{ij} \bar{\vartheta}_j \quad i = 1, 2, ..., n-1 \quad \therefore \\ p_i &= P_{ij} \bar{\vartheta}_j\end{aligned} \tag{3.46}$$

The final linear system is of the form:

$$\left(P + C\right) \bar{\vartheta} = p + c \tag{3.47}$$

$\boldsymbol{P}_{ij}$ (fluid stiffness matrix) and $\boldsymbol{C}_{ij}$ are 4(n-1) × 4(n-1) matrices, p_i and c_i are *4(n-1)* × *1* vectors.

Equation 3.46 therefore satisfies a linear system, which is solved in order to obtain the FE solutions p_b^i, by incorporating boundary conditions and load vectors ($\boldsymbol{C}_{ij}$ and c_i) accordingly. The matrices and load vectors for the pressure equation follow the same procedure as that of the displacement equation,

Like the FD-based MPET template in the previous section, the FEM based MPET formulation utilises a *(**u**, p)* coupling methodology, requiring displacement and pressure calculations to be conducted simultaneously using the same hat functions already defined in (3.30), and of course, L^2-projection.

3.5.3.9 Template for the 1D FEM-MPET method

The implementation of the coupled linear system representing the ***u**-p* formulation in the `MATLAB` environment for ease of use. In order to do this, the two systems (one for the four liquid phases, and one for the solid phase) need to be described in the appropriate manner, suitable for direct implementation into a single, larger matrix. The matrices $\boldsymbol{P}$, $\boldsymbol{C}$, $\boldsymbol{U}$ and $\boldsymbol{D}$ along with the vectors $\boldsymbol{p}$, $\boldsymbol{c}$, $\boldsymbol{\eta}$ and $\boldsymbol{d}$ are now defined for the two amalgamated systems in (3.37) and (3.47). In this work, $\boldsymbol{P}$ and $\boldsymbol{U}$ are identical (in terms of stiffness matrix), and the entries to these matrices are calculated using the hat functions and their derivatives, in combination with mid-point quadrature for the diagonal entries ($i = j$):

$$U_{ii} = P_{ii} = \int_{x_{i-1}}^{x_i} \left(N_i^{'} \right)^2 dx + \int_{x_i}^{x_{i+1}} \left(N_i^{'} \right)^2 dx = \frac{1}{h_i} + \frac{1}{h_{i+1}}, \quad i = 1, ..., n-1 \tag{3.48}$$

The first and last elements of the above diagonal must represent the fact that half-hat functions are used at the boundaries, hence these are equal to:

$$U_{11} = P_{11} = \frac{1}{h_1}$$
$$U_{nn} = P_{nn} = \frac{1}{h_n} \tag{3.49a-b}$$

The subdiagonals entries *(j = i +1)* along with the superdiagonal entries are equal to:

$$U_{i,i+1} = P_{i,i+1} = \int_{x_i}^{x_{i+1}} \left(N_{i+1}^{'} N_i^{'} \right) dx = -\frac{1}{h_{i+1}}, \quad i = 0, ..., n \tag{3.50}$$

The entries for the boundary conditions are simple to implement in 1D, as they only effect the entries in the first and last rows of the matrices, and the first and last elements of the vectors. The Dirichlet condition at the skull implies that the last element of the vector *d* is equal to zero. This condition is applied in a strong way, meaning that once the MPET system solves the system of equation and updated the initially all zero vector η with the updated parenchymal displacements, the last entry of the load vector η will always be equal to zero. Hence, $d_{nn} = \eta_{nn}=0$. The matrix *D* requires the input of the continuity of stress, defined as:

$$\begin{aligned}
&-p_v \mathbf{n} = \sigma_{ij} \cdot \mathbf{n} \ \ \therefore \\
&2G\varepsilon_{ij} \cdot \mathbf{n} + \lambda \varepsilon_{kk} \mathbf{n} - \left[\sum_{i=a,e,c,v} \left(\alpha^i - 1 \right) \right] p_v \mathbf{n} \ = 0 \ \ \therefore (\text{in } 1D): \\
&\varepsilon_{kk} \left(2G + \lambda \right) \cdot \mathbf{n} - \left[\sum_{i=a,e,c,v} \left(\alpha^i - 1 \right) \right] p_v \mathbf{n} \ = 0, \text{as } \ \varepsilon_{kk} = \varepsilon_{ij} = \partial u / \partial x \ \ \therefore \\
&\left(2G(1-\nu) \right) \partial u / \partial x \big|_{x_v} - (1-2\nu) \left[\sum_{i=a,e,c,v} \left(\alpha^i - 1 \right) p_v^i \right] = 0, \ on \ V
\end{aligned} \tag{3.51}$$

From (3.51), the influence of this Neumann condition is constrained (on the trace [356] in higher dimensions) to the ventricles.

The system involving the fluid phases is more complicated, as it possesses a mixture of both Dirichlet and Neumann conditions (Robin conditions). In addition, one must also cater for the continuity of stresses of the compartmental boundary conditions. Unifying these, the matrix *C* is defined as (for a representative system with 3 nodes):

$$\boldsymbol{C} = \left[\begin{array}{ccc|ccc|ccc|ccc}
0 & 0 & 0 & 0 & 0 & 0 & 0 & 0 & 0 & 0 & 0 & 0 \\
0 & 0 & 0 & & & & & & & & & \vdots \\
0 & 0 & 0 & & & & & & & & & \vdots \\
\hline
\vdots & & & N_c & 0 & 0 & & & & & & \vdots \\
\vdots & & & 0 & 0 & 0 & & & & & & \vdots \\
\vdots & & & 0 & 0 & 0 & & & & & & \vdots \\
\hline
0 & & & & & & E & 0 & 0 & & & 0 \\
\vdots & & & & & & 0 & 0 & 0 & & & \vdots \\
\vdots & & & & & & 0 & 0 & F & & & 0 \\
\hline
\vdots & & & & & & & & & 0 & \cdots & 0 \\
\vdots & & & & & & & & & \vdots & \ddots & \vdots \\
0 & \cdots & \cdots & \cdots & \cdots & \cdots & \cdots & \cdots & \cdots & \cdots & \cdots & 0
\end{array}\right], \text{where:} \quad \begin{aligned} E &= \left(\pi d^4 / 128 \mu^e L \right) / 4\pi k^e \left(r_1 + u_1^n \right)^2 \\ F &= \left(-\pi d^4 / 128 \mu^e L \right) / 4\pi k^e \left(r_1 + u_1^n \right)^2 \\ N_C &= Q_p / \kappa_{c \to ven} \end{aligned} \tag{3.52}$$

The CSF compartment (3rd diagonal block) requires the boundary condition:

$$Q_p = \frac{\pi d^4}{128\mu^e L}\left[p^e\left(x_v,t\right) - p^e\left(x_M,t\right)\right] - 4\pi k^e\left(x_1+u_1^n\right)^2\frac{\partial p^e\left(x_v,t\right)}{\partial x} + 4\pi\left(x_1+u_1^n\right)^2\frac{\partial u\left(x_v,t\right)}{\partial t} \quad (3.53)$$

to be discretised using Finite Differences. In (3.53), $\partial u\left(x_v,t\right)/\partial t$ is also represented in a Finite Difference form in order to account for the quasi-steady evolution of ventricular expansion, just as in the 1D cases in the previous chapter. Since the transient terms of the pressure compartments can also be discretised, the time step Δt will be the same as that used for the temporal discretisation in this case. The load vectors $\mathbf{p}+\mathbf{c}$ are given for a representative system of 3 nodes in (3.54). The vector $\mathbf{p}$ is made up of the load vectors defined by the inter-compartmental transfer in equation (3.39a-d). The combined load vector $\mathbf{p}+\mathbf{c}$ is calculated via L^2-projection in the following way:

$$\boldsymbol{p}+\boldsymbol{c} = \begin{bmatrix} \eta_1 h_1/2 \\ \eta_1(h_1+h_2)/2 \\ 0 \\ \hline \eta_2 h_1/2 \\ \eta_2(h_1+h_2)/2 \\ \eta_2(h_3)/2 \\ \hline 0 \\ \eta_3(h_1+h_2)/2 \\ 0 \\ \hline \eta_4 h_1/2 \\ \eta_4(h_1+h_2)/2 \\ 0 \end{bmatrix} + \begin{bmatrix} 0 \\ 0 \\ c_1 \\ \hline 0 \\ 0 \\ 0 \\ \hline c_2 \\ 0 \\ c_3 \\ \hline 0 \\ 0 \\ c_4 \end{bmatrix}, \text{ where } \begin{aligned} c_1 &= p_{bpa} \\ c_2 &= Q_p + 4\pi u_1^n\left(r_1+u_1^n\right)^2/\Delta t \\ c_3 &= p_{bp} + \mu^e R Q_o \\ c_4 &= p_{bp} \end{aligned} \quad (3.54)$$

For completeness, the 12×12 matrix, **P**, for the pressure compartments is given as:

$$\boldsymbol{P} = \left[\begin{array}{ccc|ccc|ccc|ccc} 1/h_1 & -1/h_1 & & \cdots & & & \cdots & & & \cdots & & \\ -1/h_1 & 1/h_1+1/h_2 & -1/h_2 & & & & & & & & & \\ & -1/h_3 & 1 & & & & & & & & & \\ \hline & & & 1/h_1 & -1/h_1 & & & & & & & \vdots \\ & & & -1/h_1 & 1/h_1+1/h_2 & -1/h_2 & & & & & & \\ \vdots & & & & -1/h_3 & 1/h_3 & & & & & & \\ \hline & & & & & & 1/h_1 & -1/h_1 & & & & \vdots \\ & & & & & & -1/h_1 & 1/h_1+1/h_2 & -1/h_2 & & & \\ \vdots & & & & & & & -1/h_3 & 1 & & & \\ \hline & & & & & & & & & 1/h_1 & -1/h_1 & \\ & & & & & & & & & -1/h_1 & 1/h_1+1/h_2 & -1/h_2 \\ \cdots & & & \cdots & & & \cdots & & & & -1/h_3 & 1 \end{array}\right] \quad (3.55)$$

Another constant, $H = 1/k^e\Delta t$, is added to the pressure block allocated for pressure displacement (P_D) coupling, in position $P_D(1,1)$. In this work, an equispaced discretisation is used for the domain: 3 $cm \leq x \leq 10$ cm. The displacement block however, must also be

accompanied by pressure blocks since the boundary conditions were discretised using a finite difference methodology, as in the SPET model produced by Wirth & Sobey [296]. The terms that are added to these blocks arise from the continuity of stress equation 4.30, so **D** is given by:

$$\boldsymbol{D} = \left[\begin{array}{ccc|ccc|ccc|ccc|ccc} 0 & 0 & 0 & C_A & 0 & 0 & C_C & 0 & 0 & C_E & 0 & 0 & C_V & 0 & 0 \\ 0 & 0 & 0 & 0 & 0 & 0 & 0 & 0 & 0 & 0 & 0 & 0 & 0 & 0 & 0 \\ 0 & 0 & 0 & 0 & 0 & 0 & 0 & 0 & 0 & 0 & 0 & 0 & 0 & 0 & 0 \end{array}\right]_{3\times 15}$$

$$\text{where:} \qquad (3.56)$$

$$C_A = \left(\alpha^c - 1\right)(1-2\nu)\big/2G(1-\nu) \qquad C_E = \left(\alpha^e - 1\right)(1-2\nu)\big/2G(1-\nu)$$
$$C_C = \left(\alpha^c - 1\right)(1-2\nu)\big/2G(1-\nu) \qquad C_V = \left(\alpha^v - 1\right)(1-2\nu)\big/2G(1-\nu)$$

3.5.3.10 Spatial semi-discretisation of the MPET equations

In this work, the Euler-backward method will be utilised to integrate the temporal segments of the liquid phases of the MPET system (in 3D), since, although it is first order accurate, it is unconditionally stable for any size of time stepping and of low computational cost. This is important in the overview of chronic HCP. Being an implicit method, it is well suited to dealing with stiff systems. The solid phases of the MPET equations are re-written as:

$$\left.\begin{aligned} \frac{\partial}{\partial t}(S^a p^a + \alpha^a \varepsilon) &= L_a + f_a \\ \frac{\partial}{\partial t}(S^c p^c + \alpha^c \varepsilon) &= L_c + f_c \\ \frac{\partial}{\partial t}(S^e p^e + \alpha^e \varepsilon) &= L_e + f_e \\ \frac{\partial}{\partial t}(S^v p^v + \alpha^v \varepsilon) &= L_v + f_v \end{aligned}\right\} \text{where:} \quad \begin{aligned} L_a &= \left(k_a/\mu_a\right)\nabla^2 p_a, \quad & f_a &= -\left|\hat{s}_{a\to c}\right| \\ L_c &= \left(k_c/\mu_c\right)\nabla^2 p_c, \quad & f_c &= \left|\hat{s}_{a\to c}\right| - \left|\hat{s}_{c\to e}\right| - \left|\hat{s}_{c\to v}\right| \\ L_e &= \left(k_e/\mu_e\right)\nabla^2 p_e, \quad & f_e &= \left|\hat{s}_{c\to e}\right| - \left|\hat{s}_{e\to v}\right| \\ L_v &= \left(k_v/\mu_v\right)\nabla^2 p_v, \quad & f_v &= \left|\hat{s}_{c\to v}\right| + \left|\hat{s}_{e\to v}\right| \end{aligned} \qquad (3.57a\text{-}d)$$

It is noted again here that the constant S^i for each pressure compartment is described as the amalgamated compressibility of both fluid and solid phases.

The variational formulation of the liquid phases must now be outlined to satisfy the spatial semi-discretisation. One now has to multiply each pressure compartment, *i*, by a test function $N^{pi}(x, t)$, and integrate by parts:

$$\begin{aligned} \int_I f_i N^{pi} dx &= \int_I \left(S^i \dot{p}^i + \alpha^i \dot{\varepsilon}\right) N^{pi} dx - \int_I L_i N^{pi} dx \\ &= \int_I \left(S^i \dot{p}^i + \alpha^i \dot{\varepsilon}\right) N^{pi} dx + \int_I \nabla p^i \nabla N^{pi} dx - \left[\left(p^{i'}(x) N^{pi}(x)\right)\right]_{x_s}^{x_v} \end{aligned} \qquad (3.58)$$

$$\text{where} \quad i = a, c, e, v$$

The appropriate test and trial space of each compartment (*a*, *c*, *e* and *v*) is:

$$\left.\begin{aligned}
N_a^{pa} &= \{N^{pa} : \left\|N^{pa'}(\cdot,\mathrm{t})\right\|_{L^2(\mathrm{I})} < \infty, \left\|N^{pa}(\cdot,\mathrm{t})\right\|_{L^2(\mathrm{I})} < \infty, N^{pa}(x_s,\mathrm{t}) = p_{bpa}\} \\
N^{pc} &= \{N^{pc} : \left\|N^{pc'}(\cdot,\mathrm{t})\right\|_{L^2(\mathrm{I})} < \infty, \left\|N^{pc}(\cdot,\mathrm{t})\right\|_{L^2(\mathrm{I})} < \infty\} \\
N_e^{pe} &= \{N^{pe} : \left\|N^{pe'}(\cdot,\mathrm{t})\right\|_{L^2(\mathrm{I})} < \infty, \left\|N^{pe}(\cdot,\mathrm{t})\right\|_{L^2(\mathrm{I})} < \infty, N^{pe}(x_s,\mathrm{t}) = p_{bp} + \mu^e RQ_0\} \\
N_v^{pv} &= \{N^{pv} : \left\|N^{pv'}(\cdot,\mathrm{t})\right\|_{L^2(\mathrm{I})} < \infty, \left\|N^{pv}(\cdot,\mathrm{t})\right\|_{L^2(\mathrm{I})} < \infty, N^{pv}(x_s,\mathrm{t}) = p_{bp}\}
\end{aligned}\right\} \qquad (3.59\text{a-d})$$

It is appropriate to point out here that the norms in (4.38a-d), $\left\|N^{pi}\right\| = \left\|N^{pi}(\cdot,\mathrm{t})\right\|$ are only functions of time, *t*, and not *x*. Using the aforementioned spaces, the variational formulations of (4.36a-d) become:

Find $p_h^a, p_h^c, p_h^e, p_h^v$, such that for every fixed $t \in J$, $\left[p^a, p^c, p^e, p^v\right] \in \left[N_a^{pa}, N^{pc}, N_e^{pe}, N_v^{pv}\right]$ and:

$$\int_I \left(S^i \dot{p}^i + \alpha^i \dot{\varepsilon}\right) N^{pi} dx + \int_I \nabla p^i \nabla N^{pi} dx - \left[\left(p^{i'}(x) N^{pi}(x)\right)\right]_{x_s}^{x_v} = \int_I f_i N^{pi} dx, \qquad \forall N^{pi} \in \left[N_a^{pa}, N^{pc}, N_e^{pe}, N_v^{pv}\right], \quad t \in J \qquad (3.60)$$

It was assumed that $0 = t_0 < t_1 < \ldots < t_m = T$ and that a partition in the time interval *J* into *m* subintervals by defining $J_\ell = (t_{\ell-1}, t_\ell]$ with time steps $\Delta t_\ell = t_\ell - t_{\ell-1}$, $\ell = 1, \ldots, m$. The spatial semi-discretisation is performed by letting the already defined interval *I* correspond to the mesh that is used, in addition to letting $\left[p_h^a, p_h^c, p_h^e, p_h^v\right] \in \left[N_{h,a}^{pa}, N_h^{pc}, N_{h,e}^{pe}, N_{h,v}^{pv}\right]$ be the space of continuous piecewise linears. The space discrete variational formulation is acquired by:

Find $p_h^a, p_h^c, p_h^e, p_h^v$, such that for every fixed $t \in J$, $\left[p_h^a, p_h^c, p_h^e, p_h^v\right] \in \left[N_{h,a}^{pa}, N_h^{pc}, N_{h,e}^{pe}, N_{h,v}^{pv}\right]$ and using the interior hat functions as before one is led to:

$$\int_I \left(S^i \dot{p}_h^i + \alpha^i \dot{\varepsilon}\right) N^{pi}(x) dx + \int_I \nabla p_h^i \nabla N^{pi}(x) dx - \left[\left(p_h^{i'}(x) N^{pi}(x)\right)\right]_{x_s}^{x_v} = \int_I f_i N^{pi}(x) dx, \ t \in J \qquad (3.61)$$

Unlike in 3.44, where $\overline{\vartheta}_j$ were the (*n*-1) unknown coefficients to be determined, one has to use time dependent nodal values $\overline{\vartheta}_j(t)$. The ansatz in (3.44) is updated to accommodate this fact, since it is now sought that solutions $\left[p_h^a, p_h^c, p_h^e, p_h^v\right]$ are required for every fixed time *t*, as a linear combination of hat functions $N^{pi}(x)$ and time dependent nodal coefficients $\overline{\vartheta}_j(t)$:

$$p_h^i(x,t) = \sum_{j=1}^{n-1} \overline{\vartheta}_j(t) N^{pi}(x) \qquad (3.62)$$

(3.62) is now substituted back into (3.61), and one obtains:

$$\sum_{j=1}^{n-1}\dot{\bar{\vartheta}}_j(t)\left(S^i\right)\int_I N^{pj}\left(x\right)N^{pi}(x)dx+\sum_{j=1}^{n-1}\dot{\bar{\vartheta}}_j(t)\left(\alpha^i\right)\int_I N_\varepsilon^{pj}\left(x\right)N_\varepsilon^{pi}(x)dx+\ldots$$
$$\ldots+\sum_{j=1}^{n-1}\bar{\vartheta}_j(t)\int_I \nabla N^{pi}\left(x\right)\nabla N^{pi}(x)dx-\Omega_{BC}=\int_I f_i N^{pi}(x)dx,\ \ i,j=1,\ldots,n-1,\quad t\in J \tag{3.63}$$

Introducing the following:

$$M_{ij}^{p}=\int_I N^{pj}(x)N^{pi}(x)dx,\qquad M_{ij}^{\varepsilon}=\int_I N_\varepsilon^{pj}(x)N_\varepsilon^{pi}(x)dx$$
$$A_{ij}^{p}=\int_I \nabla N^{pi}(x)\nabla N^{pi}(x)dx,\quad b_i\left(t\right)=\int_I f_i N^{pi}(x)dx \tag{3.64}$$
$$\Omega_{BC}=\text{Boundary Conditions}$$

One may now write the previous equation in the form of a system of n-1 ODE's for the required nodal coefficients:

$$\left(S^i\right)\sum_{j=1}^{n-1}M_{ij}^{p}\dot{\bar{\vartheta}}_j(t)+\left(\alpha^i\right)\sum_{j=1}^{n-1}M_{ij}^{\varepsilon}\dot{\bar{\vartheta}}_j(t)+\sum_{j=1}^{n-1}A_{ij}^{p}\bar{\vartheta}_j(t)-\Omega_{BC}(t)=b_i\left(t\right),\ \ i,j=1,\ldots,n-1,\quad t\in J \tag{4.44}$$

Simplifying the above representation, one obtains in matrix form:

$$\left(S^i\right)M_{ij}^{p}\dot{\bar{\vartheta}}_j(t)+\left(\alpha^i\right)M_{ij}^{\varepsilon}\dot{\bar{\vartheta}}_j(t)+A_{ij}^{p}\bar{\vartheta}_j(t)-\Omega_{BC}(t)=b_i\left(t\right),\quad t\in J \tag{3.65}$$

The spatial semi-discretisation of (3.65) is evident since there is no spatial variable present. Finally, time derivatives $\dot{\bar{\vartheta}}_j(t)$ can be replaced with a backward difference formula (BDF)/ quotient $\dot{\bar{\vartheta}}_j(t)\approx\left(\bar{\vartheta}_\ell-\bar{\vartheta}_{\ell-1}\right)/\Delta t_\ell$ in order to obtain:

$$\left(S^i\right)M^{p}\left[\left(\bar{\vartheta}_\ell-\bar{\vartheta}_{\ell-1}\right)/\Delta t_\ell\right]+\left(\alpha^i\right)M^{\varepsilon}\left[\left(\bar{\vartheta}_\ell-\bar{\vartheta}_{\ell-1}\right)/\Delta t_\ell\right]+A^{p}\bar{\vartheta}_\ell-\Omega_{BC,\ell}=b_\ell,\quad\therefore$$
$$\left(S^i\right)M^{p}\left[\left(\bar{\vartheta}_\ell-\bar{\vartheta}_{\ell-1}\right)\right]+\left(\alpha^i\right)M^{\varepsilon}\left[\left(\bar{\vartheta}_\ell-\bar{\vartheta}_{\ell-1}\right)\right]+\Delta t_\ell A^{p}\bar{\vartheta}_\ell-\Delta t_\ell\Omega_{BC,\ell}=\Delta t_\ell b_\ell,\quad\therefore \tag{3.66}$$
$$\left[\left(S^i\right)M^{p}+\left(\alpha^i\right)M^{\varepsilon}+\Delta t_\ell A^{p}\right]\bar{\vartheta}_\ell-\left[\left(S^i\right)M^{p}+\left(\alpha^i\right)M^{\varepsilon}\right]\bar{\vartheta}_{\ell-1}=\Delta t_\ell b_\ell+\Delta t_\ell\Omega_{BC,\ell}$$

In the above, a distinction is made between the mass matrix of the time dependent pressure and strain with the relevant superscript, p and ε. In order for the transient simulation to commence, the system uses the vector ($\bar{\vartheta}_{\ell=0}$) corresponding to the nodal values of the orthogonal projection of the quasi-stationary MPET simulation, so when ($\mathbf{u}(\mathbf{x},0)$, $p^a(\mathbf{x},0)$, $p^c(\mathbf{x},0)$, $p^e(\mathbf{x},0)$, $p^v(\mathbf{x},0)$) when $\partial/\partial t\rightarrow 0$.

In the MPET discretization template, the aforementioned conditions are used along with an implicit backward Euler step to feed the two starting vectors of a 2nd order accurate BDF(2) method. This method is well suited to stiff problems in addition to being able to accommodate large step-sizes

Stability estimates are useful in determining the long term behaviour of the simulated solutions produces by executing the MPET template. Loosely speaking, the FEA of the liquid phases is bounded in time by the constant source terms (in the form given thus far), in addition to the initial conditions. If one further proceeds and fully discretises the aforementioned equations, the pressure with respect to the continuous piecewise linear functional approximation is additionally bounded by the time step (Δt_ℓ).

3.5.4 Variational formulation in 2D and 3D

In this section, the FEA of the MPET equations will be outlined. It is important to note that the steps taken to derive the 2D formulation is similar in concept to the 1D approach, since it is necessary to obtain the variational form and then approximate the solution in the space of continuous piecewise linear functions (triangular and tetrahedral meshes in this case). The first subsection will focus on the differences in the hat functions for the use with triangular (and the tetrahedral element modification is given where applicable), along with the consequent variational formulation, FEA, and the derivation of the linear system of the liquid phases in 2D (once again, and in 3D where applicable).

The second subsection will utilise a more consistent solid mechanics framework for the MPET derivation, since the computer implementation in this form is more robust with respect to the solid phase of the MPET system. In addition, higher quadratic triangular elements are developed, utilising Gaussian quadrature for the 2D case (this will only be described in the *Conclusions & Future Work* section). Finally a Newton-Galerkin approach is also presented in order to solve the non-linear MPET system, and applied to the case of non-linear compartmental permeability in 2D for the CSF/ISF compartment. The latter methodology only serves as an indicator for future work.

3.5.4.1 Liquid phases of the MPET equations

Triangular Meshing

The construction of the required continuous piecewise polynomial space in two dimensions is preceded by the creation of a suitable mesh (triangulations and tetrahedrals in 2D and 3D respectively) for the domain in higher dimensional problems. Once triangulation has been achieved, one then proceeds in constructing basis functions over this triangulation. Finally, the assembly of the local stiffness matrices and load vectors for each element are deduced based on the weak form (Galerkin method) and then solved.

Any domain may be approximated by a polygon which can then act as the template for triangulation. The mesh parameters that are of general importance in the 2D case are:

$$\left.\begin{aligned} \Omega_p &= \text{Polygons} \rightarrow K_1 \cup K_2 \ldots \cup K_{n_t} \\ K_j &= \text{Triangles} \rightarrow j = 1, \ldots, n_e \\ N_i &= \text{Nodes} \rightarrow i = 1, \ldots, n_p \\ h_j &= \max_{K \in \Lambda} \{K_j\} \\ \rho_j &= \text{Encircle} \rightarrow d_K \\ h &= \max\{h_j\} \\ \rho &= \min\{\rho_j\} \end{aligned}\right\} \tag{3.67}$$

In the above parameters, the encircle represents the diameter of the inscribed circle within a triangle, Λ represents the mesh of Ω as a set Λ of triangles K, n_t are the number of elements and n_p are the number of nodes.

For the triangulations that will take place, it is important to appreciate the data structure that is used to represent the discretised mesh in the MATLAB workspace. In this work, the point ($\boldsymbol{P}_m$) and connectivity matrix ($\boldsymbol{T}_m$) are used. The point matrix contains the coordinates of the nodes (n_i), and is of size $2\times n_p$. The connectivity matrix contains the numbering of the three nodes on each triangle K_j, where the ordering is assumed in a counter-clockwise direction. It should be noted that the induction of the ordering scheme is independent of starting location. $\boldsymbol{T}_m$ is of size $3\times n_t$. This data structure was chosen as it allows for the seamless extension into higher dimensions, the use of different element types and also the ability to import meshes from other mesh generators, such as CFD-GEOM or DistMesh [359] if required.

In this work, MATLAB's 2D Delaunay triangulation [360] was used since it ensured that the circumcircle associated with each triangle contains no other point in its interior, in addition to the interior angles of each triangle being maximal. Of course, when dealing with more complicated domains such as slices incorporating cerebral ventricles, the latter property may not always be respected in its most stringent form. To circumvent this, methods of triangular refinement such as Rivara and Regular refinement are necessary [361]. Other advantages include their well-grounded extension to parallel processing [362,363].

In the 2D section of this work, three geometries were investigated. The first was an annulus, with an outer radius of 10 *cm*, and a punctured region of radius 3 *cm*. The aforementioned radial dimensions correspond to the dimensions used in the 1D models. The second geometry that was used was a circle of radius 10 *cm* and a 'punctured peanut', which was constructed from two overlapping circles (both of radius 3 *cm*). The coordinates of the centre of the two inner circles was (1.5 *cm*, 0) and (-1.5 *cm*, 0). Finally, the third geometry was a realistic polygonal representation of the cross section of the cerebral ventricles, and a pseudo-anatomical representation of the skull, obtained from the same DICOM data described in §3.1. The outer skull was smoothed and made slightly smaller (in the overall area), in order to save computational resources.

For the 3D simulations, NETGEN 5.1(an open source, automatic 3D tetrahedral mesh generator) was used to construct spherical shells of the same outer and punctured radii as in the 2D case, namely that of the annular and peanut representations.

Meshing steps in 2D

For the 2D geometries, MATLAB's `delaunayTriangulation` class was used to create the simplified annular and 'peanut' regions from a set of points. These points are defined using CSG models (Constructive Solid Geometry models), which in this work are circles (and their combination) and generic polygonal regions for more accurate representations of patient specific geometries. In this work, it was important to harness the usefulness of the Decomposed Geometry Matrix methodology employed by MATLAB in its general use within the PDE Toolbox, without evoking the need to specifically use this toolbox for solving the set of PDEs defining the MPET equations. The complexity of solving the set of MPET equations with their associated (and evolving) boundary conditions does not allow for the use of MATLAB's simple FEM based PDE toolbox. Indeed, it can be said that solving systems of PDE's within the toolbox environment can prove to be quite cumbersome and counterproductive, due to the plethora of modifications required to standardise MATLAB's

scripts and protocols. It is recommended that a numerical framework is drawn up from scratch, which ultimately only utilises the maturity of MATLAB's environment to create the required domain representations which are discretised via Delaunay triangulation.
In order to define the domain used for the meshing, the *decsg* function is used to decompose the CSG model into minimal regions. The CSG model is represented by the Geometry Description matrix, and the corresponding decomposed geometry is characterized by the Decomposed Geometry matrix. The *decsg* command returns the minimal regions that represent the geometry defined by the set formula *(Skull – Ventricles)*, defining the two concentric circles. The minus sign in the set formula represents a set difference. The precedence of this set formula can be controlled by parentheses for more exotic geometries. Finally, the *Name Space* matrix within the *decsg* function is also utilised, and is a text matrix that relates the columns in the matrix representing the geometry to variable names in the set formula. Each column in the *Name Space* matrix has a sequence of characters, embellished with spaces. Each character column assigns a name to the corresponding geometric object and in doing so one may refer to a specific object in CSG form in the set formula.

Finally, the final Decomposed Geometry matrix comprises a representation of the decomposed geometry in terms of disjointed minimal regions. Each edge segment of the minimal regions corresponds to a column in the final matrix. In each column, the second and third rows cover the starting and ending x-coordinate, and the fourth and fifth rows are occupied by the y-coordinate. Rows six and seven contain left and right minimal region labels with respect to the counter clockwise direction (on circle and ellipse segments) prompted by the start and end points. For the annular (and 'peanut') region, the 1st edge segments' row is unity throughout. The 8th and 9th rows contain the coordinates of the centre, whilst the 10th row contains the length of the radius.

Once the geometry has been specified, the next step is to create the triangular mesh via the use of the *initmesh* function within the MATLAB workspace. This function uses a Delaunay triangulation algorithm that is relatively powerful and robust. It gives the user various properties to explore, such as: a maximum edge size, mesh growth rate, edge triangulation, jiggling [sic] the triangular mesh by adjusting the node point positions (increasing the quality of the triangulation) and even the option to use earlier versions of the meshing algorithm. The execution of *initmesh* allows for the output of the point, connectivity and edge matrices. In the latter matrix, the 1st and 2nd rows comprise the indices of the starting and ending point, the 3rd and 4th rows contain the starting and ending parameter values, the 5th row contains the edge segment number and finally the 6th and 7th rows provide the user with the left- and right-hand side subdomain numbers.

3.5.5 Space of Continuous Piecewise Polynomials in 2D and 3D

If K represents a triangle, then:

$$\wp_1(K) = \{\varsigma : \varsigma = \omega_1 + x\omega_2 + y\omega_3, (x,y) \in K,\ (\omega_1, \omega_2, \omega_3) \in \mathbb{R}\} \tag{3.68}$$

represents the space of corresponding linear functions on the triangle. However, since the nodal values are used as the DOF, an elementary requirement is that a nodal basis is used. This basis also portrays the Delta function property (see equation 3.32). The continuity of ζ between triangles K is guaranteed if:

$$Z_h = \{\varsigma : \varsigma \in C^0(\Omega), \varsigma|_K \in \wp_1(K),\ \forall K \in \Lambda\} \tag{3.69}$$

In the above, Z_h is the space of all possible continuous ($C^0(\Omega)$) piecewise linear polynomial functions. Once again, we have the similar result that any function ζ in Z_h is represented by its nodal values $\{\varsigma(N_j)\}_{j=1}^{n_p}$. The hat functions Z_h for the nodes $\{\varsigma(N_j)\}_{j=1}^{n_p} \subset Z_h$ once again satisfy the Delta function property. The support of the hat function described are the triangles encapsulating the node in question, N_j. Using this description of the hat function, any function ζ in Z_h is represented by:

$$\varsigma = \sum_{i=1}^{n_p} \chi_i N_i \tag{3.70}$$

In the above equation, the nodal values of ζ are given by $\chi_i = \zeta(N_i),\ i = 1, \ldots, n_p$. It should be apparent that in the 3D case, there would be an additional spatial parameter (z) and an additional coefficient, ω_4.

3.5.6 Variational formulation of the liquid phases in 2D and 3D

In this section the 2D FEM for the numerical solution of the MPET system will be outlined. Intermediate steps as in the 1D development will be omitted, and emphasis will be given to the final representations that will be used. In addition, the extension to the 3D case is given where applicable.

Multiplying each pressure compartment by a test function, and integrate using Green's formula (leading on from the Divergence Theorem) to obtain in 2D (and in 3D, as Green's theorem holds in three dimensions):

$$\begin{aligned} \iint_\Omega \eta_i \varsigma^{pi}\, dxdy &= \iint_\Omega \Delta p^i \varsigma^{pi}\, dxdy \\ &= \iint_{\partial\Omega} n \cdot \nabla p^i \cdot \varsigma^{pi}\, dxdy - \iint_\Omega \nabla p^i \cdot \nabla \varsigma^{pi}\, dxdy \end{aligned} \tag{3.71}$$

$$\text{where}\quad \Delta = \frac{\partial^2}{\partial x^2} + \frac{\partial^2}{\partial y^2},\quad i = a, c, e, v$$

The appropriate test and trial space of each compartment remains unchanged:

$$
\begin{aligned}
Z_a^{pa} &= \{\varsigma^{pa} : \left\|\varsigma^{pa'}\right\|_{L^2(\Omega)} < \infty, \left\|\varsigma^{pa}\right\|_{L^2(\Omega)} < \infty, \varsigma^{pa}\big|_{\Gamma_s} = p_{bpa}\} \\
Z^{pc} &= \{\varsigma^{pc} : \left\|\varsigma^{pc'}\right\|_{L^2(\Omega)} < \infty, \left\|\varsigma^{pc}\right\|_{L^2(\Omega)} < \infty\} \\
Z_e^{pe} &= \{\varsigma^{pe} : \left\|\varsigma^{pe'}\right\|_{L^2(\Omega)} < \infty, \left\|\varsigma^{pe}\right\|_{L^2(\Omega)} < \infty, \varsigma^{pe}\big|_{\Gamma_s} = p_{bp} + \mu^e RQ_0\} \\
Z_v^{pv} &= \{\varsigma^{pv} : \left\|\varsigma^{pv'}\right\|_{L^2(\Omega)} < \infty, \left\|\varsigma^{pv}\right\|_{L^2(\Omega)} < \infty, \varsigma^{pv}\big|_{\Gamma_s} = p_{bp}\}
\end{aligned}
\tag{3.72a-d}
$$

Of course, in 3D, equation 3.71 is modified appropriately to allow for the additional spatial dimension. In the above spaces, the skull is represented by $\Gamma_s = \partial\Omega_s$. The variational formulation is therefore:

Find $p^a, p^c, p^e, p^v \in \left[Z_a^{pa}, Z^{pc}, Z_e^{pe}, Z_v^{pv}\right]$ such that:

$$
\iint_{\Omega} \eta_i \zeta^{pi} dxdy = \iint_{\Gamma_s} n \cdot \nabla p^i \cdot \zeta^{pi} dxdy - \iint_{\Omega} \nabla p^i \cdot \nabla \zeta^{pi} dxdy \tag{3.73}
$$

The FEA approximation is dealt with by replacing $\left[Z_a^{pa}, Z^{pc}, Z_e^{pe}, Z_v^{pv}\right]$ with $\left[Z_{h,a}^{pa}, Z_h^{pc}, Z_{h,e}^{pe}, Z_{h,v}^{pv}\right]$ in the same spirit as equation (3.43). In order to solve the resulting system of quasi-stationary pressure based equations, the assembly of the stiffness matrix and boundary conditions is required. The stiffness matrix is defined as:

$$
P_{ij}^K = \iint_{\Omega} \nabla \zeta_j^{pi} \cdot \nabla \zeta_i^{pi} dxdy, \;\; i, j = 1, 2, 3 \tag{3.74}
$$

Considering that a hat function, ζ, is a linear function (see equation (3.68)) on each node ($N_i = (x^i, y^i)$) triangle K, and displaying the Delta function property for each node, the coefficients $\left(\omega_1^i, \omega_2^i, \omega_3^i\right)$ take the form:

$$
\omega_1^i = \left(x^j y^k - x^k y^j\right) / 2|K|, \quad \omega_2^i = \left(y^j - y^k\right) / 2|K|, \quad \omega_3^i = \left(x^k - x^j\right) / 2|K| \tag{3.75}
$$

In the above equation, it has been assumed that there is a cyclic permutation of the indices i, j and k over the nodes $i = 1, 2, 3$. The denominator $2|K|$ represents the determinant of the system matrix, where $|K|$ represents the area of the triangle K. One may also write the hat functions for each triangle in a form utilising the vector of natural basis $(1, x, y)$ for $\wp_1(K)$, and obtain a 3×3 *moment matrix* of the form:

$$
m = \begin{bmatrix} 1 & x_1 & y_1 \\ 1 & x_2 & y_2 \\ 1 & x_3 & y_3 \end{bmatrix} \tag{3.76}
$$

which aids in creating a test of whether the hat functions constructed possess the partition of unity property, linear field reproduction, and delta function property provided the matrix in (3.76) is of full rank [357].

The stiffness matrix is therefore:

$$
P_{ij}^K \approx |K| \left(\omega_2^i \omega_2^j + \omega_3^i \omega_3^j\right), \;\; i, j = 1, 2, 3 \tag{3.77}
$$

When considering the load vectors and mass matrix, it is important to mention the importance of quadrature. In this work, the use of the simple corner quadrature (2D extension of the Trapezoidal rule) is used. It is given as:

$$\iint_{\Omega} f dxdy \approx \sum_{i=1}^{3} \left(f(N_i) \right) |K| /3 \tag{3.78}$$

Relying on higher order accuracy via the use of combinations of hat functions being taken into consideration when calculating the right hand side load vectors (at each node, like in corner quadrature) is not required owing to the fact that the right hand side load vectors are represented by source or sink terms, with no spatial dependence.

For the mass matrix, quadrature may also be used in evaluating the integral of the product of two hat functions, however Eisenberg and Malvern [364] developed integration formula (via induction) using natural coordinate systems in linear, triangular and tetrahedral domains. In 2D and 3D therefore:

$$\left.\begin{aligned} (2\mathrm{D}): \iint_{\Omega} \zeta_1^m \zeta_2^n \zeta_3^p dxdy &= \frac{2m!n!p!}{(m+n+p+2)!} |K| \\ (3\mathrm{D}): \iiint_{\Omega} \zeta_1^m \zeta_2^n \zeta_3^p \zeta_4^q dxdydz &= \frac{6m!n!p!q!}{(m+n+p+q+3)!} |V| \end{aligned}\right\} \{m,n,p,q\} \in \mathbb{Z}^+ \tag{3.79}$$

In the 3D formulation above, $|V|$ denotes tetrahedral volume. For the scalar mass matrix in 2D, one obtains:

$$\begin{aligned} M_{ij}^K &= \iint_{\Omega} \zeta_i \zeta_j dxdy = \frac{1}{12}\left(1+\delta_{ij}\right)|K| \therefore \\ M_{ij}^K &= \frac{1}{12}\begin{bmatrix} 2 & 1 & 1 \\ 1 & 2 & 1 \\ 1 & 1 & 2 \end{bmatrix} |K| \end{aligned} \tag{3.80}$$

In (3.80), δ_{ij} is the Kronecker delta. For the load vectors $\boldsymbol{p}_i^K$:

$$\iint_{\Omega} \eta_q \zeta_i dxdy \approx \eta_q(N_i) |K| /3, \;\; i = 1,2,3 \;\; \& \;\; q = a,e,c,v \tag{3.81}$$

The boundary matrix **C** and boundary vector **c** (see equation (3.47)) in this work utilise the edge of the boundaries of the domain, specifically the cerebral ventricles and skull. One can therefore utilise the integration formula from Eisenberg and Malvern for a linear domain, $\partial\Omega$, specifically:

$$C_{ij}^E = \int_{\partial\Omega} \zeta_1^m \zeta_2^n ds = \frac{m!n!}{(m+n+1)!} |E| = \frac{1}{6}\left(1+\delta_{ij}\right)|E| = \frac{1}{6}\begin{bmatrix} 2 & 1 \\ 1 & 2 \end{bmatrix} |E| \tag{3.82}$$

where $|E|$ defines the edge length in 2D, and the 2D surface in the 3D case. The boundary matrix **C** in (3.82) is used as the template to apply the Neumann part of the boundary conditions at the skull and ventricles. Any Neumann condition (for instance the Capillary and CSF/ISF compartment) that is necessary will have to be multiplied directly by (3.82). The load vector $\boldsymbol{c}_i^E$ is defined in a similar way as above, however the edge length is once again utilised, by letting the integer n in (4.61) equal to naught, hence:

$$\frac{1!0!}{(1+0+1)!}|E|=\frac{1}{2}(1+\delta_i)|E| \tag{3.83}$$

The above equation only holds for constants taken into consideration through the use of Robin boundary conditions. Finally, a brief note is made on the application of Dirichlet conditions. All of the liquid phases apart from the capillary compartment possess Dirichlet type boundary conditions, in addition to the solid phase which will be detailed in the next section. It is important therefore to outline the methodology of applying these conditions in a quick and efficient manner, since the simplified nature of their application in the 1D derivation may seem obvious. In fact, in the 2D methodology used in this work, assuming the Dirichlet condition for the arterial compartment, p_{bpa}, the solution to the problem requires the trial space $Z_a^{pa}=\{\varsigma^{pa}:\|\varsigma^{pa'}\|_{L^2(\Omega)}<\infty,\|\varsigma^{pa}\|_{L^2(\Omega)}<\infty,\varsigma^{pa}|_{\Gamma_s}=p_{bpa}\}$, whilst using the test space Z_0^{pa}. It is therefore important to use a new affine subspace:

$$Z_{h,\Gamma_s}^{pi}=\{\varsigma^i\in Z_h^i:\varsigma^i|_{\Gamma_s}=g_D^i\} \tag{3.84}$$

In the above space, g_D^i represents the Dirichlet boundary condition of the i^{th} liquid phase compartment. In order therefore to derive a finite element approximation of p_h^i, it must be augmented in the form:

$$p_h^i=p_{h,0}^i+p_{h,g_D^i}^i \tag{3.85}$$

This allows for the convenient deduction that since one is in possession of $p_{h,g_D^i}^i$ by the mere fact that this quantity represents the given Dirichlet boundary condition (and so $p_{h,g_D^i}^i$ is equal to zero in the interior nodes), it is only necessary to determine $p_{h,0}^i$. This does not violate any fundamental principle in the FEM, since Galerkin orthogonally still holds. From a stiffness matrix and load vector point of view, the system that is solved (for ζ_0^i, which provides the nodal values $p_{h,0}^i$) in this case is:

$$\begin{bmatrix} C_{00} & C_{0g_D^i} \\ \mathbf{0} & I \end{bmatrix}\begin{bmatrix} \zeta_0^i \\ \zeta_{g_D^i}^i \end{bmatrix}=\begin{bmatrix} p_0 \\ p_{g_D^i} \end{bmatrix} \quad \therefore$$
$$\zeta_0^i=(C_{00})^{-1}\left(p_0-C_{0g_D^i}\zeta_{g_D^i}^i\right) \quad \&$$
$$I\zeta_{g_D^i}^i=p_{g_D^i} \tag{3.86}$$

As already mentioned, n_p represents the number of nodes, whilst the interior nodes are n_i. The peripheral nodes on the boundary are therefore $n_b = n_p - n_i$. The block matrices $C_{00}, C_{0g_D^i}$ and the identity matrix I are of size: $n_i \times n_i$, $n_i \times n_b$ and $n_b \times n_b$ respectively. The vectors ζ_0^i, $\zeta_{g_D^i}^i$, p_0 and $p_{g_D^i}$ have dimensions of: $n_i \times 1$, $n_b \times 1$, $n_i \times 1$ and $n_b \times 1$ respectively. $\mathbf{0}$ is the $n_b \times n_b$ block matrix of zeros. This methodology is also seamlessly extendable to the 3D case.

3.5.7 Boundary conditions in higher dimensions

An important consideration is that the boundary conditions for the CSF/ISF compartment are given in terms of (2.53) and (2.54):

$$\left.\begin{aligned} Q_{abs} &= Q_{HP} + \oint_S \left(-\frac{k_e}{\mu_e} \nabla p^e \right) \cdot \mathbf{n} ds \quad \text{on} \quad \Gamma_S \\ \dot{V} &= Q_p - Q_{HP} - Q_s - \oint_V \left(-\frac{k_e}{\mu_e} \nabla p^e \right) \cdot \mathbf{n} ds \quad \text{on} \quad \Gamma_V \end{aligned}\right\} \tag{3.87a-b}$$

In the simulations considered in this work, $\dot{V}$ is equal to zero when considering the quasi-stationary 1D cases (both in the C++ based FDM and the FEM) with no source/sink terms in order to give the Dirichlet boundary conditions at the skull of the CSF/ISF compartment as $p_{bp} + \mu^e R Q_0$, since the venous system in the skull absorbs the amount of CSF produced in the cerebroventricular system. For the 2D and 3D MPET models, the boundary conditions are represented as in (3.87a-b).

3.5.8 Variational formulation of the solid phase in 2D and 3D

One may rewrite the equations in (3.23) for the solid phase in terms of the effective stress $\boldsymbol{\sigma}'$ $= \boldsymbol{\sigma}_{\boldsymbol{eff}}$ - $\Sigma \alpha^i p \boldsymbol{I}$:

$$\left.\begin{aligned} -\nabla \cdot \boldsymbol{\sigma}' &= \boldsymbol{F} \quad in\ \Omega \\ \boldsymbol{\sigma}' &= \underbrace{2G\varepsilon(\boldsymbol{u}) + \lambda \varepsilon(\boldsymbol{u})\mathbf{I}}_{effective\ stress} - \sum_{i=a,e,c,v} \left(\alpha^i p_i \right) \mathbf{I} \quad in\ \Omega \\ \boldsymbol{u} &= \mathbf{0} \quad on\ \Gamma_s \end{aligned}\right\} \tag{3.88a-c}$$

Since (3.88c) indicates a Dirichlet boundary condition, it must be incorporated in the derivation of the weak form:

$$N = \left\{ \nu \in \left[\mathrm{H}^1(\Omega) \right]^{n \geq 2} : N|_{\Gamma_s} = 0 \right\} \tag{3.89}$$

From equation 3.89, N is the Hilbert space, with all smooth displacement vectors vanishing at the skull boundary, Γ_s. Multiplying (3.88a) with a test function ν, where $\nu \in N$, and once again integrating using Green's Theorem, the linear and bilinear forms of the equation are given by:

$$
\begin{aligned}
&\left(-\nabla\cdot\sigma',v\right)=\left(\boldsymbol{F},v\right)\ \therefore\\
&\qquad\Rightarrow\sum_{i,j=1}^{3}\left(-\frac{\partial\sigma'_{ij}}{\partial x_j},v_i\right)=\left(\boldsymbol{F},v\right)\\
&\qquad\Rightarrow\sum_{i,j=1}^{3}\left(-\sigma'_{ij},n_j v_i\right)_{\partial\Omega}+\left(\sigma'_{ij},\frac{\partial v_i}{\partial x_j}\right)=\left(\boldsymbol{F},v\right)\ \therefore\\
&\left(\int_{\Omega}\sigma':\nabla v\right)=\left(\boldsymbol{F},v\right)
\end{aligned}
\tag{3.90}
$$

The last relation involved the contraction operator. In addition, the zero displacement boundary condition at the skull is also assumed.

Considering that any matrix may be decomposed into symmetric and anti-symmetric segments, the gradient of the hat function may be replaced with the strain as a function of the test function v. In the total stress tensor $\boldsymbol{\sigma'}$, one may also replace: $\nabla\cdot v$ with $\mathbf{I}:\varepsilon(v)$. The weak form of (3.88) is therefore: Find $u\in N$ such that

$$
\left.
\begin{aligned}
&a(u,v)=l(v)\quad\forall v\in N,\ \text{where:}\\
&a(u,v)=2G\left(\varepsilon(u):\varepsilon(v)\right)+\lambda\left(\nabla\cdot u,\nabla\cdot v\right)-\sum_i\left(\alpha^i p_i,\nabla\cdot v\right)\\
&l(v)=\left(f,v\right)
\end{aligned}
\right\}
\tag{3.91}
$$

Existence, uniqueness and regularity of similar consolidation problems can be found in the elegant work of Showalter and Showalter and Su [365,366]. These details are omitted, as their derivation is beyond the scope of this work.

The FEA can be taken into account when each component of the displacement $\mathbf{u}$ (u, v, w) is approximated by shape regular continuous piecewise linear functions. These can be linear triangles in 2D and linear tetrahedrals in 3D. Subsequent refinement of the elements to higher orders is also possible. Hence, for a shape regular mesh on Ω:
Find the trial function $u_h\in N_h$ so:

$$
a\left(u_h,v\right)=l\left(v\right)\quad\forall v\in N_h
\tag{3.92}
$$

Of course, for (3.92) to be valid,

$$
N_h=\left\{v\in N:v\big|_K\in\left[\wp_1(K)\right]^{n\geq 2},\ \forall K\in M\right\}
\tag{3.93}
$$

Where $M=\{K\}$, is the shape regular mesh (tetrahedrals in 3D, triangles in 2D) on the domain Ω. The associated mass matrices in 2D (M^K) and 3D (M^V) [357] are:

$$M_{ij}^{K}=\frac{1}{12}\begin{bmatrix} 2 & 0 & 1 & 0 & 1 & 0 \\ & 2 & 0 & 1 & 0 & 1 \\ & & 2 & 0 & 1 & 0 \\ & & & 2 & 0 & 1 \\ & sym & & & 2 & 0 \\ & & & & & 2 \end{bmatrix}|K| \quad \& \quad M_{ij}^{V}=\frac{1}{20}\begin{bmatrix} 2 & 0 & 0 & 1 & 0 & 0 & 1 & 0 & 0 & 1 & 0 & 0 \\ & 2 & 0 & 0 & 1 & 0 & 0 & 1 & 0 & 0 & 1 & 0 \\ & & 2 & 0 & 0 & 1 & 0 & 0 & 1 & 0 & 0 & 1 \\ & & & 2 & 0 & 0 & 1 & 0 & 0 & 1 & 0 & 0 \\ & & & & 2 & 0 & 0 & 1 & 0 & 0 & 1 & 0 \\ & & & & & 2 & 0 & 0 & 1 & 0 & 0 & 1 \\ & & & & & & 2 & 0 & 0 & 1 & 0 & 0 \\ & & & & & & & 2 & 0 & 0 & 1 & 0 \\ & & sym & & & & & & 2 & 0 & 0 & 1 \\ & & & & & & & & & 2 & 0 & 0 \\ & & & & & & & & & & 2 & 0 \\ & & & & & & & & & & & 2 \end{bmatrix}|V| \tag{3.94}$$

3.5.9 Newton-Galerkin method

Since a volume reduction leads to a smaller pore size and consequently a lower permeability, the CSF/ISF compartment is augmented to include a non-linear permeability. Equation 3.57c is augmented to compete with the 1D analogy of incorporating AQP4 sensitisation via:

$$\left.\frac{\partial}{\partial t}(S^e p^e+\alpha^e\nabla\cdot\mathbf{u})=L_e+f_e\right\}\text{where}: L_e=\nabla\cdot[\psi_{csf}\cdot\nabla p^e] \quad f_e=\left|\dot{s}_{c\to e}\right|-\left|\dot{s}_{e\to v}\right| \tag{3.95}$$

where $\psi_{csf}(p)=-(k_e/\mu_e)e^{(p/2p_{ref})}$. A brief excursion using the Newton-Galerkin Method [367] of the quasi-stationary case of the aforementioned liquid phase is conducted. One may proceed in the following manner:

Insert $p_h^e=p_0^e+\delta p^e$ into the weak form of $-\nabla\cdot[\psi_{csf}\cdot\nabla p^e]=f_e,\ \forall\lambda^e\in H^1(\Omega)$, where one multiplies by a test function, $\lambda^e\in\Lambda^e=H^1(\Omega)$. It is noted that p_0^e is an approximation to p^e, and δp^e is the corresponding correction. One then proceeds with a Taylor expansion of the function $\psi_{csf}(p)=\psi_{csf}(p_0^e+\delta p^e)$ around p_0^e whilst inserting this into the weak formulation. A linear equation for the correction δp^e is obtained by neglecting any terms of $O(\delta p^2)$ and above in the Taylor expansion and iterating with $p_0^e+\delta p^e$ as new solution guesses. By writing $\delta p^e=\sum_{i=1}^{n_i}w_i\varphi_i$ and inserting into the finite element approximation of the relevant liquid phase, one then needs the solution of the set of n_i equations for the unknowns w_i by calculating the relevant residual vector ($n_i\times 1$) and Jacobian matrix ($n_i\times n_i$) in the form $\mathbf{J}w=\boldsymbol{\rho}$ where:

$$\begin{aligned} J_{ij}&=\left(\psi_{csf}\left(p_h^0\right)\nabla\varphi_j,\nabla\varphi_i\right)+\left(\psi_{csf}^{'}\left(p_h^0\right)\varphi_j\nabla p_h^0,\nabla\varphi_i\right),\quad i,j=1,\ldots,n_i \\ \rho_i&=\left(f_e,\varphi_i\right)-\left(\psi_{csf}\left(p_h^0\right)\nabla p_h^0,\nabla\varphi_i\right),\quad i=1,\ldots,n_i \end{aligned} \tag{3.96}$$

3.6 Iterative methods for FEM based large sparse linear systems

3.6.1 Transpose-Free QMR method (TFQMR)

In this work, a preference was given to iterative solvers over their direct counterparts for the solution of the final linear MPET system of equations. Since the FEM was used, it is important to note that the resulting matrices are in, general, very sparse. This is due to the basis functions already outlined interacting primarily within their immediate neighbourhood, owing to their inherent support structure across the domain. A class of iterative methods that is deemed suitable in coping with the general sparsity of the matrices involved in the FEM solutions are those with an associated projection onto Krylov subspaces. Research into Krylov subspace methods for solving non-symmetric (as in the MPET system) linear systems is an active field of research and new methods are constantly being developed. Well known Krylov methods are the Conjugate Gradient method (CG), Generalised Minimal Residual method (GMRES), Conjugate Gradient on the Normal equations methods (CGNE), Bi-Conjugate Gradient method (BiCG), Conjugate Gradient Squared method (CGS) and finally the Quasi Minimal Residual method (QMR). Of interest in this work is the method developed by Freund [368], namely the Transpose-Free QMR method (TFQMR).

The BiCG, CGS and TFQMR methods involve Galerkin-type operations in their build up. The CG family is often used in numerical methods, however they can exhibit irregular convergence behaviour and premature breakdown [369]. This is of paramount importance when considering the MPET system, since it is a notoriously difficult system to solve even in simple consolidation problems. The TFQMR algorithm is also a *Biorthogonalisation method*, however it may be considered as a quasi-minimal residual version of the CGS algorithm [370], since it lacks certain coefficient matrix/vector (and, of course, its transpose) multiplications and tends to offer smoother convergence than the BiCG method. Although slightly more expensive [369], the TFQMR method offers a stability in the solution process that is much needed, considering the ill-conditioned nature of the MPET template. In this work, the use of TFQMR is handled by a mature algorithm within the MATLAB environment.

In addition to the use of this iterative solver, preconditioning was also required in all three dimensions covered by the MPET framework. An indication in the application of TFQMR with the relevant preconditioning can be seen in Figure 3.7. The QMR family of methods are known to converge well when combined with the suitable preconditioners, such as SSOR, Jacobi and Sparse incomplete LU factorization (ILU). Garcia and colleagues provide various examples of numerical experiments with interesting adaptations of a modified QMR technique [371]. In this work, the use of preconditioning was important in order to help accelerate the rate of convergence, in addition to improving the spectral properties of the combined stiffness and load matrices (when Neumann conditions are used). Figure 3.7 outlines the general solution process and is analogous to Figures 3.4-3.5. It also indicates the type of

preconditioning used. Any additional parameters preferred, such as a desired tolerance limit, maximum iteration count or even the use of reverse (and sparse reverse) Cuthill-McKee reordering algorithms [372,373] are given below. In the aforementioned reordering, the general characteristics is a reduction of bandwidth, especially useful in sparse systems.

3.6.2 Specific conditions used

As can be seen in Figure 3.7, there are sub-segments (white shading) indicating the type of preconditioning used, and the respective output that is used to feed the `TFQMR` solver. In this research, sparse incomplete *LU* factorisation was preferred, owing to the level of sparsity in the stiffness matrices of both solid and fluid phases. In addition to merely choosing the type of factorisation, one has to fully accommodate the level of ill-conditioning, and in the MPET's case, this required pivoting. Fortunately, the `TFQMR` algorithm being implemented within `MATLAB`'s matrix decomposition library allows for pivoting and thresholding to be accommodated quite seamlessly. With the exception of the diagonal entries, which are retained regardless of satisfying the criterion, the entries of the unit lower triangular matrix are tested against a specified drop tolerance of 10^{-80} before being scaled by the pivot. For the `TFQMR` solver, a maximum of 5000 iterations was also specified, along of course with the *L* and *U* matrices given by the *ILU* factorisation as suitable preconditioners. In general, the strategy adopted here was to focus on finding a good preconditioner rather than the most efficient accelerator, as is recommended for very sparse matrices [374]. The relative residual norm, maximum iteration count and a vector of residual norms at each iteration were obtained and used in deciphering the complexity of the stiff MPET system. Finally, in the 3D formulation, symmetric reverse Cuthill-McKee ordering [2] was used on all of the sparse matrices. Details of the relevant improvements are discussed in the relevant 3D section.

3.6.3 A dual-grid development algorithm for the 1D system

The reasoning behind attempting a dual or multi-grid solver was that as the Poisson ratio approaches $\nu \rightarrow 0.5$, or near complete incompressibility, it is known that linear elements generally provide wildly oscillating results for general elasticity problems [375]. It will become evident in the next chapter (where a strain-dependent permeability was utilised), that the final results relating to the use of more complicated MPET templates could be susceptible to varying degrees of oscillatory behaviour in the final solution anyway, let alone the dependency on the degree of oscillation to the magnitude of Poisson's ratio. In this work, a value of 0.35 was used throughout, and the final system seems to compensate for any erratic behaviour when using the FEM formulation. It can also be seen (in the next chapter) that having a Poisson's ratio that is too low $\nu < 0.15$ seems to overestimate the ventricular displacement quite substantially. This is an important observation since in a fully three dimensional cerebral environment, voxels encompassing different degrees of elasticity could in theory produce questionable levels of displacement, especially if a superposition of 1D models was used to estimate the level of the global parenchymal displacement in the brain. To dispel any possibility of erratic phenomena at varying levels of Poisson ratio, a dual grid iterative solver was

developed in order to observe the levels of over or under estimation of the ventricular displacement with varying *v*. The basic idea behind this dual grid solution method is the need to diffuse any high frequency components of error using a very simple and inexpensive iterative solver such as *Richardson's iteration* scheme on a fine grid, whilst the low frequency segments of the error are dealt with any conventional direct solvers of choice on a coarser grid.

In conventional *V-cycle* techniques, one refrains from the use of direct solvers altogether, however since this method is applied to a 1D template, there are fewer number of nodes, and so slightly more expensive methodologies can be afforded. A *prolongation operator* was built to handle the transfer the information from between coarse and fine mesh, whilst a *restriction operator* transfers the data from the fine to coarse mesh. The fine grid comprises of a stiffness matrix and load vector, whilst the coarse grid possesses a separate stiffness matrix. Richardson's relaxation parameter was $h/400$, where h is the grid spacing of the fine grid, whilst a maximum iteration count of 4 was suffice. For the outer iteration loop of the dual-grid solver, 5 iterations were used. The number of grid nodes used was also increased, to 640, to allow for the full capability of the technique to be felt, hence the number of fine nodes was set to 640, whilst the number of coarse nodes was set to 320. Within the outer loop of the dual-grid solver, sparse incomplete *LU* factorization was used as a preconditioner to the `TFQMR` iterative solver.

This chapter has shown the steps required to implement the discretisation of the MPET system in a one dimensional, coupled FDM-CFD manner, a one dimensional standalone FDM based solver and also a generic nth dimensional FEM based templates. The one dimensional methods utilised spherical symmetry, whereas the latter FEM based MPET discretisation relaxes this constraint. This is the first time that the MPET system has been discretised using the FEM. It is also the first time that the MPET system has been implemented in two and three dimensions. Another novelty of the method is the inclusion of the transient pressure and strain terms for the fluid phases, which are implemented in two and three dimensions. Furthermore, a dual-grid solution method is presented to diffuse the high frequency components of error using Richardson's iteration scheme on a fine grid, whilst the low frequency segments of the error are dealt with the `TFQMR` iterative solver on the coarser grid. A Newton-Galerkin scheme is also presented for the CSF/ISF compartment, in anticipation of future developments that will be required for the VPH-DARE@IT project described in §4.6. The results and discussion of implementing these schemes will now follow

---

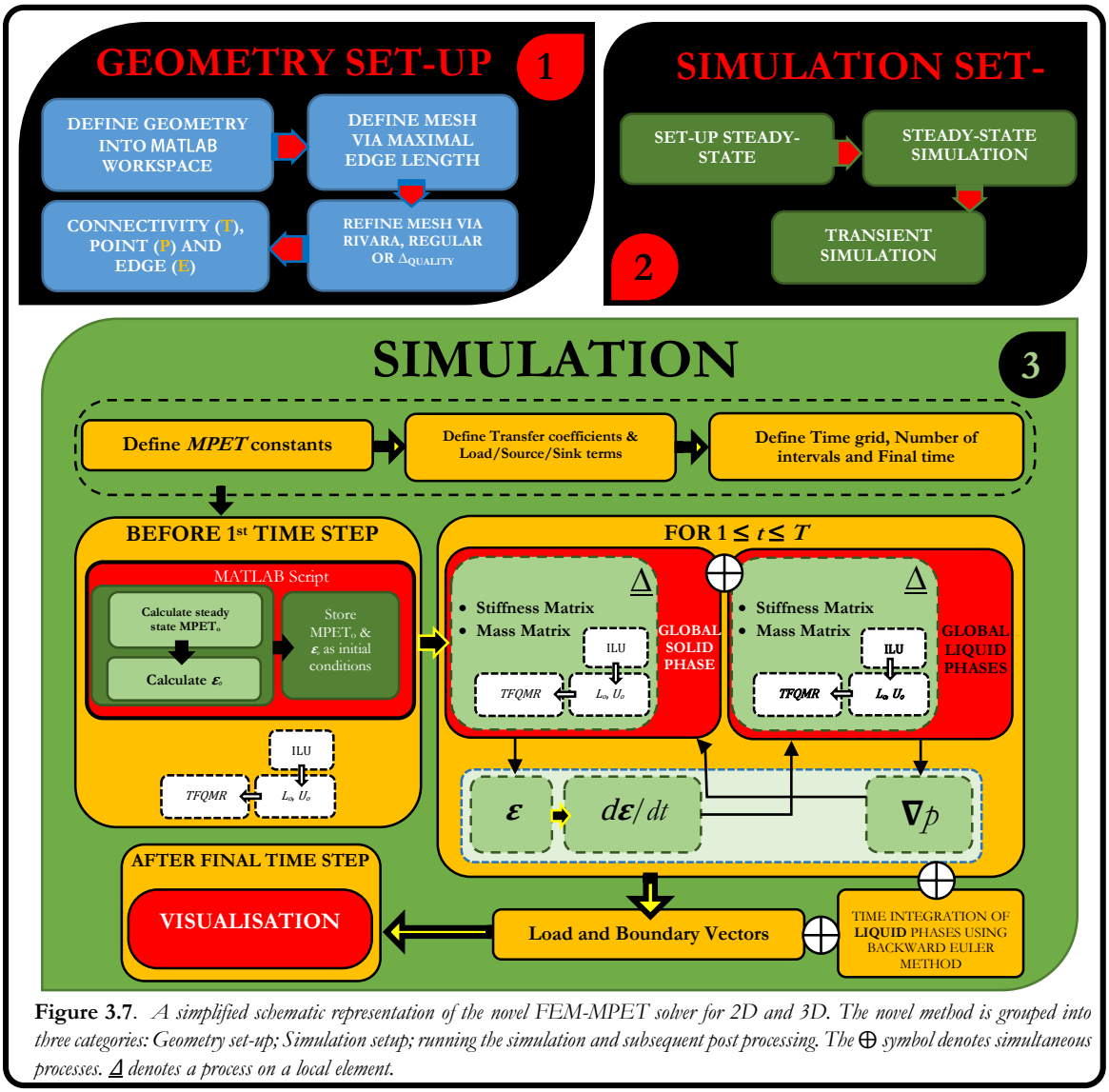

Figure 3.7. *A simplified schematic representation of the novel FEM-MPET solver for 2D and 3D. The novel method is grouped into three categories: Geometry set-up; Simulation setup; running the simulation and subsequent post processing. The ⊕ symbol denotes simultaneous processes. $\underline{\Delta}$ denotes a process on a local element.*

CHAPTER 4

Exploring Hydrocephalus and its treatment using MPET: Results & Discussion

This aim of this chapter is to observe and discuss the resuts based on the implementation of the numerical templates described in the previous chapter. Derivative pathologies of acute HCP are firstly investigated, utilising the 1D FDM-CFD platform. Pathologies investigated here involve ventricular enlargement due to aqueductal stenosis and fouth ventricle outlet obstruction. Whether or not the symptoms can be alleviated via the use of two surgical means, namely endoscopic third and fourth ventriculostomy is also observed. The one dimensional FDM based strain-dependent permeability formulation examines both acute HCP and the perceived underlying causes of NPH. Finally, the FEM templates are applied over one, two and three dimensions to examine both acute and chronic HCP.

The results from the 1D FDM-CFD have been published in the following:

1) Vardakis et al., Exploring the Efficacy of Endoscopic Ventriculostomy for Hydrocephalus Treatment via a Multicompartmental Poroelastic Model of CSF Transport: A Computational Perspective, PLoS one, 8 (2013) e84577.

2) Vardakis et al., Multicompartmental Poroelasticity as a Platform for the Integrative Modeling of Water Transport in the Brain, in: G.A. Holzapfel, E. Kuhl (Eds.) Computer Models in Biomechanics, Springer Netherlands, 2013, pp. 305-316.

4.1 Results: 1D FDM-CFD

4.1.1 Aqueductal stenosis

Figure 4.1 shows the application of the MPET model to obstructive HCP with the addition of ETV, along with the swelling factor of AQP4 being taken into account. The inclusion of the choroid plexus' geometrical representation within the ventricular system and its coupling with the MPET model are also taken into account in these results. The hydraulic diameter, d, for the open, mild and severe cases is given in Table 2.1 as 3.00 *mm*, 1.25 *mm* and 0.80 *mm* respectively. It can be seen from Figure 4.1a that the ventricular displacement increases from approximately 0.67 *mm* in the open aqueduct to approximately 0.82 *mm* in the mild case of aqueductal stenosis. The severe case presents the highest level of ventricular displacement of around 3.28 *mm*.

The application of ETV substantially reduced the level of ventricular displacement to 0.70 *mm* for the mild case and around 2.25 *mm* for the severe case. This is a fair reduction in both cases, but especially for the mildly stenosed case, as its ventricular displacement level has been reduced to a level resembling the case of the open aqueduct. All of the aforementioned ventricular displacement values are taken at r_v. In addition, all of the displacements reduced to

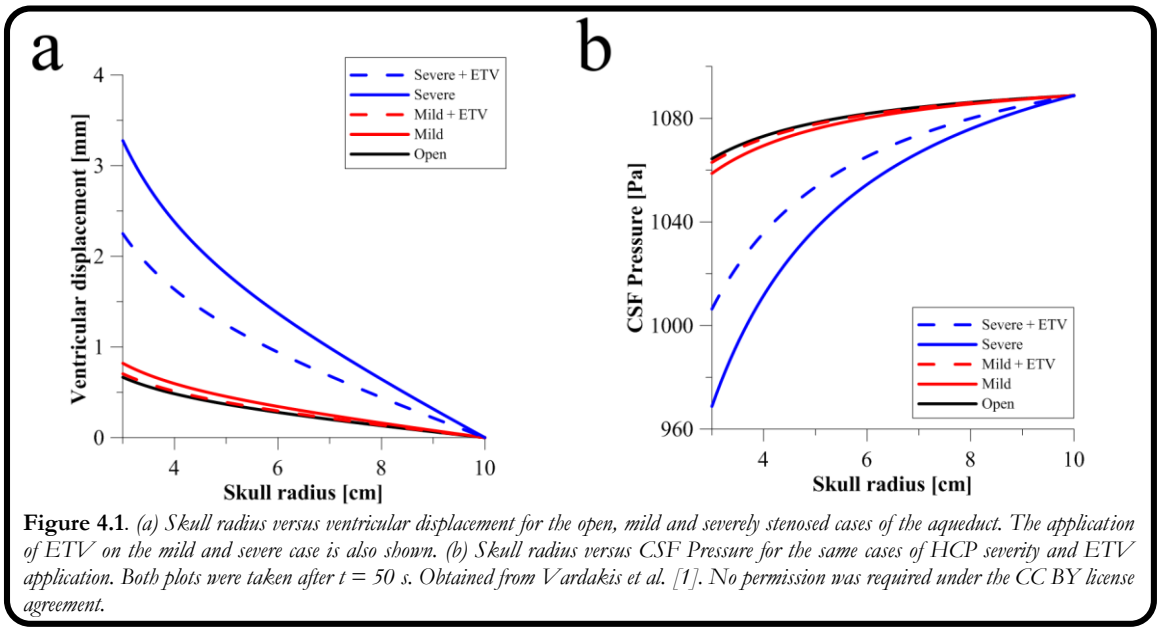

Figure 4.1. *(a) Skull radius versus ventricular displacement for the open, mild and severely stenosed cases of the aqueduct. The application of ETV on the mild and severe case is also shown. (b) Skull radius versus CSF Pressure for the same cases of HCP severity and ETV application. Both plots were taken after t = 50 s. Obtained from Vardakis et al. [1]. No permission was required under the CC BY license agreement.*

zero at the skull $(u(r_i,t) = 0)$ since the boundary condition imposed on the system at this point was that of a rigid, adult skull.

The CSF pressure variation to aqueductal stenosis shown in Figure 4.1b indicates a similar trend. There is a decrease from approximately 1064.38 *Pa* in the open case to, 1058.73 *Pa* in the mild case and finally reducing to 968.77 *Pa* in the severe case. The introduction of ETV increased the CSF Pressure from its decreasing levels to 1062.97 *Pa* and 1006.36 *Pa* for the mild and severe cases of aqueductal stenosis. It should also be noted that all CSF pressures converge to 1088.77 *Pa* on the skull, as expected, since this value corresponds to the absorption resistance boundary condition. As can be seen from Table 4.1, the peak velocity in the aqueduct increases substantially between stenosis severity levels. In the open aqueduct, it is measured to be approximately 15.6 cm/s (Reynolds number of ~524), whereas in the mild and severe cases, this increases to 45.4 cm/s (Reynolds number of ~635) and 72.8 cm/s respectively (Reynolds number of ~650).

As expected, once ETV has been applied, the peak velocity in the aqueduct falls to 16.8 cm/s (Reynolds number of ~235) and 17.1 cm/s (Reynolds number of ~153) for the mild and severe case respectively. The WSS values at the surface of the aqueduct (also see Figure 4.2) display a similar trend. The peak WSS value at the surface of the open aqueduct was measured to be just less than 0.9 N/m^2, whilst for the mild and severe cases of stenosis this increased to around 5.8 and 12.2 N/m^2 respectively. The WSS was alleviated by the application of ETV (see Table 4.1), and this followed a decline from the aforementioned values to 1.5 N/m^2 for both the mild and severe cases. The pressure difference between the lateral and fourth ventricles was used as a final comparator. As can be seen from Table 4.1, large fluctuations can exist with the application of aqueductal stenosis. The average pressure difference between the lateral and fourth ventricle was found to be roughly around 18 *Pa*. Once stenosis occurred, this increased from 18 to 94 *Pa* in the mild case and up to 241 *Pa* in the severe case. Once again the application of ETV helped rectify the large fluctuations back to normal levels, 15 and 20 *Pa* respectively. The velocity in the central canal did not exceed 2

cm/s for all above cases. The porosity of the choroid plexus fluctuated between 0.675 and 0.775 for all cases in this study. The average velocity coming out of the entrance of the arteries to the choroid plexus was approximately 40 *mm/s*, given the boundary condition of 2 *kPa* at the inlet of the arteries.

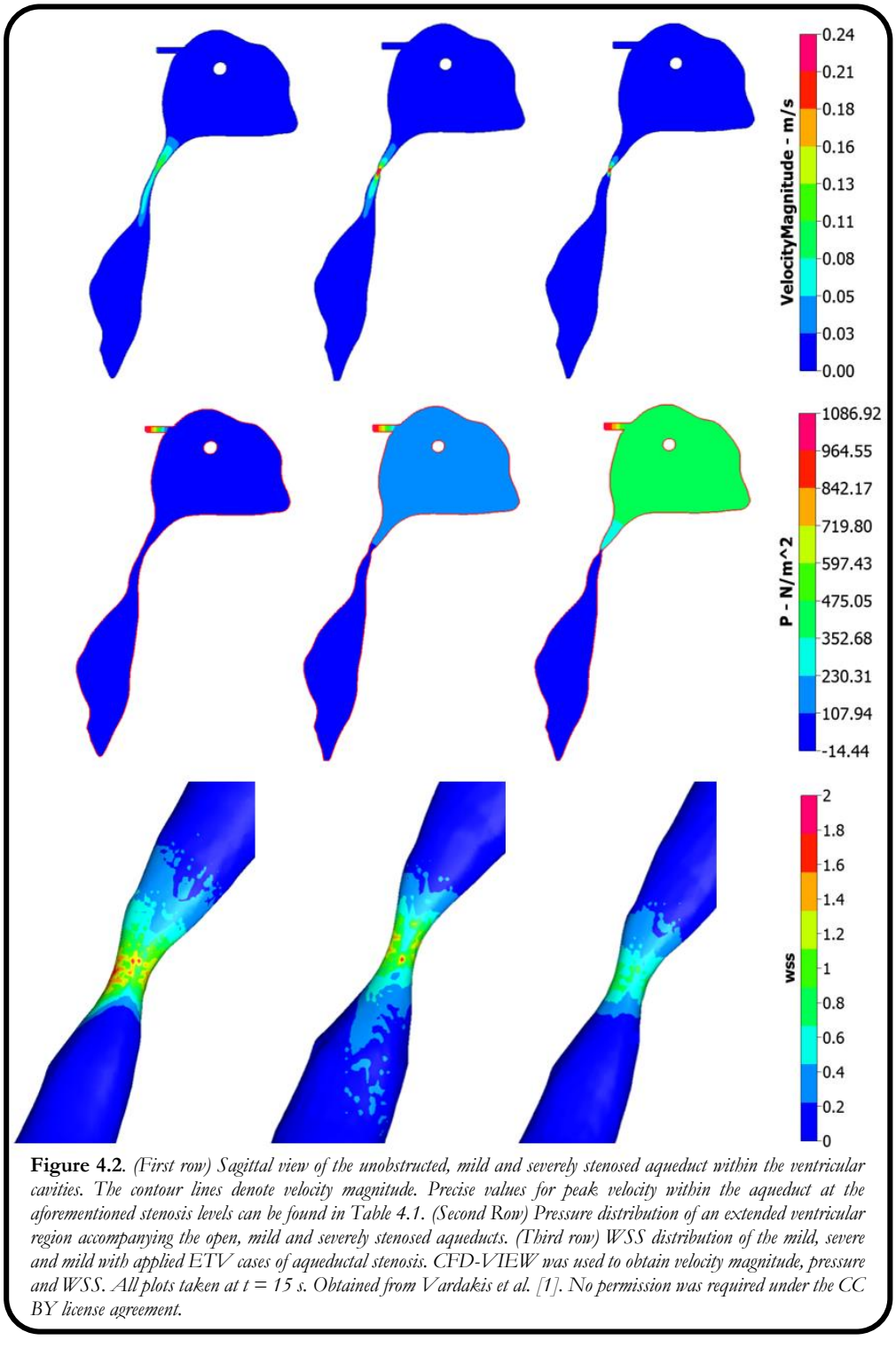

Figure 4.2. *(First row) Sagittal view of the unobstructed, mild and severely stenosed aqueduct within the ventricular cavities. The contour lines denote velocity magnitude. Precise values for peak velocity within the aqueduct at the aforementioned stenosis levels can be found in Table 4.1. (Second Row) Pressure distribution of an extended ventricular region accompanying the open, mild and severely stenosed aqueducts. (Third row) WSS distribution of the mild, severe and mild with applied ETV cases of aqueductal stenosis. CFD-VIEW was used to obtain velocity magnitude, pressure and WSS. All plots taken at t = 15 s. Obtained from Vardakis et al. [1]. No permission was required under the CC BY license agreement.*

Table 4.1. *The values of hydraulic diameter D_h, peak velocity v_p, peak Reynolds number Re_p, wall shear stress (WSS) and pressure difference (between isolated points in the lateral ventricle and fourth ventricle) ⊿P, for an open, mild and severely stenosed aqueduct of Sylvius. The above values once ETV has been applied are also given. All values obtained at t = 50s*

Severity	D_h [mm]	v_p [cm/s]	Re_p	WSS [N/m²]	ΔP [Pa]
Open	3.00	15.59	523.93	0.87	18
Mild	1.25	45.37	635.31	5.84	94
Mild ⊕ ETV	1.25	16.76	234.69	1.50	15
Severe	0.80	72.75	649.46	12.22	241
Severe ⊕ ETV	0.80	17.08	153.08	1.51	20

Figure 4.3 shows the change in CSF content (Equation 3.3) for the three cases of aqueductal stenosis. The primary aim of observing this relationship is to confirm that there is an expansion in the region close to the ventricles, and a subsequent compression against the rigid skull in the surrounding parenchyma. Negative values of ζ indicate fluid being squeezed out of the brain. The positive values of ζ indicates the existence of tissue damage adjacent to the cerebral ventricles. As expected, a larger degree of aqueductal stenosis corresponds to a larger CSF change in tissue adjacent to the ventricles and in addition, a large section of tissue (most likely grey matter) compression (between a radius of 7-10 *cm*). These results correlate well with other work in the literature [287,292].

4.1.2 Fourth Ventricular Outlet Obstruction (FVOO)

In addition to the implication of applied stenosis on the aqueduct, fourth ventricular outlet obstruction was investigated. This was done in order to help to elucidate the consequence of applying EFV and comparing this to ETV. As can be seen from Table 4.2, occluding both the foramina of Luschka slightly increases the peak velocity from 15.6 *cm/s* in the open aqueduct to 16.5 *cm/s*. The peak velocity through the foramen of Magendie increases from 2.4 *cm/s* in the open case to 8.9 *cm/s*, followed in the same fashion by the peak velocity in the central canal, from 2.0 *cm/s* to 8.7 *cm/s*.

The equivalent ventricular displacement for such an occlusion was 1.33 *mm* (see Figure 4.4), whilst the CSF pressure reduces from 1064.38 *Pa* to 1039.89 *Pa*. The pressure difference stays at ~17 *Pa*, irrespective of this occlusion. This is in contrast to the stenosis of the Sylvian aqueduct which resulted in over a five-fold increase in the mild case alone. This contrast is further fortified by the similar WSS values at the surface of the aqueduct. The application of

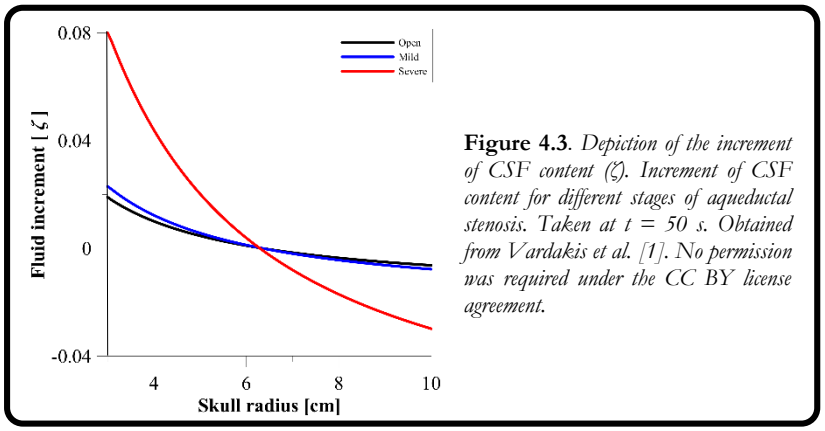

Figure 4.3. *Depiction of the increment of CSF content (ζ). Increment of CSF content for different stages of aqueductal stenosis. Taken at t = 50 s. Obtained from Vardakis et al. [1]. No permission was required under the CC BY license agreement.*

ETV and EFV to this dual occlusion has varying consequences. ETV approximately halves the peak velocity in the aqueduct whilst EFV keeps it approximately constant at 16.2 *cm/s*. As expected, since EFV is taking place in a closer vicinity to the occlusion, the peak flow rate through the foramen of Magendie (8.9 *cm/s* under the influence of this occlusion) shows a larger reduction than that of the ETV application (3.0 *cm/s* as opposed to 4.2 *cm/s*). The same trend applies to the central canal, where its initial peak velocity under occlusion of the bilateral foramina (8.7 *cm/s*) is reduced to 3.9 *cm/s* (ETV) and 2.6 *cm/s* (EFV) respectively.
ETV reduces the pressure difference between lateral and fourth ventricles quite considerably (from 17 *Pa* to 6.6 *Pa*), whilst EFV forces a slight decrease in this value (16.7 *Pa*). The same applies to the WSS, since this is reduced from around 0.8 N/m^2 to ~0.3 N/m^2, whilst in contrast it slightly decreases with the application of EFV (see Table 4.2).

The application of ETV and EFV reduces the ventricular displacement to 0.87 *mm* and 0.77 *mm*, whilst the CSF pressure increases to 1057.04 *Pa* and 1060.57 *Pa* respectively. The situation is similar for the occluded Magendie. The peak velocity through the aqueduct increases from 15.6 *cm/s* in the patent aqueduct case (Table 4.2) to 16.6 *cm/s*.

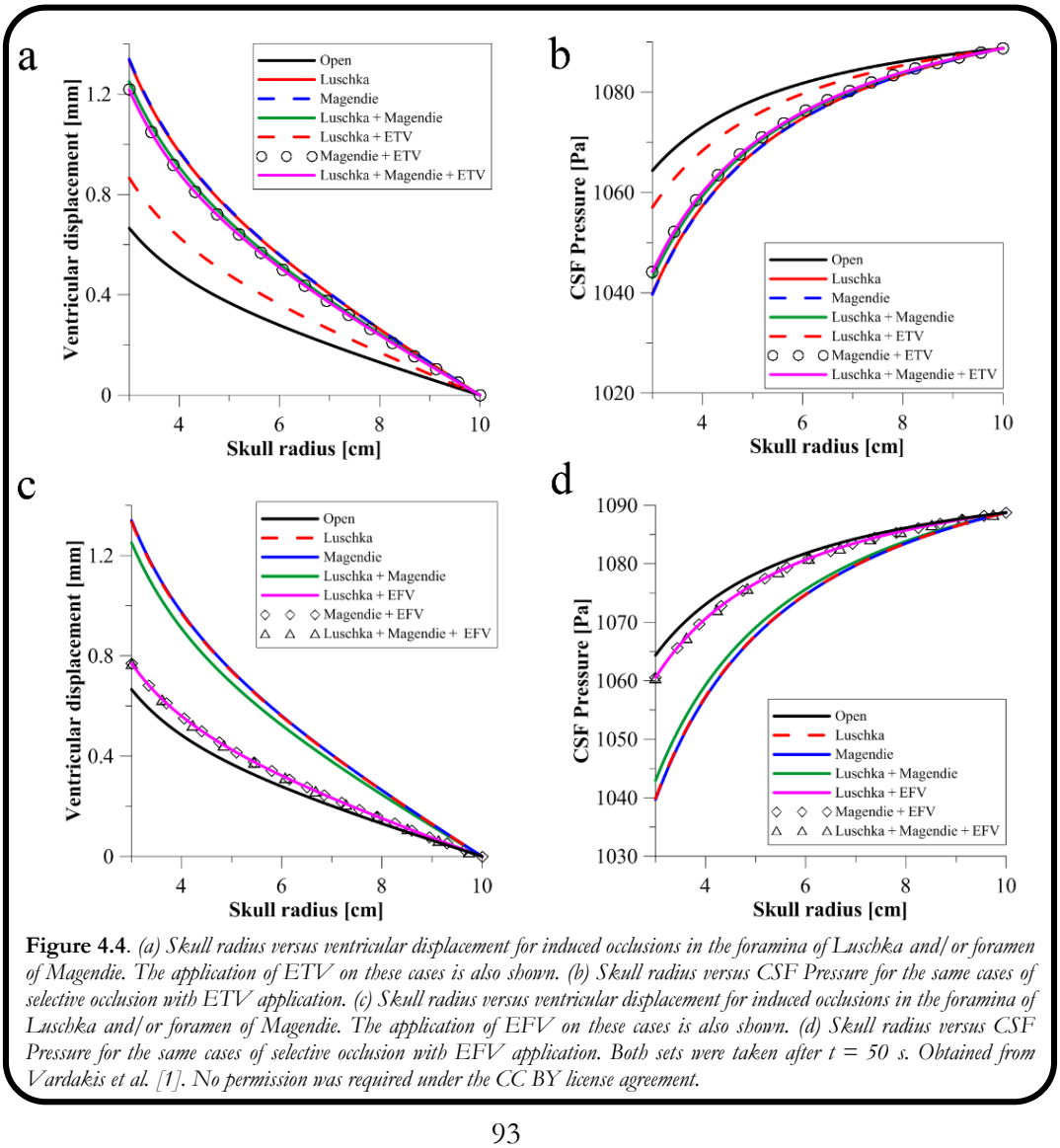

Figure 4.4. *(a) Skull radius versus ventricular displacement for induced occlusions in the foramina of Luschka and/or foramen of Magendie. The application of ETV on these cases is also shown. (b) Skull radius versus CSF Pressure for the same cases of selective occlusion with ETV application. (c) Skull radius versus ventricular displacement for induced occlusions in the foramina of Luschka and/or foramen of Magendie. The application of EFV on these cases is also shown. (d) Skull radius versus CSF Pressure for the same cases of selective occlusion with EFV application. Both sets were taken after t = 50 s. Obtained from Vardakis et al. [1]. No permission was required under the CC BY license agreement.*

The peak velocity through the bilateral foramina stays fairly constant at 2.9 *cm/s*, a slight increase from 2.4 *cm/s* in comparison with the same healthy case. The peak velocity through the central canal displays a slight increase from 2.0 *cm/s* to 2.6 *cm/s*, whilst the pressure difference remains relatively unchanged at ~17 *Pa*. The ventricular displacement and CSF pressure remain identical to the case of the occluded bilateral foramina. The WSS value slightly decreases, from around 0.9 N/m^2 to ~0.82 N/m^2. Comparing ETV and EFV for this occlusion, it is evident that ETV reduces the pressure difference with greater effect (from 17.4 *Pa* to 6.8 *Pa*), whilst EFV reduces it only marginally to 16.7 *Pa*. The peak velocities in the central canal, bilateral foramina and aqueduct are reduced to a greater extent with the application of ETV as opposed to EFV. Applying ETV and EFV reduces the ventricular displacement to just under 1.22 *mm* and 0.77 *mm* respectively. CSF pressure increases to 1044.12 *Pa* for the ETV case, whilst for EFV it increases to 1060.56 *Pa*.

The final scenario involves the occlusion of all fourth ventricle exits except the central canal. The peak aqueduct velocity decreases slightly from 15.6 *cm/s* to 15.0 *cm/s*, whilst through the central canal it increases drastically from 2 *cm/s* to 35.5 *cm/s*. In addition, the WSS possesses a modest value of 0.63 N/m^2. The pressure difference remains more or less constant, decreasing by just 2.1 *Pa* when compared to the open case. The ventricular displacement increases to approximately 1.25 *mm*, whilst the CSF pressure decreases to 1042.95 *Pa*. Applying ETV, we see a reduced peak velocity through the aqueduct to a greater extent than EFV (which increases compared to the combined obstruction of Luschka and Magendie); however EFV reduces the velocity in the central canal (4.6 *cm/s* as opposed to 5.6 *cm/s*). Finally, the pressure difference assumes a larger value due to ETV (~6 *Pa*) as opposed to its competing neurosurgical technique (which raises it to ~18 *Pa*).

Further investigation in the vicinity of the ETV outlet was required to justify the lower than expected pressure difference between the lateral and fourth ventricles. The velocity magnitude of CSF near the lower region (from just above the ETV outlet (point P1 on Figure 4.5) and linearly extending horizontally towards the aqueduct (point P2 on Figure 4.5)) of the third ventricle was noted to be in the range of 5.5 cm/s to 0.14 cm/s for the occluded Luschka's (Occ. Lus.), 5.7 cm/s to 0.14 cm/s for the occluded Magendie (Occ. Mag.) and finally 5.4 cm/s to 0.13 cm/s for the tri-exit occlusion (Occ. Mag. And Lus.).

Applying ETV, the respective ranges were: 8 *cm/s* to 0.065 *cm/s* (Occ. Lus.), 7.77 to 0.057 *cm/s* (Occ. Mag.) and 8.36 *cm/s* to 0.072 *cm/s* (Occ. Mag. And Lus.). The pressure range was also monitored in the same lower third ventricle region as that of the aforementioned CSF velocities. The pressures ranges before and after ETV were: from 21.0 *Pa* to 7.6 *Pa* (Occ. Lus.), 17.8 *Pa* to 6.9 *Pa* (Occ. Mag) and 80 *Pa* to 7.9 *Pa* (Occ. Mag. and Lus.). In the same order, the peak ETV outlet velocities were 12 *cm/s*, 11 *cm/s* and 12 *cm/s* respectively.

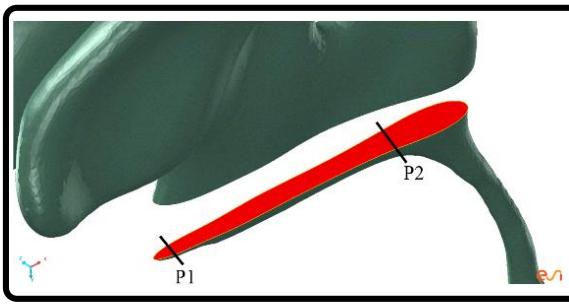

Figure 4.5. *The lower region of the third ventricle used to evaluate the ranges of CSF velocity and pressure before and after ETV. The range was taken between points P1 and P2. Obtained from Vardakis et al. [1]. No permission was required under the CC BY license agreement.*

Table 4.2. *The values of peak velocity v_p (in the aqueduct (a), Magendie (m), Luschka (l, average) and central canal (cc)), pressure difference between isolated points in the lateral ventricle and fourth ventricle, ⊿P and wall shear stress (WSS) are given for the occluded foramina of Luschka and foramen of Magendie. The peak velocity values for endoscopic third and fourth ventriculostomy (ETV, EFV) are also displayed. All values obtained at t = 50s.*

FVOO location	v_p(a) [cm/s]	v_p(m) [cm/s]	v_p(l) [cm/s]	v_p(cc) [cm/s]	ΔP [Pa]	WSS [N/m²]
Luschka (Lu)	16.52	8.90	Occluded	8.70	17	0.83
Magendie (Ma)	16.55	Occluded	2.93	2.62	17	0.82
Lu ⊕ Ma	15.01	Occluded	Occluded	35.48	16	0.63
Lu ⊕ ETV	8.92	4.22	Occluded	3.89	< 10	0.29
Ma ⊕ ETV	9.04	Occluded	1.43	1.06	< 10	0.33
(Lu ⊕ Ma) ⊕ ETV	8.47	Occluded	Occluded	5.59	< 10	0.31
Lu ⊕ EFV	16.17	3.00	Occluded	2.62	17	0.79
Ma ⊕ EFV	16.17	Occluded	1.67	1.27	17	0.79
(Lu ⊕ Ma) ⊕ EFV	17.02	Occluded	Occluded	4.58	18	0.86

4.1.3 Flow visualization

Figure 4.6a portrays the most complex flow found within the cerebroventricular system, namely in the fourth ventricle. As can be seen, two vortices (red arrows) have developed from the complicated partition of CSF flow arising from the aqueduct of Sylvius (which largely determines the nature of the CSF flow in the fourth ventricle), and they both rotate in an anti-clockwise direction. The other portion of CSF travels along the floor of the fourth ventricle and leaves via the three foramina (satisfying the second category of systolic centrifugal CSF flow). Flow exits through the foramen of Magendie and a comparatively low amount through the central canal. Figure 4.6b-d show representations of the velocity streamlines in an open,

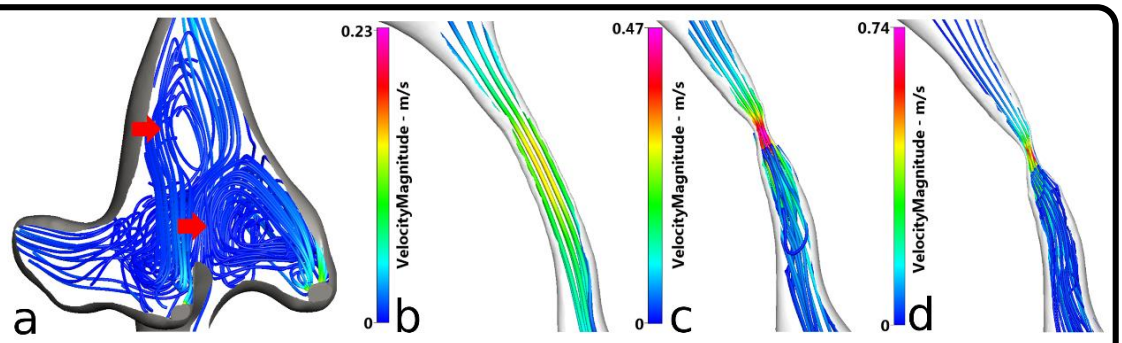

Figure 4.6. *(a) View of the velocity streamlines of the aqueduct and fourth ventricle in a healthy patient in the sagittal plane. Two vortices are identified via the red arrows. (b) A more focused representation of the velocity streamlines of the aqueduct in a healthy patient. (c) Velocity streamlines of the mildly stenosed aqueduct. (d) Velocity streamlines of the severely stenosed aqueduct. CFD-VIEW was used to obtain all streamlines. All plots taken at t = 15s. Obtained from Vardakis et al. [1]. No permission was required under the CC BY license agreement.*

mild and severly stenosed aqueduct. CSF flow was generally slow in the lateral ventricles and conformed to the centrifugal based classification outlined in Stadlbauer *et al.* [337]. In addition, areas of dead zones and recirculation were noticed in the lateral ventricles. The third ventricle obeyed the second category of systolic cranio-caudal flow, described in detail in the same literature. Matsumae *et al.* [338] provide good evidence of CSF velocity and CSF pressure gradients in the cranial space using 4D-PC MRI. A good account of many of the characterisitcs desribed thus far are reiterated, along with the welcome confirmation that CSF velocity is in the order of cm/s within the cerebral ventricles, and that the pressure gradients in a pre and post operative case of a patient with secondary hydrocephlus (treated with a shunt) are of similar magnitude, and therefore clinically relevant.

4.2 Results: Strain-Dependent Permeability Simulations

In this section, a succinct account of the influence of incorporating a strain-dependent permeability on the CSF compartment is given. Although this is an important evolution of the MPET framework, it is not the primary focus of this work. Instead, it is highlighted how an improved qualitative understanding in tackling some of the more intricate questions surrounding both acute and communicating hydrocephalus is provided by adopting such a model.

4.2.1 Numerical experiments of the 1D-solver

Figure 4.7a depicts the linear relation between ventricular displacement and grid spacing for the strain-dependent permeability MPET solver. A good indicator of the truncation error can be obtained by monitoring both the qualitative and quantitative resemblance to the MPET model already under consideration. In previous studies [339], only the ventricular displacement was used as a metric of comparison. Observing the pressure profile (Figure 4.7b), one may observe that the coupling methodology for the stiff MPET template along with its constituent strain-dependent permeability property for the CSF compartment introduces an unwelcome level of overestimation in the pressure profiles when the grid discretisation is too coarse (20 or 40 nodes). Using a coarse grid tends to violate the zero displacement boundary condition at the skull in addition to error-prone pressure profiles.

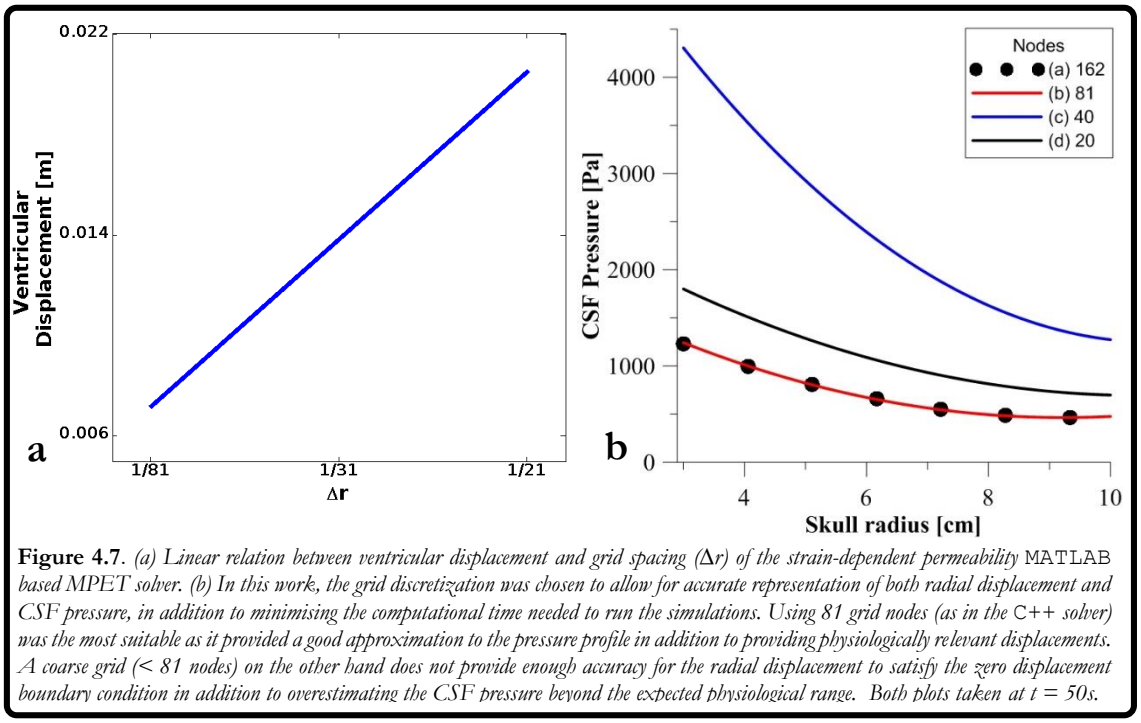

Figure 4.7. *(a) Linear relation between ventricular displacement and grid spacing (Δr) of the strain-dependent permeability* MATLAB *based MPET solver. (b) In this work, the grid discretization was chosen to allow for accurate representation of both radial displacement and CSF pressure, in addition to minimising the computational time needed to run the simulations. Using 81 grid nodes (as in the* C++ *solver) was the most suitable as it provided a good approximation to the pressure profile in addition to providing physiologically relevant displacements. A coarse grid (< 81 nodes) on the other hand does not provide enough accuracy for the radial displacement to satisfy the zero displacement boundary condition in addition to overestimating the CSF pressure beyond the expected physiological range. Both plots taken at t = 50s.*

In this study a grid discretisation with 81 nodes was used for the simulations. This level not only follows smoothly from the previous CFD-MPET coupling methodology, but also produces results that are qualitatively similar to the original MPET displacement profiles. The aim here is not to suffer high computational costs due to an increase in the grid size, whilst producing sound approximations for both displacement and pressure. The CSF pressure profile is in good agreement with the CFD-MPET studies and within the physiological range expected. The variation in the displacement is expected, due to the additional overall stiffness of the system which has been borne out of necessity to accommodate the strain-dependent permeability (which is in exponential form), and the non-linear MPET framework based on a uniformly spaced mesh with half mesh points ($\check{r}_{j+1/2}$). There was added effort to aid the numerical simulations when comparing to a similar effort by Sobey & Wirth (2006) on their SPET model, since the template represented here was given initial conditions based on the original MPET system used in the CFD-MPET coupling to aid with the calculation of the strain at the first iteration.

4.2.2 Aqueductal stenosis

Figure 4.8a provides the predicted values for parenchymal tissue displacement and CSF pressure for varying levels of aqueductal stenosis (1.25 *mm* and 0.8 *mm*) under both a strain independent ($M' = 0$) and strain dependent permeability ($M' = 4.3$) constraint. For the patent aqueduct cases (3 *mm* diameter, $M' = 0$ and $M' = 4.3$), the maximum ventricular displacement was 2.8 and 0.62 *cm* respectively, whilst for the ventricular pressures were 3123 and 1303 *Pa* respectively. The transmantle pressure differences for the same cases was 2267 and 888 *Pa*.

In a similar descriptive format, the mildly stenosed aqueduct (1.25 *mm* diameter) displayed ventricular displacements of 0.55 (*M'* = 0) and 1.17 *cm* (*M'* = 4.3), whilst for the CSF pressure at the ventricles, values of 3799 (M' = 0) and 1840 *Pa* was obtained (*M'* = 4.3). Transmantle pressures of 2763 and 1287 *Pa* were recorded. Finally, for the severely stenosed aqueduct (0.8 *mm*), the values of ventricular displacement for *M'* = 0 and *M'* = 4.3 were 0.48 and 1.19 *cm*, whilst the ventricular pressure was recorded as 3818 and 2318 *Pa*. Once again, the corresponding transmantle pressures of 2777 Pa and 1635 *Pa* were observed for the most severe case.

Table 4.3 depicts the results for fluid increment, radial and effective stresses and fluid velocity. The permutations are level of aqueductal stenosis and three additional simulations based on varying the Biot-Willis parameter, α. All the simualtions compared strain independent and strain dependent permeability for the CSF compartment. As can be seen from the table, the fluid increment tends to increase with increasing stenosis, by up to 78% in the ventricles of the severe strain-dependent case. The strain independent case overestimates the fluid increment in general, and the increase between open and severe cases is approximately 22%. Within the parenchyma (6.5 *cm*), the fluid increment in the strain-dependent case increases by over 68% (between open and severe case), whilst a slightly smaller increase of 61% is recorded for the skull. When considering the radial effective stress, there were great reductions made between open and severe stenosis in the three recorded regions (ventricles, skull and parenchyma), of the order of 80%, 77% and 76% respectively. The tangential stresses varied far less, and for the same regions the percentage changes are approximately 2%, -1% and -2% respectively.

The fluid velocity at the ventricles and the skull is seen to drastically increase from 0.55 to 1.03 $\mu m/s$ and from 0.12 to 0.25 $\mu m/s$. Interesting results can also be garnered when the Biot-Willis parameter deviates from unity. When $\alpha < 1$, the strain-dependent case shows a general trend of increasing fluid increment, tangential effective stress and fluid velocity in all

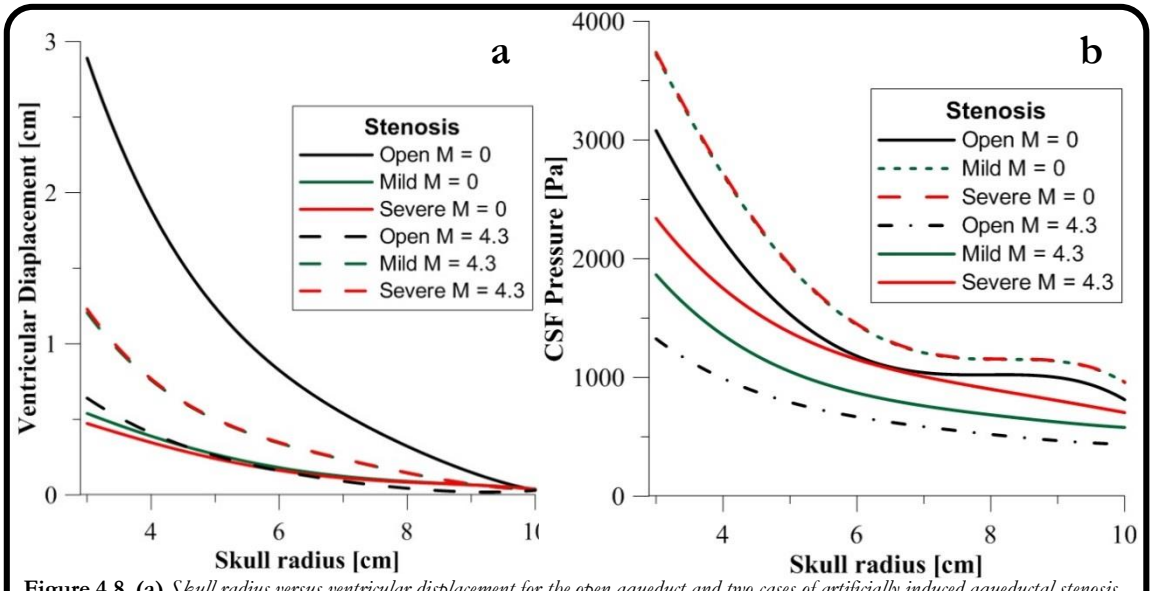

Figure 4.8. **(a)** *Skull radius versus ventricular displacement for the open aqueduct and two cases of artificially induced aqueductal stenosis (mild, 1.25 mm diameter and severe, 0.8 mm diameter). These cases were simulated under the premise of strain independence (M = 0) and strain dependence (M = 4.3).* **(b)** *Skull radius versus CSF pressure for the same cases of aqueductal stenosis. It clear from this plot that the transmantle pressure gradient varies quite significantly between the simulated cases. Both sets were taken after t = 50 s.*

Table 4.3. *The values of ventricular displacement u* (cm), *fluid increment ζ, radial effective stress, σ_{rr}, tangential effective stress, $\sigma_{\varphi\varphi} = \sigma_{\theta\theta}$ and fluid velocity, v. The units for the effective stresses is* Pa and for velocity they are μm/s. *The fluid increment is a dimensionless quantity. The bracketed terms: V, S and P denote values for the* ***V****entricles,* ***S****kull and* ***P****arenchyma (6.5 cm). All values obtained at t = 50s and utilise the deformed radius. M' = 0 or 4.3.*

Stenosis	M	u (V)	ζ (V)	ζ (S)	ζ (P)	σ_{rr} (V)	σ_{rr} (S)	σ_{rr} (P)	$\sigma_{\varphi\varphi}$ (V)	$\sigma_{\varphi\varphi}$ (S)	$\sigma_{\varphi\varphi}$ (P)	v (V)	v (S)
Open	0	2.8	4.8	1.3	1.7	-3575	- 942	-1213	-633	-640	-633	1.9	0.3
Mild	0	0.6	5.8	1.6	2.0	-3867	-1044	-1353	-638	-647	-648	2.0	0.2
Severe	0	0.5	5.8	1.6	2.0	-3876	-1047	-1357	-639	-648	-648	2.0	0.2
Open	4.3	0.6	2.0	0.6	1.0	-1389	-413	-632	-631	-643	-638	0.6	0.1
Mild	4.3	1.2	2.8	0.8	1.2	-2011	-600	-846	-620	-650	-650	0.9	0.2
Severe	4.3	1.2	3.6	1.0	1.6	-2493	-730	-1111	-618	-649	-649	1.0	0.3
α = 0.9	0	0.6	1.6	0.8	1.2	-1059	-720	-476	-580	-582	-583	-0.03	-0.06
α = 0.8	0	0.6	1.6	0.8	1.2	-948	-424	-641	-515	-518	-517	-0.03	-0.06
α = 1.2	0	0.7	1.6	0.8	1.2	-1389	-628	-952	-773	-778	-776	0.03	-0.06
α = 0.9	4.3	1.0	1.8	0.8	1.0	-1093	-593	-476	-579	-576	-580	0.3	-0.1
α = 0.8	4.3	2.0	12.7	7.0	4.1	-6834	-3735	-2174	-504	-507	-510	2.5	0.8
α = 1.2	4.3	0.5	-0.1	0.1	0.02	-1196	-230	-179	-912	-754	-762	0.2	-0.02

of the regions considered, whilst there was a general reduction in radial effective stress. It is interesting to note here that there was a complete reversal in the direction of the fluid velocity at both the ventricles and the skull. However, when α > 1, there was an increase in fluid increment and fluid velocity, but both the tangential and radial effective stresses were lowered profoundly.

4.2.3 Outflow resistance and Parenchymal Source or Sink

Figure 4.9 depicts the results obtained by varying the outflow resistance via the arachnoid granulations by one order of mignitude either side of $R = 8.5 \cdot 10^{13}\ m^{-3}$ along with simultaneously adding either a source ($1.4 \cdot 10^{-6}\ s^{-1}$) or sink ($-1.4 \cdot 10^{-6}\ s^{-1}$) term. A source term of zero magnitude is also compared. It can be seen from Figure 4.9a that any deviation of outflow resistance from the original value generates larger ventricular displacments. All of the curves in the plot decrease to zero, owing to the rigid skull boundary condition. Adding a sink to the parenchymal tissue whilst keeping the ouflow resistance at normal levels generates a large ventricular displacement of 2.6 *cm*. The largest displacment of 3.03 *cm* is witnessed for the case of increased outlow resistance ($8.5 \cdot 10^{14}\ m^{-3}$) and no source term.

A reduced ouflow resistance with the addition of a source term also generates large ventricular displacements of just over 2 *cm*. It is noted that the cases involving both an increased or a decreased outflow resistance but also include a sink term allowed for the values of ventricular displacement to be within the vicinity (6% and 29% increase respectively) of the simulated results for the open aqueduct (0.62 *cm*). Figure 4.9b allows for the evaluation of the transmantle pressure gradient for the same cases as already described. The greatest transmantle pressure gradient (2901*Pa*) was witnessed for the increase in outlfow resistance but with no source. Once again, adding a sink to the original MPET provides a steep gradient of 1422 *Pa*. The lowest gradient of 888 *Pa* was that of the control case ($R = 8.5 \cdot 10^{13}\ m^{-3}$ and Source = 0). A case worth noting is that of an increased resistance along with a sink term. As for the displacment curve, this CSF pressure plot followed that of the control case very closely, however the pressure at the skull and ventricles was lower by 62 Pa and 7 Pa respectively.

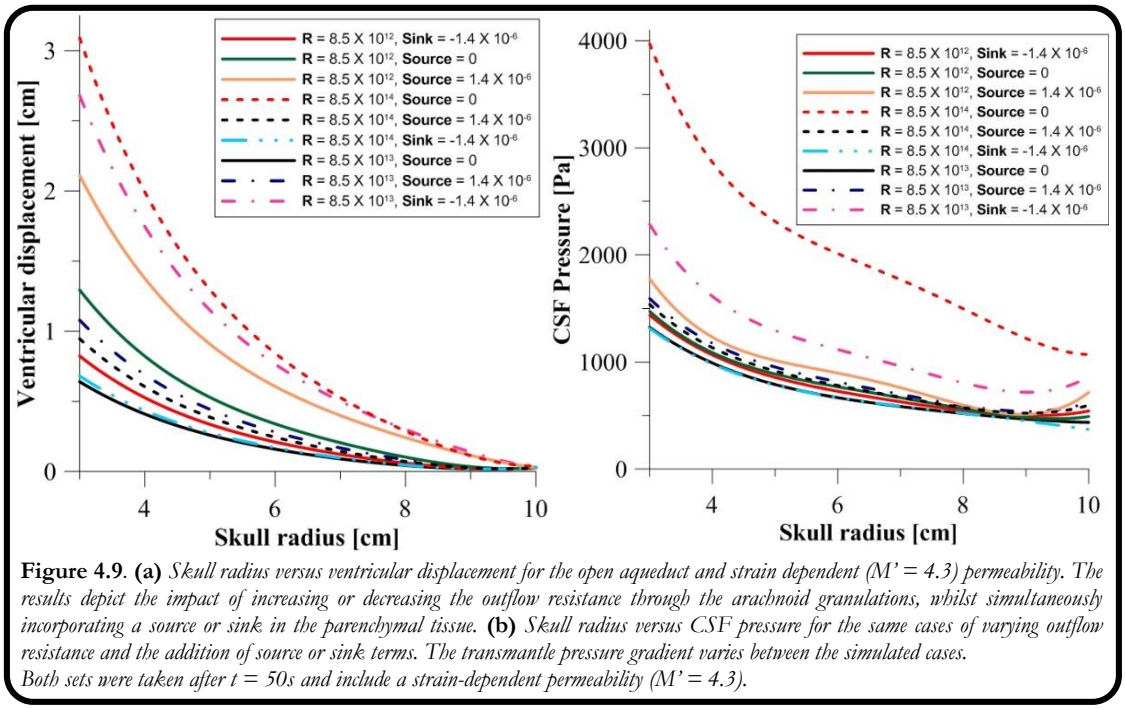

Figure 4.9. **(a)** *Skull radius versus ventricular displacement for the open aqueduct and strain dependent (M' = 4.3) permeability. The results depict the impact of increasing or decreasing the outflow resistance through the arachnoid granulations, whilst simultaneously incorporating a source or sink in the parenchymal tissue.* **(b)** *Skull radius versus CSF pressure for the same cases of varying outflow resistance and the addition of source or sink terms. The transmantle pressure gradient varies between the simulated cases. Both sets were taken after t = 50s and include a strain-dependent permeability (M' = 4.3).*

4.2.4 Varying Parenchymal Source or Sink along with CSF permeability

Figure 4.10 shows the results of ventricular displacement and CSF pressure, outlining the impact of varying both the magnitude of the source, specifically $0.7 \cdot 10^{-6}$ s^{-1} and $1.4 \cdot 10^{-6}$ s^{-1} (or sink, $-1.4 \cdot 10^{-6}$ s^{-1}) term and lowering the permeability of the CSF compartment by up to two orders of magnitude. A sink term representing a value from the MPET simulations ($|\hat{s}_{e \to e}|$ -

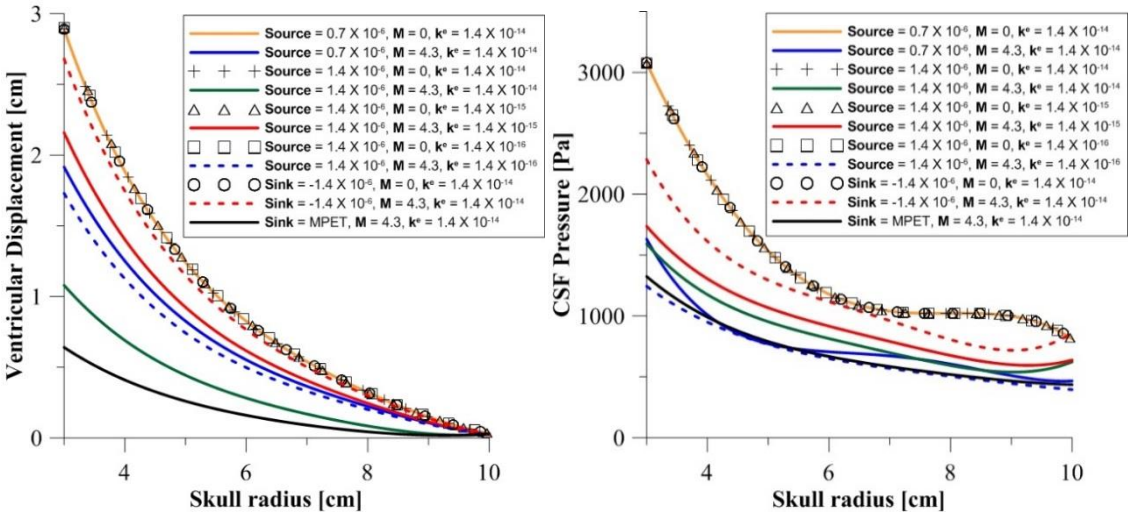

Figure 4.10. **(a)** *Skull radius versus ventricular displacement for the open aqueduct and strain dependent/independent (M = 4.3 and 0) permeability. The results depict the impact of increasing or decreasing the source or sink in the parenchymal tissue and changing permeability (it should be noted that k^e represents the value of k_0 in equation 2.50) for the CSF compartment.* **(b)** *Skull radius versus CSF pressure for the same cases of source or sink terms with changing permeability. The transmantle pressure gradient varies between the simulated cases. Both sets were taken after t = 50s.*

$|\hat{s}_{e\to v}| \approx -9.9\cdot10^{-14}\ s^{-1}$) is also shown as an additional comparator. Consideration is also given to the same cases involving strain independent permeability as a comparison.

What is interesting to note from both figures is that all variations of the strain independent comparators provided the same results. It is clearly evident that for a CSF compartmental permeability of $1.4\cdot10^{-14}\ m^2$, increasing the magnitude of the source term reduces the overall ventricular displacement (from 1.88 *cm* to 1.05 *cm* in the ventricles). This increase of $7\cdot10^{-7}\ s^{-1}$ in source term strength provides a more exotic effect for the CSF pressure. Firstly, the ventricular pressure is slightly reduced from 1535 *Pa* to 1526 *Pa*, whilst the pressure at the skull is increased by a greater amount, from 371 *Pa* to 357 *Pa* respectively. The overall change in transmantle pressure gradient is 195 *Pa* for this small rise in source term strength. In addition, the parenchymal pressure drops below the MPET comparator (sink) between approximately 4.4 *cm* and 5.4 *cm* before it moves back to expected levels at around 7.5 *cm*. It then drops off between 8.7 *cm* and the skull (10 *cm*). When the source term is kept constant ($1.4\cdot10^{-6}\ s^{-1}$) and reducing the permeability by two separate orders of magnitude (from $1.4\cdot10^{-14}$ m^2 to $1.4\cdot10^{-15}\ m^2$ and $1.4\cdot10^{-16}\ m^2$), it can be seen that a one order of magnitude decrease raises the ventricular displacment above 2 *cm*, while decreasing it further actually reduces it to approximately 1.7 *cm*. The CSF pressure in the ventricles displays a similar trend, increasing to 1677 *Pa* and then reducing to 1229 *Pa*. The transmantle pressure gradients are 1099 *Pa* and 840 *Pa* repsectively.

The sensitivity to the sink term is depicted by comparing a drastic change in magnitude (order of 10^{-6} and 10^{-14} in the MPET case). The ventricular displacement here ranges from 2.63 *cm* to 0.62 *cm*, whilst the transmantle pressure is drastically reduced by 38% (1422 to 888 *Pa*). The ventricular and skull pressure on the other hand decreases with decreasing sink strength, from 2161 *Pa* to 1303 *Pa* and from 739 *Pa* to 415 *Pa* respectively.

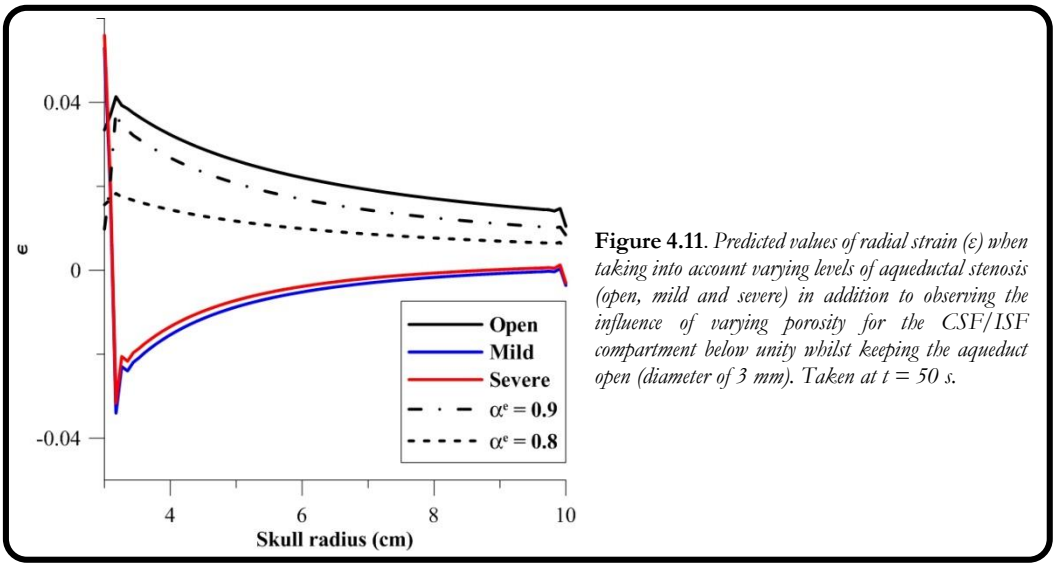

Figure 4.11. *Predicted values of radial strain (ε) when taking into account varying levels of aqueductal stenosis (open, mild and severe) in addition to observing the influence of varying porosity for the CSF/ISF compartment below unity whilst keeping the aqueduct open (diameter of 3 mm). Taken at t = 50 s.*

4.3 Discussion: ESI Multiphysics coupled with C++ solver

In this work, obstructive HCP was investigated via the gradual stenosis of the aqueduct of Sylvius (open, mild and severe), and the occlusion of individual, or a combination of outlets of the fourth ventricle. The physical comparators used to describe the effects of this induced HCP include ventricular displacement, CSF pressure, peak velocities, pressure difference between lateral and fourth ventricle and wall shear stress. These comparators are also used to give an indication of the alleviating effects of the two surgical procedures proposed.

It is evident from the results garnered in this study that the central canal does not simply act as a pathway for CSF flow. Gupta *et al.* [52] speculate that very little fluid passes through this ventricular boundary, and indeed this may seem to be the case under typical aqueductal stenosis (see Figure 4.2, first row). It was found that the peak velocity through the central canal did not exceed 2 cm/s in all cases of aqueductal stenosis, and what was surprising was that this magnitude reduced with an accompanying increase in stenosis severity.

A noticeable difference is seen during the cases of FVOO, where the peak velocity in the central canal exceeded 35 cm/s during the combined occlusion of the bilateral foramina and the foramen of Magendie. The application of both ETV and EFV reduced the impact of the occlusions on the central canal for nearly all cases; however, ETV did so with greater success, as can be seen from the results in Table 4.2. The ventricular displacement was noted to increase with increasing severity of aqueductal stenosis, up to a maximum of 3.28 mm. It should be noted that since the main goal of this work was to compare the efficacy of both ETV and EFV interventions, chronic levels of hydrocephalic development were not pursued here. This is however, within the scope and capability of the methodology [102]. In addition, the CSF pressure abided inversely to this notion, reducing to 968.77 *Pa* in the severe case.

Likewise, applying ETV at the floor of the third ventricle reduces both the ventricular displacement and CSF compartmental pressure to manageable levels. Figure 4.2 (third row) shows the effect aqueductal stenosis has on the WSS. The WSS values increase substantially from the open to the mild and severe cases. The peak velocity is raised 3 and 4 times the value of the open case. Such observations are similar to the results of previous work done on the investigation of flow dynamics undergoing aqueductal stenosis [340,341].

As the aqueduct tries to maintain the laminar CSF flow through the third and fourth ventricle by assisting in repelling the core of central fluid from the aqueductal wall effects [155,340], a pressure difference develops (see Figure 4.2, second row) to help maintain this flow of CSF (rising from around 18 *Pa* to 94 and 241 *Pa* in the mild and severely stenosed cases), and during aqueductal stenosis, gliosis could be perceived to induce the further narrowing of the stenosed perimeter [153,155]. Such pressure gradients are also encountered in the literature [149,302]. During atresia (by translucent membranes) of the bilateral foramina or foramen of Magendie [205,342], the pressure difference between the lateral ventricle cavity and the fourth ventricle remains at approximately 17 *Pa*. The effect that atresia of the fourth ventricular exits has on the CSF flow within the ventricular system is questionable. Provided

that not all of the exits of the fourth ventricle are blocked (i.e. the central canal remains open), the peak aqueductal velocity would decrease by a relatively modest amount (15.0 cm/s), as in the case of the tri-exit closure (bilateral foramina and foramen of Magendie). The bulk flow increase would directly be associated with the central canal, as in the simulated case. The peak aqueductal velocity increased substantially to 35.5 cm/s.

One could appreciate that such a form of pronounced atresia could initiate secondary pathologies to FVOO, such as Syringomyelia. Indeed, recent developments indicate an increase in the expression of AQP4 in conjunction with the level of central canal occlusion and subsequent dilation [343]. This type of disorder could induce various forms of somatosensory impairment, as discussed by Hatem *et al.* [344]. Once the atresia is perforated during EFV, a largely reduced and constant aqueductal peak velocity is recorded. This is a moderate increase from that witnessed for the patent aqueduct. The central canal is alleviated from the burden of having to displace most of the CSF egress. Ventricular displacement is reduced to the same level for all cases of atresia during application of EFV, whilst the CSF pressure is elevated back to a (similar) level to that seen in the case of a healthy individual.

What is interesting is that although the management of the FVOO seems to be commensurate, ETV performed better in comparison, reducing the average peak velocity in the aqueduct for the three cases of atresia, the pressure difference ΔP being reduced further, WSS as well as ventricular displacement. CSF pressure was reduced below the levels expected from an individual with an open aqueduct. This reinforces the view of Mohanty *et al.* [206] that stipulates that ETV should be the preferred treatment for FVOO, whilst reiterating the success of ETV for tetra-ventricular HCP, as described by Carpentier *et al.* [345]. EFV can be deemed as a viable alternative, especially when cases such as the one described by Gianetti [204], where the foramen of Monro and third ventricle did not satisfy prerequisite size constraints for suitable ETV adaptation. It should be kept in mind that the basis of the accuracy of the CSF flow within all four ventricles is entirely dependent on the accuracy of the MRI acquisition process. A less accurate representation of the cerebroventricular system would alter the CSF dynamics, owing to the presently complicated placement of inlets and outlets. The anatomic MRI scans cannot help elucidate the fine surface structures present on the choroid plexuses, as these characteristics are of a scale of μm. The choroid plexus representation is seen in Figure 1.1b.

A simplified boundary condition of 2000 Pa for the arteries was utilised. Unlike previous work, the amount of CSF produced in the lateral, third and fourth ventricles was assumed identical, and not confined to a ratio in terms of total CSF produced. However, there is general agreement that there is no literature outlining the exact proportions of CSF production in the various choroid plexus sites [52], which could potentially significantly alter the CSF dynamics within the cerebroventricular system.

The unique permeability of the CSF compartment (k_e) was relaxed in this study, and given way to a fluctuating adaptation represented by Equation 3.2. The reference pressure was arbitrarily chosen to have a value of 1 kPa. If CSF pressure $P_e < P_{ref}$, then the permeability increases, whilst the converse is true for $P_e > P_{ref}$. Strictly speaking, AQP9 is also found in astrocytes and may possess a synergy in aiding AQP4 [77], however, not much else is known about this aquaglyceroprotein to warrant further consideration in this type of setup. The aim

of this varying permeability compartment was to bring to light a very simple feedback mechanism that would theoretically counteract the effects of ventricular dilation and subsequent elevations of CSF pressure through the efflux of excess CSF to the blood system [346].

The visualisations of the cranio-caudal flow are in good agreement with the categorised CSF flow patterns found using time-resolved 3D PC-MRI velocity mapping, utilising the capture of pathlines from 3D PC-MRI data (no inclusion of driving pressure fields). It should be noted that the aforementioned velocity mappings were not used on any volunteers suffering from hydrocephalic symptoms, and it was stressed that the effect of aging on the CSF flow categorisations could be ignored [337,347].

Stadlbauer *et al.* [337,348] outlined the detailed method of ascertaining the truly complicated nature of CSF flow in a variety of normal and hydrocephalic patients through the extended use of 3D PC-MRI. The segregation of the complicated nature of CSF flow has been attempted here, and their classifications warrant consideration of the ventricular geometry and its finer features, such as the interthalamic adhesion. In order to make inferences regarding the efficacy of EFV and ETV would require a large sample size (~200-300 patient geometries, where this number is comparable in size to geometry libraries obtained in the study of aneurysms, as in the @neurIST project. The project is described at *www.aneurist.org*) to ensure a wide range of geometrical variations are catered for.

One of the main reasons for considering detailed CSF flow categorisations is that areas of interest such as CSF flow diversion techniques (ETV, EFV, shunting, intracerebroventricular drug administration etc.) for treating obstructive HCP, is that one can only benefit from more detailed qualitative (and quantitative where applicable) CSF flow observations and categorisations. For instance, CSF flow dynamics are known to be influenced by the position of the interthalamic adhesion (see Figure 1.1.c), and it has been postulated that it may effect the development of HCP, since the relative position of the adhesion to the aqueduct induced higher pressure gradients in the third ventricle [349].

Levine [149] suggests that a "mini-gradient" of around 133 Pa, combined with irregular tissue compliance may lead to HCP. A similar statement was also expressed by Penn & Linninger [303], where they indicated that only small pressure differences are needed to instigate ventricular enlargement. The conclusions from the aforementioned authors support what has been obtained from conducting these simulations. For aqueductal stenosis, it can be seen from Table 4.2 that the change in pressure between lateral and fourth ventricle increases with degree of stenosis, however once ETV takes place, ΔP drops back to levels similar to pre-stenosis states. During FVOO however, we see a seemingly constant pressure difference of around 20 Pa present. Treating individual cases of obstructed Luschka or Magendie with ETV reduces ΔP to levels below those witnessed by an unobstructed configuration. This could prove to induce adverse therapeutic effects for alleviating the symptoms of HCP, and would prove an interesting scenario to validate experimentally.

The pressure difference between lateral and fourth ventricle indicates an area that requires further investigation. This is especially important for FVOO cases treated with ETV. These show lower than expected levels of WSS and peak aqueductal velocity. Once applied, ETV also manages to increase the CSF velocity in the vicinity of the outlet by an average of

75 $\mu m/s$ in all cases involving FVOO. In the vicinity of the aqueduct, the CSF velocity is reduced by an average of 0.07 cm/s. This is due to the ETV outlet itself having a high CSF exit velocity (~12 cm/s). The simplified ETV outlet boundary condition (0 Pa) will therefore need to be investigated in detail in future work, as its effects are evident. Future work should also include a simultaneous CFD analysis (directly applying boundary conditions from 3D-PC MRI results) of CSF production rates in close proximity to the CPs of the ventricles. It is also predicted that there is strong anatomic correlation to the ETV orientated results, and so the effects of the interthalamic adhesion should be investigated since the velocity is low near the aqueduct when considering this lower portion of the third ventricle. However, aqueductal velocities are much higher in the aqueduct itself, so the bulk of the flow must be heavily influenced from the geometrical aspects of the third ventricle.

The limitations surrounding the proposed MPET model include the use of a linear stress-strain relationship in light of evidently large strains. A spherically symmetric geometry which could theoretically prohibit the interpretation of the order of dilation amongst the various ventricular cavities is also an area for improvement. The simplification to quasi-stationary equations assumes altered pulsatility in the environment and does not play a role in hindering the investigation of properties over the time scale of HCP. In order to more accurately investigate their role, the more general transient equations must be solved. A constant isotropic permeability is also assumed, barring the possible effects of investigations of the diminishing of cerebral blood flow. The use of constant material parameters, such as elastic properties of the parenchyma, compartmental porosity and transfer coefficients is an additional limitation.

The quadruple MPET model introduces an additional ten parameters that are unknown; these are the Biot parameters and permeabilities of the additional blood networks, and the transfer coefficients between the fluid networks. Currently, no suitable experimental data exist and approximations are made through an extensive parametric search detailed in Tully & Ventikos [102]. The permeability, k_e, and Biot parameter, α^e, of the interstitial fluid network are approximated in the literature and we adopt the same values as published in [292]. However, such data are rare for parenchyma tissue and it is well known there are intrinsic difficulties in applying traditional mechanical tests to tissue. Clinical studies show that there is an observable difference in the properties of the white and grey matter [333,350]. There is however, a lack of appropriate experimental data to quantify these differences, hence, many current models treat the parenchyma as a homogeneous tissue [102,106,288,289,295,296,302].

Promising studies using magnetic resonance elastography (MRE) calculate the shear stiffness of cerebral tissue *in vivo*; however, they are yet to establish consistent and agreed values. Evidence of this is that the reported numbers differ by orders of magnitude [328,332,333]. Sack *et al.* [332] assume a homogeneous tissue, and do not account for the inherent differences in white and grey matter. Green *et al.* [351] on the other hand, account for these differences in their calculation of load and storage modulus. This author agrees with others in the field [315] that MRE is dependent on the assumptions already made about the tissue properties, which in turn promote inconsistencies. In addition, the lack of evidence surrounding the acquisition of shear stiffness values via the extrapolation from higher to lower excitation frequencies is also an area of ongoing investigation.

The inclusion of the choroid plexuses in the region of the lateral, third and fourth ventricles, along with a pressure inlet boundary condition of 2 *kPa* (15 *mmHg*) at these locations substantially increased the magnitude of the peak CSF velocity flowing through ventricular cavities, with the most pronounced effect being in the aqueduct. This should be expected as this is the first time that this level of detail has been attached to the inlet boundary conditions of the regionally accurate choroid plexuses, and, in addition, at all CSF producing sites (lateral, third and fourth ventricles) of the ventricular system. The level of porosity and permeability at the surface of the choroid plexuses plays an important role in ultimately determining the egressing CSF velocities; however, there is an evident lack of experimental data surrounding these values. The value of 2 *kPa* for the aforementioned boundary conditions arises from generally accepted pressure values in the relevant conflated feeding arteries. Work conducted by Bammer *et al.* [352] and Wetzel *et al.* [353] allowed for the intracranial arterial hydrodynamics to be elucidated upon through the use of time-resolved 3D PC-MRI and flow sensitized 4D MR. Peak systolic flows of around 71 *cm/s* were found in different vascular segments [353]. For the PCA for instance, which feeds the lateral ventricles, velocities as high as 63 *cm/s* were outlined [352]. Being able to accurately depict the driving mechanisms of CSF production in the form of the choroid plexuses is therefore a difficult task, as this would require the use of pressure fields and therefore pressure boundary conditions. The use of the 2 *kPa* boundary condition is assumed to be a satisfactory starting point to deliver a qualitative understanding of the interplay regarding CSF production. Currently, reliable non-invasive *in vivo* pressure measurements are not commonly obtained, and so this virtual boundary condition was chosen for simplicity, since the subarachnoid space was not taken into consideration.

There is currently no clinical literature that allows for a comparison of the MPET model, with all the sites of CSF production present. It would also be taxing to suggest at this point in time, that a comparison of the ETV and EFV procedures on artificially induced aqueductal stenosis and FVOO be made with clinical data. No MRI obtained velocities exist in these circumstances for such a comparison to be made. Shunting on the other hand, would have proven easier to simulate and compare to, however, there is an exhaustive range of literature using shunting as opposed to ETV as a method of alleviating the symptoms of aqueductal stenosis, and none for EFV alleviating the symptoms of FVOO.

4.4 Discussion: Strain-dependent permeability MATLAB solver

In this section, a new solver is proposed based on a strain-dependent permeability for the CSF/ISF compartment. The analysis of such a system is complex, and it was determined that the best approach in unravelling this complexity was to focus on the compartment in question.

4.4.1 Acute hydrocephalus

The C++ model presented in the previous chapter was linear and quasi-steady, which in essense ignores the superimposed oscillatory component arising from pulmonary , cardiac effects and posture changes. A constant permability was imposed in that model. In this section, the ISF/CSF compartment comprises of a non-linear permeability as a function of the ventricular dilatation. In this section, the early development of acute HCP is assessed (increasing aqueductal stenosis), along with the effects on CSF reabsorption in the parenchyma and SAS.

As was recorded in (§4.2.2), increasing the severity of aqueductal stenosis increases the transparenchymal pressure gradient from 888 *Pa* in the patent case to 1635 *Pa* for the severe case. It is appropriate to mention that the reason the transparenchymal pressures seem amplified is that the parenchyma is not modelled as absolutely compressible (drained Poisson ratio, $\nu = 0.35$ [287] as opposed to 0.5), and, of course, porous, which implies that any pressure against the wall of the cerebral ventricles is more aptly absorbed by the surrounding parenchymal tissue and therefore not fully transmitted to the underside of the skull. This observation is also made by Levine [149]. Overall, it must be noted that the non-linear permeability relationship for the CSF compartment allows for an increasing permeability for parenchymal tension, whilst a decreasing permeability is prevalent for parenchymal compression. In general, the periventricular region allows for a noticeable radially outward compression of the surrounding parenchyma, whilst simultaneously contributing to a circumferential stretch. The combined effect is an increase in permeability close to the ventricles. Rows four through to six in Table 4.3 depict the magnitude of the forces just described. It is visible from the results in this table that both radial and tangential effective stresses also possess transmantle differences (albeit quite small in the tangential cases), however care must be taken to not solely consider the effects at the ventricles and skull alone, and hence the reason for the additional columns relating to relevant variable values in the parenchyma.

In contrast, near the skull it was observed that the level of outward radial compression was reduced in magnitude. Increasing levels of stenosis had a strong influence in the level of radial compression near the skull, however larger differences were apparent within the parenchyma due to ventriculomegaly. It can also be seen from Table 4.3 that the tangential effective stresses show very limited variability when considering aqueductal stenosis and therefore ventriculomegaly, hence the radial component of the effective stress dominates the discussion. Figure 4.11 shows how the strain varies with radial distance from the ventricles to the skull. As can be seen, increased stenosis eventually leads to a reduced permeability in the periventricular region (3-3.5 *cm*). Provided the Biot-Willis parameter in the CSF/ISF compartment $\alpha^e \leqslant 1$, the strain diminishes when moving radially outwards towards the skull. When the compliance changes, and $\alpha^e > 1$, there is a slight radial compression at the skull. At the ventricles on the other hand, there is a sharp drop in permeability, since the radial effective stress in this instant is overwhelming at the ventricles. The transparenchymal pressure gradient between constant ($M' = 0$) and strain-dependent permeability ($M' = 4.3$) is evident in Figure 4.8b, especially when it becomes indistinguishable with increasing stenosis. The extremities

associated with not using a non-linear permeability for the aforementioned compartment are evident in the results for the briefly sigmoidal distributed pressure shown in Figure 4.8b, along with a corresponding erroneous level of ventricular displacement in Figure 4.8a (since increasing stenosis leads to a decreased level of ventriculomegaly). In addition, the variations of radial and tangential effective stresses do not vary significantly with increasing stenosis (see Table 4.3, rows 1-3). Further evidence of compression arises from the decreasing values of fluid content throughout all the simulations. The magnitude of the radial displacement, pressure and strain are similar to those witnessed by Sobey and Wirth [295], however, when considering the MPET based formulation, there is dominant radial compressive stress, as observed by Levine [149,288,289]. The latter investigator confirms the oedematous nature (higher strain and therefore higher permeability) of the periventricular parenchymal tissue during the acute stages of HCP, and owes part of the characteristic to a change in the resistance to CSF absorption at the SAS. This characteristic is now investigated, along with the increasingly accepted reasoning that CSF also gets reabsorbed within the parenchymal tissue.

4.4.2 Efficiency of CSF absorption in the parenchyma and resistance

Considering impaired CSF absorption (Figure 4.9) at the cranial periphery, there is a rise in the transmantle pressure gradient which is proportional to the overall overproduction of CSF, considering no additional sources of production or drainage within the parenchyma. It can be seen that increasing the resistance to subarachnoid absorption can lead to a substantial increase in ventricular displacement and transmantle pressure gradient. On the other hand reducing it by a factor of 10 also provides increases in ventricular displacement and pressure, however, the pressure at the skull is just above what one would expect from a healthy individual. These results correlate well with data from Bateman and Siddique [354], which investigated elevated levels of arachnoid granulation outflow resistance. Their conclusion was that hydrocephalic patients on average possessed smaller sinuses, which corresponded to an increase of R (see Table 2.1) by up to a factor of 2.5. Overall they witnessed an increase in the sinus pressure, which in this work has manifested itself in Figure 4.9b. In addition, the results of Linninger *et al.* [300] also qualitatively validate these findings, as the size of the lateral ventricles increases substantially as the outflow resistance increased incrementally. The latter investigator recorded pressures in the lateral ventricle between ~500-3500 *Pa*, which is in the range of the simulations performed here. The Poisson ratio and Biot-Willis parameter used in the latter study (parenchymal tissue) was 0.45 and 0.3 respectively. The high pressure transmission throughout their simulations is most likely due to the near incompressible value of ν, along with their comparably much higher value for E (10^4 *Pa*). The permeability was the same order of magnitude (10^{-14}). Li *et al.* [308] investigated the effects of poroelastic constants on ICP during infusion tests. They too provide results for their absorption conductance (inversely proportional to R), and reveal that a lower conductance eventually leads to a higher steady-state ICP, with typical values exceeding 4500 *Pa* in the SAS. Porosity and ν were 0.9955 and 0.35 (0.1 in the SAS) for their simulations. E was assigned a value of $3{\cdot}10^4$ *Pa*, whilst the permeability was also much higher in the SAS ($1.4{\cdot}10^{-10}$ m^2) than the grey matter ($1.4{\cdot}10^{-16}$ m^2). Introducing absorption and creation of CSF within the parenchyma in the form of a source and sink term, a deeper analysis of the ventriculomegaly and transmantle pressure gradient is

now possible. The source and sink term is the same as that used in Wirth and Sobey [296]. It is clear from Figure 4.9, that the addition of a source or sink produces results that require further analysis. For instance, a higher value of R (of the order of 10^{14}) accompanied by a source does not correspond to an intuitive additional level of ventricular enlargement or higher transmantle pressure gradient.

A corresponding mechanism for drainage which imposes itself in the form of a sink term provides predictions that are more encouraging. There is evidence that any impairment in arachnoid granulation absorption which is accompanied by ventricular expansion and higher overall ICP is alleviated by such a mechanism. The fluid water content in the parenchymal tissue is speedily reduced by the discharge of the extracellular CSF from this space. In these simulations ζ reduces from 2.3 in the periventricular region to 0.8 as the skull. This is consistent with HCP development since as the ventricle dilate the oedematous periventricular tissue becomes disrupted, and ζ begins to diminish at the cranial periphery since there is a loss of ISF whilst the parenchyma is compressed. A further observation is that in the region close to the dura, there is an attempt to alleviate the high transmantle pressure gradient. This however, could also be a result of poor pressure transmission all the way to the skull, due to the poroelastic properties of the parenchyma. An alternative explanation is that the strain approaches zero at the skull, and therefore the non-linear permeability approximates that of a constant at the region very close to the skull, hence the sudden jump due to truncation error. In general, the scheme presented in this section provides clinically acceptable results for higher values of E (9010 *Pa*), with ventricular displacement at 0.3 *cm* (stable after only 4 *s*), a lower transmantle pressure difference of 712 *Pa* (reduces as ν is increased), and a stable periventricular fluid content of 0.39 (after 5 *s*). The condition number of the system matrix is also far more stable throughout the course of the simulations at higher values of Young's modulus. The relative residual of the compartmental pressure equations can drop to between 10^{-25}–10^{-30} in as little as 3 iterations under values of $E \geq 9$ *kPa*.

The sensitivity of the MPET system to source terms is quite high, which at first sight may be welcome news for such a multiscalar system. In order to investigate this further the magnitude of the source/sink terms was kept at 10^{-6} s^{-1}, in line with a similar assessment by Wirth and Sobey [296]. The specific values of the source terms were $0.7 \cdot 10^{-6}$ s^{-1}, $1.4 \cdot 10^{-6}$ s^{-1}, whilst the sink terms were $-1.4 \cdot 10^{-6}$ s^{-1} and $-9.9 \cdot 10^{-14}$ s^{-1}. The base permeability was also decreased by factors of 10 and 10^2 respectively. The results are displayed in Figure 4.10. In these results, it is interesting to note the lack of sensitivity to the source and sink terms when considering a constant permeability ($M' = 0$). Slight variations in base permeability and the magnitude of the source/sink term ultimately have no effect on the solution curves in both displacement and pressure. It becomes increasingly apparent that alternating the size of the source/sink alone does not bring about intuitive effects. When the understanding is combined with the base permeability however, it becomes clear that the overall response of this system is heavily tied upon the strain, even at this minute level. The inherent inclusion of strain in the pressure equations shows that reducing the base permeability whilst keeping the production of CSF within the parenchyma active increases the transmantle pressure gradient. When the base permeability becomes too small (of the order of 10^{-16}), the combination with a source has adverse effects, and indeed, reduces the level of the pressure gradient in the cranial space below

the MPET control. A sink reduces both the pressure gradient and overall displacement when compared to the strain-independent case ($M' = 0$), however not at the level that would be expected.

It is thus not clear from the results garnered thus far whether a barrier to CSF drainage results in the pathogenesis of HCP development. A rather alternative approach to examining the specific pathogenesis of ventriculomegaly is also given by Wilkie *et al.* [307]. These investigators echo the notion that it is unlikely that hydrostatic pressure gradients are solely responsible for fluid absorption. They stipulate that the occurrence of ventriculomegaly must include an understanding of the more intricate roles of osmotic pressure and AQPs. They also stipulate that elasticity, permeability and absorption coefficients are related to β_1 integrin interaction in the parenchymal tissue.

4.4.3 The effect of compliance

As postulated by Levine [288], and then later by Wirth and Sobey [296,355] and Tully and Ventikos [102], compliance (the CSF volume pressure ratio) plays an important role in aiding the understanding of fluid content change for varying ventricular dilatation under isobaric conditions. The aforementioned investigators used compliance as a means of assimilating not only the changes in the increment of fluid content, but also a change in blood content within the brain vessels. For a Biot-Willis parameter equal to unity, this implies that a change in volume does not affect the blood content. In this section of the thesis, it was mentioned earlier that only the CSF compartment was taken under consideration, in order to facilitate a deeper understanding of the effects of strain (and therefore permeability) being incorporated into the system. When $\alpha^e < 1$, there is an increase in fluid content and ventricular wall displacement (from the boundary condition relating to continuity of stresses, Equation 3.7) for a given open aqueduct. As can be seen from the results in Table 4.3, there is a steep increase in fluid content throughout the parenchyma and the periventricular region as compliance is increased, since the imposing ventricular pressure is not balanced by the interstitial pressure and instead mimics a force seeking to be balanced by the elastic matrix. Overall, these are qualitatively similar to the results obtained by Wirth and Sobey [296,355] and Tully and Ventikos [102]. It is also worth mentioning that strain is tensile (however it does tend to diminish towards the skull) when $\alpha^e < 1$, as can be seen in Figure 4.11. The importance of compliance in the vicinity of this Biot-Willis parameter (α^e) range is important to consider, especially in pathologies such as NPH and BIH.

When $\alpha^e > 1$, the level of ventricular displacement rises substantially, as can be seen in Table 4.3. The transparenchymal pressure gradient is substantially lower than in any other previous simulation, 85 *Pa*. This simulation was conducted over 50 *s*, as in all other previous simulations. Wirth and Sobey [355] note that the displacement profile when $\alpha^e = 1.2$ is negative, along with a constant pressure profile. They do not indicate after how long their simulations are executed for; considering that there is an evolution in the ventricular displacement, this is an important omission. In the early stages of BIH development, negative displacement profiles are also obtained (there is a ventricular displacement of -0.27 *cm*), however depending on the length of time chosen to run these simulation, this profile disappears quite rapidly (after 5 seconds in this case). The fluid increment in the case of Biot-

Willis parameter $\alpha^e = 1.2$ shows very little variation, in contrast to the previous simulations. The non-linearity of this system is once again apparent, since considering the same case involving constant permeability reproduces very different results.

4.4.4 A note on the solver

The theoretical development of this model allows for the justification of the need to incorporate more complex relationships for the important variables in the model, such as permeability. This not only introduces new layers of complexity in the MPET framework, but also allows for a greater degree of qualitative and quantitative differentiation between different disease causalities. In these simulations, the level of ventricular displacement is, in general, amplified when comparing the similar curves (the case of a stenosed aqueduct for example) using the `C++` solver. For example, a severe stenosis reproduced 3.28 *mm* of ventricular displacement, whilst in the strain-dependent permeability simulations, this was 1.2 *cm*. The pressure profiles are also not as smooth. Such levels of discrepancy and error are expected, especially since the `C++` solver only involved one *LU* decomposition.

The non-linear MPET solver (see Figure 3.4) on the other hand required a blend of results obtained from the `C++` solver which was coded in `MATLAB` in order to provide the initial conditions, two *LU* decompositions along with a series of six combinations of the Transpose-free quasi-minimal residual method (`TFQMR`), with suitable preconditioning acquired from a separate *LU* decomposition of the specific coefficient matrix at the required loop. A tolerance level of 10^{-40} with a maximum iteration count of 20 000 was conservatively chosen for the `TFQMR` method. The pressures are solved using the deformed radius at every uniform time step ($t_k = k\Delta t$), and then used in the displacement equation which also serves as the driver for the strain (ε). The strain is calculated using a central and backward/forward difference schemes at each node. There are also three levels of interpolation used in this solver, one for the strain when used to interpolate for the pressures at $\check{r}_{j+1/2}$, and once again to obtain r_i when required for the displacement computation. The numerical scheme presented here possesses a derivative (1^{st}) boundary condition for the ventricles, and so is first order accurate, since the error and displacement vary linearly with mesh size. Of course, using pure Dirichlet conditions for all the compartments (pressure and displacement) the scheme presented here becomes second order accurate, since the truncation error is of second order.

4.5 Results & Discussion: FEM

4.5.1 The 1D-FEM MPET template

In Figure 4.12, it can readily be seen that the results for mesh independence are conclusive for the optimal 1D template (Figure 4.12a). Here, decreasing the grid size reduces the overall displacement curves in a roughly linear manner. As can be seen from the same figure, the level of ventricular displacement levels off at a grid size of 6000. In contrast, Figure 4.12b shows the effect of decreasing the Biot-Willis constant of the CSF/ISF compartment. The implication of using a very coarse mesh in the 1D simulations, for instance, using $\Delta x = 81^{-1}$ *cm* as in the previous chapter, would result in negative ventricular displacements. The curve remains negative until $\Delta x = 160^{-1}$ *cm*. It is therefore recommended to use a finer grid for mild changes in this compartmental constant in comparison to previous simulations, since decreasing any of the Biot-Willis constants should always increase the respective ventricular displacement.

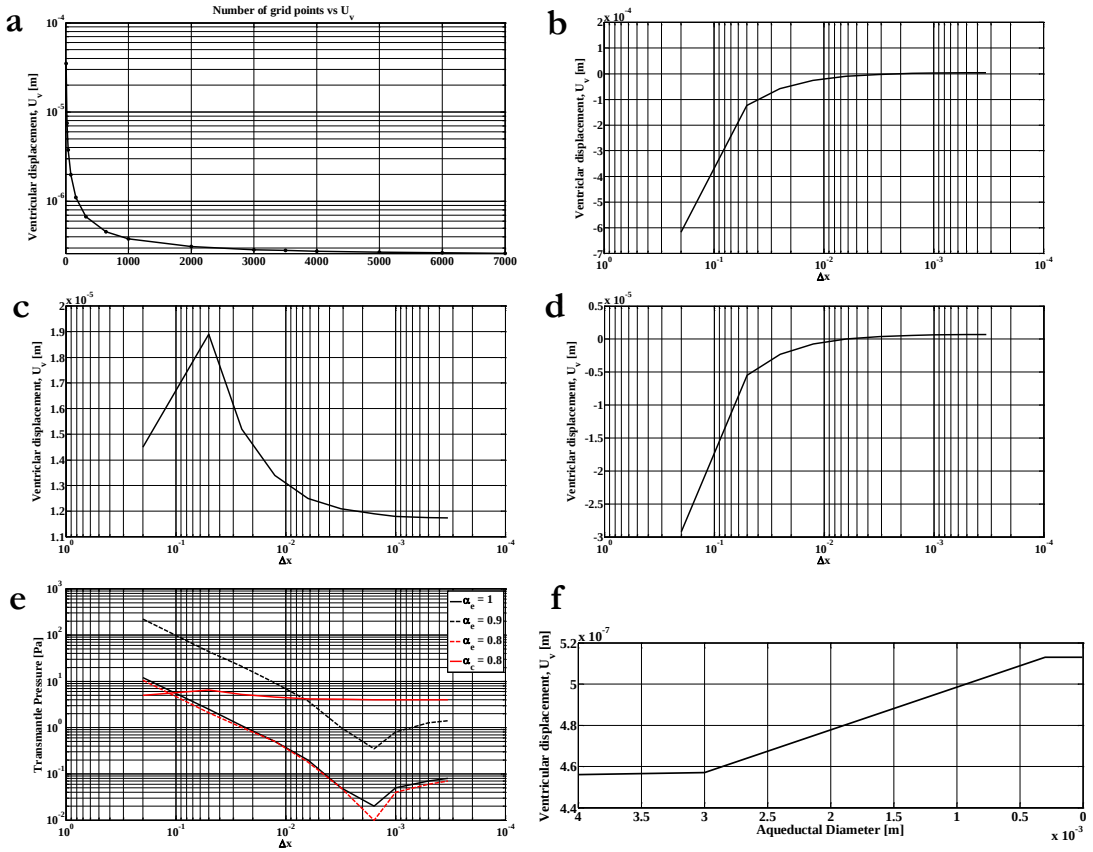

Figure 4.12. *(a) Shows the ventricular displacement versus grid spacing for the case where all compartments possess Biot-Willis constants of unity. (b) The effect of altering the Biot-Willis constant on the CSF/ISF compartment. Here* $\alpha^e = 0.9$. *All other porosity constants are kept at unity. (c)* $\alpha^e = 0.8$. *(d) In this case, the Biot-Willis porosity constant of the capillary compartment (*α^c*) is reduced to 0.8, whilst all other compartments remain at unity. This plot emphasizes the sensitivity of the ventricular displacement to alterations in porosity at different compartments. (e) In this plot, the effect of the transmantle pressure gradient is investigated for a decreasing grid spacing. This is done for the same changes in porosity described for the other plots. (f) The effect of reducing the aqueductal diameter from a patent case (4 mm) to a fully occluded aqueduct (0 mm).*

Once again, a steady U_v is reached for very fine grid refinement, indicated by the levelling off of the curve at 0.7 *μm*. Figure 4.12c shows that reducing the magnitude of the same constant further brings back U_v to positive bounds. The only point of interest here is that the model performs erratically for extremely coarse grids, and has the ability to overestimate the displacement if $h < 20^{-1}$ *cm*. As a comparison, Figure 4.12d shows the effect of reducing the Biot-Willis constant of the capillary compartment to 0.8. Here, the curve levels off at a ventricular displacement of 4.5 *μm*. A positive curve is obtained when $h = 640^{-1}$ *cm*.

As opposed to just considering the effect of Biot-Willis changes and grid spacing on displacement (and U_v in particular), the effects on the CSF transmantle pressure gradient were also investigated. As can be seen from Figure 4.12e, the sensitivity of the gradient to grid spacing possesses a similar trend to that of U_v, namely a decreasing gradient with increasing refinement.

There seems to be an underestimate of the gradient for fairly fine grids ($160 < h < 200$), before the magnitude levels off at $h < 3000^{-1}$ *cm*. The effect of the magnitude of the gradient to specific Biot-Willis parameters is also shown. A fairly constant CSF pressure gradient of approximately 4-5 *Pa* is obtained irrespective of grid spacing when α^c drops to 0.8.

When α^c is reduced by 10%, the gradient levels off at 1.4 *Pa*, whilst a 20% increase allows for a gradient of 0.07 *Pa*. What is interesting is that for grids with a size of approximately 160 nodes, there is an overlap of curves between values of porosity between different compartments. This emphasizes the sensitivity of the CSF pressure in the 1D system to changes in porosity in combination with the degree of mesh refinement.

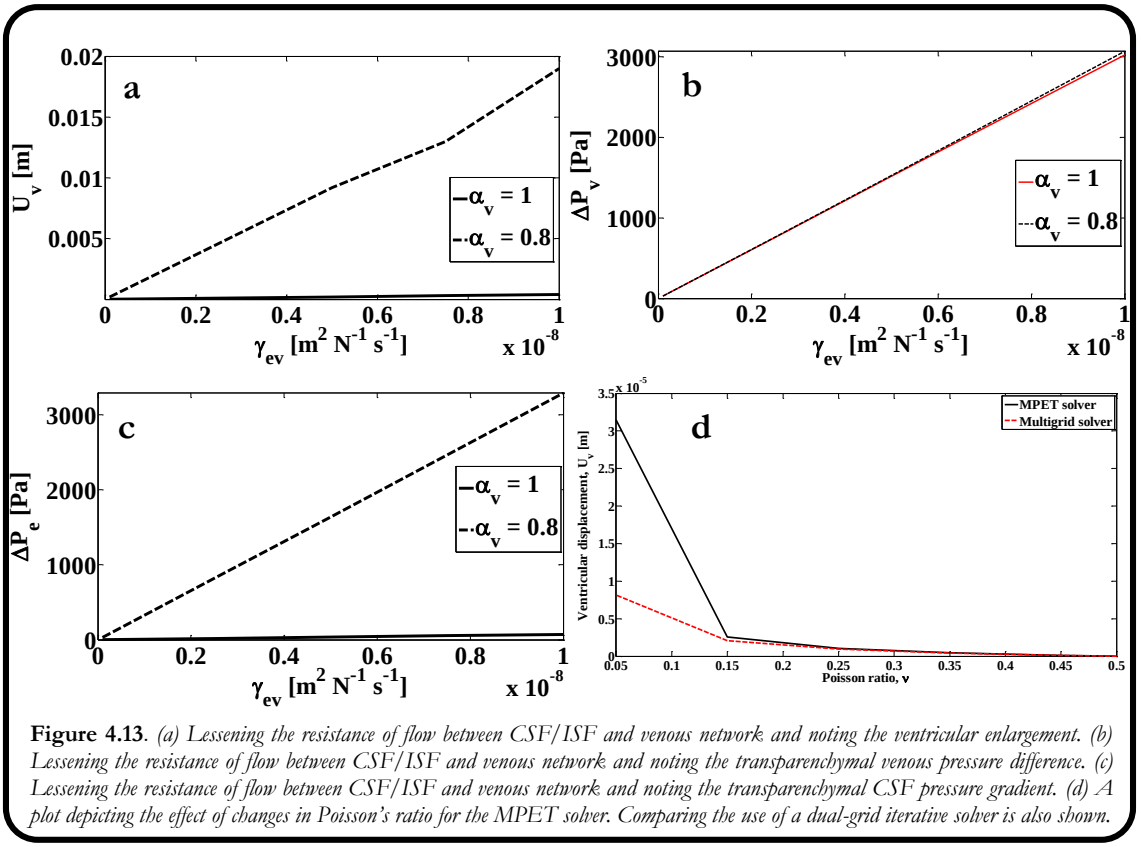

Figure 4.13. *(a) Lessening the resistance of flow between CSF/ISF and venous network and noting the ventricular enlargement. (b) Lessening the resistance of flow between CSF/ISF and venous network and noting the transparenchymal venous pressure difference. (c) Lessening the resistance of flow between CSF/ISF and venous network and noting the transparenchymal CSF pressure gradient. (d) A plot depicting the effect of changes in Poisson's ratio for the MPET solver. Comparing the use of a dual-grid iterative solver is also shown.*

Finally, it can be seen in Figure 4.12f that reducing the aqueductal diameter produces in increasing U_v The plot indicates a fairly constant ventricular displacement for diameters smaller than 0.3 *cm*.

Figure 4.13a-c depict the influence of mimicking an imposed breakdown of the blood-CSF barrier responsible for clearance though the variation of γ_{ev} within the ranges discussed by Tully & Ventikos [102], whilst keeping all other constants at the same value as in the healthy state. The measured quantities were ventricular displacement, transparenchymal venous pressure gradient and transparenchymal CSF pressure gradient. In addition, the compliance of the venous network was also altered and the same quantities measured. In all cases, increasing the magnitude of γ_{ev} resulted in an increase in the measured response, whilst altering the compliance proved to markedly alter the rate of change of displacement and CSF pressure gradient. The peak ventricular displacement for the value pair of altered compliance (1, 0.8) was (4.12 *mm*, 1.9 *cm*), whilst for the venous and CSF pressure gradients this was (3.02 *kPa*, 3.07 *kPa*) and (73 *Pa*, 3.29 *kPa*) respectively. Figure 4.13a-c can also be deemed to depict the influence of a breakdown in the clearance mechanism proposed by the paravenous pathway of the glymphatic system [98,376] with and without changes in venous vessel compliance. As can be seen from these figures, altering the amount of water that is permitted to flow between the aforementioned compartments can accelerate ventriculomegaly, which can prove detrimental in the acute stages of hydrocephalus and/or prove to influence the pressure field in the respective compartments enough to stimulate the onset of NPH. Venous compliance on the other hand, proves to be more elusive since, although it stimulated accelerated ventriculomegaly and CSF pressure gradients in the parenchyma, the influence on the venous network seems minimal. This is however, worthy of further consideration since this setup can prove to go beyond the clinical reasoning behind NPH. Unlike in previous work, where the incorporation of the influence of AQP4 was difficult to allude to, there is now a plethora of evidence to suggest that this specific AQP channel is responsible for a more definite understanding of mechanisms underlying water homeostasis in the brain [377]. The addition of electron microscopy in the assessment of biopsies of patients that were clinically diagnosed with congenital hydrocephalus, Arnold-Chiari malformation and post-meningitis hydrocephalus also display breakdown in the blood-brain barrier [216]. This ultimately corresponded to enhanced swelling characteristics in the perivascular space and astrocytic end-feet.

Figure 4.13d depicts two plots of U_v versus Poisson ratio, one solved using the conventional `TFQMR` solver method, whilst the other utilises a dual-grid solver. As can be seen from this figure, the area of stringent comparison is that of $v < 0.15$, in the region of incremental lateral expansion under the influence of compression.

The influence of Poisson's ratio is quite important, as dictated by the degree of emphasis in previous studies [268,378]. It has also been the topic of much controversy, especially when considering the flawed consolidation model of Nagashima *et al.* [285], where the value used approached complete incompressibility. Dutta-Roy *et al.* [272] confirm the need to distinguish between different values in different multi-phase consolidation models, and it should be noted that the value used in the simulations described throughout this report is a widely accepted value of 0.35 [102,106,263,272,274,287,288,292,295,296,302,350]. The use of

the dual-grid solver was developed in order to distinguish between possible over (which could be as high a multiple (over 3 times) as that depicted in the figure) or under prediction of the ventricular displacement. It is clear from figure 4.13d that the more compressible the solid matrix is, the larger the degree of variability. It is also proof that using a small-strain approximation to account for the ventricular enlargement has its limitations when considering compressible materials, especially if no refinements are made to the solver. In the range of v most likely to be used ($0.25 < v < 0.45$, assuming a more compressible nature to higher compartmental systems than biphasic models [269]), using the preferred `TFQMR` solver shows adequate overlap in numerical accuracy in order to be deemed appropriate. If the lower bound of this range is reduced further, it is evident that the possible error associated with the solution increases as $v \to 0$. To dampen the lower and higher frequency content of the error, the use of multigrid methods is recommended. The remainder of this work does not extend on the 1D application, as its scope is beyond the requirements of this work. Instead, its usefulness and easy applicability is shown on posing the legitimate question of what to do when faced with the challenge of a compound set of elasticity parameters with given computational resources (multigrid methods tend to possess less residual variation with increasing mesh refinement than one would expect, in addition to better performance for non-linear problems [379]), as will be the case in the VPH-Project (which is described at the end of this chapter). In the aforementioned project, MR Elastography and DTI are combined in order to assess the anisotropic elasticity of parenchymal tissue. In the paper by Qin *et al.* [380], a similar procedure is described for a phantom study, where the transversely isotropic model that is described portrays very clearly the influence of the compressional moduli on the stress tensor. A similar influence exists in the development of the isotropic model represented in this work, since the matrix notation developed for the FEM template in the variational formulation of the displacement equation in $\mathbb{R}^2$ and $\mathbb{R}^3$ consists of:

$$\begin{aligned}
&\sigma = \begin{bmatrix} \sigma_{11} & \sigma_{22} & \sigma_{33} & \sigma_{12} & \sigma_{23} & \sigma_{31} \end{bmatrix}^T \ \& \\
&\varepsilon = \begin{bmatrix} \varepsilon_{11} & \varepsilon_{22} & \varepsilon_{33} & 2\varepsilon_{12} & 2\varepsilon_{23} & 2\varepsilon_{31} \end{bmatrix}^T \ \therefore \ \text{since} \\
&\sigma = \Phi\varepsilon, \text{where:} \\
&\Phi = \begin{bmatrix} \lambda+2\mu & \lambda & \lambda & 0 & 0 & 0 \\ \lambda & \lambda+2\mu & \lambda & 0 & 0 & 0 \\ \lambda & \lambda & \lambda+2\mu & 0 & 0 & 0 \\ 0 & 0 & 0 & \mu & 0 & 0 \\ 0 & 0 & 0 & 0 & \mu & 0 \\ 0 & 0 & 0 & 0 & 0 & \mu \end{bmatrix}
\end{aligned} \tag{4.76}$$

where one then proceeds with the above matrix form (in $\mathbb{R}^3$) to facilitate the representation in the FEA and finally the strain and stiffness matrix and load vector.

In $\mathbb{R}^2$, there is differentiation between plane stress (last three components of stress tensor in (4.76) are equal to zero, and $\varepsilon_{33} = -(\sigma_{22}+\sigma_{33})(v/E)$) and strain (last three components of strain tensor in (4.76) are equal to zero, and $\sigma_{33} = v(\sigma_{11}+\sigma_{22})$) by augmenting the constitutive law above in (4.76) as such:

$$\widehat{\Phi}_{|\varepsilon} = \begin{bmatrix} \lambda+2\mu & \lambda & 0 \\ \lambda & \lambda+2\mu & 0 \\ 0 & 0 & \mu \end{bmatrix} \quad \& \quad \widehat{\Phi}_{|\sigma} = \frac{E}{(1-\nu)(1+\nu)} \begin{bmatrix} 1 & \nu & 0 \\ \nu & 1 & 0 \\ 0 & 0 & (1-\nu)/2 \end{bmatrix} \tag{4.77}$$

4.5.2 The 2D-FEM MPET template

Figure 4.14a shows the curve of U_v versus h_{max} for the 2D template applied on the annular geometry. As expected, using smaller elements reduces the magnitude of U_v fairly predictably. The smallest value of h_{max} on this plot is 0.003 *cm*, with a corresponding value of U_v of 5.86 *μm*. The coarsest grid of maximum side length 10^{-1} *cm* produces a U_v of 6.34 *μm*. Table 4.4 summarises the results of the plot, with added fields for the number of points (*np*), edges (*ne*) and triangular elements (*nt*). In Figure 4.14b (accompanied by Table 4.5), the influence of allowing `MATLAB` to refine the geometry where appropriate (namely anywhere with curvature) as opposed to enforcing a maximal side length is also shown. As can be seen from the plot and the table, a Level 3 mesh is optimal. This level of refinement is used throughout the 2D simulations.

As in the 1D case, the variation of U_v with v was sought, and the near linear plot in Figure 4.14c shows the ability of the 2D-MPET template to reproduce changes in Poisson's ratio without any abrupt regions, as was the case in the 1D-method. The use of a multi-grid solver was not deemed necessary in any higher (spatial) order calculations. It is also interesting to note that increasing the compliance by 20% increases the ventricular dilation to 74.8 μm when v is 0.4 and 1.9 mm when v is 0.1.

Figure 4.14d discloses the expected variation of U_v with alterations in the compliance of a compartment. In this case, the capillary compartment was used to depict the response. It should be noted that altering any of the porosity parameters from the various compartments has the same effect, owing to the type of boundary condition used in the MPET framework.

Table 4.4. *A comparison of maximum edge size and the annular mesh data, namely number of points, edges and triangles. In addition, the ventricular enlargement is also provided.*

h_{max}	n_p	n_e	n_t	U_v [μm]
0.1	56	24	88	6.37
0.05	56	24	88	5.93
0.005	2026	166	3886	5.89
0.004	3125	208	6042	5.89
0.003	5619	274	10964	5.86

Table 4.5. *A comparison of levels of regular refinement and the corresponding annular mesh data, namely number of points, edges and triangles. In addition, the ventricular enlargement is also provided. The regular refinement allows for all of the specified triangles to be divided into four triangles of the same shape.*

Refinement (h_{max} = 0.1)	n_p	n_e	n_t	U_v [μm]
L0	56	24	88	6.37
L1	200	48	352	6.33
L2	752	96	1408	5.95
L3	2912	192	5632	5.89
L4	11456	384	22528	5.89

In addition, any changes in the initial conditions of the ventricular displacement get amplified proportionally. Specifically, increasing these initial conditions by n orders of magnitude yields a proportional change in U_v.

Figure 4.14e-g depicts the variation of ventricular displacement with transparenchymal distance for the peanut geometry at different degrees of compliance. Increasing the compliance (reducing the porosity) amplifies the ventricular displacement substantially, from 7.2 μm in the healthy case to around 0.6 mm when the capillary compliance is increased to 0.8. As in Wirth & Sobey [296] and Tully & Ventikos [102], reducing the Biot-Willis constant can be inferred as evoking NPH. The effect of this porosity reduction in essence means that there is a larger proportion of force exerted on the solid matrix and in doing so the ventricle walls, as is evident by the boundary conditions in equation (2.49), allow for an increased ventricular dilation for the same given CSF pressure boundary conditions at the ventricles and skull. Figure 4.14g shows how BIH can be mimicked by decreasing the compliance (increasing the porosity) below the healthy level. As can be seen, a significant ventricular compression is achieved for a 20% decrease in compliance.

The compression characteristics are similar to those described by Wirth & Sobey [296], however the rate of compression is higher in these simulations. This is because the source term used by the aforementioned authors was of the order of 10^{-6}, whilst the typical order in the MPET model was much higher (10^{3}) due to the values of the respective transfer coefficients, relevant permeability values forming the source term for the CSF/ISF compartment and of course the pressure gradient administering the level of directional fluid transport. Finally, figure 4.14h portrays the smooth pressure gradient simulated through the arteriole/capillary compartment. As can be seen, higher gradients exist in the parenchyma, with the two peaks possessing a value of 76.7 μPa. The small gradient exists by mere virtue of the small magnitude of the Neumann boundary condition in equation (2.55), which is of the order of 10^{-5} Pa on the ventricle. Coupling this with the Neumann condition in equation (2.58), the quasi-steady MPET derives a solution expected from such a PDE dictated by Neumann conditions on both boundaries. The contour plot of the pressure gradient along with the overlapping quiver plot of gradient direction shows the steep gradient closer to the respective boundaries. A point of sizeable importance is that in the work by Tully & Ventikos [102], the boundary condition in the 1D template replaced that of (2.58) with the arterial pressure of 100 $mmHg$ in order to legitimately isolate the numerical error captured in the transition from the arterial to arteriole/capillary compartment via the penalization of afflicting numerical oscillations (the source terms do not help stabilise the solution as they were typically of the order of 10^{-1}), hence the higher order of magnitude portrayed in the publication.

In the work discussed here, this constraint may be alleviated since the FEM template is superior in handling any form of boundary conditions, namely Dirichlet, Neumann or Robin. The transmission of error between fluid compartments is also better isolated due to the loop structure adopted, and the quality of the discretisation, which ultimately plays a large role in the overall accuracy of this multi-compartmental model. The notion of mesh quality will be discussed shortly.

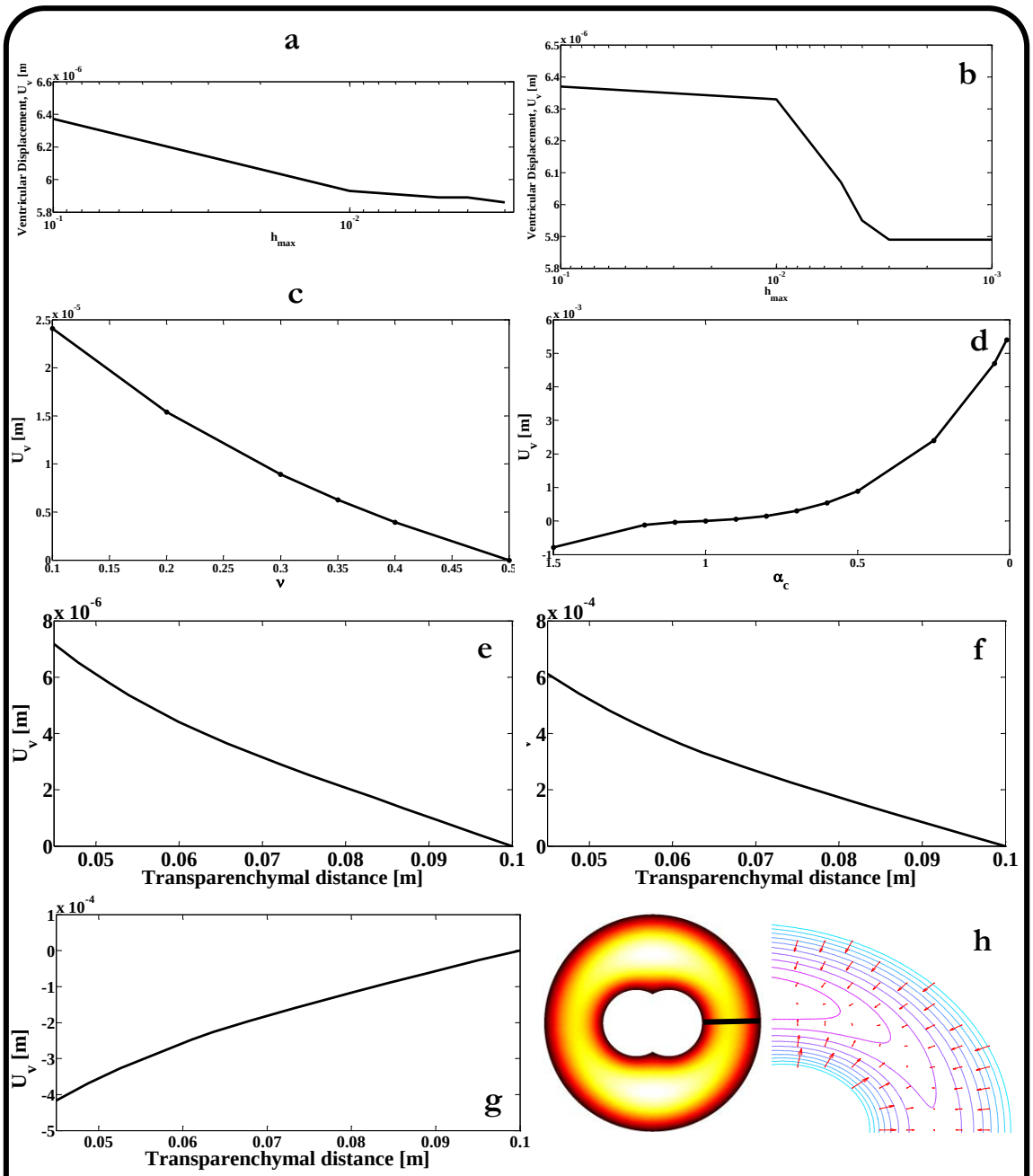

Figure 4.14. *(a) The curve of U_v versus h_{max} for the 2D template applied on the annular geometry (b) The influence of allowing MATLAB to refine the geometry, U_v versus Levels of refinement (in terms of approximate h_{max}) . (c) The variation of U_v with Poisson's ratio, ν. (d) The variation of U_v with alterations in the compliance of the capillary compartment. (e) The variation of U_v with transparenchymal distance (east facing) for the peanut geometry when α^e=1. (f) The variation of U_v with transparenchymal distance (east facing) for the peanut geometry when α^e=0.8. (g) The variation of U_v with transparenchymal distance (east facing) for the peanut geometry when α^e=1.2. (h) The capillary pressure gradient (higher in the lighter areas) and its associated contours. The black solid line indicated the east facing transparenchymal distance used to construct the plots e, f and g. A quiver plot (vectors) is also mapped on the capillary gradient to indicate gradient direction.*

Figure 4.15a-b shows the Delaunay triangulation over the annular geometry and the associated quality of the simplices. The mesh used to conduct these simulations was a Level 3 mesh (details in Table 4.5). As can be seen, the degree of refinement increases from the skull towards the ventricles. Figure 4.15c shows the arteriole/capillary pressure gradient with a Level 2 mesh, whilst Figure 4.15d magnifies the eastern segment of the pressure solution. Figures 4.15e-h show the annular geometry used to obtain solutions for the Darcy velocity of each fluid compartment. The negative sign represents the notion that flow will take place opposite to the direction of increasing pressure gradient, and is therefore interpreted differently for each compartment. The main element to consider is that the ratio of Darcy permeability and viscosity is the same for the arterial, arteriole/capillary and venous compartments ($5.24 \times 10^{-12}\ m^4/Ns$), whilst that of the CSF/ISF compartment is slightly higher at ($1.57 \times 10^{-11}\ m^4/Ns$). Both the permeability and viscosity for each compartment remain constant in each compartment. It is important to consider that the pressure gradient dictates the magnitude of the velocity, and therefore strongly dependent on the boundary conditions at the skull and ventricles. Putting the CSF velocity into perspective, the peak velocity was found to be 1.45 μm/s at the ventricles and in the direction from skull to ventricles. This value is of the same order of magnitude (μm/s) with fluid velocity distributions in other studies [296,299,304]. An evolving ventricular pressure boundary condition implies that eventually the flow direction reverses. In Figures 4.15e-h, a mesh of slightly lower density was used (by increasing the value of the maximum side length requirement before Level 3 refinement). This was done to emphasize the sensitivity of the mesh quality to the final solution. Since the ratio of permeability to viscosity is constant, the influence of the mesh quality on the pressure gradient should be readily apparent. Even for simple geometries such as two concentric circles, the influence of sporadic triangular inequality in the Delaunay triangulation (see the blue shading in Figure 4.15b) is enough to contaminate the scalar pressure field when Dirichlet boundary conditions are used. In addition, the directionality of the velocity changes if the ventricles are at a lower pressure in comparison to the skull. The capillary velocity on the other hand (which depends on the modified gradient discussed earlier), shows an elegant smoothness due to the use of Neumann conditions at both the skull and the ventricles.

Figure 4.16 shows a comparison of the simplex quality based on `DistMesh`'s radius ratio [359] and the metric used in the `MATLAB` simulations throughout:

$$Q_\Delta = 4\eta_\Delta\sqrt{3}\left(\chi_1^2+\chi_2^2+\chi_3^2\right)^{-1} \tag{4.78}$$

In the above equation, η_Δ is the area of the Delaunay triangle, and χ_i is the side length. Any value of $Q_\Delta < 0.6$ indicates an unacceptable quality [381] level (see Figure 4.15b). As can be seen from this figure, increasing the level of refinement greatly increases the quality when using the aforementioned metrics. In both cases, a simplex equal to unity denotes an isosceles triangle, with increasing degeneration for lower values. The importance of mesh quality in relation to accuracy, stability and of course convergence in a PDE solver such as the one created in this template is discussed in more detail by Park & Shontz [382], whilst a more abstract perspective on mesh quality metric creation for triangular (based for example on size, shape and maximum angle), tetrahedral, quadrilateral and hexahedral finite elements is given by Knupp [383]. Other Delaunay triangulators include `Triangle`, based on the work of Shewchuk [384]. `CFD-GEOM` also has the ability to produce very high quality meshes.

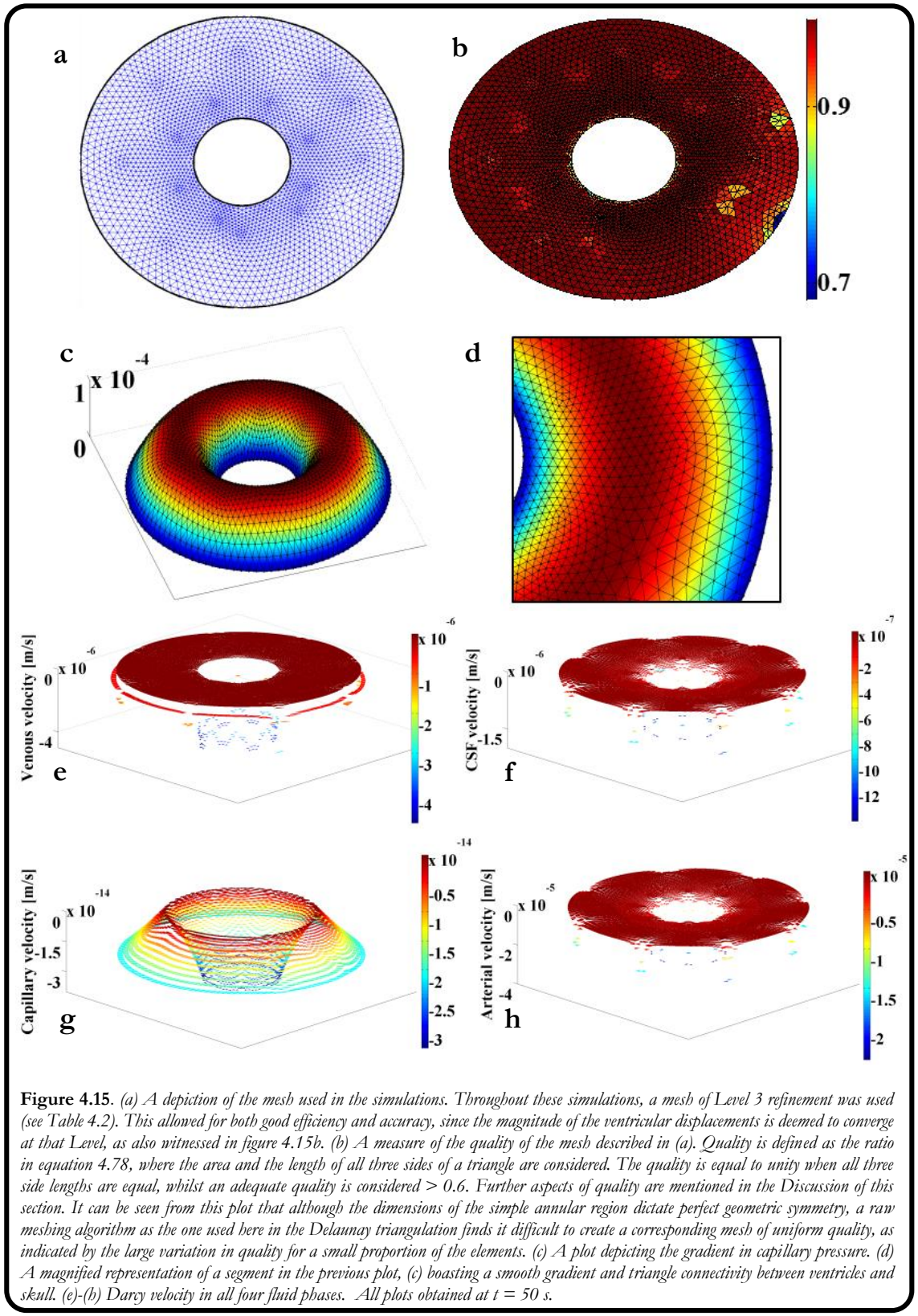

Figure 4.15. *(a) A depiction of the mesh used in the simulations. Throughout these simulations, a mesh of Level 3 refinement was used (see Table 4.2). This allowed for both good efficiency and accuracy, since the magnitude of the ventricular displacements is deemed to converge at that Level, as also witnessed in figure 4.15b. (b) A measure of the quality of the mesh described in (a). Quality is defined as the ratio in equation 4.78, where the area and the length of all three sides of a triangle are considered. The quality is equal to unity when all three side lengths are equal, whilst an adequate quality is considered > 0.6. Further aspects of quality are mentioned in the Discussion of this section. It can be seen from this plot that although the dimensions of the simple annular region dictate perfect geometric symmetry, a raw meshing algorithm as the one used here in the Delaunay triangulation finds it difficult to create a corresponding mesh of uniform quality, as indicated by the large variation in quality for a small proportion of the elements. (c) A plot depicting the gradient in capillary pressure. (d) A magnified representation of a segment in the previous plot, (c) boasting a smooth gradient and triangle connectivity between ventricles and skull. (e)-(h) Darcy velocity in all four fluid phases. All plots obtained at t = 50 s.*

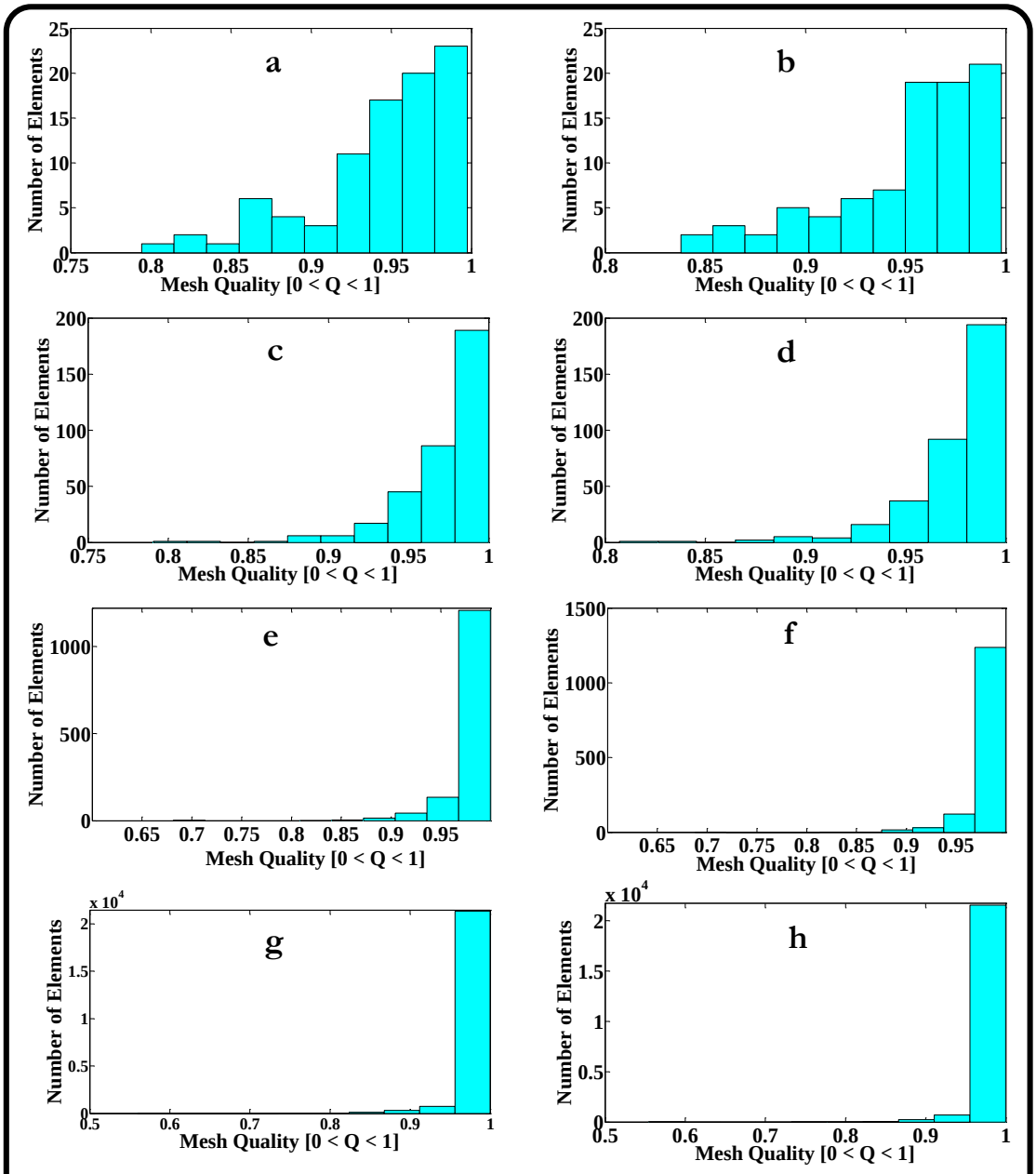

Figure 4.16. *(a) Quality of mesh based on the radius-ratio used in* `DistMesh` *for the L0 mesh. (b) Quality of mesh based on the chunkiness parameter for the L0 mesh. (c) Quality of mesh based on the radius-ratio used in* `DistMesh` *for the L1 mesh. (d) Quality of mesh based on the chunkiness parameter for the L1 mesh. (e) Quality of mesh based on the radius-ratio used in* `DistMesh` *for the L2 mesh. (f) Quality of mesh based on the chunkiness parameter for the L2 mesh. (g) Quality of mesh based on the radius-ratio used in* `DistMesh` *for the L3 mesh. (h) Quality of mesh based on the chunkiness parameter for the L3 mesh.*

Peak velocities are also found on the ventricles for this fluid phase since this was the trace with the highest assigned pressure values, dictating the overall gradient.

Figure 4.17 shows the variation of results on pseudo-anatomical geometries already described for the simpler geometries of the annular region and punctured peanut. The shape of the ventricles was roughly traced from an axial slice arising from the DICOM data of the volunteer that was used to conduct the CFD study in the previous chapter. The skull was more loosely captured and manually smoothed to aid computational efficiency and for the purpose of increasing mesh quality. The final geometry was manipulated in the same manner as the annular and peanut geometries, namely within the MATLAB framework already described. One then proceeds with the discretisation of the domain using the Delaunay triangulation already described. A key point to note in this section is that owing to the far more complicated polygonal region (ventricles), some of the sharper boundaries near the tips of the ventricles were kept for descriptive purposes. The skull and periventricular region were adequately refined using a tailor made algorithm for each iteration.

The specification of the algorithm is very simple, and quite useful in identifying bad elements. One may simply obtain the quality of the triangles based on a desired metric (such as the ones already described) and use a selection criterion or acceptable tolerance for the bad elements, find the bad elements (or focus on specific boundaries of interest) and use regular or Rivara refinement to successively improve the mesh until the termination criterion is met.

There are of course alternatives to this, including using MATLAB's built in error estimates and mesh refinement functions, namely *pdejmps* [385,386], *pdeaworst* and *pdeadgsc*. Since the fluid equations in the quasi-steady sense are effectively solved using a Poisson type solver, one is able to use this fact by using the *pdejmps* function, and using its inherent element-wise error indicator function which also utilises the L^2 - norm on each element and the jump in flux across simplex edges. The latter two mesh refinement functions help with alleviating hanging nodes within the refining process, in addition to their primary roles of being selection criteria for degenerate triangles. The use of the MATLAB based functions was avoided as the complexity of the mixture of boundary conditions in the MPET system renders their automatic use quite taxing. It is better that the user outlines simpler versions based on a metric of quality or extrapolate the use of the mature *pdejmps*-style routines in a standalone manner, as is done more frequently in dG methods.

Figure 4.17a-b shows both the simulated displacement distribution and unidirectional vectors on the contour plot, describing the influence of the Dirichlet boundary conditions on both the ventricular surface and skull. There was an increased mesh refinement at the skull and ventricles, using the aforementioned quality refinement technique. The shading in the figures was not interpolated (blended) in any way to allow for the visible and inherent smoothness in the solution. Instead, the patch faces in Figures 4.17(a, d-f) were faceted to allow disclosure of the true projection on each triangle. Coming back to the displacement, the peak ventricular displacement recorded was 6 μm, as the simulation took place for 5 seconds. The displacement field was smooth, and varied almost linearly from the ventricles to the skull in most regions, very similar to the simulation produced by Shahim *et al.* and Narsilio *et al.* [299,304]. There are however, visible (intentionally left) remnants of parenchymal triangles requiring even further refinement, especially approaching the skull.

In a blended shading of the patch surface, one does not seem to notice the effect as starkly, highlighting the importance of visually assessing the solution in detail. The contour plot for the north-east corner also shows some contours that are not rounded off to a perfect degree. It must be noted here that more inconsistent patient geometries would have the same effect (of distorting the solution), and it's arguable whether it's correct to allow a commercial to solver to completely smooth out the final solution, as opposed on just relying on the software to provide a high quality mesh.

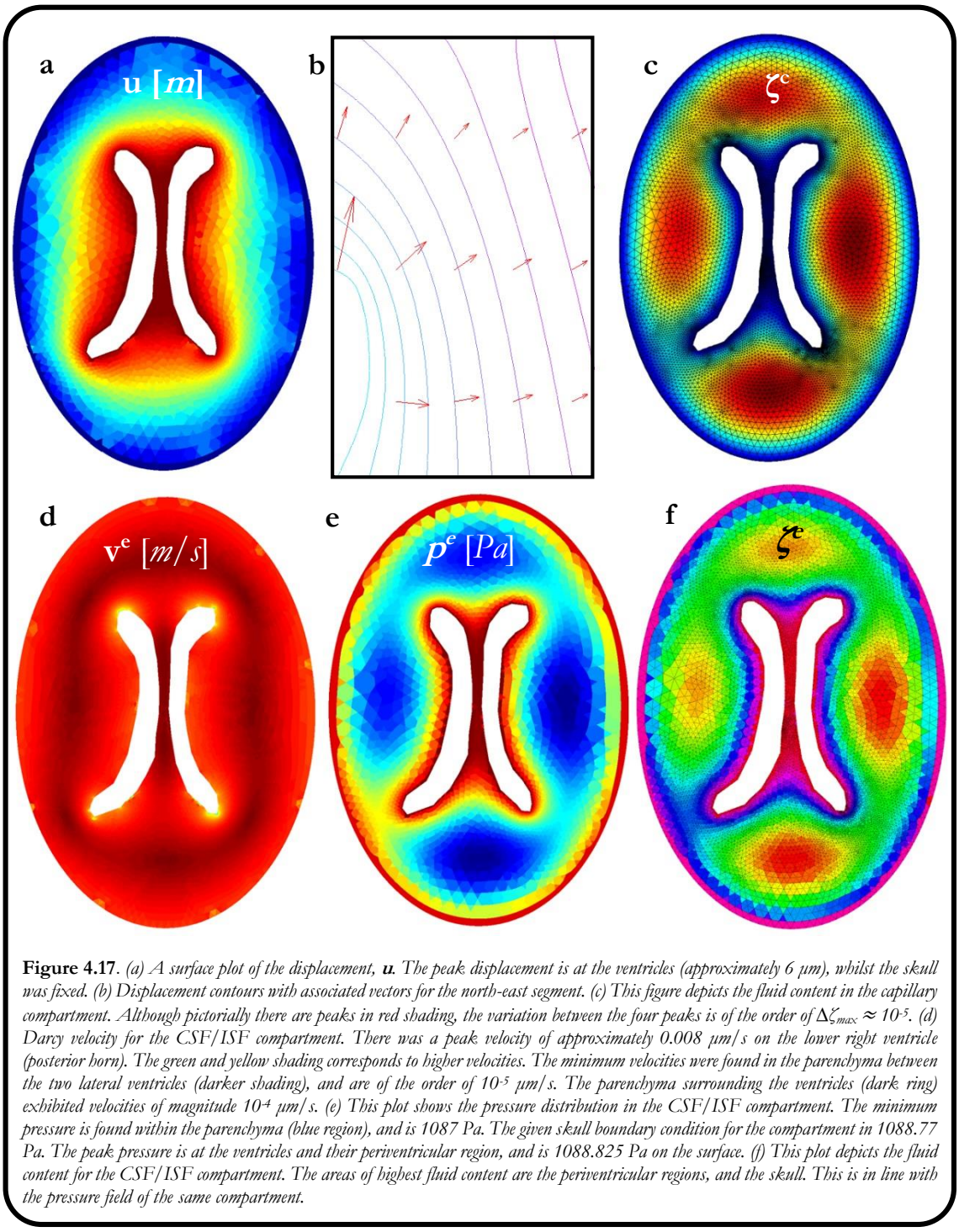

Figure 4.17. *(a) A surface plot of the displacement,* ***u****. The peak displacement is at the ventricles (approximately 6 μm), whilst the skull was fixed. (b) Displacement contours with associated vectors for the north-east segment. (c) This figure depicts the fluid content in the capillary compartment. Although pictorially there are peaks in red shading, the variation between the four peaks is of the order of* $\Delta\zeta_{max} \approx 10^{-5}$*. (d) Darcy velocity for the CSF/ISF compartment. There was a peak velocity of approximately 0.008 μm/s on the lower right ventricle (posterior horn). The green and yellow shading corresponds to higher velocities. The minimum velocities were found in the parenchyma between the two lateral ventricles (darker shading), and are of the order of* 10^{-5} *μm/s. The parenchyma surrounding the ventricles (dark ring) exhibited velocities of magnitude* 10^{-4} *μm/s. (e) This plot shows the pressure distribution in the CSF/ISF compartment. The minimum pressure is found within the parenchyma (blue region), and is 1087 Pa. The given skull boundary condition for the compartment in 1088.77 Pa. The peak pressure is at the ventricles and their periventricular region, and is 1088.825 Pa on the surface. (f) This plot depicts the fluid content for the CSF/ISF compartment. The areas of highest fluid content are the periventricular regions, and the skull. This is in line with the pressure field of the same compartment.*

Figure 4.17c shows the fluid content in the arteriole/capillary compartment, relying once again on the true boundary condition already described. It seems that a higher fluid content effects the parenchyma the most, indirectly implying the importance of depicting the blood-brain barrier separately, and extending the boundary conditions here in a spatial manner, to capture more detail in cases of blood-brain barrier breakdown. A limiting factor associated with this solution is that since the capillaries can be found troughout the parenchyma, it is highly unlikely that localised gradients develop in certain regions. The need for spatial accuracy in the governing MPET equations is highlighted here, since spatially varying source and sink terms would be ble to circumvent this type of solution. Figure 4.17d shows the Darcy velocity of the CSF/ISF compartment. As mentioned earlier, this set of simulations took place over a period of 5 *s*, in order to highlight the influence of the pressure gradient and therefore the role of the boundary conditions. It is clearly visible that higher velocity fragments accumulate at areas of high concavity, and these can be as much as two orders of magnitude higher than the minimum velocities found in the dark ring surrounding the ventricles. Again this velocity field is similar to that of Shahim *et al.* and Wirth & Sobey [296,304], where increased velocity persists around the ventricular horns of their first patient case (homogeneous and isotropic simulation). Allowing the simulation to progress for a much longer time ($t > 300$ *s*) and increasing the outflow resistance by at least 10% to induce communicating HCP, one can then appreciate the increasing pressure difference will allow for velocities that resemble those simulated by Linninger *et al.* [300].

Figure 4.17e-f show the CSF pressure distribution and CSF content in the ventricles after 5 *s*. The influence of the Neumann condition on the ventricles is apparent at these early stages, and tends to even out in the parenchyma and resembles that of the displacement surface plot in figure 4.8a after 100 *s*. This is intuitive since the transparenchymal pressure gradient increases with increasing simulation time. After 5 *s*, the fluid content is also highest in the periventricular region and the skull, whilst after 100 *s*, the peak CSF content once again becomes limited to the periventricular region. What is interesting to note is that the results obtained resemble the qualitative characteristics of the work on cerebral content conducted by Levine [288], in that the larger the ventricular displacement, the gradient of transparenchymal CSF content tends to reduce (especially if the rate of pressure increase is too rapid). As a side note, considering that periventricular lucency (first witnessed by Naidich *et al.*[387]) which is represented by increased CSF content in the periventricular regions, is assumed to result from ependymal surface breakdown which helps alleviate some of the pressure in the ventricles by allowing for some CSF extravasation (and oedema formation). Once again, this could be achieved with the possible assistance of AQP4 [63], which lines the ependymal surface. Pena *et al.* [290] theorize that the concavity of the ventricles helps accumulate expansive stresses (on their quadrilateral mesh) on the horns of the ventricles, which as is known now could induce swelling activated Cl channels such as microglia [210,388] and facilitate periventricular lucency (PVL) due to the effects on void ratio. Pena *et al.* however, cannot actively encourage a discussion around such a model since permanent changes in the parenchymal tissue would have to be considered. This would require an elastoplastic model. In addition to this, developments in FLAIR MR allow for the more accurate justification of PVL and interstitial oedema, since it must be distinguished from *ependymitis granularis*, which incorporates increased

fluid content, decreased myelin or breakdown of the ependymal lining accompanied by gliosis [208]. The different grading scales described by Ho *et al.* [208] insinuate that further information is required (such as a DTI map) in such circumstances.

It is worthy to note that increasing the transfer coefficient γ_{ev} to 1×10^{-8} $m^2N^{-1}s^{-1}$ whilst keeping all other parameters at the level of the healthy case, as in the 1D FEM simulations, there were significant changes to the relevant fluid compartments, namely the CSF/ISF and venous compartment. The CSF content can rise significantly, by over 1500%. Alternatively comparing the changes in venous compliance in Table 4.6, one can see that the venous fluid content gets influenced significantly by changes in porosity. Values of $\zeta_v > 0$ indicate fluid accumulation in the periventricular region, whilst negative values depict fluid squeezed out of the brain in the region near the skull. It is interesting to assert that changes in venous compliance effects the arterial, capillary and venous compartments, especially when $\alpha_v \leq 1$, where blood is increasingly drained (with increasing compliance) from the parenchyma. When the venous compliance exceeds unity, it can only accumulate fluid, possibly helping to explain why the ventricles can be induced to compress rather than expand under decreased compliance ($\alpha_v > 1$).

4.5.2.1 Newton-Galerkin method approach

Figure 4.18 shows the application of a non-linear model created specifically for the CSF/ISF compartment. Newton's method was used, as it is known to converge quickly [367]. The main reason for bringing this method to light is to appreciate its complexity when being used with clinical data acquired from the VPH-DARE@IT project described in §4.4. It is customary to mention that any function $\ell(p^e)$ posing as the coefficient of the PDE:

$$-\nabla\cdot\left(\ell\left(p^e\right)\nabla p^e\right)=\eta_3 \quad \text{in} \quad \Omega \tag{4.79}$$

is assumed to be a positive function, and represented by a polynomial in p^e. In this example:

$$\ell\left(p^e\right)=k_0^e e^{\left(p/2p_{ref}\right)} \tag{4.80}$$

where p_{ref} is a reference pressure (equal to unity for simplicity). In (4.79), the right hand side is the same as function as that in equation (3.39c). As can be seen from Figure 4.18a, the correction 2-norm of the CSF/ISF pressure correction, $||\delta pe^{(k)}||$ decreases rapidly with increasing number of Newton steps, k. This is an important aspect of the method (rapid convergence), however what is more pleasing is that this convergence was achieved under the application of very (intentionally) irregular skull and ventricle boundary conditions (described in the caption), in addition to non-linear permeability. The effect of this non-linear function has been kept more stable by not incorporating strain, and this is justified, since although this author (in the previous chapter) in addition to With & Sobey [296] use an exponentially varying strain in their non-linear model, it is should be more apparent that the permeability should be influenced by fluid content, as described by Mow *et al.* [389] and later by Levine [288].

Momjian and Bichsel [298] used a hydraulic permeability as a function of void ratio for their simulations, where the bulk influence of this alteration resulted in similar fields for void ratio, Young's modulus and to a much lesser degree, ventricular displacement (although the

quality factor defined in this work was much higher). In anticipation of this fact for future work, a simple non-linear function was used to primarily assess the validity of the setup.

4.5.3 The 3D-FEM MPET template

In this section, a brief outline of the extension on the use of four node tetrahedrals (*Tet4*) with flat surfaces is made. It is common knowledge that the 3D tetrahedral element is the most general three dimensional element. In the build-up of the 1D and 2D FEM templates, it was indicated (wherever possible) as to how the extension on to 3D is made. The *Tet4* element has, for each of its four nodes, three translational degrees of freedom allowing full spatial deformation, but also being demanding in terms of computing resources.

It is useful to disclose at this point the specifications of the PC used to conduct these simulations, as the interested reader will find the use of *Tet4* elements on such a system of equations computationally demanding, and in some cases prohibitively slow if the required computational resources are not allocated for.

The main specifications of the machine used is: *Intel*® *Xeon*® E5520 CPU with Gainestown 45*nm* Technology at 2.27*GHz* with 24.0 *GB* Triple-Channel DDR3 at 533 *MHz* RAM, running on a 64-bit Windows 7 Enterprise OS (SP 1) with an NVIDIA Quadro NVS 295 graphics card.

Table 4.6*. This table outline the changes in fluid content for the different fluid compartment of the pseudo-anatomically accurate geometry under the influence of varying venous compliance.*

α_v	ζ_a	ζ_c	ζ_e	ζ_v
0.8	$-3.9\cdot10^{-4}/0.01$	$-3.1\cdot10^{-4}/-3.1\cdot10^{-4}$	$4.5\cdot10^{-4}/4.5\cdot10^{-4}$	$-3.9\cdot10^{-4}/1.1\cdot10^{-4}$
1	$-2.2\cdot10^{-5}/0.01$	$-2.2\cdot10^{-5}/-2.2\cdot10^{-5}$	$8.1\cdot10^{-4}/8.1\cdot10^{-4}$	$-2.2\cdot10^{-5}/4.8\cdot10^{-4}$
1.5	$3.2\cdot10^{-4}/0.01$	$3.9\cdot10^{-4}/3.9\cdot10^{-4}$	0.001/0.001	$3.2\cdot10^{-4}/8.2\cdot10^{-4}$

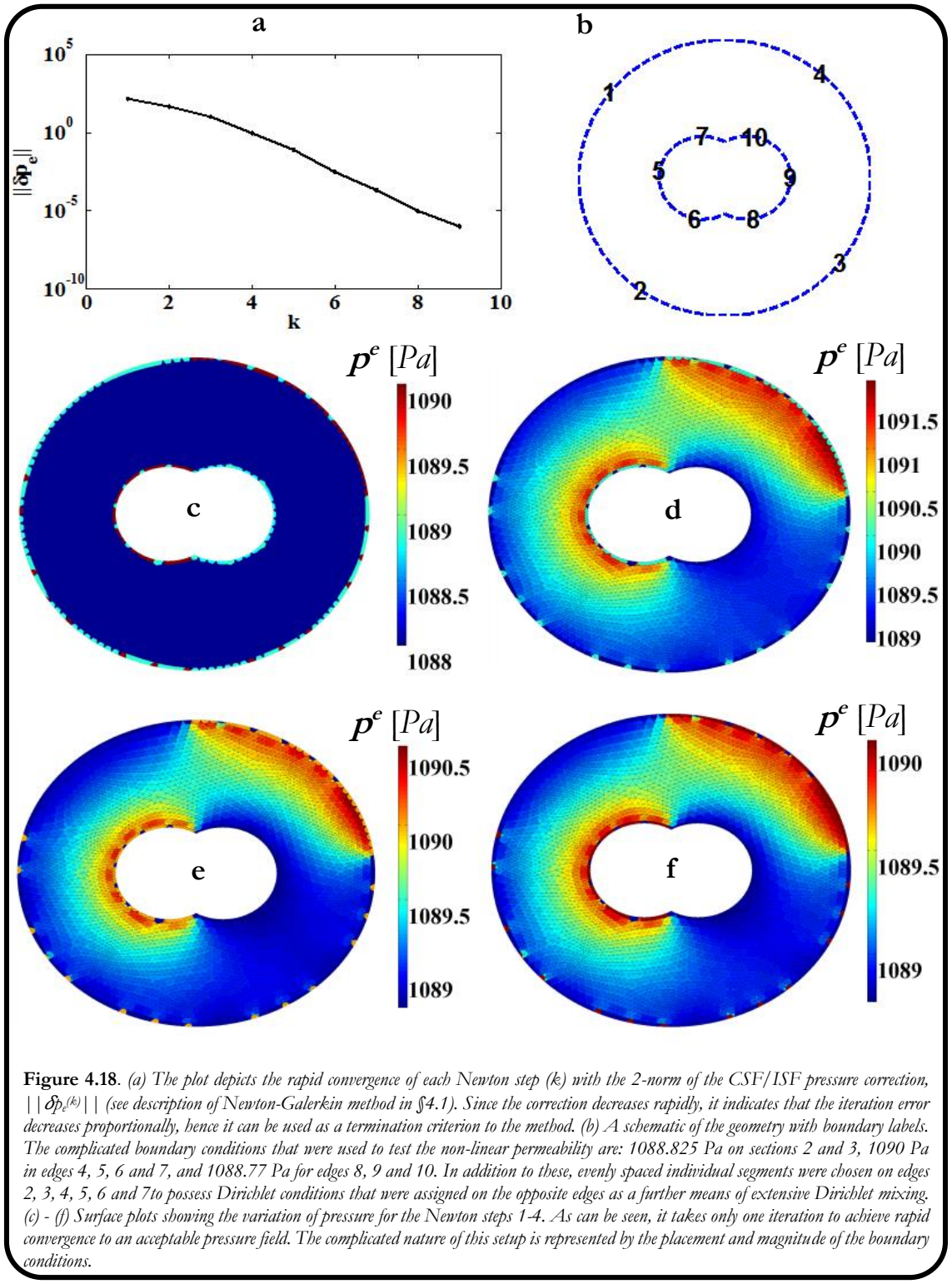

Figure 4.18. *(a) The plot depicts the rapid convergence of each Newton step (k) with the 2-norm of the CSF/ISF pressure correction, $||\delta p_e^{(k)}||$ (see description of Newton-Galerkin method in §4.1). Since the correction decreases rapidly, it indicates that the iteration error decreases proportionally, hence it can be used as a termination criterion to the method. (b) A schematic of the geometry with boundary labels. The complicated boundary conditions that were used to test the non-linear permeability are: 1088.825 Pa on sections 2 and 3, 1090 Pa in edges 4, 5, 6 and 7, and 1088.77 Pa for edges 8, 9 and 10. In addition to these, evenly spaced individual segments were chosen on edges 2, 3, 4, 5, 6 and 7to possess Dirichlet conditions that were assigned on the opposite edges as a further means of extensive Dirichlet mixing. (c) - (f) Surface plots showing the variation of pressure for the Newton steps 1-4. As can be seen, it takes only one iteration to achieve rapid convergence to an acceptable pressure field. The complicated nature of this setup is represented by the placement and magnitude of the boundary conditions.*

Some general recommendations when setting a 3D solver include the need to have as many straight edges as possible within the discretised domain, and that higher order elements such as the quadratic tetrahedral element (*Tet10*) with 10 nodes may also be used, however in many cases in domains with excessive curvature, this could pose as a disadvantage in the numerical integration [357]. For this reason, and for the purpose of saving computational resources, the *Tet4* element was constructed and used in these simulations. It should be mentioned here that the primary purpose of this section is to prove the organic extension of the FEM methodology used thus far into three dimensional space, and to develop a working solver that can handle the MPET equations and boundary conditions correctly. At this point it is also important to stress the need to possess a mesh of high quality, and to simultaneously allow for mesh refinement. Although `MATLAB` can handle tetrahedral meshes, it was important to test the capability and robustness of the 3D FEM template by using an external mesh generator. There are many open source tetrahedral mesh generators, such as `DistMesh`, `iso2mesh`, `TetGen` and `NETGEN` to name a few. `NETGEN 5.1` (*www.netgen-mesher.sourceforge.net*) was used as it can take the form of a standalone executable with its own GUI on a Windows based OS, in addition to the possibility of being used as a `C++` library.

There are two main mesh generation algorithms offered, Delaunay and Advancing Front, where elements form individually from the boundary towards the centre [390]. The CSG format is also offered, only this time an external script is written in the form of an `ASCII` file. The geometries are defined by the Euler Operations (union, intersection and complement) provided from primitives (half space, cylinder, sphere, elliptic cylinder, ellipsoid, cone and ortho-brick). Flags can also be used to assign a maximal mesh size on different solids and also to identify different surfaces, which is useful when applying the boundary conditions. Triangulated surfaces (in *STL* format) are also supported, however complicated geometries like the cerebroventricular system used in the previous chapter are not currently easily supported, owing to the extensive external manipulation and smoothing on `Blender`. It should be noted that assigning boundary conditions on complex geometries is not a trivial task, and the use of other mesh generators such as `DistMesh` only offer easy relief for very primitive problems. Using `MATLAB`, one may approach this via a mixture of convex hull and Delaunay triangulation operations, with additional binary encoding on ventricular and skull nodes.

Figure 4.19 shows the evolutionary creation of the geometries used in this simulation in addition to the quality based on the ratio between the radius of the largest inscribed sphere and the smallest circumscribed sphere [359]. The maximum displacement witnessed in the punctured sphere simulations decreases with increasing refinement. Specifically, the average (for the three components of displacement) for the coarse, medium and fine refinements can be seen in Table 4.7.

In addition, the minimum and maximum [*max*, *min*] parenchymal displacements (averaged over the three displacement components) for α_c =1.2, 1 and 0.8 are also given as solution pairs (in μm): [-55, -156], [11, 13] and [75, 535].

Figure 4.20 shows the successful application of the 3D-MPET template. It is emphasised here that the 3D template was conducted using an implicit Euler-backward time

***Table 4.7**. A table outlining the number of nodal coordinates used (n_p), number of surface shell elements (n_e) and number of tetrahedral elements (n_t) for the punctured sphere model. The maximum ventricular displacement is also given (by adding the sum of the squares of each displacement component).*

Punctured sphere	n_p	n_e	n_t	$U_{Vm\ (\mu m)}$
Coarse	169	240	609	214
Medium	1065	960	4872	145
Fine	7480	3840	38976	5.69

integration scheme. This therefore requires an additional parameter S^j for the amalgamated compressibility, in the fluid compartments (equations 4.2b-e). The same value of S^j as that of Li *et al.* [308] was used for all fluid compartments, specifically, 0.45 μPa^{-1} (based on their observations and comparisons of simulated infusion curve experiments).

It is important to define the deformed and strained tetrahedron domain which is important when considering the solution of the fluid equations. The three normal strains ε_i (i = 1, 2, 3) parallel to the coordinate axis x_i (i = 1, 2, 3) and the three shear strain components $\tau_{ij} = \tau_{ji}$ (i , j = 1, 2 ,3; $i \neq j$) within the corresponding (i - j) - plane. In addition, from Figure 4.12, these quantities are defined as:

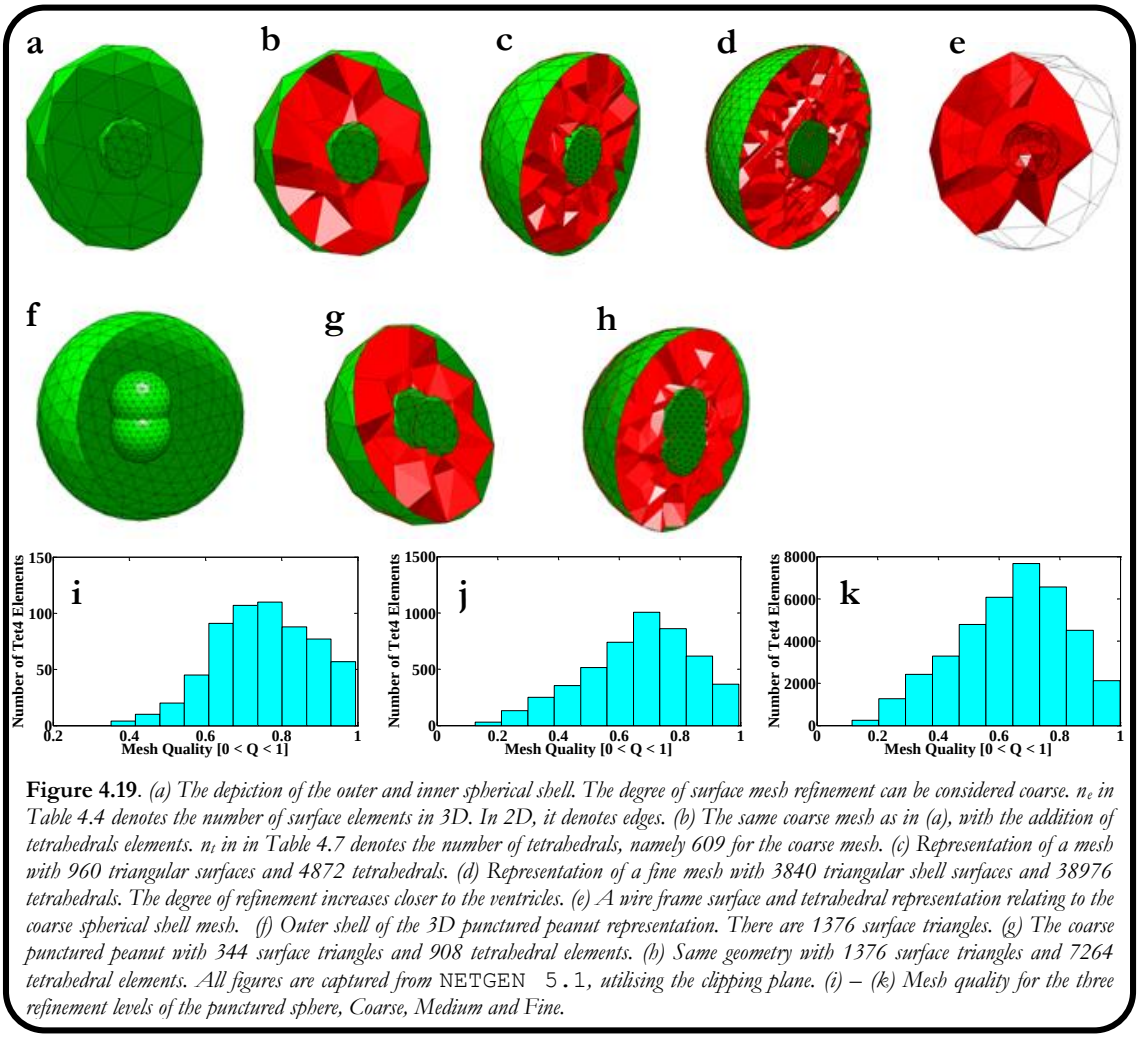

Figure 4.19. *(a) The depiction of the outer and inner spherical shell. The degree of surface mesh refinement can be considered coarse. n_e in Table 4.4 denotes the number of surface elements in 3D. In 2D, it denotes edges. (b) The same coarse mesh as in (a), with the addition of tetrahedrals elements. n_t in in Table 4.7 denotes the number of tetrahedrals, namely 609 for the coarse mesh. (c) Representation of a mesh with 960 triangular surfaces and 4872 tetrahedrals. (d) Representation of a fine mesh with 3840 triangular shell surfaces and 38976 tetrahedrals. The degree of refinement increases closer to the ventricles. (e) A wire frame surface and tetrahedral representation relating to the coarse spherical shell mesh. (f) Outer shell of the 3D punctured peanut representation. There are 1376 surface triangles. (g) The coarse punctured peanut with 344 surface triangles and 908 tetrahedral elements. (h) Same geometry with 1376 surface triangles and 7264 tetrahedral elements. All figures are captured from* `NETGEN 5.1`*, utilising the clipping plane. (i) – (k) Mesh quality for the three refinement levels of the punctured sphere, Coarse, Medium and Fine.*

$$\varepsilon_1 = \frac{\partial \boldsymbol{u}_1}{\partial x_1}, \quad \varepsilon_2 = \frac{\partial \boldsymbol{u}_2}{\partial x_2} \quad \varepsilon_3 = \frac{\partial \boldsymbol{u}_3}{\partial x_3} \quad \&$$
$$\tau_{12} = \frac{\partial \boldsymbol{u}_1}{\partial x_1} + \frac{\partial \boldsymbol{u}_2}{\partial x_1} \quad \tau_{23} = \frac{\partial \boldsymbol{u}_2}{\partial x_3} + \frac{\partial \boldsymbol{u}_3}{\partial x_2} \quad \tau_{31} = \frac{\partial \boldsymbol{u}_3}{\partial x_1} + \frac{\partial \boldsymbol{u}_1}{\partial x_3} \tag{4.81}$$

Using index notation, one obtains expressions for the above equations in compact form, utilising the shape functions $h_{ip}\left(x_j\right);\left(i, j = 1,2,3 \text{ and } p = 1,...,4\right)$:

$$\varepsilon_i\left(x_j\right) = \sum_p u_{ip} \cdot \frac{\partial h_p\left(x_j\right)}{\partial x_i} \; ; \; \left(i, j = 1,...,3 \; ; \; p = 1,...,4\right)$$
$$\tau_{ij}\left(x_k\right) = \sum_p \left(u_{ip} \cdot \frac{\partial h_p\left(x_k\right)}{\partial x_j} + u_{jp} \cdot \frac{\partial h_p\left(x_k\right)}{\partial x_i} \right) \; ; \; \left(i, j, k = 1,...,3 \; ; \; i \neq j \; ; \; p = 1,...,4\right) \tag{4.81a-b}$$

The interested reader should refer to the texts of Hagedorn and Schnell *et al.* [5] (also referenced in the caption of Figure 4.21).

Figure 4.20a shows the combined displacement of all three components, *u*, *v* and *w*. As mentioned in the figure, the peak ventricular displacement recorded was 58 *μm*. The distortion in the colour shading arises from the overlapping displacement contributions of the three components, in combination with the impact of the pressure gradients arising from the ***u***-*p* formulation.

Figure 4.20b-d shows the pressure distribution of the arterial, CSF/ISF and venous compartments respectively. Further details on the shading, visibility and quality is given after Figure 4.23 below. Figure 4.20e shows the CSF/ISF pressure distribution after allowing the transient 3D MPET template to run for 20 *s*. Finally, 4.20f portrays a magnification of the ventricular region, when displaying the combined displacement solution in 4.20a, albeit with a better contrast in shading for visibility.

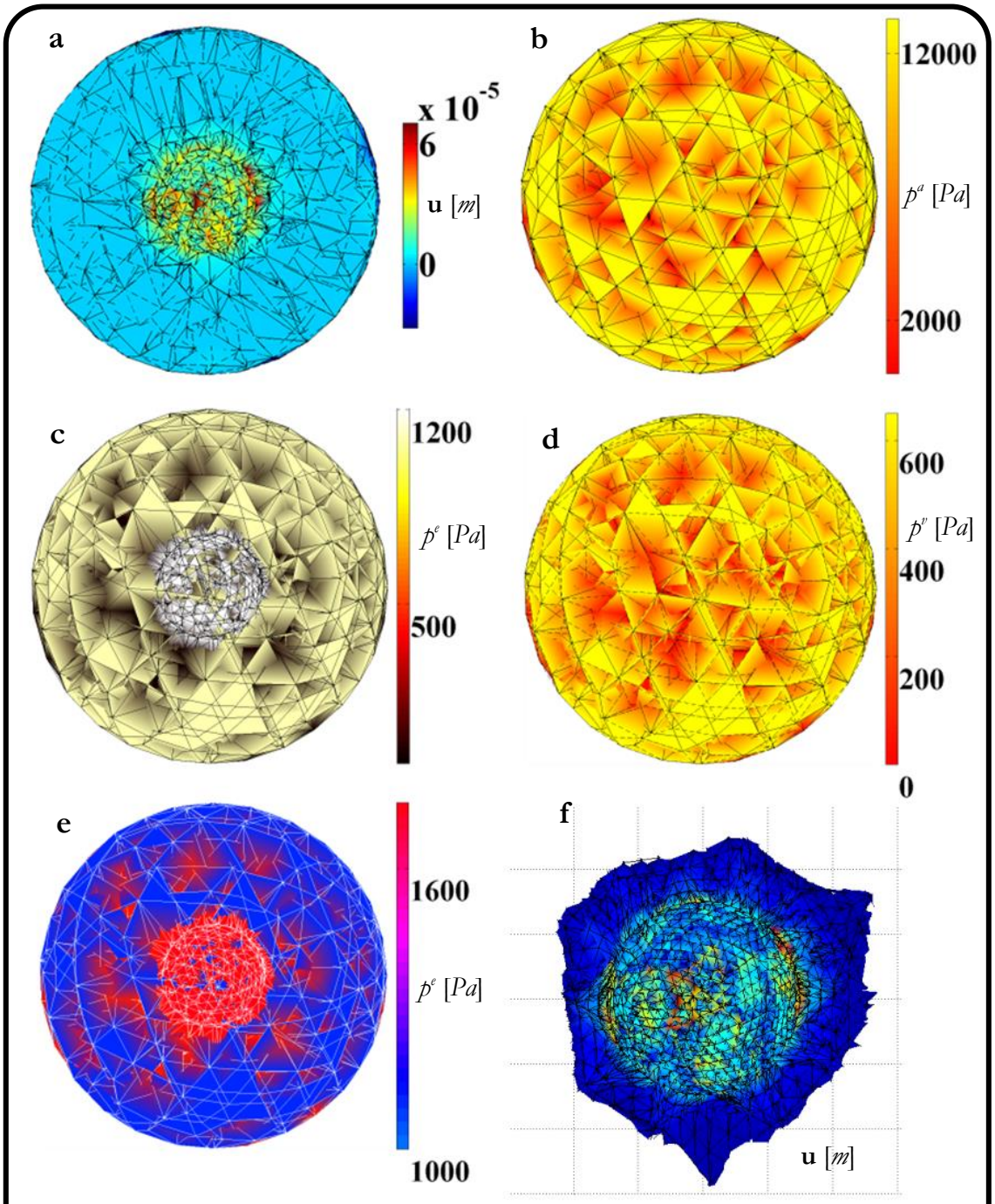

Figure 4.20. *(a) A depiction of the combined displacement of the three components of* ***u****. The peak ventricular displacement recorded was 58 μm. (b) The distribution of the pressure field of the arterial compartment. As can be seen, the skull possesses values reflecting the boundary condition, namely 13.3 × 10³ Pa. The reason for the lack in visibility of the punctured sphere representing the ventricles is that the boundary condition of the skull is higher than the ventricles, so the surface of the skull dominates visibility. (c) The pressure field for the CSF/ISF compartment. The pressure on the ventricles after 5 seconds of simulation is 1202 Pa. The pressure at the skull was fixed at 1088.77 Pa, as requested by the boundary conditions. (d) The pressure field of the venous compartment. The fixed Dirichlet boundary condition of 650 Pa at the skull dominates visibility. (e) The pressure field of the CSF/ISF compartment after 20 seconds of transient simulation. The pressure at the ventricles rises to 1741 Pa, whilst the skull continues to have an assigned pressure of 1088.77 Pa. (f) A magnified view of the u-component of ventricular displacement after 5 seconds of simulation.*

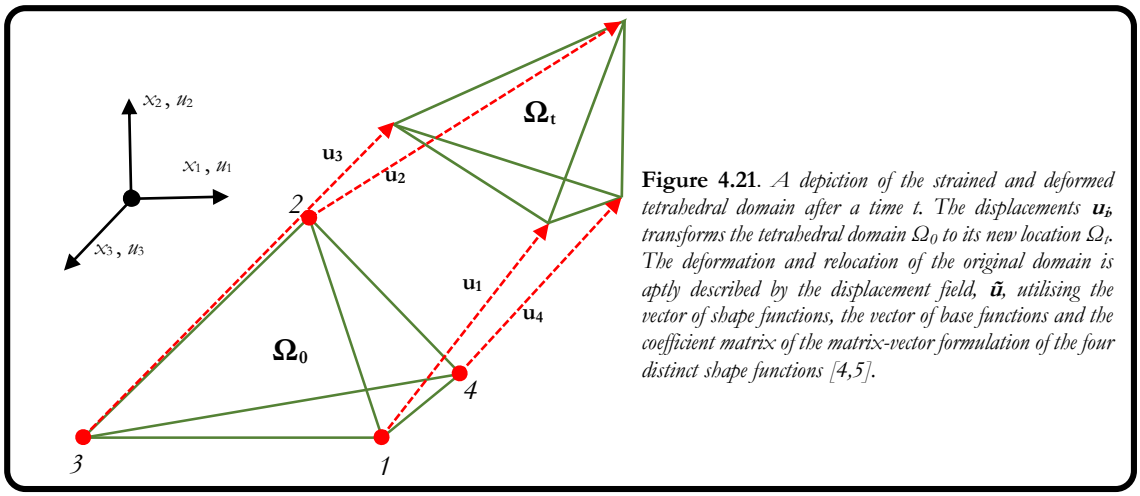

Figure 4.21. *A depiction of the strained and deformed tetrahedral domain after a time t. The displacements* $\boldsymbol{u_i}$*, transforms the tetrahedral domain* Ω_0 *to its new location* Ω_t*. The deformation and relocation of the original domain is aptly described by the displacement field,* $\tilde{\mathbf{u}}$*, utilising the vector of shape functions, the vector of base functions and the coefficient matrix of the matrix-vector formulation of the four distinct shape functions [4,5].*

Figure 4.22 confirms the methodology used for the solid matrix displacement equation by primarily checking that there are no displacements when assuming complete incompressibility ($v = 0.5$), along with the expected increase in overall ventricular and parenchymal displacement for $v \rightarrow 0$. It can also be seen in Figure 4.22d that when v is very close to zero, the ventricular expansion results in similar displacements throughout the whole parenchyma.

Figure 4.23 outlines the simulated results obtained when using the punctured peanut geometry, in order to assess the effect of an altered geometry with sharper areas of tetrahedral refinement, as would be the case in the region between the two overlapping spheres. Figure 4.23a shows the simulated displacement of $\mathbf{u}(u)$. A peak displacement of 10 μm was witnessed, at the point of intersecting spheres. The distribution of displacement on the surface of the ventricles and the periventricular parenchymal region was lower. Figure 4.23b shows the results for simulated displacement $\mathbf{u}(u, v, w)$. As expected overall parenchymal displacement increases.

Figure 4.23c gives the details of two meshes that were tested for the punctured peanut geometry, with the finer mesh preferred. Figures 4.23d-f show the results for the CSF/ISF pressure distribution in the sagittal and coronal plane and a magnified portion of the north-west segment of the ventricles in the coronal plane. The colour scheme was amended (with the addition of darker parenchymal regions for higher contrast) to assist in the visualisation of the mesh. The ventricular pressure was at 1200 *Pa*, whilst the skull had a fixed pressure of 1088.77 *Pa*.

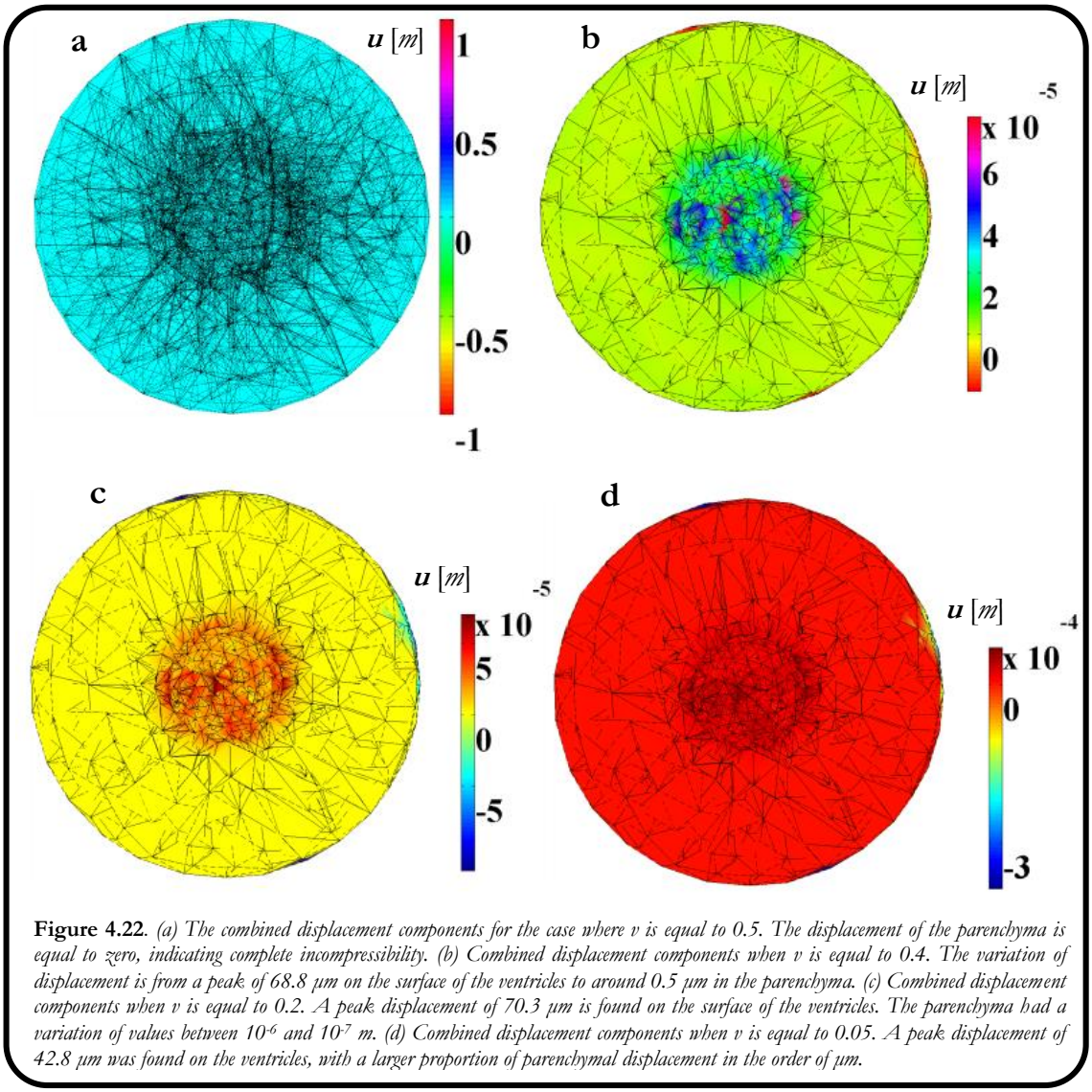

Figure 4.22. *(a) The combined displacement components for the case where v is equal to 0.5. The displacement of the parenchyma is equal to zero, indicating complete incompressibility. (b) Combined displacement components when v is equal to 0.4. The variation of displacement is from a peak of 68.8 μm on the surface of the ventricles to around 0.5 μm in the parenchyma. (c) Combined displacement components when v is equal to 0.2. A peak displacement of 70.3 μm is found on the surface of the ventricles. The parenchyma had a variation of values between 10^{-6} and 10^{-7} m. (d) Combined displacement components when v is equal to 0.05. A peak displacement of 42.8 μm was found on the ventricles, with a larger proportion of parenchymal displacement in the order of μm.*

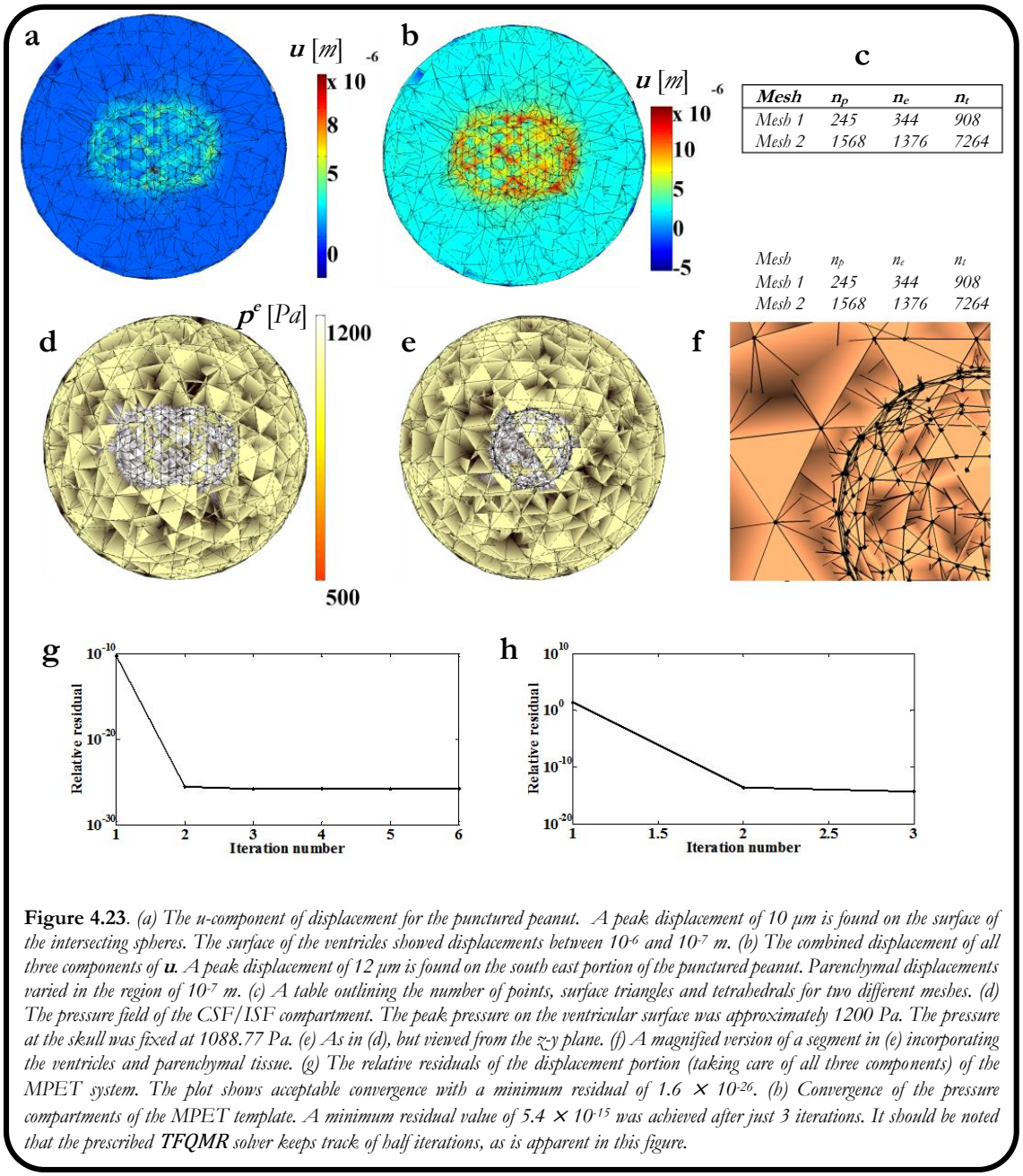

Figure 4.23. *(a) The u-component of displacement for the punctured peanut. A peak displacement of 10 μm is found on the surface of the intersecting spheres. The surface of the ventricles showed displacements between 10^{-6} and 10^{-7} m. (b) The combined displacement of all three components of* ***u****. A peak displacement of 12 μm is found on the south east portion of the punctured peanut. Parenchymal displacements varied in the region of 10^{-7} m. (c) A table outlining the number of points, surface triangles and tetrahedrals for two different meshes. (d) The pressure field of the CSF/ISF compartment. The peak pressure on the ventricular surface was approximately 1200 Pa. The pressure at the skull was fixed at 1088.77 Pa. (e) As in (d), but viewed from the z-y plane. (f) A magnified version of a segment in (e) incorporating the ventricles and parenchymal tissue. (g) The relative residuals of the displacement portion (taking care of all three components) of the MPET system. The plot shows acceptable convergence with a minimum residual of 1.6×10^{-26}. (h) Convergence of the pressure compartments of the MPET template. A minimum residual value of 5.4×10^{-15} was achieved after just 3 iterations. It should be noted that the prescribed* ***TFQMR*** *solver keeps track of half iterations, as is apparent in this figure.*

It should be mentioned at this point that there is difficulty is visualising solutions imported from external mesh generators, that involve a cG setup methodology such as the one described in this work, which can be considered one of the very few disadvantages of exploring the MPET solution without the use of third party software. To circumvent part of this problem, an effective solution is to manipulate the triangular mesh plot function in MATLAB (*trimesh*). Once an effective script was written in MATLAB to ensure the reordering of elements confirmed a counter-clockwise orientation to comply with the 2D formulation (to avoid erroneous visualisation of the solution), the connectivity and point matrices were used to facilitate the representation of the desired solution. Various additional patch property options need to be catered for, such as an interpolated face colouring scheme, vertex edge lighting and

face lighting (Affects at the vertices and also linearly interpolated across the faces. This option is needed in order to view curved surfaces). More information on these features can be found on MATLAB's exhaustive online documentation centre.

Finally, Figures 4.23g-h allow one to follow the progress of the TFQMR solver by plotting the relative residual obtained at each iteration for both the solid matrix and fluid phases separately. The convergence to the desired set tolerance of 10^{-26} or displacement and 10^{-15} for the fluid compartments can be seen. This rapid convergence was aided by the preconditioning techniques described earlier, in addition to symmetric reverse Cuthill-McKee ordering. The effect on the sparsity is shown for the coarse punctured sphere geometry, in Figure 4.24.

It should be kept in mind that sparse reverse Cuthill-McKee ordering (*srco*) is especially useful in larger and sparser matrices (finer meshes). As can be seen, using the finer mesh (Figures 4.24c-d), the influence on the bandwidth (*bw*) becomes more pronounced (the *bw* is 704 for the fluid compartments before application of *srco*, and 193 after). In a very fine punctured spherical geometry, the size of the matrices that could be tested were of size 29920 × 29920 for the pressure compartments and 20996 × 20996 for the solid phase.

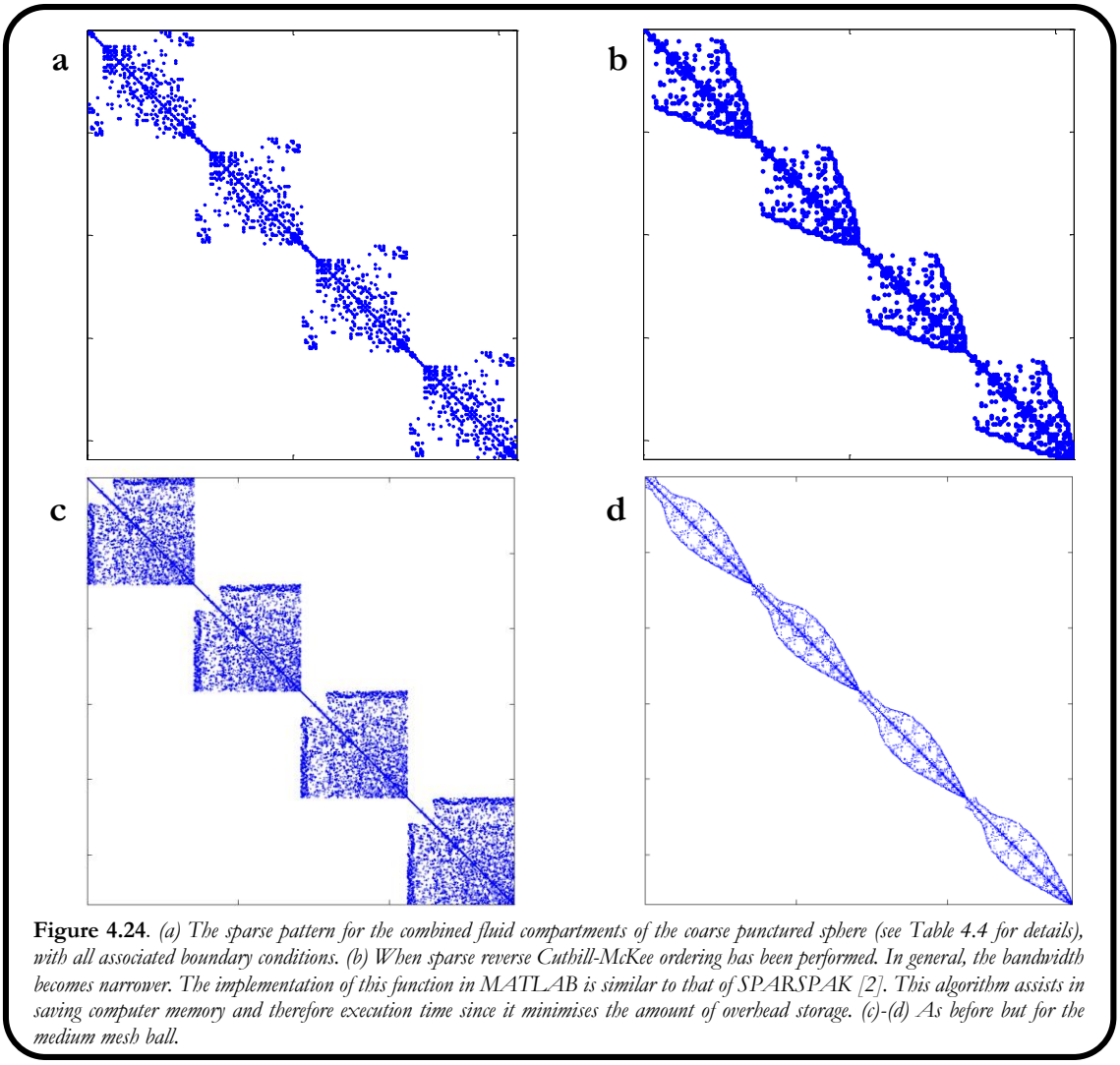

Figure 4.24. *(a) The sparse pattern for the combined fluid compartments of the coarse punctured sphere (see Table 4.4 for details), with all associated boundary conditions. (b) When sparse reverse Cuthill-McKee ordering has been performed. In general, the bandwidth becomes narrower. The implementation of this function in MATLAB is similar to that of SPARSPAK [2]. This algorithm assists in saving computer memory and therefore execution time since it minimises the amount of overhead storage. (c)-(d) As before but for the medium mesh ball.*

4.6 The VPH-DARE@IT project

In this project the development of a computational modelling framework for an MPET model with a 3D, spatio-temporally variable properties distribution is envisaged. What is planned is that the casting of such a model in an anatomically accurate, image-derived framework will hpefully aid in the understanding of dementia, through an MPET modelling approach that accounts for environmental influences on metabolism, biophysics, physiology, clinical biomarkers and lifestyle. More specifically, the MPET PDE based template described in this thesis will be directly linked to an additional layer defining the glymphatic system, in addition to lifestyle factors and other relevant imported boundary conditions. This assimilated framework will then be linked with a metabolic modelling based platform, in addition to utilising novel data acquired through imaging. A key element to note here is that the 3D transient FEM based MPET template will also be used to form part of a module within the CFD-ACE+ multiphysics suite and its adoption is currently going through rigorous testing.

Conclusions

The preceding chapters have shown that it is possible to develop a conceptual model depiciting interesting characterisitcs allied to acute and chronic hydrocephalus, and two of its many treatment algorithms. The three main discretisation techniques, namely the finite difference method (FDM), a coupled FDM - FVM and a standalone FEM solver based on linear triangles was used in this work. Chapter 3 was written in a manner that emphasised the outline of the methodology behind the construction of such a solver, and it is natural to expect that further developments will need to take place before practical utilisation is possible. Such developments are explained in this chapter, along with possible future advances expected from such a framework.

5.1 Main Conclusions

The aim of this thesis was to begin to unravel the full complexity of the MPET field equations and as a consequence, the modelling complexity of HCP, with the help of established and new discretisation techniques. The FDM was explored in its own right, via a non-linear application of strain-dependent permeability, whilst the FDM-MPET template was also coupled with a FVM based commercial CFD solver. The spherically symmetric FDM based approaches allow for a wide breadth of HCP based conditions to be explored. In this report, the acute form of HCP was investigated through artificially induced aqueductal stenosis and FVOO. Emerging surgical techniques such as ETV and EFV were incorporated into the coupled FDM-CFD framework, and allowed for a more subtle investigation of whether or not such surgery facilitates the decline in ventriculomegaly and transparenchymal pressure gradient. The non-linear form (strain-dependent permeability) of the FDM-MPET system was also used to capture the effects of aqueductal stenosis, however its main use was to elucidate the evolution of the communicating form of HCP (through the theoretical lens of AQP4), by encapsulating the variations witnessed in the efficiency of CSF absorption within the parenchyma, along with possible defective outflow resistance, Compliance was also investigated, which aids any discussion around NPH and BIH.

The FEM was used to discretise the MPET system (relaxing the constraint of spherical symmetry) in one, two and three dimensions, in addition to establishing a separate dual-grid (in 1D) and non-linear solver using the Newton-Galerkin method (in 2D). The n^{th} dimensional discretisation using the FEM allows for added spatial detail in interrogating communicating HCP though measures already defined in the FDM based approaches. The primary purpose

of the FEM based approach was to establish a working framework able to handle the stiff quadruple-MPET system, and its associated boundary conditions in $\mathbb{R}^n$, whilst simultaneously addressing the need for spatial recognition of the features of ventriculomegaly, such as periventricular lucency or interstitial oedema.

The incorporation of the FEM method described in the previous chapter is currently in the process of being implemented within the `ESI` environment. The consequence of formally embedding the template into an established and mature environment is that parallelisation will be possible, which needless to say will allow for an easier handling of a patient specific geometrical atlas. Segmenting, smoothing and meshing the ventricle atlas used in §3 involved various stages with varying complexity. The VPH project will aid in implementing a streamlined process of rapid segmentation, smoothing and meshing of detailed structural images. Novel in-vivo techniques in poroelastic and viscoelastic parameter estimation from MRE (including DTI to interrogate white and grey matter), micro-scale imaging for the understanding of permeability, Diffusion Spectrum Imaging, boundary condition estimation through intracranial blood and CSF velocity vector imaging and further brain fibre architecture will equip the MPET model to the degree necessary to finally conduct clinically relevant investigations in HCP through the broader reach of a dementia project. The list of techniques used to fortify the MPET model as clinically useful for diagnosis is not exhaustive, as there is a strong emphasis to continuously evolve one's understanding of the interaction between cerebral fluid production, transport and drainage.

Using HCP as a test bed, one is able to account for the necessary mechanisms in both a macro and microscopic sense. In this study, both chronic and acute HCP was investigated, along with emerging surgical techniques. An emphasis was also placed on evolving the numerical techniques used in conducting such analyses. It was important to accommodate the cG FEM into the overall picture, since it allows for rapid and more advanced techniques through its more formal underpinning of functional analysis. Discontinuous Galerkin based techniques apply more favourable aspects of discretisation methods (FDM, FVM and FEM), along with better efficiency for higher order grids. The mathematical foundations of the method are strong, with great potential, however the technique is still in its nascent stage of impending use.

Finally, it is envisaged that new observations into the biology of cerebral fluid flow (such as perivascular *CSF-ISF* fluid exchange) and its interaction with the surrounding parenchyma, will demand the evolution of the MPET model to reach a level of complexity that could allow for an experimentally guided exploration of areas that would otherwise prove too intricate and intertwined under conventional settings. A possible outline of such future directions will now be described, along with some of the more critical aspects surrounding the work presented in this thesis.

5.2 Future Direction

As in any numerical template, there is a critical emphasis on the assumptions and boundary conditions used to make assertions about any pathophysiology. In this work, a spherically symmetric geometry was used to conceptualise the development of the FDM based MPET templates. This assumption was necessary to allow for the smooth transition between SPET and MPET, in addition to being able to compare results to the pertinent literature [295,296]. Such a framework was not solely created to account for a critical quantitative assessment of the results with clinical observations, but instead it can be used to orchestrate a better qualitative understanding of the areas of possible concern for more clinically demanding models in communicating HCP. The quasi-steady assumption in the aforementioned templates also negates the effects of pulsatility in the blood and CSF compartments, however this assumption provides the opportunity to investigate the more intrinsic properties over the time scale of HCP, such as defective CSF/ISF production or absorption, increased outflow resistance at the arachnoid granulations and compartmental compliance. An additional assumption is that of a rigid ventricular wall in the CFD simulations. Ventricular surface motion is expected to alter the CSF dynamics significantly, especially in light of pulsatility in the aforementioned compartments. An important development would be to account for this wall motion via an interpolation scheme extracted from MRI scans.

The reasoning behind the development of the FEM based MPET framework is more straightforward. In addition to providing an organic way of extending the MPET model to include further compartments, the mathematical foundations of the model allow for a more accurate parenchymal displacement, not to mention the better immunity from the various numerical influences surrounding the stiffness of the MPET system. This is important to consider, since within the long term perspective use of this system is to incorporate detailed information surrounding the glymphatic clearance system.

As it was seen in §4 and in previous work [102], the impact of the source/sink terms in the MPET system (which are inherently associated with fluid transport between the various compartments) are important. The effects of these terms however, need better understanding as it seems that using the 1D FDM based templates amplified the effects of altering these parameters. It can be postulated that the use of the source/sink terms in their current form may only be useful in one dimension. The compartmental foundation of the current MPET system may well have to be augmented to account for the added spatial dimensionality in the transfer of fluid between the various blood and CSF/ISF compartments. Closer inspection of the source/sink terms in equation (2.41) shows the reliance on the pressure difference between two compartments. Enhancing the ability of the source terms to capture spatial variations will add substantial detail to such a modelling framework. As hydrostatic pressure is the driving force behind the MPET framework, it is important to appreciate the important contribution of incorporating the colloid osmotic pressure (and possibly the full set of Starling's forces) within the intercompartmental transfer mechanism. This would assists in the more accurate modelling of the capillary filtration process through via the fluid content in the capillary compartment.

Additional limitations to the model include the incorporation of arterial and venous segments within a general continuum methodology, which is slightly counter-intuitive. The reasoning behind this assumption is that within the parenchyma, arterioles and venules are always in close proximity to feeding arteries and draining veins, even though the latter vessels are in much smaller numbers. Their importance in the case of the simple hydrocephalic model proposed in this work is evident in the boundary conditions of the model, hence their inclusion in higher spatial dimensions. A more exact representation of a voxel/continuum method would theoretically be to better represent the capillary bed, with the possible inclusion of the efferent and afferent arterioles, in addition to a glial compartment. Furthermore, a feedback mechanism taking into account the biological response of the brain to pathological insult would also have to be investigated in order to better represent the natural physiological response. This mechanism would probably have to incorporate actions better suited in mimicking the blood brain barrier, such as the regulation of AQP4, in addition to other useful metrics, such as a micro-scale wall shear stress or the impact on tight junction modulation within a neurovascular unit.

It should also be reiterated that although the transient form of the fluid phases was finally utilised in three-dimensions, the static equilibrium equation for the multiple-network poroelastic medium was used. It is envisaged that the field equations will be extended to include the influence of the acceleration terms, further enhancing the detail that can be extracted from such a system. In addition, the modelling of a two or three -dimensional wave propagated in a porous medium infiltrated by four or more fluid compartments represents a very demanding challenge. Further complexity is exacerbated when requiring the time-domain to be catered for. Frequency limits will need to be investigated, and possible Biot specific adaptations to this problem include a Johnson-Koplik-Dashen (JKD) expression [391]. Recent efforts to produce tractable numerical techniques in this field include the work by Blanc *et al.* [392], however their results are limited to physical parameters which are constant and discontinuous across their modelled interfaces. This type of modelling platform is promising, however significant amendments and parallelisation will have to be made to allow for the realisation of continuously variable porous media, anisotropy and multiple scattering.

Mechanical properties play a big role in the accuracy of the MPET model, and fundamental uncertainties are complicated to overcome. In inhomogeneous multi-phasic materials such as brain parenchyma, the Poisson's ratio depends on the definition of strain in addition to the material properties and conditions of testing (drained or undrained). The definition of strain used is also important from the kinematic point of view [393]. The justification for using a value of $\nu = 0.35$ is given in the previous chapter. Promising studies in magnetic resonance elastography (MRE) and motion-sensitive phase contrast MRI are providing new avenues in quantifying volumetric strain, tissue compressibility, anisotropy and shear modulus, however there is no set of standard or globally accepted values currently in place [326,333,334,394-397]. Furthermore, maturation of parameters over time is also of paramount importance, since it would help in the assessment of HCP over longer time periods [398]. In the VPH-DARE project, various image based biomarkers will be gathered to help in the assessment of mechanical parameters of the solid matrix as a function of ageing and neurodegeneration. The same project will also allow for the estimation of permeability required

for the fluid phases, through an experimental investigation of micro-scale transport. Collaborators within the project will use a similar set up to that of Iliff *et al.* [98]. Promising novel techniques in imaging are also likely to play a role in this area in the near future, such as the use of acoustic techniques with microbubbles to obtain super resolution velocity maps of cerebral vasculature [399]. This will help bridge the gap in terms of acquiring experimentally relevant permeability values for the diffusion equations of the MPET system, in addition to a better understanding of astrocytic swelling, solute clearance and microscale fluid transport. These parameters are deemed highly important, since the contribution of the porosity (and therefore the effective stress) is likely to be a function of permeability, instead of the current linear relationship (constant Biot-Willis parameters used throughout) between fluid and the solid matrix displacement.

The functional relationship between permeability and strain will also be investigated, where full use of the Newton-Galerkin methodology presented in §4 will be made. It is likely that the relationship between permeability and strain will deviate from the relationship in equation (3.95), however the stability of the method allows for a wide spectrum of relationships to be incorporated. Possible relationships include the permeability as a function of any dimensionless quantity (such as the fluid content [288,389] of an individual, or the weighted combination of multiple compartments). The limits of the Newton-Galerkin approach under the VPH guided MPET template will have to be investigated, in order to provide estimates of the extent of compatibility across the full breadth of clinically relevant scenarios.

The MPET field equations are based on a linearized elasticity, and it is noted that Taylor & Miller [275] provide sound reasoning why this constitutive relationship is adequate for the study of HCP. It is trivial to suggest that with the time scales associated with the inclusion of the inertial terms (cardiac pulsations or breathing), the use of viscoelasticity (or more likely poroviscoleasticity [400,401]) will need to be used as a constitutive relation. The current work allows for the assessment of acute and chronic hydrocephalus under the auspice of linearized elasticity. However, under very large strains, which would be accompanied by substantial (and asymmetric) ventriculomegaly, a non-linearly elastic or poroviscoelastic constitutive law should also be assessed, in the event of severe over or under estimation of the ventricular dilation or compartmental pressures.

The transport law used in the fluid phase continuity equation (2.32) is Darcy's Law. In this system, one is able to use a variety of laws to describe the transport of percolating fluid. Darcy's law was used as it is was assumed that flow in the porous medium is laminar with low Reynolds number. However, it can be envisaged that at very low percolation speeds, the interaction between the fluid filled pores and surrounding matrix becomes increasingly important, and other more detailed applications of Darcy's law exists [403]. Other popular models include the Blake-Kozeny-Carman (BKC) and Ergun equations respectively. The prior is especially useful in describing highly complex flow through porous media. Capillary bundle models are unidirectional models limited to 1D flow situations, and depict flow channels as a bundle of tubes within the porous medium [404]. Corrugated capillary bundle models are used in modelling a pore space with converging and diverging characteristics [405]. A detailed and well written feature article on Non-Newtonian flow in porous media is that of Sochi [406],

where references are provided for BKC models utilising bundled capillaries, tangled capillaries and tortuosity. The main point to address here is that the MPET template can accommodate more elaborate transport laws, which better suit the specific rheology of the parenchymal medium. Distinction and interaction between different transport laws can for instance be made between white and grey matter, since it is known these would display separate anisotropic characteristics which could be served by more detailed fluid flux representations [395,407].

The more detailed numerical aspects of the poroelasticity equations and their solution methods need to be investigated in greater depth for the three dimensional cases. In the previous chapter, the transient formulation was developed for the three dimensional MPET system. The transient effects however, were focused on the diffusion equations of the fluid phases. The full inclusion of the inertial terms will result in a complicated and (in all likelihood) ill-conditioned system if no additional modifications are sought. Efficient and robust solvers will undoubtedly have to be investigated, preferably based on the Krylov subspace [408]. Researchers [409] have outlined in detail the effects of critical parameters (such a critical time step) for their FE integrated coupled poroelastic models. In addition, arguments are made on remedying ill-conditioning in addition to assessing the relationship of the critical time step to a proportional mixture of parameters of the solid matrix (such as Young's modulus), that of the percolating fluid (permeability) and element volume or area. Preconditioners can also play a pivotal role in the stabilisation of consolidation problems, and cannot be overlooked [410]. Stokes *et al.* [411] outline the care required when confronted with 3D poroelastic FEA of biological tissue, and warn of the threat of numerical instability with unknown magnitude and error type if the fluid phases are not checked for numerical instabilities. What is not discussed however, is the importance of the layout of the numerical template in handling the coupled systems, an area of which great emphasis was given in this work. From the solutions in the previous chapter, it could be seen that there was no sign of wild oscillations in the FEM based solutions, fortifying the robust and effective nature of the setup in handling large sparse system matrices. It is anticipated that further investigation into mixed finite elements will also be required to complete the simplex based assessment of poroelastic behaviour. Important contributions to sophisticated methodologies include the work by Wheeler et al [412], Korsawe *et al.* [413], Tchnonkova *et al.* [414], Rohan *et al.* [415] and Ferronato [416]. It will also be prudent to consider the novel approaches in solving Darcy's equations and Darcy-Stokes flow using mixed finite element methods [417,418]. Nearly incompressible elasticity may also be tackled through rigorous mathematical formulations such as that of Lamichhane [419,420]. Finally, more elaborate discretisation techniques in Isogeometric FEA [421] and Hybridizable Discontinous Galerkin (HDG) methods could also be pursued [422,423].

In light of the inevitable shift towards mixed finite element methods and discontinuous Galerkin (dG) based methods, important milestones were surpassed in developing such higher order methodologies. Further to the cG approach of the previous chapter which was based on linear triangles in two dimensions, a quadratic Lagrange triangle element based discretisation framework was also developed. As expected, a canonical basis for the space of quadratic polynomials was used, in the form $\{1, r, s, r^2, rs, s^2\}$. The Lagrange elements are C^0 continuous elements, meaning that they are continuous, but possess discontinuous derivatives across their boundaries (making them suitable to approximate any function in the H^1 space).

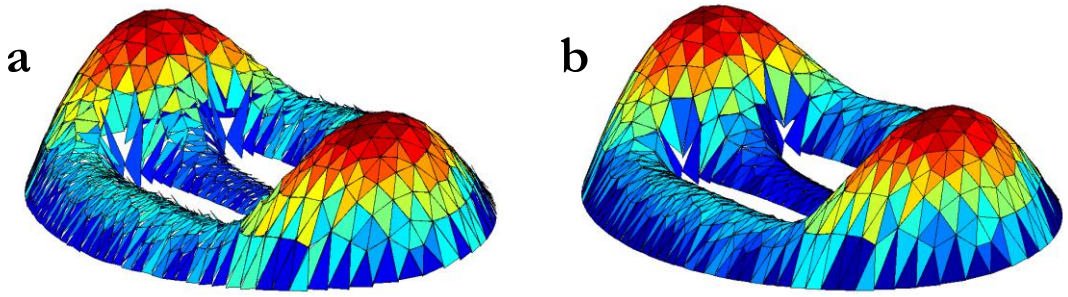

Figure 5.1. *Solution of a generic diffusion PDE. A simple representation of a skull with two punctured ellipses as ventricles, where a generic Neumann condition was ascribed on the boundaries, along with a source term equal to unity. The discretisation was based on the SIPG scheme. The maximum side length of the triangular simplex was 0.005 cm. The penalisation parameter was 0.5 in (a) and 8.5 in (b). It is evident that the penalty term influences the smoothness of the solution.*

In this setup, it was possible to implement curved boundaries, using two dimensional isoparametric mapping. The manner of creating the quadratic elements used a reformulated numbering scheme from the linear elements which allows for the renumbering of the edges, and which ultimately allows for the simple addition of nodes into the existing matrix structures for the node coordinates and element connectivity. This methodology allows for simple modifications to be made to the `MATLAB` code, specifically within the *for* loop for the stiffness matrix. As required, such a scheme is wrapped up with standard n^{th} order Gauss quadrature. This scheme produces higher quality meshes, however the deviation from the qualitative results already presented was minimal. The only improvements that are worth mentioning were at the level of the curved skull and ventricular boundary, which are expected. The main reason for embarking on this path of higher order elements was to accelerate the learning process for the possible use of other more advanced elements with higher continuity properties.

At some point within the VPH-DARE life-cycle, the use of MPET will incorporate more accurate transport and flow properties. An important consideration is that of mass balance. The family of cG methods used to devise the FEM based MPET template support a global mass balance over the whole of the cerebral domain. To remedy this with a more local approach, dG methods should be used [424-426]. A good comparison between generic properties of all the popular methods of discretising PDEs is given in Hesthaven & Warburton [425] and more specific comparisons between *cG* and *dG* methods is given by Rivière [424]. The use of local mesh refinement is also easier, since a typical set-up of such templates requires more general admissions when using the space of discontinuous polynomials.

There are various forms of the dG method in the literature, but the variations are limited to the choice of the specific penalization values (varies the jump of the solution between the elements). Variations include the Symmetric/Nonsymmetric Interior Penalty Galerkin method (*SIPG* & *NIPG*), Global Element method, *NIPG 0* and Incomplete Interior Penalty Galerkin method (*IIPG*) [424]. At this point in time, a *SIPG* scheme has been developed for the fluid phases in 2D (see Figure 5.1). A 3D extension has also been developed, and although in the preliminary stages, it has the ability to vary the order (n^{th} order) of the basis functions (which are not continuous across the element boundaries).

This section has thus far described some of the challenges that await application of the MPET methodology. This work is an initial step towards assessing the MPET system with a

numerical perspective. Addressing some of the challenges described in this section will allow the necessary formalism and mathematical rigour expected to cater for the adoption of evolving physiological concepts.

Modelling the parenchyma as a poroelastic medium with the ependymal lining of the ventricles and blood vessels treated as a linearly/nonlinearly elastic membrane model would aid in understanding the underlying effects of the poroelastic influence on pulsating pressure. This is a highly complex procedure, and is generally classified as a coupled FSI problem. A partitioned approach could be applied (in a similar spirit to the VPH project, where the fluidic aspects are left to CFD, whilst the poroelastic medium is solved using FEM) with the aid of Lie operator splitting and Arbitrary Lagrangian-Eulerian (ALE) mapping. This would allow the inertial components arising from any structural considerations to be merged with the fluidic elements in the boundary conditions, leaving the elastodynamic aspects to be solved separately. Similar methods have been recently attempted by Bukač *et al.* [427] and Muha and Čanić [428], for arterial blood flow and more conventional applications. It is also likely that peristaltic flow through a porous medium will also have to be considered in more detail in such a case [429]. Any future mathematical derivations aligned to developments in this area would have to keep in mind that the assumption of a rigid skull in adults may not exist in practice [430], and that any angular acceleration of the skull produces a definite brain deformation [431]. A non-rigid skull condition can also open the MPET framework into the realm of infantile HCP [432].

Fiber Tractography (FT) from DWI can be used simultaneously to the FEM template already produced. An FT and FEM methodology may be used to produce better surgical approaches to ETV, VPS, and EFV, since alternative pathways leading to the surgery could be sought (in addition to assessing more intricate features allied to craniotomy), and therefore possibly contributing to more favourable complication rates for the popular procedures associated with HCP. FT also contributes to a better understanding of oedema, and therefore a whole host of pathologies, as it would allow for the direct incorporation of microscale effects into any future modelling methodology. Additional aspects would be the insertion of curves on a current mesh. In 2D, recent work to improve this process has been conducted by Zaide and Ollivier-Gooch [433]. In such a setup, minimal adjustment to the original topology while maintaining the original sizing of the mesh was achieved. Additional meshing innovations could be used, such as that of Park *et al.* [434], where tracking of ventriculomegaly is tracked via a Level Set Method and warping technique, which can justify its use in large deformations. In general, mesh generation will be encountered as its quality can vary depending on the complexity of the geometries at hand.

Alternatives to shunting, ETV, and EFV can be investigated, such as the interesting case of endoscopic aqueductoplasty (EA) [435,436]. Erşahin [436] gives a candid view of the procedure based in his experience, and there are mixed feelings as to its general applicability due to its high reclosure rate [437]. Selection of patients is deemed highly important [436,438], and there is a growing consensus on its preferential use in cases involving an isolated fourth ventricle [438,439]. Performing the procedure on a membranous stenosis is also less traumatic than performing ETV. The use of a stent in this procedure has produced mixed results [439-441]. Recently, Schroeder *et al.* [437] compared CSF flow of patients undergoing ETV and EA

and emphasized the poorly understood nature of the reclosure of the aqueduct. Higher overall CSF flow was found in the ETV cases. Such a study would benefit from a CFD analysis similar to that in §3. Other investigations could include endoscopic transventricular transaqueductal Magendie and Luschka foraminoplasty for FVOO treatment [442], treatment of syringomyelia (associated with HCP [443]) with ETV (and assess Gardner's hydrodynamic theory [444]), and shunting towards the calvaria diploë via an extended MPET template (for bone) [445]. In the aforementioned models, use of control volume analysis in combination with flow sensitive MRI could be made. This is a non-invasive, fast and accurate technique that relates fluid flow and pressure information [446]. A patient risk framework can also be developed and coupled to the MPET system based on the concept of stochastic differential equation analysis of CSF, as described in the work by Raman [447]. Such a framework would help control a shunt valve mechanism.

The role of cilia has recently been investigated by Siyahhan *et al.* [448] in order to assess their impact on near wall dynamics. Choroid plexus pulsations were taken into account in these simulations through a source term in the continuity equation, whilst ventricular surface pulsations were applied through interpolated values via brain reconstruction. WSS dictated cilia orientation (assuming no pulsatility in CSF and wall). The impact of pulsatility was interesting, especially on the lateral ventricles, where the fluid phases were either dominated by inertia or the pulsating motion of the ependymal lining. Cilia was deemed to possess strong flow aligning capabilities in the areas it was measured in. A similar study utilising the MPET framework could be used in conjunction with the knowledge that experimental evidence (in mice) exists on ventriculomegaly being impacted by cilia defects of the choroid plexus and ventricular ependyma [449]. The near wall flow effects on the choroid plexus due to impairment of ciliary motility may influence drug transport in the brain [450], age dependent effects of Aβ transporters (and therefore AD development) and aquaporin-1 transport which is therefore likely to induce more noticeable effects at the periventricular region [451]. The influence of cilia lining the aqueduct would also be useful in assessing the influence of narrow regions on the directional beating of cilia and the subsequent near wall effects.

Enhancing the biofidelity of the MPET framework by attempting to model the effects of ageing or sex on different properties of the brain should also be expected. Prange and Marguiles [331] attempted this in 2002, by providing age-dependent material parameters for their modified Ogden formulation, the age and sex specific cerebral arterial inflow and CSF flow characteristics outlined in Daners *et al.* [452], tortuosity of arterioles in white matter, venous collagenosis and leukoaraiosis.

Investigations further down the line include the use of an extended (or separate system altogether) MPET framework (to include additional compartments or coupled with a simple lumped parameter model) to model the contribution of shear stress to the modulation of tight junctions and overall integrity of the blood-brain barrier, the influence of the pulsations of the Circle of Willis, fluid transport in Syringomyelia, NMO, Glaucoma and structural changes in the cerebral microvasculature during and after mild TBI (which could provide more detailed insight into venous compliance and ICP [453] in these patients) .

References

[1] Vardakis JC, Tully BJ, Ventikos Y (2013) Exploring the Efficacy of Endoscopic Ventriculostomy for Hydrocephalus Treatment via a Multicompartmental Poroelastic Model of CSF Transport: A Computational Perspective. PLoS one 8: e84577.

[2] Georqe A, Liu WH (1981) Computer Solution of Large Sparse Positive Definite Systems. Englewood Cliffs, N.J.: Prentice Hall, Inc.

[3] Detournay E, Cheng AH-D (1993) Fundamentals of poroelasticity. In: Fairhurst C, editor. Comprehensive Rock Engineering: Principles, Practice and Projects, Vol II, Analysis and Design Method: Pergamon Press. pp. 113-171.

[4] Schnell W, Gross D, Hauger W (1995) Technische Mechanik 2 - Elastostatik. Berlin: Springer Verlag.

[5] Hagedorn P (1995) Technische Mechanik, Band 2 : Festigkeitslehre. Frankfurt am Main: Verlag Harri Deutsch.

[6] Marinkovic S, Gibo H, Milisavljevic M, Djulejic V, Jovanovic V (2005) Microanatomy of the Intrachoroidal Vasculature of the Lateral Ventricle. Operative Neurosurgery 57: 22-36.

[7] Mayr WT, Pittock SJ, McClelland RL, Jorgensen NW, Noseworthy JH, et al. (2003) Incidence and prevalence of multiple sclerosis in Olmsted County, Minnesota, 1985-2000. Neurology 61: 1373-1377.

[8] Fujii K, Lenkey C, Rhoton A (1980a) Microsurgical anatomy of the choroidal arteries: Lateral and third ventricles. Journal of Neurosurgery 52: 165-188.

[9] Fujii K, Lenkey C, Rhoton A (1980b) Microsurgical anatomy of the choroidal arteries: Fourth ventricle and cerebellopontine angles. Journal of Neurosurgery 52: 504-524.

[10] Sharifi M, Ciolkowski M Fau - Krajewski P, Krajewski P Fau - Ciszek B, Ciszek B The choroid plexus of the fourth ventricle and its arteries.

[11] Prince M, Prina M, Guerchet M, International AsD (2013) World Alzheimer Report (Journey of Caring. An analysis of long-term care for dementia.). Alzheimer's Disease International (ADI).

[12] Gerland P, Raftery AE, Ševčíková H, Li N, Gu D, et al. (2014) World population stabilization unlikely this century. Science.

[13] United Nations DoEaSA, Population Division (2013) World Population Ageing 2013. New York.

[14] (NIA) NIoA, (NIH) NIoH, Services USDoHaH (2011) World Health Organization: Global Health and Aging.

[15] Effertz T, Mann K (2013) The burden and cost of disorders of the brain in Europe with the inclusion of harmful alcohol use and nicotine addiction. European Neuropsychopharmacology 23: 742-748.

[16] Collins PY, Patel V, Joestl SS, March D, Insel TR, et al. (2011) Grand challenges in global mental health. Nature 475: 27-30.

[17] Gustavsson A, Svensson M, Jacobi F, Allgulander C, Alonso J, et al. (2011) Cost of disorders of the brain in Europe 2010. European Neuropsychopharmacology 21: 718-779.

[18] Luengo-Fernandez R, Leal J, Gray AM (2012) UK research expenditure on dementia, heart disease, stroke and cancer: are levels of spending related to disease burden? European Journal of Neurology 19: 149-154.

[19] Fineberg NA, Haddad PM, Carpenter L, Gannon B, Sharpe R, et al. (2013) The size, burden and cost of disorders of the brain in the UK. J Psychopharmacol 27: 761-770.

[20] Di Marco LY, Marzo A, Muñoz-Ruiz M, Ikram MA, Kivipelto M, et al. (2014) Modifiable Lifestyle Factors in Dementia: A Systematic Review of Longitudinal Observational Cohort Studies. Journal of Alzheimer's Disease 42: 119-135.

[21] Plassman BL, Langa KM, Fisher GG, Heeringa SG, Weir DR, et al. (2007) Prevalence of Dementia in the United States: The Aging, Demographics, and Memory Study. Neuroepidemiology 29: 125-132.

[22] Chakravarty A (2004) Unifying concept for Alzheimer's disease, vascular dementia and normal pressure hydrocephalus – a hypothesis. Medical Hypotheses 63: 827-833.

[23] Bateman GA (2004) Pulse wave encephalopathy: a spectrum hypothesis incorporating Alzheimer's disease, vascular dementia and normal pressure hydrocephalus. Medical Hypotheses 62: 182-187.

[24] Matsumae M, Kikinis R, Morocz IA, Lorenzo AV, Sandor T, et al. (1996) Age-related changes in intracranial compartment volumes in normal adults assessed by magnetic resonance imaging. J Neurosurg 84: 982-991.

[25] Corns R, Martin A (2012) Hydrocephalus. Neurosurgery 30: 142-148.

[26] Sakka L, Coll G, Chazal J (2011) Anatomy and physiology of cerebrospinal fluid. European Annals of Otorhinolaryngology 128: 309-316.

[27] Cserr H (1971) Physiology of the Choroid Plexus. Physiological Reviews 51: 273-311.

[28] Irani D (2009) Cerebrospinal Fluid in Clinical Practice. Philadelphia, PA, USA: Saunders Elsevier.

[29] Knigge K, Schock S, Ching M, Scott D, Krobish-Dudley G (1974) Role of the ventricular system in neuroendocrine processes: synthesis and distribution of thyrotropin releasing factor (TRF) in the hypothalamus and third ventricle. Canadian Journal of Neurological Sciences 1: 74-84.

[30] Pollay M, Curl F (1967) Secretion of cerebrospinal fluid by the ventricular ependyma of the rabbit. American Journal of Physiology 213: 1031-1038.
[31] Johanson CE, Duncan III JA, Klinge PM, Brinker T, Stopa E, et al. (2008) Multiplicity of cerebrospinal fluid functions: New challenges in health and disease. Cerebrospinal Fluid Research 5: 1-32.
[32] Takahashi H, Tanaka H, Fujita N, Murase K, Tomiyama N (2011) Variation in supratentorial cerebrospinal fluid production rate in one day: measurement by nontriggered phase-contrast magnetic resonance imaging. Jpn J Radiol 29: 110-115.
[33] Redzic ZB, Segal MB (2004) The structure of the choroid plexus and the physiology of the choroid plexus epithelium. Advanced Drug Delivery Reviews 56: 1695-1716.
[34] Nilsson C, Stahlberg F, Thomsen C, Henriksen O, Herning M, et al. (1992) Circadian variation in human cerebrospinal fluid production measured by magnetic resonance imaging. Am J Physiol Regul Integr Comp Physiol 262: R20-R24.
[35] Charles R, Gahl G (2009) Imaging (Normal and Abnormal). Cerebrospinal Fluid Disorders: Informa Healthcare. pp. 66-109.
[36] Brinker T, Stopa E, Morrison J, Klinge P (2014) A new look at cerebrospinal fluid circulation. Fluids Barriers CNS 11: 10.
[37] MacAulay N, Zeuthen T (2010) Water transport between CNS compartments: contributions of aquaporins and cotransporters. Neuroscience 168: 941-956.
[38] Owler B, Pitham T, Wang D (2010) Aquaporins: relevance to cerebrospinal fluid physiology and therapeutic potential in hydrocephalus. Cerebrospinal Fluid Research 7: 1-12.
[39] Praetorius J, Nielsen S (2006) Distribution of sodium transporters and aquaporin-1 in the human choroid plexus. American Journal of Physiology 291: 59-67.
[40] Damkier HH, Brown PD, Praetorius J (2010) Epithelial pathways in choroid plexus electrolyte transport. Physiology 25: 239-249.
[41] Speake T, Whitwell C, Kajita H, Majid A, Brown P (2001) Mechanism of CSF secretion by the Choroid Plexus. Microscopy Research and Technique 52: 49-59.
[42] Cushing H. Studies in Intracranial physiology & surgery: the third circulation, the Hypophysis, the Gliomas : the Cameron prize lectures delivered at the University of Edinburgh; 1925. Oxford.
[43] Bruni JE (1998) Ependymal Development, Proliferation and Functions: A Review. Microscopy Research and Technique 41: 2-13.
[44] Collins P, Fairman S (1990) Repair of the ependyma in hydrocephalic brains. Neuropathology & Applied Neurobiology 16: 45-56.
[45] Sarnat HB (1995) Ependymal reactions to injury. A review. Journal of Neuropatology & Experimental Neurology 54: 1-15.
[46] Schipper HM (1998) Astrocytes in Brain Aging and Neurodegenration. Texas: R.G. Landes Company.
[47] Luo J, Shook B, Daniels S, Conover J (2008) Subventricular Zone-Mediated Ependyma Repair in the Adult Mammalian Brain. The Journal of Neuroscience 28: 3804-3813.
[48] Faivre E (1854) Recherches sur la Structure du conarium ct des plexus choroides chez l'homme et chez les animaux. Compt Rend Acad d Sc xxxiv.
[49] Dandy WE (1929) Where is Cerebrospinal Fluid Absorbed? JAMA 92: 2012-2014.
[50] Abbott JN (2004) Evidence for bulk flow of brain interstitial fluid: significance for physiology and pathology. Neurochemistry International 45: 545-552.
[51] Linninger AA, Xenos M, Zhu DC, Somayaji MR, Kondapalli S, et al. (2007) Cerebrospinal Fluid Flow in the Normal and Hydrocephalic Human Brain. IEEE Transactions on Biomedical Engineering 54: 291-302.
[52] Gupta S, Soellinger M, Boesiger P, Poulikakos D, Kurtcuoglu V (2009) Three-Dimensional Computational Modeling of Subject-Specific Cerebrospinal Fluid Flow in the Subarachnoid Space. Biomechanical Engineering 131.
[53] Redzic ZB (2013) Studies on the human choroid plexus in vitro. Fluids and Barriers of the CNS 10: 1-7.
[54] Strazielle N, Egea JFG (2000) Choroid Plexus in the Central Nervous System: Biology and Physiopathology. Journal of Neuropathology and Experimental Neurology 59: 561-574.
[55] Redzic Z, Preston J, Duncan J, Chodobski A, Chodobska J (2005) The Choroid Plexus-Cerebrospinal Fluid System: From Development to Aging. Current Topics in Developmental Biology 71: 1-52.
[56] May P, Sgouros S (2010) Treatment of Hydrocephalus in the Modern Era (1950s-Current Date). In: Mallucci C, Sgouros S, editors. Cerebrospinal Fluid Disorders. New York: Informa Healthcare USA, Inc. pp. 63-109.
[57] Wolburg H, Paulus W (2010) Choroid Plexus: biology and pathology. Acta Neuropathology 119: 75-88.
[58] Dziegielewska KM, Ek J, Habgood MD, Saunders NR (2001) Development of the choroid plexus. Microscopy Research and Technique 52: 5-20.
[59] King LS, Agre P (1996) Pathophysiology of the aquaporin water channels. Amn Rev Physiol 58: 619-648.
[60] Agre P (2006) The Aquaporin Water Channels. Proceedings of the American Thoracic Society 3: 5-13.

[61] Buffoli B (2010) Aquaporin biology and nervous system. Current Neuropharmacology 8: 97-104.
[62] Gutierrez AM, Gonzalez E, Echevarria M, Hernandez CS, Whittembury G (1995) The proximal cell tube (PST) basolateral cell membrane water channel: selectivity characterisitics. Journal of Membr Biol 143: 189-197.
[63] Papadopoulos MC, Verkman AS (2013) Aquaporin water channels in the nervous system. Nat Rev Neurosci 14: 265-277.
[64] Day RE, Kitchen P, Owen DS, Bland C, Marshall L, et al. (2014) Human aquaporins: Regulators of transcellular water flow. Biochimica et Biophysica Acta (BBA) - General Subjects 1840: 1492-1506.
[65] Ishibashi K (2006) Aquaporin subfamily with unusual NPA boxes. Biochimica et Biophysica Acta 1758: 989-993.
[66] Yakata K, Hiroaki Y, Ishibashi K, Sohara E, Sasaki S, et al. (2007) Aquaporin-11 containing a divergent NPA motif has normal water channel activity. Biochimica et Biophysica Acta 1768: 688-693.
[67] Kozaki K, Ishii D, Ishibashi K (2008) Intracellular aquaporins: clues for intracellular water transport. Eur J Physiol 456: 701-707.
[68] Benga O, Huber J, Vincent (2012) Brain water channel proteins in health and disease Molecular Aspects of Medicine 33: 562-578.
[69] Wang D, Nykanen M, Yang N, Winlaw D, North K, et al. (2011) Altered cellular localization of aquaporin-1 in experimental hydrocephalus in mice and reduced ventriculomegaly in aquaporin-1 deficiency. Molecular and Cellular Neuroscience 46: 318-324.
[70] Praetorius J (2007) Water and solute secretion by the choroid plexus. Archive European Journal of Physiology 454: 1-18.
[71] Benga G (2012) The first discovered water channel protein, later called aquaporin 1: Molecular characteristics, functions and medical implications. Molecular Aspects of Medicine 33: 518-534.
[72] Zelenina M (2010) Regulation of brain aquaporins. Neurochemistry International 57: 468-488.
[73] Benfenati V, Ferroni S (2010) Water transport between CNS compartments: functional and molecular interactions between aquaporins and ion channels. Neuroscience 168: 926-940.
[74] Zador Z, Bloch O, Yao X, Manley GT (2007) Aquaporins: role in cerebral edema and brain water balance. In: Weber JT, Maas AIR, editors. Progress in Brain Research: Elsevier. pp. 185-194.
[75] Yool AJ (2007) Aquaporins: Multiple Roles in the Central Nervous System. Neuroscientist 13: 470-485.
[76] Arcienega II, Brunet JF, Bloch J, Badut J (2010) Cell locations for AQP1, AQP4 and 9 in the non-human primate brain. Neuroscience 167: 1103-1114.
[77] Badaut J, Regli L (2004) Distribution and possible roles of aquaporin 9 in the brain. Neuroscience 129: 969-979.
[78] Fukuda AM, Pop V, Spagnoli D, Ashwal S, Obenaus A, et al. (2012) Delayed increase of astrocytic aquaporin 4 after juvenile traumatic brain injury: Possible role in edema resolution? Neuroscience 222: 366-378.
[79] Huber VJ, Tsujita M, Nakada T (2012) Aquaporins in drug discovery and pharmacotherapy. Molecular Aspects of Medicine 33: 691-703.
[80] Loreto C, Reggio E (2010) Aquaporin and vascular diseases. Curr Neuropharmacol 8: 105-111.
[81] Thrane AS, Rangroo Thrane V, Nedergaard M (2014) Drowning stars: reassessing the role of astrocytes in brain edema. Trends in Neurosciences 37: 620-628.
[82] Thrane AS, Rappold PM, Fujita T, Torres A, Bekar LK, et al. (2011) Critical role of aquaporin-4 (AQP4) in astrocytic Ca2+ signaling events elicited by cerebral edema. Proc Natl Acad Sci U S A 108: 846-851.
[83] Ribatti D, Ranieri G, Annese T, Nico B (2014) Aquaporins in cancer. Biochimica et Biophysica Acta (BBA) - General Subjects 1840: 1550-1553.
[84] Verkman AS, Hara-Chikuma M, Papadopoulos MC (2008) Aquaporins--new players in cancer biology. J Mol Med (Berl) 86: 523-529.
[85] Skjolding AD, Holst AV, Broholm H, Laursen H, Juhler M (2013) Differences in distribution and regulation of astrocytic aquaporin-4 in human and rat hydrocephalic brain. Neuropathology and Applied Neurobiology 39: 179-191.
[86] Stivaros S, Jackson A (2007) Changing concepts of cerebrospinal fluid hydrodynamics: Role of phasecontrast magnetic resonance imaging and implication for cerebral microvascular disease. Neurotherapeutics 4: 511–522.
[87] Johnston M (2003) The importance of lymphatics in cerebrospinal fluid transport. Lymphatic research and Biology 1: 41-46.
[88] Johnston M, Papaiconomou C (2002) Cerebrospinal Fluid Transport: a Lymphatic Perspective. News Physiol Sci 17: 227-230.
[89] Pollay M (2010) The function and structure of the cerebrospinal fluid outflow system. Cerebrospinal Fluid Research 7: 1-20.
[90] Walter B, Valera V, Takahashi S, Ushiki T (2006) The olfactory route for cerebrospinal fluid drainage into the peripheral lymphatic system. Neuropathology and Applied Neurobiology 32: 388-396.
[91] Edsbagge M, Tsell M, Jacobsson L, Wikkelso C (2004) Spinal CSF absorption in healthy individuals. American Journal Physiology Reguationl Integrative Computational Physiology 287: 1450-1455.

[92] Oshio K, Watanabe H, Song Y, Verkman AS, Manley GT (2005) Reduced cerebrospinal fluid production and intracranial pressure in mice lacking choroid plexus water channel Aquaporin-1. The FASEB Journal 19: 76-78.
[93] Bloch O, Auguste K, Manley G, Verkman A (2006) Accelerated progression of kaolin-induced hydrocephalus in aquaporin-4 deficient mice. Cerebral Blood Flow Metabolism 26: 1527-1537.
[94] Mao X, Enno T, Del Bigio M (2006) Aquaporin-4 changes in rat brain with severe hydrocephalus. European Journal of Neuroscience 23: 2929-2936.
[95] Shen X, Miyajima M, Ogino I, Arai H (2006) Expression of the water channel protein aquaporin-4 in the H-Tx rat: possible compensatory role in spontaneously arrested hydrocephalus. Neurosurgery 105: 459-464.
[96] Oi S, Rocco CD (2006) Proposal of "evolution theory in cerebrospinal fluid dynamics" and minor pathway hydrocephalus in developing immature brain. Child's Nervous System 22: 662-669.
[97] Symss N, Oi S (2013) Theories of cerebrospinal fluid dynamics and hydrocephalus: historical trend. J Neurosurg Pediatr 11: 170-177.
[98] Iliff JJ, Wang M, Liao Y, Plogg BA, Peng W, et al. (2012) A Paravascular Pathway Facilitates CSF Flow Through the Brain Parenchyma and the Clearance of Interstitial Solutes, Including Amyloid β. Sci Transl Med 4: 1-11.
[99] Bulat M, Klarica M (2011) Recent insights into a new hydrodynamics of the cerebrospinal fluid. Brain Research Reviews 65: 99-112.
[100] Skjolding AD, Rowland IJ, Sogaard LV, Praetorius J, Penkowa M, et al. (2010) Hydrocephalus induced dynamic spatiotemporal regulation of aquaporin-4 expression in the rat brain. Cerebrospinal Fluid Research 7: 1-13.
[101] Esiri MM, Gay D (1990) Immunological and neuropathological significance of the Virchow-Robin space. Journal of the Neurological Sciences 100: 3-8.
[102] Tully B, Ventikos Y (2011) Cerebral water transport using multiple-network poroelastic theory: application to normal pressure hydrocephalus. Journal of Fluid Mechanics 667: 188-215.
[103] Rekate HL (2009) A contemporary definition and classification of hydrocephalus. Semin Pediatr Neurol 16: 9-15.
[104] Thompson D (2009) Hydrocephalus. Neurosurgery 27: 130-134.
[105] Stagno V, Navarette EA, Mirone G, Esposito F (2012) Management of Hydrocephalus Around the World. World Neurosurgery.
[106] Vardakis JC, Tully BJ, Ventikos Y (2013) Multicompartmental Poroelasticity as a Platform for the Integrative Modeling of Water Transport in the Brain. In: Holzapfel GA, Kuhl E, editors. Computer Models in Biomechanics: Springer Netherlands. pp. 305-316.
[107] Wilson R, Williams M (2009) Disorders of intracranial pressure and cerebrospinal fluid circulation. In: Irani D, editor. Cerebrospinal Fluid in Clinical Practice. Philadelphia: Saunders Elsevier. pp. 99-104.
[108] Stewart D, Johnson D, Myers G (1975) Hydrocephalus as a complication of jugular catheterization during total parenteral nutrition. J Pediatr Surgery 10: 771-777.
[109] Biedert S, Wolfshörndl H (1994) The Extraventricular Obstructive Hydrocephalus. Fortschr Neurol Psychiatr 62: 405-408.
[110] Karmazyn B, Dagan O, Vidne BA, Horev G, Kornreich L (2002) Neuroimaging findings in neonates and infants from superior vena cava obstruction after cardiac operation. Pediatr Radiol 32: 806-810.
[111] Greitz D (2004) Radiological assessment of hydrocephalus: new theories and implications for therapy. Neurosurg Rev 27: 145-165.
[112] Bergsneider M, Egnor MR, Johnston M, Kranz D, Madsen JR, et al. (2006) What we don't (but should) know about hydrocephalus. Journal of Neurosurgery:Pediatrics 104: 157-159.
[113] Krefft TA, Graff-Radford NR, Lucas JA, Mortimer JA (2004) Normal pressure hydrocephalus and large head size. Alzheimer Dis Assoc Disord 18: 35-37.
[114] Bech-Azeddine R, Gjerris F (2009) Idiopathic Normal Pressure Hydrocephalus. Cerebrospinal Fluid Disorders: CRC Press. pp. 284-299.
[115] Luetmer PH, Huston J, Friedman JA, Dixon GR, Petersen RC, et al. (2002) Measurement of cerebrospinal fluid flow at the cerebral aqueduct by use of phase-contrast magnetic resonance imaging: Technique validation and utility in diagnosing idiopathic normal pressure hydrocephalus. Neurosurgery 50: 534–543.
[116] Hakim S, Adams RD (1965) The special clinical problem of symptomatic hydrocephalus with normal cerebrospinal fluid pressure. Observations on cerebrospinal fluid hydrodynamics. J Neurol Sci 2: 307-327.
[117] Marmarou A, Young HF, Aygok GA, Sawauchi S, Tsuji O, et al. (2005) Diagnosis and management of idiopathic normal-pressure hydrocephalus: a prospective study in 151 patients. J Neurosurg 102: 987-997.
[118] Kang K, Ko P-W, Jin M, Suk K, Lee H-W (2014) Idiopathic normal-pressure hydrocephalus, cerebrospinal fluid biomarkers, and the cerebrospinal fluid tap test. Journal of Clinical Neuroscience 21: 1398-1403.
[119] Shprecher D, Schwalb J, Kurlan R (2008) Normal pressure hydrocephalus: diagnosis and treatment. Curr Neurol Neurosci Rep 8: 371-376.
[120] Rosseau G (2011) Normal Pressure Hydrocephalus. Disease-a-Month 57: 615-624.

[121] Williams MA, Relkin NR (2013) Diagnosis and management of idiopathic normal-pressure hydrocephalus. Neurol Clin Pract 3: 375-385.
[122] Malm J, Graff-Radford NR, Ishikawa M, Kristensen B, Leinonen V, et al. (2013) Influence of comorbidities in idiopathic normal pressure hydrocephalus — research and clinical care. A report of the ISHCSF task force on comorbidities in INPH. Fluids and Barriers of the CNS 10.
[123] Relkin N, Marmarou A, Klinge P, Bergsneider M, Black PM (2005) Diagnosing idiopathic normal-pressure hydrocephalus. Neurosurgery 57: S4-16; discussion ii-v.
[124] Gallia GL, Rigamonti D, Williams MA (2006) The diagnosis and treatment of idiopathic normal pressure hydrocephalus. Nat Clin Pract Neuro 2: 375-381.
[125] Brean A, Eide PK (2008) Prevalence of probable idiopathic normal pressure hydrocephalus in a Norwegian population. Acta Neurol Scand 118: 48-53.
[126] Tanaka N, Yamaguchi S, Ishikawa H, Ishii H, Meguro K (2009) Prevalence of possible idiopathic normal-pressure hydrocephalus in Japan: the Osaki-Tajiri project. Neuroepidemiology 32: 171-175.
[127] Krauss JK, Halve B (2004) Normal pressure hydrocephalus: survey on contemporary diagnostic algorithms and therapeutic decision-making in clinical practice. Acta Neurochirurgica 146: 379-388.
[128] Tisell M, Hoglund M, Wikkelso C (2005) National and regional incidence of surgery for adult hydrocephalus in Sweden. Acta Neurol Scand 112: 72-75.
[129] Klassen BT, Ahlskog JE (2011) Normal pressure hydrocephalus: how often does the diagnosis hold water? Neurology 77: 1119-1125.
[130] Marmarou A, Young HF, Aygok GA (2007) Estimated incidence of normal pressure hydrocephalus and shunt outcome in patients residing in assisted-living and extended-care facilities. Neurosurg Focus 22: E1.
[131] Conn HO (2011) Normal pressure hydrocephalus (NPH): more about NPH by a physician who is the patient. Clinical Medicine 11: 162-165.
[132] Alisky J (2008) Normal pressure hydrocephalus co-existing with a second dementia disorder. Neuropsychiatr Dis Treat 4: 301-304.
[133] Evans WA, Jr (1942) An encephalographic ratio for estimating ventricular enlargement and cerebral atrophy. Archives of Neurology & Psychiatry 47: 931-937.
[134] Tullberg M, Jensen C, Ekholm S, Wikkelso C (2001) Normal pressure hydrocephalus: vascular white matter changes on MR images must not exclude patients from shunt surgery. AJNR Am J Neuroradiol 22: 1665-1673.
[135] Sasaki M, Honda S, Yuasa T, Iwamura A, Shibata E, et al. (2008) Narrow CSF space at high convexity and high midline areas in idiopathic normal pressure hydrocephalus detected by axial and coronal MRI. Neuroradiology 50: 117-122.
[136] Akai K, Uchigasaki S, Tanaka U, Komatsu A (1987) Normal pressure hydrocephalus. Neuropathological study. Acta Pathol Jpn 37: 97-110.
[137] Bech RA, Waldemar G, Gjerris F, Klinken L, Juhler M (1999) Shunting effects in patients with idiopathic normal pressure hydrocephalus; correlation with cerebral and leptomeningeal biopsy findings. Acta Neurochir (Wien) 141: 633-639.
[138] Smith EE (2010) Leukoaraiosis and Stroke. Stroke 41: S139-S143.
[139] Boon AJW, Tans JTJ, Delwel EJ, Egeler-Peerdeman SM, Hanlo PW, et al. (1999) Dutch Normal-Pressure Hydrocephalus Study: the role of cerebrovascular disease. Journal of Neurosurgery 90: 221-226.
[140] Graff-Radford NR, Knopman DS, Penman AD, Coker LH, Mosley TH (2013) Do systolic BP and pulse pressure relate to ventricular enlargement? Eur J Neurol 20: 720-724.
[141] Qvarlander S, Lundkvist B, Koskinen LO, Malm J, Eklund A (2013) Pulsatility in CSF dynamics: pathophysiology of idiopathic normal pressure hydrocephalus. J Neurol Neurosurg Psychiatry 84: 735-741.
[142] Dombrowski S, Crutchfield K, Ligon K, Becker J, Luciano M (2009) Evidence for CSF-vascular compliance coupling in normal pressure hydrocephalus. Cerebrospinal Fluid Research 6: 1-2.
[143] Baledent O, Gondry-Jouet C, Meyer ME, De Marco G, Le Gars D, et al. (2004) Relationship between cerebrospinal fluid and blood dynamics in healthy volunteers and patients with communicating hydrocephalus. Invest Radiol 39: 45-55.
[144] Bateman GA (2008) The pathophysiology of idiopathic normal pressure hydrocephalus: cerebral ischemia or altered venous hemodynamics? AJNR Am J Neuroradiol 29: 198-203.
[145] Kalani MYS, Turner JD, Nakaji P (2013) Treatment of refractory low-pressure hydrocephalus with an active pumping negative-pressure shunt system. Journal of Clinical Neuroscience 20: 462-466.
[146] Hunn BHM, Mujic A, Sher I, Dubey AK, Peters-Willke J, et al. (2014) Successful treatment of negative pressure hydrocephalus using timely titrated external ventricular drainage: a case series. Clinical Neurology and Neurosurgery 116: 67-71.
[147] Filippidis AS, Kalani MY, Nakaji P, Rekate HL (2011) Negative-pressure and low-pressure hydrocephalus: the role of cerebrospinal fluid leaks resulting from surgical approaches to the cranial base. J Neurosurg 115: 1031-1037.
[148] Akins P, Guppy K, Axelrod Y, Chakrabarti I, Silverthorn J, et al. (2011) The Genesis of Low

Pressure Hydrocephalus. Neurocritical Care 15: 461-468.
[149] Levine DN (2008) Intracranial pressure and ventricular expansion in hydrocephalus: Have we been asking the wrong questions? J Neurol Sci 269: 1-11.
[150] Clarke MJ, Maher CO, Nothdurft G, Meyer F (2006) Very low pressure hydrocephalus. Report of two cases. J Neurosurg 105: 475-478.
[151] Cinalli G, Spennato P, Aliberti F, Cianciulli E (2010) Aqueductal stenosis. In: Mallucci C, Sgouros S, editors. Cerebrospinal Fluid Disorders. New York: Informa Healthcare USA, Inc. pp. 154-188.
[152] Jellinger G (1986) Anatomopathology of non-tumoral aqueductal stenosis. Journal Neurosurgical Science 1: 1-16.
[153] Beckett RS, Netsky MG, Zimmerman HM (1950) Developmental Stenosis of the Aqueduct of Sylvius. Am J Pathol 26: 755–787.
[154] Russel D (1949) Observations on the pathology of hydrocephalus. Med Res Council,spec rep series No265 His Majesty's Stationary Office, London.
[155] Spennato P, Tazi S, Bekaert O, Cinalli G, Decq P (2013) Endoscopic Third Ventriculostomy for idiopathic Aqueductal Stenosis. World Neurosurgery.
[156] Turnbull IM, Drake CG (1966) Membranous Occlusion of the Aqueduct of Sylvius. Journal of Neurosurgery 24: 24-34.
[157] Lifshutz JI, Johnson WD (2001) History of hydrocephalus and its treatments. Neurosurg Focus 11: E1.
[158] Warf BC (2010) Pediatric hydrocephalus in East Africa: prevalence, causes, treatments, and strategies for the future. World Neurosurg 73: 296-300.
[159] Warf BC (2010) Treatment of Hydrocephalus in the Developing World. In: Mallucci C, Sgouros S, editors. Cerebrospinal Fluid Disorders. New York: Informa Healthcare USA, Inc. pp. 555-565.
[160] Bergsneider M, Miller C, Vespa PM, Hu X (2008) Surgical management of adult hydrocephalus. Neurosurgery 62: SHC-643-SHC-660610.1227/1201.neu.0000316269.0000382467.f0000316267.
[161] Fritsch MJ, Doerner L, Kienke S, Mehdorn HM (2005) Hydrocephalus in children with posterior fossa tumors: role of endoscopic third ventriculostomy. J Neurosurg 103: 40-42.
[162] Torres-Corzo JG, Tapia-Perez JH, Vecchia RR, Chalita-Williams JC, Sanchez-Aguilar M, et al. (2010) Endoscopic management of hydrocephalus due to neurocysticercosis. Clin Neurol Neurosurg 112: 11-16.
[163] Kakarla UK, Kim LJ, Chang SW, Theodore N, Spetzler RF (2008) Safety and Accuracy of Bedside External Ventricular Drain Placement. Operative Neurosurgery 63: 162-167.
[164] Sgouros S, Kombogiorgas D (2010) Cerebrospinal Fluid Shunts. In: Mallucci C, Sgouros S, editors. Cerebrospinal Fluid Disorders. New York: Informa Healthcare USA, Inc. pp. 438-456.
[165] Sainte-Rose C, Piatt J, Renier D, Pierre-Kahn A, Hirsch J, et al. (1992) Mechanical complications in shunts. Pediatr Neurosurg 17: 2-9.
[166] Blount J, Campbell J, Haines S (1993) Complications in ventricular cerebrospinal fluid shunting. Neurosurg Clin N Am 4: 633-656.
[167] Sainte-Rose C (1993) Shunt obstruction: a preventable complication? Pediatr Neurosurg 19: 156-164.
[168] Sgouros S, Malluci C, Walsh A, Hockley A (1995) Long-Term Complications of Hydrocephalus. Pediatric Neurosurgery 23: 127-132.
[169] Boch A, Hermelin E, Sainte-Rose C, Sgouros S (1998) Mechanical dysfunction of ventriculoperitoneal shunts caused by calcification of the silicone rubber catheter. Journ Neurosurg 88: 975-982.
[170] Wang K, Chang W, Shih T, Huang C, Tsai N, et al. (2004) Infection of cerebrospinal fluid shunts: causative pathogens, clinical features, and outcomes. Jpn J Infect Dis 57: 44-48.
[171] Siomin V, Constantini S (2010) Repeat Endoscopic Third Ventriculostomy. In: Mallucci C, Sgouros S, editors. Cerebrospinal Fluid Disorders. New York: Informa Healthcare USA, Inc. pp. 522-523.
[172] Wells DL, Allen JM (2013) Ventriculoperitoneal Shunt Infections in Adult Patients. AACN Advanced Critical Care 24: 13-14 10.1097/NCI.1090b1013e3182860b3182862.
[173] Verma A, Mohan S, Gupta A (2011) Ventriculo-peritoneal shunts can cause liver injury, juxta and intrahepatic pseudocysts: Imaging findings and review literature. Clinical Neurology and Neurosurgery.
[174] Patwardhan RV, Nanda A (2005) Implanted Ventricular Shunts in the United States: The billion dollar a year cost of hydrocephalus treatment. Neurosurgery 56: 139-145.
[175] Nigim F, Critchlow JF, Schneider BE, Chen C, Kasper EM (2014) Shunting for hydrocephalus: analysis of techniques and failure patterns. Journal of Surgical Research 191: 140-147.
[176] Nakajima M, Miyajima M, Ogino I, Sugano H, Akiba C, et al. (2014) Use of External Lumbar Cerebrospinal Fluid Drainage and Lumboperitoneal Shunts with Strata NSC Valves in Idiopathic Normal Pressure Hydrocephalus: A Single-Center Experience. World Neurosurgery.
[177] Hellwig D, Grotenhuis J, Tirakotai W, Riegel T, Schulte D, et al. (2005) Endoscopic third ventriculostomy for obstructive hydrocephalus. Neurosurgical Review 28: 1-34.

[178] Ferrer A, Notaris Md (2012) Third Ventriculostomy and Fourth Ventricle outlets obstruction. World Neurosurgery.
[179] Mugamba J, Stagno V (2012) Indication for ETV. World Neurosurgery.
[180] Woodworth GF, See A, Bettegowda C, Batra S, Jallo GI, et al. (2012) Predictors of Surgery-Free Outcome in Adult Endoscopic Third Ventriculostomy. World Neurosurgery 78: 312-317.
[181] Vogel TW, Bahuleyan B, Robinson S, Cohen AR (2013) The role of endoscopic third ventriculostomy in the treatment of hydrocephalus. J Neurosurg: Pediatrics: 1-8.
[182] Gliemroth J, Käsbeck E, Kehler U (2014) Ventriculocisternostomy versus ventriculoperitoneal shunt in the treatment of hydrocephalus: A retrospective, long-term observational study. Clinical Neurology and Neurosurgery 122: 92-96.
[183] Rangel-Castilla L, Barber S, Zhang YJ (2012) The Role of Endoscopic Third Ventriculostomy in the Treatment of Communicating Hydrocephalus. World Neurosurgery 77: 555-560.
[184] Dusick JR, McArthur DL, Bergsneider M (2008) Success and complication rates of endoscopic third ventriculostomy for adult hydrocephalus: a series of 108 patients Surgical Neurology 69: 5-15.
[185] Shi J, Fu W, Wu Q, Zhang H, Zheng Z, et al. (2012) Endoscopic third ventriculostomy associated 3D-construcive inference steady state MRI for obstructed hydrocephalus: A retrospective study. linical neurology and neurosurgery: Article in Press.
[186] Takasuna H, Goto T, Kakizawa Y, Miyahara T, Koyama J, et al. (2012) Use of a micromanipulator system (NeuRobot) in endoscopic neurosurgery. Journal of Clinical Neuroscience 19: 1553-1557.
[187] Gaab MR (2013) Instrumentation: Endoscopes and Equipment. World Neurosurgery 79: S14.e11-S14.e21.
[188] Farin A, Aryan HE, Ozgur B, Parsa A, Levy M (2005) Endoscopic Third Ventriculostomy. 1.
[189] Teo C, Kadrian D, Hayhurst C (2012) Endoscopic Management of Complex Hydrocephalus. World Neurosurgery: 1-8.
[190] Grotenhuis JA, Al-Kheshen SMA-S, Mohammed KE (2010) Endoscopy for Hydrocephalus—General Aspects. In: Mallucci C, Sgouros S, editors. Cerebrospinal Fluid Disorders. New York: Informa Healthcare USA, Inc. pp. 496-507.
[191] Decq P, Guerinel CL, Palfi S, Djindjian M, Keravel Y, et al. (2000) A new device for endoscopic third ventriculostomy. J Neurosurgery 93: 509-512.
[192] Brasil AV, Schneider FL (1993) Anatomy of Liliequist's membrane. Neurosurgery 32: 956-960; discussion 960-951.
[193] Guillaume DJ, Teo C (2010) Endoscopic Management of Specific Disease Entities. In: Mallucci C, Sgouros S, editors. Cerebrospinal Fluid Disorders. New York: Informa Healthcare USA, Inc. pp. 508-517.
[194] Pitskhelauri DI, Konovalov AN, Kopachev DN, Samborsky DI, Melnikova-Pitskhelauri TV (2012) Microsurgical Third Ventriculostomy with Stenting in Intrinsic Brain Tumors Involving Anterior Third Ventricle. World Neurosurgery 77: 785.e783-785.e789.
[195] Kandaswamy J, Mallucci C (2010) ETV in Shunt Malfunction. In: Mallucci C, Sgouros S, editors. Cerebrospinal Fluid Disorders. New York: Informa Healthcare USA, Inc. pp. 519-521.
[196] Hellwig D, Giordano M, Kappus C (2013) Redo Third Ventriculostomy. World Neurosurgery 79: S22.e13-S22.e20.
[197] Kulkarni AV, Drake JM, Kestle JRW, Mallucci CL, Sgouros S, et al. (2010) Endoscopic Third Ventriculostomy Vs Cerebrospinal Fluid Shunt in the Treatment of Hydrocephalus in Children: A Propensity Score - Adjusted Analysis. Neurosurgery 67: 588-593.
[198] Kulkarni AV (2010) Predicting Success of ETV in Children with Hydrocephalus. In: Mallucci C, Sgouros S, editors. Cerebrospinal Fluid Disorders. New York: Informa Healthcare USA, Inc. pp. 526-527.
[199] Kandasamy J, Yousaf J, Mallucci C (2013) Third Ventriculostomy in Normal Pressure Hydrocephalus. World Neurosurgery 79: S22.e21-S22.e27.
[200] Bisht A, Suri A, Bansal S, Chandra PS, Kumar R, et al. (2014) Factors affecting surgical outcome of endoscopic third ventriculostomy in congenital hydrocephalus. Journal of Clinical Neuroscience 21: 1483-1489.
[201] Salvador SF, Oliveira J, Pereira J, Barros H, Vaz R (2014) Endoscopic third ventriculostomy in the management of hydrocephalus: Outcome analysis of 168 consecutive procedures. Clinical Neurology and Neurosurgery 126: 130-136.
[202] Eshra MA (2013) Endoscopic third ventriculostomy in idiopathic normal pressure hydrocephalus. Alexandria Journal of Medicine.
[203] Bonis PD, Tamburrini G, Mangiola A, Pompucci A, Mattogno PP, et al. (2013) Post-traumatic hydrocephalus is a contraindication for endoscopic third-ventriculostomy: Isn't it? Clinical Neurology and Neurosurgery 115: 9-12.
[204] Gianetti A, Malheiros A, Silva M (2011) Fourth ventriculostomy: an alternative treatment for hydrocephalus due to atresia of the Magendie and Luschka foramina. Neurosurgical Pediatrics 7: 152-156.
[205] Longatti P, Fiorindi A, Feleti A, D'Avella D, Martinuzzi A (2008) Endoscopic anatomy of the fourth ventricle. Journal of Neurosurgery 109: 530-535.

[206] Mohanty A, Biswas A, Satish S, Vollmer DG (2008) Efficacy of Endoscopic Third Ventriculostomy in Fourth Ventricular Outlet Obstruction. Neurosurgery 63: 905-914.
[207] Raslan A, Bhardwaj A (2007) Medical management of cerebral edema. Neurosurg Focus 22: E12.
[208] Ho M-L, Rojas R, Eisenberg RL (2012) Cerebral Edema. American Journal of Roentgenology 199: W258-W273.
[209] Donkin JJ, Vink R (2010) Mechanisms of cerebral edema in traumatic brain injury: therapeutic developments. Curr Opin Neurol 23: 293-299.
[210] Fukuda A, Badaut J (2012) Aquaporin 4: a player in cerebral edema and neuroinflammation. Journal of Neuroinflammation 9: 1-9.
[211] Siasios J, Kapsalaki EZ, Fountas KN (2012) Surgical Management of Patients with Chiari I Malformation. International Journal of Pediatrics 2012: 10.
[212] Schijman E (2004) History, anatomic forms, and pathogenesis of Chiari I malformations. Child's Nervous System 20: 323-328.
[213] Guillaume DJ, Menezes AH (2009) Hydrocephalus in Chiari Malformation and Other Craniovertebral Junction Abnormalities. Cerebrospinal Fluid Disorders: CRC Press. pp. 300-317.
[214] el Gammal T, Mark EK, Brooks BS (1988) MR imaging of Chiari II malformation. AJR Am J Roentgenol 150: 163-170.
[215] Esenwa CC, Leaf DE (2013) Colpocephaly in adults. BMJ Case Rep 2013.
[216] Castejon OJ (2009) Blood-brain barrier ultrastructural alterations in human congenital hydrocephalus and Arnold-Chiari malformation. Folia Neuropathol 47: 11-19.
[217] Iskandar BJ, Hedlund GL, Grabb PA, Oakes WJ (1998) The resolution of syringohydromyelia without hindbrain herniation after posterior fossa decompression. Journal of Neurosurgery 89: 212-216.
[218] Markunas CA, Tubbs RS, Moftakhar R, Ashley-Koch AE, Gregory SG, et al. (2012) Clinical, radiological, and genetic similarities between patients with Chiari Type I and Type 0 malformations. Journal of Neurosurgery: Pediatrics 9: 372-378.
[219] NINDS (2013) Chiari Malformation Fact Sheet. NIH Publication No. 13-4839
[220] Munshi I, Frim D, Stine-Reyes R, Weir BK, Hekmatpanah J, et al. (2000) Effects of posterior fossa decompression with and without duraplasty on Chiari malformation-associated hydromyelia. Neurosurgery 46: 1384-1389; discussion 1389-1390.
[221] Pritz MB (2003) Surgical Treatment of Chiari I Malformation: Simplified Technique and Clinical Results. Skull Base 13: 173-177.
[222] Wen L, Ma C, Wang H, Hu Z (2014) The role of hydrocephalus in the development of Chiari I malformation and syringomyelia. Journal of the neurological sciences 344: 240-242.
[223] Isik N, Elmaci I, Silav G, Celik M, Kalelioglu M (2009) Chiari malformation type III and results of surgery: a clinical study: report of eight surgically treated cases and review of the literature. Pediatr Neurosurg 45: 19-28.
[224] Hauser SL, Oksenberg JR (2006) The Neurobiology of Multiple Sclerosis: Genes, Inflammation, and Neurodegeneration. Neuron 52: 61-76.
[225] Sicotte N (2011) Neuroimaging in Multiple Sclerosis: Neurotherapeutic Implications. Neurotherapeutics 8: 54-62.
[226] Orton SM, Herrera BM, Yee IM, Valdar W, Ramagopalan SV, et al. (2006) Sex ratio of multiple sclerosis in Canada: a longitudinal study. Lancet Neurol 5: 932-936.
[227] Whitacre CC, Reingold SC, O'Looney PA, Blankenhorn E, Brinley F, et al. (1999) A Gender Gap in Autoimmunity: Task Force on Gender, Multiple Sclerosis and Autoimmunity*. Science 283: 1277-1278.
[228] Compston A, Coles A (2008) Multiple sclerosis. The Lancet 372: 1502-1517.
[229] Fox RJ, Beall E, Bhattacharyya P, Chen JT, Sakaie K (2011) Advanced MRI in Multiple Sclerosis: Current Status and Future Challenges. Neurologic Clinics 29: 357-380.
[230] Wuerfel J, Paul F, Beierbach B, Hamhaber U, Klatt D, et al. (2010) MR-elastography reveals degradation of tissue integrity in multiple sclerosis. NeuroImage 49: 2520-2525.
[231] Damal K, Stoker E, Foley JF (2013) Optimizing therapeutics in the management of patients with multiple sclerosis: a review of drug efficacy, dosing, and mechanisms of action. Biologics 7: 247-258.
[232] Koch-Henriksen N (1999) The Danish Multiple Sclerosis Registry: a 50-year follow-up. Mult Scler 5: 293-296.
[233] Sklar FH, Diehl JT, Beyer CW, Jr., Clark WK (1980) Brain elasticity changes with ventriculomegaly. J Neurosurg 53: 173-179.
[234] Sklar FH, Elashvili I (1977) The pressure-volume function of brain elasticity. Physiological considerations and clinical applications. J Neurosurg 47: 670-679.
[235] Lim ST, Potts DG, Deonarine V, Deck MDF (1973) Ventricular compliance in dogs with and without aqueductal obstruction. Journal of Neurosurgery 39: 463-473.
[236] Marques F, Sousa JC, Sousa N, Palha JA (2013) Blood-brain-barriers in aging and in Alzheimer's disease. Mol Neurodegener 8: 38.
[237] Rekate HL (1994) Circuit diagram of the circulation of cerebrospinal fluid. Pediatr Neurosurg 21: 248-252; discussion 253.
[238] Wostyn P, Van Dam D, Audenaert K, De Deyn PP (2011) Increased Cerebrospinal Fluid

Production as a Possible Mechanism Underlying Caffeine's Protective Effect against Alzheimer's Disease. Int J Alzheimers Dis 2011: 617420.
[239] Rekate HL (1994) The usefulness of mathematical modeling in hydrocephalus research. Childs Nerv Syst 10: 13-18.
[240] Kress BT, Iliff JJ, Xia M, Wang M, Wei H, et al. (2014) Impairment of paravascular clearance pathways in the aging brain. Annals of Neurology: n/a-n/a.
[241] Stevens SA, Lakin WD (2000) Local Compliance Effects on the Global Pressure-Volume Relationship in Models of Intracranial Pressure Dynamics. Mathematical and Computer Modelling of Dynamical Systems 6: 445-465.
[242] Silverberg G, Mayo M, Saul T, Fellmann J, McGuire D (2006) Elevated cerebrospinal fluid pressure in patients with Alzheimer's disease. Cerebrospinal Fluid Res 3: 7.
[243] Baruch K, Deczkowska A, David E, Castellano JM, Miller O, et al. (2014) Aging-induced type I interferon response at the choroid plexus negatively affects brain function. Science 346: 89-93.
[244] Standridge SM (2010) Idiopathic Intracranial Hypertension in Children: A Review and Algorithm. Pediatric Neurology 43: 377-390.
[245] Gordon NS (2006) Idiopathic intracranial hypertension. European Journal of Paediatric Neurology 10: 1-4.
[246] Degnan AJ, Levy LM (2011) Pseudotumor Cerebri: Brief Review of Clinical Syndrome and Imaging Findings. American Journal of Neuroradiology 32: 1986-1993.
[247] Monro A (1783) Observations of structure and function of the nervous system. Edinburgh: Creech and Johnson.
[248] Kellie G (1824) Appearances observed in the dissection of two-individuals; death from cold and congestion of the brain. . Trans Med-Chir Society Edinburgh: 1-84.
[249] Magendie F (1842) Recherches anatomique et physiologique sur le liquide cephalo-rachidien ou cerebro-spinal. Paris.
[250] Burrows G (1846) On disorders of the cerebral circulation. London: Longman, Brown, Green and Longmans.
[251] Guinane JE (1972) An equivalent circuit analysis of cerebrospinal fluid hydrodynamics. American Journal of Physiology 223: 425-430.
[252] Sivaloganathan S, Tenti G, Drake JM (1998) Mathematical pressure volume models of the cerebrospinal fluid. Applied Mathematics and Computation 94: 243-266.
[253] Marmarou A, Shulman K, Rosende R (1978) A nonlinear analysis of the cerebrospinal fluid system and intracranial pressure dynamics. Journal of Neurosurgery 48: 332-344.
[254] Spertell RB (1980) The response of brain to transient elevations in intraventricular pressure. J Neurol Sci 48: 343-352.
[255] Karni Z, Bear J, Sorek S, Pinczewski Z (1987) Quasi-steady-state compartmental model of intracranial fluid dynamics. Medical and Biological Engineering and Computing 25: 167-172.
[256] Sorek S, Bear J, Karni Z (1988) A non-steady compartmental flow model of the cerebrovascular system. Journal of Biomechanics 21: 695-704.
[257] Lakin WD, Stevens SA, Tranmer BI, Penar PL (2003) A whole-body mathematical model for intracranial pressure dynamics. Journal of Mathematical Biology 46: 347-383.
[258] Lakin WD, Stevens SA, Penar PL (2007) Modeling Intracranial Pressures in Microgravity: The Influence of the Blood-Brain Barrier. Aviation, Space, and Environmental Medicine 78: 932-936.
[259] Elliott NS, Lockerby DA, Brodbelt AR (2011) A lumped-parameter model of the cerebrospinal system for investigating arterial-driven flow in posttraumatic syringomyelia. Med Eng Phys 33: 874-882.
[260] Payne SJ (2006) A model of the interaction between autoregulation and neural activation in the brain. Mathematical Biosciences 204: 260-281.
[261] Payne SJ, Tarassenko L (2006) Combined transfer function analysis and modelling of cerebral autoregulation. Ann Biomed Eng 34: 847-858.
[262] Egnor M, Rosiello A, Zheng L (2001) A Model of Intracranial Pulsations. Pediatr Neurosurg 35: 284-298.
[263] Clatz O, Litrico S, Delingette H, Paquis P, Ayache N (2007) Dynamic Model of Communicating Hydrocephalus for Surgery Simulation. IEEE Transactions On Biomedical Engineering 54: 755-758.
[264] Otahal J, Stepanık Z, Kaczmarska A, Marsık F, Broz Z, et al. (2007) Simulation of cerebrospinal fluid transport. Advances in Engineering Software 38: 802-809.
[265] Ursino M, Di Giammarco P (1991) A mathematical model of the relationship between cerebral blood volume and intracranial pressure changes: The generation of plateau waves. Annals of Biomedical Engineering 19: 15-42.
[266] Ursino M, Lodi CA (1997) A simple mathematical model of the interaction between intracranial pressure and cerebral hemodynamics. J Appl Physiol (1985) 82: 1256-1269.
[267] Fard PJ, Tajvidi MR, Gharibzadeh S (2007) High-pressure hydrocephalus: a novel analytical modeling approach. J Theor Biol 248: 401-410.
[268] Clarke M, Meyer F (2007) The history of mathematical modelling in hydrocephalus. Neurosurgical Focus 22: E3.
[269] Franceschini G, Bigoni D, Regitnig P, Holzapfel GA (2006) Brain tissue deforms similarly to filled elastomers and follows consolidation

theory. Journal of the Mechanics and Physics of Solids 54: 2592-2620.
[270] Bottan S, Schmid Daners M, de Zelicourt D, Fellner N, Poulikakos D, et al. (2013) Assessment of intracranial dynamics in hydrocephalus: effects of viscoelasticity on the outcome of infusion tests. J Neurosurg 119: 1511-1519.
[271] Drapaca CS, Tenti G, Rohlf K, Sivaloganathan S (2006) A Quasi-linear Viscoelastic Constitutive Equation for the Brain: Application to Hydrocephalus. Journal of Elasticity 85: 65-83.
[272] Dutta-Roy T, Wittek A, Miller K (2008) Biomechanical modelling of normal pressure hydrocephalus. Journal of Biomechanics 41: 2263-2271.
[273] Kohandel M, Sivaloganathan S, Tenti G, Drake JM (2006) The constitutive properties of the brain parenchyma Part 1. Strain energy approach. Med Eng Phys 28: 449-454.
[274] Lefever JA, Jaime García J, Smith JH (2013) A patient-specific, finite element model for noncommunicating hydrocephalus capable of large deformation. Journal of Biomechanics 46: 1447-1453.
[275] Taylor Z, Miller K (2004) Reassessment of brain elasticity for analysis of biomechanisms of hydrocephalus. Journal of Biomechanics 37: 1263-1269.
[276] Wilkie KP, Drapaca CS, Sivaloganathan S (2010) A theoretical study of the effect of intraventricular pulsations on the pathogenesis of hydrocephalus. Applied Mathematics and Computation 215: 3181-3191.
[277] Biot MA (1941) General Theory of Three-Dimensional Consolidation. Journal of Applied Physics 12: 155-164.
[278] Biot MA (1941) General Theory of Three-Dimensional Consolidation. 12.
[279] Biot MA (1956a) Theory of Deformation of a Porous Viscoelastic Anisotropic Solid. Journal of Applied Physics 27: 459-467.
[280] Biot MA (1956b) General Solutions of the Equations of Elasticity and consolidation for a Porous material. Journal of Applied Mechanics: 91-96.
[281] Biot MA, Willis DG (1957) The Elastic Coefficients of the Theory of Consolidation. Journal of Applied Mechanics: 594-601.
[282] Berryman JG (2002) Extension of Poroelastic Analysis to Double-Porosity Materials: New Technique in Microgeomechanics. Journal of Engineering Mechanics: 840-846.
[283] Hakim S (1971) Biomechanics of hydrocephalus. Acta Neurol Latinoam: 169-194.
[284] Hakim S, Venegas J, Burton J (1976) The physics of the cranial cavity, hydrocephalus and normal pressure hydrocephalus: mechanical interpretation and mathematical model. Surg Neurol 5: 187-210.
[285] Nagashima T, Tamaki N, Matsumoto S, Horwitz B, Sequchi Y (1987) Biomechanics of hydrocephalus: a new theoretical model. Neurosurgery 21: 898-904.
[286] Drake JM, Mostachfi O, Tenti G, Sivaloganathan S (1996) Realistic simple mathematical model of brain biomechanics for computer simulation of hydrocephalus and other brain abnormalities. Can J Neurol Sci 23.
[287] Kaczmarek M, Subramaniam R, Neff S (1997) The hydromechanics of hydrocephalus: Steady-state solutions for cylindrical geometry. Bulletin of Mathematical Biology 59: 295-323.
[288] Levine DN (1999) The Pathogenesis of Normal Pressure Hydrocephalus: A Theoretical Analysis. Bulletin of Mathematical Biology 61: 875-916.
[289] Levine DN (2000) Ventricular size in pseudotumor cerebri and the theory of impaired CSF absorption. Journal of the Neurological Sciences 177: 85-94.
[290] Peña A, Bolton M, Whitehouse H, Pickard JD (1999) Effects of Brain Ventricular Shape on Periventricular Biomechanics: A Finite-element Analysis. Neurosurgery 45.
[291] Peña A, Harris NG, Bolton MD, Czosnyka M, Pickard JD (2002) Communicating Hydrocephalus: The Biomechanics of Progressive Ventricular Enlargement Revisited. In: Czosnyka M, Pickard J, Kirkpatrick P, Smielewski P, Hutchinson P, editors. Intracranial Pressure and Brain Biochemical Monitoring: Springer Vienna. pp. 59-63.
[292] Smillie A, Sobey I, Molnar Z (2005) A hydroelastic model of hydrocephalus. J Fluid Mech 539: 417-443.
[293] Sivaloganathan S, Stastna M, Tenti G, Drake JM (2005) Biomechanics of the brain: A theoretical and numerical study of Biot's equations of consolidation theory with deformation-dependent permeability. International Journal of Non-Linear Mechanics 40: 1149-1159.
[294] Sivaloganathan S, Stastna M, Tenti G, Drake JM (2005) A viscoelastic approach to the modelling of hydrocephalus. Applied Mathematics and Computation 163: 1097-1107.
[295] Sobey I, Wirth B (2006) Effect of non-linear permeability in a spherically symmetric model of hydrocephalus. Mathematical Medicine and Biology 23: 339-361.
[296] Wirth B, Sobey I (2006) An axisymmetric and fully 3D poroelastic model for the evolution of hydrocephalus. Mathematical Medicine and Biology: 1-26.
[297] Song F-q, Xu Y-s, Li H-m (2007) Blood flow in capillaries by using porous media model. Journal of Central South University of Technology 14: 46-49.
[298] Momjian S, Bichsel D (2008) Nonlinear poroplastic model of ventricular dilation in

hydrocephalus. Journal of Neurosurgery 109: 100-107.
[299] Narsilio G, Shen X, Wang H, Smith D, Egan G (2008) Hydrocephalus: A Realistic Porous-Media Model with Geometry Based on Neuroimaging. In: Wang R, Shen E, Gu F, editors. Advances in Cognitive Neurodynamics ICCN 2007: Springer Netherlands. pp. 565-569.
[300] Linninger AA, Sweetman B, Penn R (2009) Normal and hydrocephalic brain dynamics: the role of reduced cerebrospinal fluid reabsorption in ventricular enlargement. Ann Biomed Eng 37: 1434-1447.
[301] Liu F, Lollis SS, Ji S, Paulsen KD, Hartov A, et al. (2009) Model-based estimation of ventricular deformation in the cat brain. Med Image Comput Comput Assist Interv 12: 308-315.
[302] Tully B, Ventikos Y (2009) Coupling poroelasticity and CFD for cerebrospinal fluid hydrodynamics. IEEE Transactions on Biomedical Enginerring 56: 1644-1651.
[303] Penn RD, Linninger A (2009) The Physics of Hydrocephalus. Pediatr Neurosurg 45: 161-174.
[304] Shahim K, Drezet JM, Molinari JF, Sinkus R, Momjian S (2010) Finite element analysis of normal pressure hydrocephalus: influence of CSF content and anisotropy in permeability. Applied Bionics and Biomechanics 7: 187-197.
[305] Shahim K, Drezet JM, Martin BA, Momjian S (2012) Ventricle equilibrium position in healthy and normal pressure hydrocephalus brains using an analytical model. J Biomech Eng 134: 041007.
[306] Sobey I, Eisentrager A, Wirth B, Czosnyka M (2012) Simulation of cerebral infusion tests using a poroelastic model. International Journal of Numerical Analysis and Modeling, Series B 3: 52-64.
[307] Wilkie KP, Nagra G, Johnston M (2012) A mathematical analysis of physiological and molecular mechanisms that modulate pressure gradients and facilitate ventricular expansion in hydrocephalus. International Journal of Numerical Analysis and Modeling, Series B 3: 65-81.
[308] Li X, von Holst H, Kleiven S (2013) Influences of brain tissue poroelastic constants on intracranial pressure (ICP) during constant-rate infusion. Comput Methods Biomech Biomed Engin 16: 1330-1343.
[309] Wirth B, Sobey I, Eisenträger A (2014) Conditions for choking in a poroelastic flow model. IMA Journal of Applied Mathematics 79: 254-273.
[310] Fin L, Grebe R (2003) Three dimensional modeling of the cerebrospinal fluid dynamics and brain interactions in the aqueduct of sylvius. Comput Methods Biomech Biomed Engin 6: 163-170.
[311] Kurtcuoglu V, Poulikakos D, Ventikos Y (2005) Computational modelling of the mechanical behaviour of the cerebrospinal fluid system. J Biomechanical Engineering 127: 264-269.
[312] Linninger AA, Tsakiris C, Zhu DC, Xenos M, Roycewicz P, et al. (2005) Pulsatile Cerebrospinal Fluid Dynamics in the Human Brain. IEEE Transactions on Biomedical Engineering 52: 557-565.
[313] Kurtcuoglu V, Soellinger M, Summers P, Boomsma K, Poulikakos D, et al. (2007) Computational investigation of subject-specific cerebrospinal fluid flow in the third ventricle and aqueduct of Sylvius. Journal of Biomechanics 40: 1235-1245.
[314] Howden L, Giddings D, Power H, Aroussi A, Vloeberghs M, et al. (2008) Three-dimensional cerebrospinal fluid flow within the human ventricular system. Computer Methods in Biomechanics and Biomedical Engineering 11: 123-133.
[315] Sweetman B, Xenos M, Zitella L, Linninger AA (2011) Three-dimensional computational prediction of cerebrospinal fluid flow in the human brain. Computers in Biology and Medicine 41: 67-75.
[316] Kurtcuoglu V (2011) Computational Fluid Dynamics for the Assessment of Cerebrospinal Fluid Flow and Its Coupling with Cerebral Blood Flow. In: Miller K, editor. Biomechanics of the Brain: Springer New York. pp. 169-188.
[317] Kurtcuoglu V (2012) Pulsatile cerebrospinal fluid flow in the cranial subarachnoid space. Neurology, Psychiatry and Brain Research 18: 66-67.
[318] Bottan S, Poulikakos D, Kurtcuoglu V (2012) Phantom model of physiologic intracranial pressure and cerebrospinal fluid dynamics. IEEE Trans Biomed Eng 59: 1532-1538.
[319] Wang H (2000) Theory of Linear Poroelasticity with Applications to Geomechanics andHydrogeology: Princeton University Press.
[320] Terzaghi Kv (1936) The shearing resistance of saturated soils. Proc 1st ICSMFE 1: 54-56.
[321] Zienkiewicz OC, Chan AHC, Pastor M, Schrefler BA, Shiomi T (1999) Computational Geomechanics with special Reference to Earthquake Engineering. England, UK: John Wiley & Sons Ltd.
[322] Gassmann F (1951) Elastic Waves Through a Packing of Spheres. Geophysics 16: 673-685.
[323] Carroll MM, Katsube N (1983) The Role of Terzaghi Effective Stress in Linearly Elastic Deformation. Journal of Energy Resources Technology 105: 509-511.
[324] Mehrabian A, Abousleiman YN (2014) Generalized Biot's theory and Mandel's problem of multiple-porosity and multiple-permeability poroelasticity. Journal of Geophysical Research: Solid Earth 119: 2013JB010602.
[325] Rice JR, Cleary MP (1976) Some basic stress diffusion solutions for fluid-saturated elastic porous media with compressible constituents. Reviews of Geophysics 14: 227-241.

[326] Weaver JB, Pattison AJ, McGarry MD, Perreard IM, Swienckowski JG, et al. (2012) Brain mechanical property measurement using MRE with intrinsic activation. Phys Med Biol 57: 7275-7287.
[327] Murphy MC, Huston J, Jack CR, Glaser KJ, Manduca A, et al. (2011) Decreased brain stiffness in Alzheimer's disease determined by magnetic resonance elastography. Journal of Magnetic Resonance Imaging 34: 494-498.
[328] Streitberger K-J, Wiener E, Hoffmann J, Freimann FB, Klatt D, et al. (2011) In vivo viscoelastic properties of the brain in normal pressure hydrocephalus. NMR in Biomedicine 24: 385-392.
[329] Streitberger K-J, Sack I, Krefting D, Pfüller C, Braun J, et al. (2012) Brain Viscoelasticity Alteration in Chronic-Progressive Multiple Sclerosis. PLoS ONE 7: e29888.
[330] Freimann F, Streitberger K-J, Klatt D, Lin K, McLaughlin J, et al. (2012) Alteration of brain viscoelasticity after shunt treatment in normal pressure hydrocephalus. Neuroradiology 54: 189-196.
[331] Prange MT, Margulies SS (2002) Regional, Directional, and Age-Dependent Properties of the Brain Undergoing Large Deformation. Journal of Biomechanical Engineering 124: 244-252.
[332] Sack I, Beierbach B, Hamhaber U, Klatt D, Braun J (2008) Non-invasive measurement of brain viscoelasticity using magnetic resonance elastography. NMR Biomed 21: 265-271.
[333] Kruse SA, Rose GH, Glaser KJ, Manduca A, Felmlee JP, et al. (2008) Magnetic Resonance Elastography of the Brain. NeuroImage 39: 231-237.
[334] Johnson CL, McGarry MDJ, Gharibans AA, Weaver JB, Paulsen KD, et al. (2013) Local mechanical properties of white matter structures in the human brain. NeuroImage 79: 145-152.
[335] Wang ZJ, Srinivasan K (2002) An adaptive Cartesian grid generation method for 'Dirty' geometry. Int J Numer Meth Fluids 39: 703-717.
[336] LaSalle D, Karypis G. Multi-Threaded Graph Partitioning; 2013 19 May 2013 - 23 May 2013; Hyatt Regency Cambridge, Boston, Massachusetts USA.
[337] Stadlbauer A, Salomonowitz E, Riet W, Buchfelder M, Ganslandt O (2010) Insight into the patterns of cerebrospinal fluid flow in the human ventricular system using MR velocity mapping. NeuroImage 51: 42-52.
[338] Matsumae M, Hirayama A, Atsumi H, Yatsushiro S, Kuroda K (2014) Velocity and pressure gradients of cerebrospinal fluid assessed with magnetic resonance imaging. J Neurosurg 120: 218-227.
[339] Tully BJ (2010) Allostasis of cerebral water: modelling the transport of cerebrospinal fluid: University of Oxford.
[340] Jacobson EE, Fletcher DF, Morgan MK, Johnston IH (1996) Fluid Dynamics of the Cerebral Aqueduct. Pediatric Neurosurgery 24: 229-236.
[341] Jacobson EE, Fletcher DF, Morgan MK, Johnston IH (1999) Computer modelling of the cerebrospinal fluid flow dynamics of aqueduct stenosis. Med Biol Eng Comput 37: 59-63.
[342] Longatti P, Fiorindi A, Feletti A, Baratto V (2006) Endoscopic opening of the foramen of magendie using transaqueductal navigation for membrane obstruction of the fourth ventricle outlets. Technical note. J Neurosurg 105: 924-927.
[343] Zhang Y, Ping Zhang Y, Shields L, Zheng Y, Xu X-M, et al. (2012) Cervical Central Canal Occlusion Induces Noncommunicating Syringomyelia. Neurosurgery.
[344] Hatem SM, Attal N, Ducreux D, Gautron M, Parker F, et al. (2010) Clinical, functional and structural determinants of central pain in syringomyelia. Brain 133: 3409-3422.
[345] Carpentier A, Brunelle F, Philippon J, Clemenceau S (2001) Obstruction of Magendie's and Luschka's foramina. Cine-MRI, aetiology and pathogenesis. Acta Neurochir (Wien) 143: 517-521; discussion 521-512.
[346] Tait MJ, Saadoun S, Bell BA, Papadopoulos MC (2008) Water movements in the brain: role of aquaporins. TRENDS in Neurosciences 31: 37-43.
[347] Buonocore M (1998) Visualizing blood flow patterns using streamlines, arrows, and particle paths. Magn Reson Med 40: 210-226.
[348] Stadlbauer A, Salomonowitz E, Brenneis C, Ungersbock K, van der Riet W, et al. (2012) Magnetic resonance velocity mapping of 3D cerebrospinal fluid flow dynamics in hydrocephalus: preliminary results. Eur Radiol 22: 232-242.
[349] Cheng S, Bilston, L (2010) The effects of interthalamic adhesion position on cerebrospinal fluid dynamics in the cerebral ventricles. Biomechanics 43: 579-582.
[350] Cheng S, Bilston L (2007) Unconfined compression of white matter. Journal Biomechanics 40: 117-124.
[351] Green MA, Bilston LE, Sinkus R (2008) In vivo brain viscoelastic properties measured by magnetic resonance elastography. NMR Biomed 21: 755-764.
[352] Bammer R, Hope TA, Aksoy M, Alley MT (2007) Time-resolved 3D quantitative flow MRI of the major intracranial vessels: Initial experience and comparative evaluation at 1.5T and 3.0T in combination with parallel imaging. Magnetic Resonance in Medicine 57: 127-140.
[353] Wetzel S, Meckel S, Frydrychowicz A, Bonati L, Radue EW, et al. (2007) In vivo assessment and visualization of intracranial arterial hemodynamics with flow-sensitized 4D MR imaging at 3T. American Journal of Neuroradiology 28: 433-438.
[354] Bateman GA, Siddique SH (2014) Cerebrospinal fluid absorption block at the vertex

in chronic hydrocephalus: obstructed arachnoid granulations or elevated venous pressure? Fluids Barriers CNS 11: 11.
[355] Wirth B, Sobey I (2009) Analytic solution during an infusion test of the linear unsteady poroelastic equations in a spherically symmetric model of the brain. Math Med Biol 26: 25-61.
[356] Brezis H (2011) Functional Analysis, Sobolev Spaces and Partial Differential Equations: Springer New York.
[357] Liu GR, Quek SS (2013) The Finite Element Method (A Practical Course). USA: Butterworth-Heinemann. 464 p.
[358] Crouzeix M, Thomee V (1987) The Stability in Lp and Wp1 of the L2-Projection onto Finite Element Function Spaces. Mathematics of Computation 48: 521-532.
[359] Persson PO, Strang G (2004) A Simple Mesh Generator in MATLAB. SIAM Review 46: 329-345.
[360] de Berg M, Cheong O, van Kreveld M, Overmars M (2008) Computational Geometry: Algorithms and Applications: Springer-Verlag.
[361] Rivara MC (1984) Algorithms for refining triangular grids suitable for adaptive and multigrid techniques. International Journal for Numerical Methods in Engineering 20: 745-756.
[362] Xin S-Q, Wang X, Xia J, Mueller-Wittig W, Wang G-J, et al. (2013) Parallel computing 2D Voronoi diagrams using untransformed sweepcircles. Computer-Aided Design 45: 483-493.
[363] Evans DJ, Stojmenović I (1989) On parallel computation of Voronoi diagrams. Parallel Computing 12: 121-125.
[364] Eisenberg MA, Malvern LE (1973) On finite element integration in natural co-ordinates. International Journal for Numerical Methods in Engineering 7: 574-575.
[365] Showalter RE (2000) Diffusion in Poro-Elastic Media. Journal of Mathematical Analysis and Applications 251: 310-340.
[366] Showalter RE, Su N (2001) Partially saturated poroelastic medium. Discrete and Continous Dynamical Systems Series B 1: 403-420.
[367] Deuflhard P (2011) Newton Methods for Nonlinear Problems: Affine Invariance and Adaptive Algorithms; Bank R, Graham RL, Stoer J, Varga R, Yserentant H, editors. Berlin: Springer-Verlag.
[368] Freund RW (1993) A transpose-free quasi-minimal residual algorithm for non-Hermitian linear systems. SIAM J Sci Comput 14: 470-482.
[369] Barrett R, Berry M, Chan TF, Demmel J, Donato JM, et al. (1987) Templates for the Solution of Linear Systems: Building Blocks for Iterative Methods.
[370] Sonneveld P (1989) CGS, A Fast Lanczos-Type Solver for Nonsymmetric Linear systems. SIAM Journal on Scientific and Statistical Computing 10: 36-52.
[371] García MD, Flórez E, Suárez A, González L, Montero G (2005) New implementation of QMR-type algorithms. Computers & Structures 83: 2414-2422.
[372] Cuthill EH, Mckee JM. Reducing the Bandwidth of Sparse Symmetric Matrices; 1969; New Jersey. Brondon Press. pp. 157-172.
[373] Flórez E, García MD, González L, Montero G (2002) The effect of orderings on sparse approximate inverse preconditioners for non-symmetric problems. Advances in Engineering Software 33: 611-619.
[374] Saad Y (2003) Iterative Methods for Sparse Linear Systems: Society for Industrial and Applied Mathematics.
[375] Zienkiewicz OC, Taylor RL (2000) The Finite Element Method. Oxford: Butterworth-Heinemann.
[376] Iliff JJ, Lee H, Yu M, Feng T, Logan J, et al. (2013) Brain-wide pathway for waste clearance captured by contrast-enhanced MRI. The Journal of Clinical Investigation 123: 1299-1309.
[377] Nagelhus EA, Ottersen OP (2013) Physiological roles of aquaporin-4 in brain. Physiol Rev 93: 1543-1562.
[378] Tenti G, Drake JM, Sivaloganathan S (2000) Brain biomechanics: mathematical modeling of hydrocephalus. Neurol Res 22: 19-24.
[379] Dumett MA, Vassilevski P, Woodward CS (2002) A Multigrid Method for Nonlinear Unstructured Finite Element Elliptic Equations SIAM Journal on Scientific Computing.
[380] Qin EC, Sinkus R, Geng G, Cheng S, Green M, et al. (2013) Combining MR elastography and diffusion tensor imaging for the assessment of anisotropic mechanical properties: A phantom study. Journal of Magnetic Resonance Imaging 37: 217-226.
[381] Bank RE (1990) PLTMG: a software package for solving elliptic partial differential equations: users' guide 6.0. Philadelphia: Society for Industrial and Applied Mathematics. xiv, 164 p. p.
[382] Park J, Shontz SM (2011) An Alternating Mesh Quality Metric Scheme for Efficient Mesh Quality Improvement. Procedia Computer Science 4: 292-301.
[383] Knupp PM (2003) Algebraic mesh quality metrics for unstructured initial meshes. Finite Elements in Analysis and Design 39: 217-241.
[384] Shewchuk JR (1996) Triangle: Engineering a 2D Quality Mesh Generator and Delaunay Triangulator. Selected papers from the Workshop on Applied Computational Geormetry, Towards Geometric Engineering: Springer-Verlag. pp. 203-222.
[385] Eriksson K, Johnson C (1991) Adaptive Finite Element Methods for Parabolic Problems I: A Linear Model Problem. SIAM Journal on Numerical Analysis 28: 43-77.

[386] Johnson C (1987) Numerical solution of partial differential equations by the finite element method. Cambridge: Cambridge University Press.
[387] Naidich TP, Epstein F, Lin JP, Kricheff II, Hochwald GM (1976) Evaluation of Pediatric Hydrocephalus by Computed Tomography. Radiology 119: 337-345.
[388] Schlichter LC, Mertens T, Liu B (2011) Swelling activated Cl- channels in microglia: Biophysics, pharmacology and role in glutamate release. Channels (Austin) 5: 128-137.
[389] Mow VC, Kuei SC, Lai WM, Armstrong CG (1980) Biphasic Creep and Stress Relaxation of Articular Cartilage in Compression: Theory and Experiments. Journal of Biomechanical Engineering 102: 73-84.
[390] Schöberl J (1997) NETGEN An advancing front 2D/3D-mesh generator based on abstract rules. Computing and Visualization in Science 1: 41-52.
[391] Johnson DL, Koplik J, Dashen R (1987) Theory of dynamic permeability and tortuosity in fluid-saturated porous media. Journal of Fluid Mechanics 176: 379-402.
[392] Blanc E, Chiavassa G, Lombard B (2013) A time-domain numerical modeling of two-dimensional wave propagation in porous media with frequency-dependent dynamic permeability. The Journal of the Acoustical Society of America 134: 4610-4623.
[393] Kaczmarek M (1992) On kinematics in the theory of multiphase media, comparison between two traditions. Mechanics Research Communications 19: 361-368.
[394] Hirsch S, Klatt D, Freimann F, Scheel M, Braun J, et al. (2013) In vivo measurement of volumetric strain in the human brain induced by arterial pulsation and harmonic waves. Magnetic Resonance in Medicine 70: 671-683.
[395] Feng Y, Okamoto RJ, Namani R, Genin GM, Bayly PV (2013) Measurements of mechanical anisotropy in brain tissue and implications for transversely isotropic material models of white matter. Journal of the Mechanical Behavior of Biomedical Materials 23: 117-132.
[396] Sahoo D, Deck C, Willinger R (2014) Development and validation of an advanced anisotropic visco-hyperelastic human brain FE model. Journal of the Mechanical Behavior of Biomedical Materials 33: 24-42.
[397] Guo J, Hirsch S, Fehlner A, Papazoglou S, Scheel M, et al. (2013) Towards an elastographic atlas of brain anatomy. PLoS One 8: e71807.
[398] Shulyakov AV, Cenkowski SS, Buist RJ, Del Bigio MR (2011) Age-dependence of intracranial viscoelastic properties in living rats. Journal of the Mechanical Behavior of Biomedical Materials 4: 484-497.
[399] Christensen-Jeffries K, Browning R, Tang MX, Dunsby C, Eckersley R (2014) In Vivo Acoustic Super-Resolution and Super-Resolved Velocity Mapping Using Microbubbles. IEEE Trans Med Imaging.
[400] Mehrabian A, Abousleiman Y (2011) General solutions to poroviscoelastic model of hydrocephalic human brain tissue. Journal of Theoretical Biology 291: 105-118.
[401] Bemer E, Boutéca M, Vincké O, Hoteit N, Ozanam O (2001) Poromécanique : de la poroélasticité linéaire à la poroélasticité non linéaire et la poroviscoélasticité. Oil & Gas Science and Technology - Rev IFP 56: 531-544.
[402] Yeh C-S, Chen S-M, Teng T-J, Lee Y-J (2006) On formulation of a transition matrix for electroporoelastic medium and application to analysis of scattered electroseismic wave. The Journal of the Acoustical Society of America 120: 3672-3693.
[403] Shenoy AV (1993) Darcy-Forchheimer natural, forced and mixed convection heat transfer in non-Newtonian power-law fluid-saturated porous media. Transport in Porous Media 11: 219-241.
[404] Kozicki W, Tiu C (1988) A unified model for non-Newtonian flow in packed beds and porous media. Rheologica Acta 27: 31-38.
[405] Pearson JRA, Tardy PMJ (2002) Models for flow of non-Newtonian and complex fluids through porous media. Journal of Non-Newtonian Fluid Mechanics 102: 447-473.
[406] Sochi T (2010) Non-Newtonian flow in porous media. Polymer 51: 5007-5023.
[407] Hansen MB, Jespersen SN, Leigland LA, Kroenke CD (2013) Using diffusion anisotropy to characterize neuronal morphology in gray matter: the orientation distribution of axons and dendrites in the NeuroMorpho.org database. Frontiers in Integrative Neuroscience 7.
[408] Chen X, Phoon KK, Toh KC (2007) Partitioned versus global Krylov subspace iterative methods for FE solution of 3-D Biot's problem. Computer Methods in Applied Mechanics and Engineering 196: 2737-2750.
[409] Ferronato M, Gambolati G, Teatini P (2001) Ill-conditioning of finite element poroelasticity equations. International Journal of Solids and Structures 38: 5995-6014.
[410] Bergamaschi L, Ferronato M, Gambolati G (2007) Novel preconditioners for the iterative solution to FE-discretized coupled consolidation equations. Computer Methods in Applied Mechanics and Engineering 196: 2647-2656.
[411] Stokes I, Chegini S, Ferguson S, Gardner-Morse M, Iatridis J, et al. (2010) Limitation of Finite Element Analysis of Poroelastic Behavior of Biological Tissues Undergoing Rapid Loading. Annals of Biomedical Engineering 38: 1780-1788.
[412] Wheeler M, Xue G, Yotov I (2013) Coupling multipoint flux mixed finite element methods with

continuous Galerkin methods for poroelasticity. Computational Geosciences 18: 57-75.
[413] Korsawe J, Starke G, Wang W, Kolditz O (2006) Finite element analysis of poro-elastic consolidation in porous media: Standard and mixed approaches. Computer Methods in Applied Mechanics and Engineering 195: 1096-1115.
[414] Tchonkova M, Peters J, Sture S (2008) A new mixed finite element method for poro-elasticity. International Journal for Numerical and Analytical Methods in Geomechanics 32: 579-606.
[415] Rohan E, Shaw S, Wheeler MF, Whiteman JR (2013) Mixed and Galerkin finite element approximation of flow in a linear viscoelastic porous medium. Computer Methods in Applied Mechanics and Engineering 260: 78-91.
[416] Ferronato M, Castelletto N, Gambolati G (2010) A fully coupled 3-D mixed finite element model of Biot consolidation. Journal of Computational Physics 229: 4813-4830.
[417] Mardal K, Tai X, Winther R (2002) A Robust Finite Element Method for Darcy--Stokes Flow. SIAM Journal on Numerical Analysis 40: 1605-1631.
[418] Arioli M, Manzini G (2006) A network programming approach in solving Darcy's equations by mixed finite-element methods. ETNA Electronic Transactions on Numerical Analysis 22: 41-70.
[419] Lamichhane BP (2014) A mixed finite element method for nearly incompressible elasticity and Stokes equations using primal and dual meshes with quadrilateral and hexahedral grids. Journal of Computational and Applied Mathematics 260: 356-363.
[420] Lamichhane BP (2009) Inf-sup stable finite-element pairs based on dual meshes and bases for nearly incompressible elasticity. IMA Journal of Numerical Analysis 29: 404-420.
[421] Irzal F, Remmers JJC, Verhoosel CV, de Borst R (2013) Isogeometric finite element analysis of poroelasticity. International Journal for Numerical and Analytical Methods in Geomechanics 37: 1891-1907.
[422] Kirby R, Sherwin S, Cockburn B (2012) To CG or to HDG: A Comparative Study. Journal of Scientific Computing 51: 183-212.
[423] Fu Z, Gatica LF, Sayas F-J (2013) Matlab tools for HDG in three dimensions.
[424] Rivière B (2008) Discontinuous Galerkin Methods for Solving Elliptic and Parabolic Equations: Society for Industrial and Applied Mathematics. 201 p.
[425] Hesthaven JS, Warburton T (2008) Nodal Discontinuous Galerkin Methods: Algorithms, Analysis, and Applications. New York, NY: Springer-Verlag New York Inc.
[426] Cockburn B, Karniadakis GE, Shu CW (2000) Discontinuous Galerkin Methods: Theory, Compuration and Applications: Springer.
[427] Bukac M, Zunino P, Yotov I (2013) Explicit partitioning strategies for the interaction between a fluid and a multilayered poroelastic structure: an operator-splitting approach. Preprint submitted to Elsevier.
[428] Muha B, Čanić S (2010) A nonlinear, 3D fluid-structure interaction problem driven by the time-dependent dynamic pressure data: a constructive existence proof. Communications in Information and Systems 13: 357 – 397.
[429] Nadeem S, Akram S (2011) Peristaltic Flow of a Maxwell Model Through Porous Boundaries in a Porous Medium. Transport in Porous Media 86: 895-909.
[430] Mascarenhas S, Vilela GH, Carlotti C, Damiano LE, Seluque W, et al. (2012) The new ICP minimally invasive method shows that the Monro-Kellie doctrine is not valid. Acta Neurochir Suppl 114: 117-120.
[431] Sabet AA, Christoforou E, Zatlin B, Genin GM, Bayly PV (2008) Deformation of the human brain induced by mild angular head acceleration. J Biomech 41: 307-315.
[432] Tully HM, Dobyns WB (2014) Infantile hydrocephalus: A review of epidemiology, classification and causes. European Journal of Medical Genetics 57: 359-368.
[433] Zaide D, Ollivier-Gooch C (2014) Inserting a Curve into an Existing Two Dimensional Unstructured Mesh. In: Sarrate J, Staten M, editors. Proceedings of the 22nd International Meshing Roundtable: Springer International Publishing. pp. 93-107.
[434] Park J, Shontz SM, Drapaca CS (2012) Automatic boundary evolution tracking via a combined level set method and mesh warping technique: application to hydrocephalus. Proceedings of the 2012 international conference on Mesh Processing in Medical Image Analysis. Nice, France: Springer-Verlag. pp. 122-133.
[435] Oi S, Hidaka M, Honda Y, Togo K, Shinoda M, et al. (1999) Neuroendoscopic surgery for specific forms of hydrocephalus. Child's Nervous System 15: 56-68.
[436] Ersahin Y (2007) Endoscopic aqueductoplasty. Childs Nerv Syst 23: 143-150.
[437] Schroeder C, Fleck S, Gaab MR, Schweim KH, Schroeder HW (2012) Why does endoscopic aqueductoplasty fail so frequently? Analysis of cerebrospinal fluid flow after endoscopic third ventriculostomy and aqueductoplasty using cine phase-contrast magnetic resonance imaging. J Neurosurg 117: 141-149.
[438] Fritsch MJ, Schroeder HW (2013) Endoscopic aqueductoplasty and stenting. World Neurosurg 79: S20.e15-28.
[439] Cinalli G, Spennato P, Savarese L, Ruggiero C, Aliberti F, et al. (2006) Endoscopic aqueductoplasty and placement of a stent in the cerebral aqueduct in

the management of isolated fourth ventricle in children. J Neurosurg 104: 21-27.
[440] da Silva LR, Cavalheiro S, Zymberg ST (2007) Endoscopic aqueductoplasty in the treatment of aqueductal stenosis. Childs Nerv Syst 23: 1263-1268.
[441] Fritsch MJ, Kienke S, Mehdorn HM (2004) Endoscopic aqueductoplasty: stent or not to stent? Childs Nerv Syst 20: 137-142.
[442] Torres-Corzo J, Sanchez-Rodriguez J, Cervantes D, Rodriguez-Della Vecchia R, Muruato-Araiza F, et al. (2014) Endoscopic transventricular transaqueductal Magendie and Luschka foraminoplasty for hydrocephalus. Neurosurgery 74: 426-435; discussion 436.
[443] Kawaguchi T, Fujimura M, Tominaga T (2009) Syringomyelia with obstructive hydrocephalus at the foramens of Luschka and Magendie successfully treated by endoscopic third ventriculostomy. Surg Neurol 71: 349-352, discussion 352.
[444] Pillay PK, Awad IA, Hahn JF (1992) Gardner's hydrodynamic theory of syringomyelia revisited. Cleve Clin J Med 59: 373-380.
[445] Nzekwu E, Louie M, Scott D, Lundgren H, Pugh JA, et al. (2013) Numerical model for intraosseous infusion of the human calvarium for hydrocephalus shunting. Comput Methods Biomech Biomed Engin.
[446] Cohen B, Voorhees A, Wei T (2011) Magnetic resonance velocity imaging derived pressure differential using control volume analysis. Fluids and Barriers of the CNS 8.
[447] Raman K (2011) A stochastic differential equation analysis of cerebrospinal fluid dynamics. Fluids and Barriers of the CNS 8.
[448] Siyahhan B, Knobloch V Fau - de Zelicourt D, de Zelicourt D Fau - Asgari M, Asgari M Fau - Schmid Daners M, Schmid Daners M Fau - Poulikakos D, et al. (2014) Flow induced by ependymal cilia dominates near-wall cerebrospinal fluid dynamics in the lateral ventricles.
[449] Swiderski R, Agassandian K, Ross J, Bugge K, Cassell M, et al. (2012) Structural defects in cilia of the choroid plexus, subfornical organ and ventricular ependyma are associated with ventriculomegaly. Fluids and Barriers of the CNS 9.
[450] Pardridge WM (2011) Drug transport in brain via the cerebrospinal fluid. Fluids and Barriers of the CNS 8.
[451] Keep RF, Smith DE (2011) Choroid plexus transport: gene deletion studies. Fluids and Barriers of the CNS 8.
[452] Daners SM, Knobloch V, Soellinger M, Boesiger P, Seifert B, et al. (2012) Age-specific characteristics and coupling of cerebral arterial inflow and cerebrospinal fluid dynamics. PLoS One 7: e37502.
[453] Pomschar A, Koerte I, Lee S, Laubender RP, Straube A, et al. (2013) MRI evidence for altered venous drainage and intracranial compliance in mild traumatic brain injury. PLoS One 8: e55447.
[454] Rhie CM, Chow WL (1983) Numerical study of the turbulent flow past an airfoil with trailing edge separation. AIAA Journal 21: 1525-1532.
[455] Doormal JV, Raithby G (1984) Enhancements of the SIMPLE method for predicitng incompressible fluid flows. Heat Transfer 7: 147-163.
[456] Ruge JW, Stüben K (1987) Algebraic multigrid (AMG) In: McCormick SF, editor. Multigrid methods. Philadelphia: SIAM. pp. 73–130.
[457] (2011, 11 July 2011). "First CSF Hydrodynamics Symposium." Retrieved 22 January, 2015, from http://www.multimedia.ethz.ch/conferences/2011/csf.
[458] Schloegel, K., et al. (2000). Parallel Multilevel Algorithms for Multi-constraint Graph Partitioning. Euro-Par 2000 Parallel Processing. A. Bode, T. Ludwig, W. Karl and R. Wismüller, Springer Berlin Heidelberg. 1900: 296-310.
[459] Karypis, G. and V. Kumar (1999). "Parallel Multilevel series k-Way Partitioning Scheme for Irregular Graphs." SIAM Review 41(2): 278-300.
[460] Kock-Jensen, C., Clemmensen, S.,Andersen, B. B. (1989). "Percutaneous insertion of CSF ventriculoatrial shunts - a new technique." Acta Neurochirurgica 96(1-2): 76-79.
[461] Agarwal, G. C., Berman, B. M., Stark, L. (1969). "A Lumped Parameter Model of the Cerebrospinal Fluid System." Biomedical Engineering, IEEE Transactions on BME-16(1): 45-53.

Appendix: Computational Fluid Dynamics

This Appendix provides some of the background material relevant to CFD, and its more specific use within the MPET-CFD model.

The objective of Computational Fluid Dynamics (CFD) is to solve numerically the PDEs that govern the motion of fluid flow. The equations describing the Newtonian fluid flow motion are the Navier-Stokes equations and the continuity equation which cannot be solved analytically (apart from a few special cases), thus the need of numerical solutions.

A1.1 Components of a numerical solution method

The most important ingredients of a numerical solution method are:

1. **The mathematical model** - *This comprises the set of the PDEs and associated boundary conditions that must be solved. This set includes the continuity equation and, for Newtonian fluids, the Navier-Stokes equations. Depending on the type of flow, the equations take the appropriate form i.e. two- or three dimensional, for compressible or incompressible fluids, for viscous or inviscid fluids etc. If additional physical processes exist, additional equations, which model these processes, are added to the set along with their corresponding boundary conditions.*
2. **Discretisation method** - *The next step is the selection of the discretisation method, which approximates each PDE with a set of linear algebraic equations. The solution of the linear system provides an approximation to the solution of the PDE at discrete locations in space (and time for transient problems). There are 3 main discretisation methods: the finite difference (FD), the finite volume (FV) and the finite element method (FEM).* `CFD-ACE+` *employs the FV method.*
3. **Coordinate and basis vector systems** - *The form of the equation to be solved depends on the coordinate system and the basis vectors used. One can solve the Navier-Stokes equations written in Cartesian, cylindrical, spherical, curvilinear orthogonal or non-orthogonal coordinate systems which may be fixed or moving. The choice depends on the flow that is simulated and affects the grid type to be used. One also has to select the basis in which vectors and tensors are to defined (fixed or variable, covariant or contravariant etc.).*
4. **Numerical Grid** – *The numerical grid divides the solution domain into a number of cells and thus the discrete locations were the variables are to be calculated, are defined. There are several types of numerical grids, such as structured grids, block-structured grids and unstructured meshes.*
5. **Finite approximations** – *For finite volume (FV) methods, the surface and volume integrals must be approximated.*
6. **Solution method** – *The discretisation process yields a large system of algebraic equations. The choice of the solver depends on the grid type and the number of nodes involved in each algebraic equation.*
7. **Convergence criteria** – *Iterative procedures terminate when a convergence criterion is met. Deciding when to stop the iterative process is important both from the accuracy and efficiency point of view.*

A1.2 Discretisation method

In the FV method, the domain is subdivided into a number of control volumes (CV) and at the centroid of each CV lies a computational node in which the variable value is to be calculated. The PDE is integrated over each CV and the resulting surface and volume integrals must be approximated using suitable relations involving the value of the variable at the centroid of the CV as well as the values at the centroids of the surrounding volumes. Interpolation is used to express the value of a variable at the CV face to the values of the CV-centres on either side of the face. One algebraic equation is obtained for each CV in which the value at the centroid of the CV itself and the surrounding centroids are unknowns.

The FV method can be applied to any grid type so it is suitable for complex geometries. The grid defines only the CV faces and is not related to a coordinate system. The method, by construction, is conservative as long as the surface integrals are the same for the CVs on either side of the face. Additionally, all the terms that must approximated have physical meaning and this also contributes to the popularity of the method.

A2.1 Basic equations of fluid mechanics

The basic equations in fluid mechanics are based on the following universal laws:

1. *Conservation of mass.*
2. *Newton's second law*
3. *Conservation of energy*

The PDE that results from the application of the Conservation of Mass law to a fluid element is call the Continuity Equation. Newton's Second law results in three momentum equations and the Conservation of Energy law (which is identical to the First Law of Thermodynamics) results in the energy equation.

In addition to these equations, we need additional relationships between properties in order to close the system of the equations. An example of such relationship is the equation of state which relates the thermodynamic variable pressure (p), density (ϱ) and temperature (T). The PDEs are obtained by applying the above laws in a fluid element.

A2.1.1 The continuity equation

The continuity equation is expressed as:

$$\frac{\partial \rho}{\partial t} + \nabla \bullet (\rho \boldsymbol{u}) = 0 \tag{A1.1}$$

For an incompressible fluid, the density ϱ is constant, so the equation (A1.1) becomes:

$$\nabla \bullet \boldsymbol{u} = 0 \tag{A1.2}$$

Equation (A1.2) is said to be in strong conservative form (or divergence form). For PDEs to have this form, all terms must have the form of the divergence of a vector or a tensor.

A2.1.2 The momentum equations

The application of Newton's second law in a fluid element leads to the three following momentum equations in directions x, y and z respectively:

$$\rho\frac{Du}{Dt}=\frac{\partial(-p+\tau_{xx})}{\partial x}+\frac{\partial\tau_{yx}}{\partial y}+\frac{\partial\tau_{zx}}{\partial z}+SM_x$$
$$\rho\frac{Dv}{Dt}=\frac{\partial\tau_{xy}}{\partial x}+\frac{\partial(-p+\tau_{yy})}{\partial y}+\frac{\partial\tau_{zy}}{\partial z}+SM_y \qquad \text{(A1.3a-c)}$$
$$\rho\frac{Dw}{Dt}=\frac{\partial\tau_{xz}}{\partial x}+\frac{\partial\tau_{yz}}{\partial y}+\frac{\partial(-p+\tau_{zz})}{\partial z}+SM_z$$

In order to arrive at the equations above, two types of forces are assume to act on the element: surface forces (pressure forces and viscous forces) and body forces (gravity, for instance). The pressure and viscous forces are shown explicitly in the above equations while the body forces are included in the momentum source terms: SM_x, SM_y and SM_z. Du/Dt, Dv/Dt and Dw/Dt are called total or substantive derivatives and denote the change with respect to time of u, v and w velocities along a fluid path. $\tau_{i,j}$ denote the viscous stresses. The most useful forms of the momentum equations for fluid flows are obtained by introducing a suitable model for the viscous stresses $\tau_{i,j}$.

In many fluid flows the viscous stresses can be expressed as functions of the local deformation rate. For Newtonian fluids**,** the viscous stresses are proportional to the rates of deformation. The following relation is often used in the literature:

$$\tau_{i,j}=2\mu\, e_{i,j}-\frac{2}{3}\mu\delta_{i,j}\nabla\bullet\mathbf{u} \qquad \text{(A1.4)}$$

In the above, $\delta_{i,j}$ is the Kronecker delta. For incompressible fluids, the second term on the right hand side of eq. A1.4 is zero because of the continuity equation. For non-Newtonian fluids, the relation between the stress tensor and the velocity is defined by a set of PDEs. The 6 individual components of the stress tensor are substituted into the momentum equations described previously and with some additional rearrangement, we get the conservative form of the Navier-Stokes equations which govern the time-dependent, three-dimensional fluid flow of a compressible Newtonian fluid (in a Cartesian coordinate system):

$$\frac{\partial(\rho u)}{\partial t}+\nabla\bullet(\rho u\mathbf{u})=-\frac{\partial p}{\partial x}+\frac{\partial}{\partial x}\left[\mu\frac{\partial u}{\partial x}\right]+\frac{\partial}{\partial y}\left[\mu\frac{\partial u}{\partial y}\right]+\frac{\partial}{\partial z}\left[\mu\frac{\partial u}{\partial z}\right]+s_{Mx}+SM_x$$
$$\frac{\partial(\rho v)}{\partial t}+\nabla\bullet(\rho v\mathbf{u})=-\frac{\partial p}{\partial y}+\frac{\partial}{\partial x}\left[\mu\frac{\partial v}{\partial x}\right]+\frac{\partial}{\partial y}\left[\mu\frac{\partial v}{\partial y}\right]+\frac{\partial}{\partial z}\left[\mu\frac{\partial v}{\partial z}\right]+s_{My}+SM_y \qquad \text{(A1.5a-c)}$$
$$\frac{\partial(\rho w)}{\partial t}+\nabla\bullet(\rho w\mathbf{u})=-\frac{\partial p}{\partial z}+\frac{\partial}{\partial x}\left[\mu\frac{\partial w}{\partial x}\right]+\frac{\partial}{\partial y}\left[\mu\frac{\partial w}{\partial y}\right]+\frac{\partial}{\partial z}\left[\mu\frac{\partial w}{\partial z}\right]+s_{Mz}+SM_z$$

where $s_{Mx} = \left[\frac{\partial}{\partial x}\left(\mu\frac{\partial u}{\partial x}\right)+\frac{\partial}{\partial y}\left(\mu\frac{\partial v}{\partial x}\right)+\frac{\partial}{\partial z}\left(\mu\frac{\partial w}{\partial x}\right)\right]+\frac{\partial}{\partial x}\left(-\frac{2}{3}\mu\nabla\bullet\mathbf{u}\right)$. Similar equations exist for s_{My} and s_{Mz}.

A2.1.3 The Energy equation

By applying the first law of thermodynamics in a fluid element, we obtain the energy equation:

$$\rho\frac{DE}{Dt} = -\nabla\bullet p\mathbf{u} + \left[\frac{\partial(u\tau_{xx})}{\partial x}+\frac{\partial(u\tau_{yx})}{\partial y}+\frac{\partial(u\tau_{zx})}{\partial z}+\frac{\partial(v\tau_{xy})}{\partial x}+\frac{\partial(v\tau_{xy})}{\partial y}+\ldots\right.$$
$$\left.\ldots+\frac{\partial(v\tau_{zy})}{\partial z}+\frac{\partial(w\tau_{xz})}{\partial x}+\frac{\partial(w\tau_{yz})}{\partial y}+\frac{\partial(w\tau_{zz})}{\partial z}\right]+\nabla\bullet(k\,\nabla T)+S_E \qquad \text{(A1.6)}$$

where E is the specific energy of the fluid defined as the sum of the internal thermal energy and the kinetic energy i.e. $E = i + \frac{1}{2}(u^2+v^2+w^2)$ and S_E denotes the rate of increase of energy due to sources (per unit volume per unit time). Also T is the fluid temperature (in K) and k is the thermal conductivity of the fluid (units $W/m/K$). In the special case of incompressible fluid, we have $I = cT$. We can then cast the previous equation into an equation for temperature (T):

$$\rho c\frac{DT}{Dt} = \nabla\bullet(k\,\nabla T) + \left[\tau_{xx}\frac{\partial u}{\partial x}+\tau_{yx}\frac{\partial u}{\partial y}+\tau_{zx}\frac{\partial u}{\partial z}+\tau_{xy}\frac{\partial v}{\partial x}+\tau_{yy}\frac{\partial v}{\partial y}+\ldots\right.$$
$$\left.\ldots+\tau_{zy}\frac{\partial v}{\partial z}+\tau_{xz}\frac{\partial w}{\partial x}+\tau_{yz}\frac{\partial w}{\partial y}+\tau_{zz}\frac{\partial w}{\partial z}\right]+S_T \qquad \text{(A1.7)}$$

The motion of a fluid is described by the equations presented so far: the continuity equation, the 3 momentum equations and the energy equation. The number of unknowns however are: the three velocity components (u, v, w), the pressure (p), the temperature (T), the internal energy (i) and the density (ρ). Further relations can be obtained by invoking the assumption of thermodynamic equilibrium (perfect gas relations) in order to close the complete system of seven equations and seven unknowns, provided that initial and boundary conditions are applied. This means that, even though the properties of a fluid element change rapidly from place to place, the fluid can thermodynamically adjust itself to the new conditions so quickly that the changes are essentially instantaneous.

As it can be seen, the linkage between the energy and the momentum equations is through the variation of pressure as a result of pressure and temperature variations in the flow field. For incompressible fluids there is no link between the energy and the mass and momentum conservation equations. This equation then needs to be solved separately if the problem involves heat transfer.

A2.1.4 The general form of the Transport equation

The PDEs presented above (i.e the continuity, the 3 momentum equations and the temperature equation) can be cast in the following expanded general transport equation for the variable Φ:

$$\underbrace{\frac{\partial(\rho\,\Phi)}{\partial t}}_{\substack{\text{unsteady}\\ \text{term}}} + \underbrace{\nabla\bullet(\rho \boldsymbol{u}\Phi)}_{\substack{\text{convection}\\ \text{term}}} = \underbrace{\nabla\bullet(\Gamma\nabla\Phi)}_{\substack{\text{diffusion}\\ \text{term}}} + \underbrace{S_\Phi}_{\substack{\text{source}\\ \text{term}}} \qquad \text{(A1.8)}$$

The general variable Φ can take the values: 1 (for the continuity equation), u, v, w (for the three momentum equations), T (for temperature). Coefficient Γ is called diffusion coefficient and it is equal to 0 for the continuity equation, equal to μ for the momentum equations and k for the temperature equation.

In order to bring out the common features of the equations one had to hide the terms that are not shared to the source terms. The above equation is the starting point for computational procedures for the FV method.

A3.1 The Finite Volume Method (FVM)

A3.1.1 Integrating the general Transport equation

Using the finite volume method we can obtain discretised expressions of the governing equations by integrating them in control volumes (CV) that surround each computational

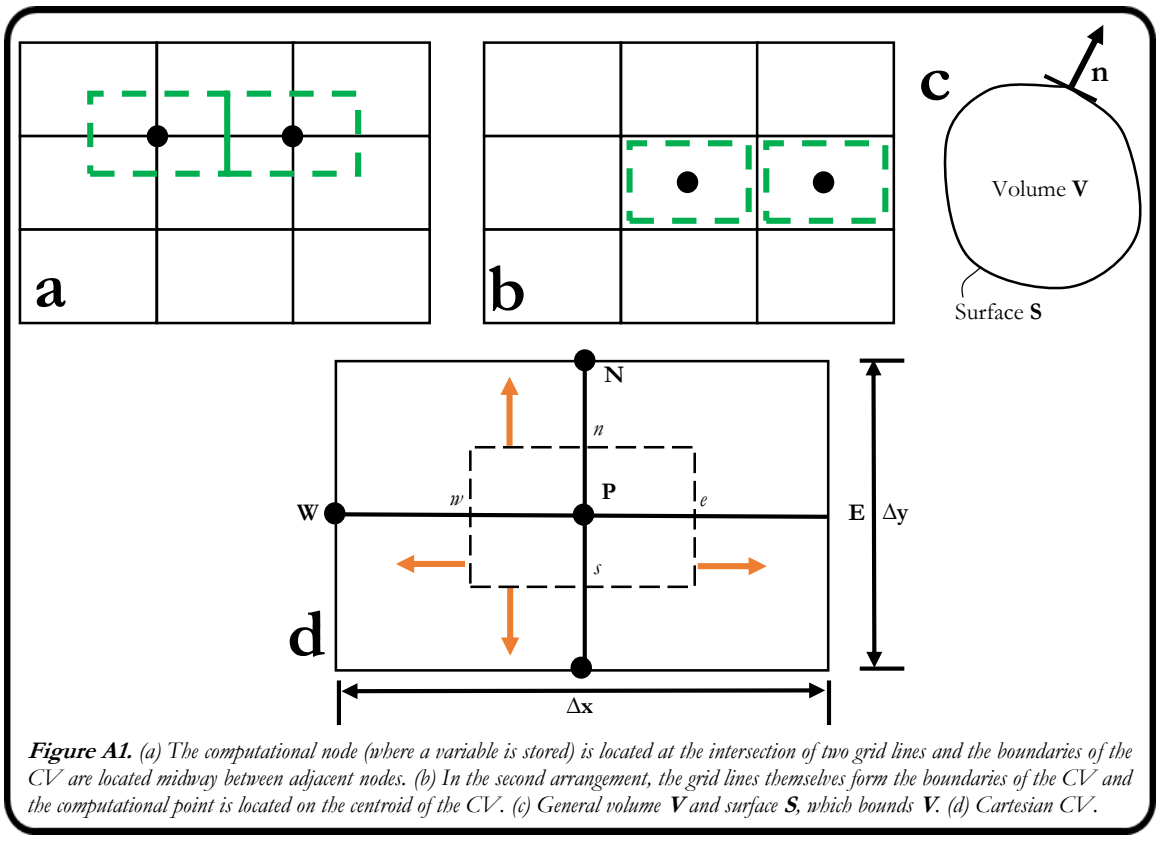

Figure A1. *(a) The computational node (where a variable is stored) is located at the intersection of two grid lines and the boundaries of the CV are located midway between adjacent nodes. (b) In the second arrangement, the grid lines themselves form the boundaries of the CV and the computational point is located on the centroid of the CV. (c) General volume* ***V*** *and surface* ***S****, which bounds* ***V****. (d) Cartesian CV.*

node. There are two arrangement of variables as shown in the following figure. In the first one (Figure A1a) the computational node (where a variable is stored) is located at the intersection of two grid lines and the boundaries of the CV are located midway between adjacent nodes. In the second arrangement (Figure A1b), the grid lines themselves form the boundaries of the CV and the computational point is located on the centroid of the CV. Both options have been used in the past with success. Note also that the CVs do not overlap and each face of the CV is unique to the two CVs, which lie on either side of it.

The integration of the generic transport equation (A1.8) on each CV is based on Green's theorem to convert volume integrals containing a divergence term into surface integrals. These terms are subsequently evaluated as fluxes at the surface of each cell in the computational domain. Let **n** be unit normal vector on ***S***, which is assumed to be positive when drawn outward with respect to the volume ***(V)*** enclosed by ***S*** (Figure A1c).

CFD-ACE+'s numerical solvers use a co-located cell-centre variable arrangement. This means that all dependant variables and material properties are stored at the cell centre, ***P*** (see Figure A1d) and the grid lines form the boundaries of the volumes; thus, the average value of any quantity in the control volume is given by value at the cell centre. The collocated arrangement is very convenient from the point of view of implementation in contrast to the staggered arrangement. However, a special interpolation practise must be used to obtain the velocity at the faces of the volumes in order to avoid the checker-board pressure field. The general transport equation (A1.8) can be expanded and integrated over a control volume cell, Ω:

$$\underbrace{\int_{\Omega}\frac{\partial(\rho\,\Phi)}{\partial t}\,d\Omega}_{\substack{\textit{unsteady}\\ \textit{term (1)}}}+\underbrace{\int_{\Omega}\nabla\bullet(\rho\boldsymbol{u}\Phi)\,d\Omega}_{\substack{\textit{convection}\\ \textit{term (2)}}}=\underbrace{\int_{\Omega}\nabla\bullet(\Gamma\nabla\Phi)\,d\Omega}_{\substack{\textit{diffusion}\\ \textit{term (3)}}}+\underbrace{\int_{\Omega}S_{\Phi}\;d\Omega}_{\substack{\textit{source}\\ \textit{term (4)}}} \tag{A1.9}$$

In time-dependent problems it is also necessary to integrate with respect to time *t* over a small interval ⊿*t* from, say, *t* until *t* + ⊿*t*, hence:

$$\underbrace{\int_{\Delta t}\frac{\partial}{\partial t}\left(\int_{\Omega}(\rho\,\Phi)d\Omega\right)dt}_{\substack{\textit{unsteady}\\ \textit{term (1)}}}+\underbrace{\int_{\Delta t}\int_{\Omega}\nabla\bullet(\rho\boldsymbol{u}\Phi)d\Omega\,dt}_{\substack{\textit{convection}\\ \textit{term (2)}}}=\underbrace{\int_{\Delta t}\int_{\Omega}\nabla\bullet(\Gamma\nabla\Phi)\,d\Omega dt}_{\substack{\textit{diffusion}\\ \textit{term (3)}}}+\underbrace{\int_{\Delta t}\int_{\Omega}S_{\Phi}\;d\Omega dt}_{\substack{\textit{source}\\ \textit{term (4)}}} \tag{A1.10}$$

A3.1.2 Integrating the transient term (1) from Equation A1.9

$$\int_{\Omega}\frac{\partial(\rho\,\Phi)}{\partial t}\,d\Omega=\frac{\rho^{k}\Phi^{k}\Omega^{k}-\rho^{k-1}\Phi^{k-1}\Omega^{k-1}}{\Delta t} \tag{A1.11}$$

In the above equation *k* denotes the current time and *k-1* the previous time and Δ*t* is the time step. Ω is the CV, and may be time dependent (although moving grids are not used in this research).

A3.1.3 Integrating the Convection term (2) from Equation A1.10

The convection term is a volume integral of a divergence term, hence:

$$\int_{\Omega} \nabla\bullet(\rho \boldsymbol{u}\Phi)d\Omega = \oint_{\partial\Omega} \rho \boldsymbol{u}\Phi\bullet \boldsymbol{n}dS = \sum_{e}\left(\rho_e \boldsymbol{u}_e^n \Phi_e\right)A_e = \sum_{e}\left(C_e A_e\right) \tag{A1.12}$$

In the above equation, the subscript e denotes the face of the current computational cell (see Figure A2), A_e is the area of the face of the cell and $\boldsymbol{u}^n_e$ is the velocity normal to the face. C_e can be described as the flux through the face and its evaluation is dealt with in the discussion below relating to pressure-volume coupling. The value at face e, Φ_e, can be evaluated through a variety of interpolation schemes that provide varying levels of numerical stability and accuracy.

A first order accurate interpolation scheme that is used to discretize the convection term is namely the First-Order Upwind Scheme. This numerically stable scheme is used to express Φ at the face of the cell, e. In this scheme, the upstream grid point is used, so Φ_e equals either Φ_{T1} or Φ_{T2} depending on the direction of flow at the cell face e. Hence:

$$\Phi_e^{UP} = \begin{cases} \Phi_{T1} & if\ v_e^n > 0 \\ \Phi_{T2} & if\ v_e^n < 0 \end{cases} \tag{A1.3}$$

In this research, a second order accurate central difference scheme was used for higher accuracy. In this scheme, Φ_e is evaluated via a weighted average (linear) of Φ at the cell centres of two adjacent triangles, namely T1 and T2. Hence:

$$\Phi_e^{CD} = \gamma_e \Phi_{T1} + \left(1-\gamma_e\right)\Phi_{T2} \tag{A1.14}$$

In the above equation, γ_e is the geometric weighting function at face e.

CFD-ACE+ introduces a damping parameter to the above scheme in the form of a blend between central differences and upwind in order to mitigate the effect of inherent instabilities in the scheme, along with the damping of instabilities when using the above equation with iterative methods:

$$\Phi_e^{CD} = \eta\Phi_e^{UP} + \left(1-\eta\right)\Phi_e^{CD} \tag{A1.14}$$

where η is the blending coefficient; if $\eta = 0$, the full central differences scheme is recovered, while $\eta = 1$ yields the full upwind scheme. In this work, $\eta = 0.3$ was chosen when considering the cases for aqueductal stenosis, whilst, $\eta = 1$ was chosen for the cases involving the simulation of ETV and EFV.

Other schemes available on CFD-ACE+ include a Second Order Upwind Scheme with Limiter, Smart Scheme and a third order scheme.

A3.1.4 Integrating the Diffusion term (3) from Equation A1.10

The discretization of the diffusion term is conducted in the following manner:

$$\int_{\Omega} \nabla\bullet(\Gamma\nabla\Phi)d\Omega = \int_{A} \Gamma(\nabla\Phi)\mathbf{n}dA = \sum_{e} \Gamma_e \left(\frac{\partial\Phi}{\partial n}\right)_e A_e$$

where the unit vector in Figure A2 is defined as :

$$\left(\frac{\partial\Phi}{\partial n}\right) = \frac{1}{\boldsymbol{n}\bullet\boldsymbol{e}}\left(\frac{\partial\Phi}{\partial e} - \boldsymbol{e}\bullet\boldsymbol{\tau}\frac{\partial\Phi}{\partial\tau}\right) \qquad \text{(A1.15)}$$

the diffusion term (3) becomes :

$$\int_{\Omega} \nabla\bullet(\Gamma\nabla\Phi)d\Omega = \sum_{e} \frac{\Gamma_e}{\boldsymbol{n}\bullet\boldsymbol{e}}\left(\frac{\partial\Phi}{\partial e}\right)_e A_e - \sum_{e} \frac{(\boldsymbol{e}\bullet\boldsymbol{\tau})\Gamma_e}{\boldsymbol{n}\bullet\boldsymbol{e}}\left(\frac{\partial\Phi}{\partial\tau}\right)_e A_e$$

where the final form has utilised: $\left(\frac{\partial\Phi}{\partial e}\right)_e = \frac{\Phi_{T2} - \Phi_{T1}}{\delta_{T1,T2}}$ and $\left(\frac{\partial\Phi}{\partial\tau}\right)_e = \frac{\Phi_{C2} - \Phi_{C1}}{\delta_{C1,C2}}$, where $\delta_{T1,T2}$ and $\delta_{C1,C2}$ represent the distances between T1 and T2 and C1 and C2 respectively.

A3.1.5 Integrating the Source term (4) from Equation A1.10

The source terms are linearized and integrated over the control volume using the latest value of Φ (which is taken at the previous iteration):

$$\int_{\Omega} S_\Phi d\Omega = S^U + S^P\Phi_P, \text{ where } S^P = S_p\Omega \text{ and } S^U = S_u\Omega \qquad \text{(A1.16)}$$

A3.2.1 Velocity-Pressure Coupling: Continuity and Mass evaluation

The continuity equation governing mass conservation cannot be written in the form of the general convection-diffusion equation. It is used to determine the pressure field in the pressure-based method as employed in CFD-ACE+. Integrating the mass conservation equation over a finite volume cell, one obtains:

$$\frac{\partial\rho}{\partial t} + \nabla\bullet(\rho\boldsymbol{u}) = \dot{m} \quad \therefore$$

$$\frac{\rho^k\Omega^k - \rho^{k-1}\Omega^{k-1}}{\Delta t} + \sum_{e} \rho_e u_e^n A_e = \dot{m}\,\Omega^k, \text{ where:} \qquad \text{(A1.17)}$$

$$u_e^n = n_x u_e + n_y u_e + n_z u_e$$

The latter relation represents the face-normal component of the velocity at face e, which is obtained by the inner product of the velocity vector (u, v, w) and the face-normal unit vector (n_x, n_y, n_z). Since the fluid density and velocities are available at cell centres, their respective face values need to be interpolated from cell-centre values. Linear interpolation de-couples the velocity and pressure fields giving rise to checkerboard instability. In CFD-ACE+, the checkerboard problem is circumvented by calculating the cell-face mass flux by averaging the momentum equation to the cell faces and relating the cell face velocity directly to the local pressure gradient. The details can be found in Rhie and Chow [454].

A3.2.2 Velocity-Pressure Coupling: Pressure Correction and SIMPLEC algorithm

Solutions of the three momentum equations (A1.3) yield the three Cartesian components of velocity. Even though pressure is an important flow variable, no governing equation for pressure is presented albeit its importance. Pressure-based methods utilize the continuity equation to formulate an equation for pressure, and many exist, such as SIMPLE, SIMPLER (SIMPLE Revised), SIMPLEC and PISO (Pressure Implicit with Splitting of Operators). The SIMPLE method is essentially a guess-and-correct procedure for the calculation of pressure on a staggered grid arrangement. In CFD-ACE+, the SIMPLEC (Semi-Implicit Method for Pressure-Linked Equations – Consistent) scheme has been adopted, based on the work of Van Doormal and Raithby [455]. SIMPLEC follows the same steps as the SIMPLE algorithm, with the difference that the momentum equations are manipulated so that the SIMPLEC velocity correction equations omit terms that are less significant than those in SIMPLE. The algorithm is derived from the finite difference form of the momentum equation for the cell centre of the triangle T1:

$$\Psi_{T1} v_{T1} = \left(\sum_i \Psi_i v_i + S_U \right)_{T1} - \left(\sum_e p_e A_e \boldsymbol{n}_e \right)_{T1} \tag{A1.18}$$

In the above equation, Ψ is the link coefficient and S_U is the linearized source term described earlier. The subscripts e and i denote each face of the cell and each adjoining cell, respectively. To initiate the SIMPLEC calculation process a pressure field p^* is guessed in order to solve the discretised momentum equations to yield the velocity components from A1.18 such that:

$$\Psi_{T1} v^*_{T1} = \left(\sum_i \Psi_i v^*_{T1} + S_U \right)_{T1} - \left(\sum_e p^*_e A_e \boldsymbol{n}_e \right)_{T1} \tag{A1.19}$$

Using the above equation however will still not satisfy continuity, hence using the corrections v' and p' will aid in finding an improved solution:

$$v = v^* + v' \qquad p = p^* + p' \tag{A1.20a-b}$$

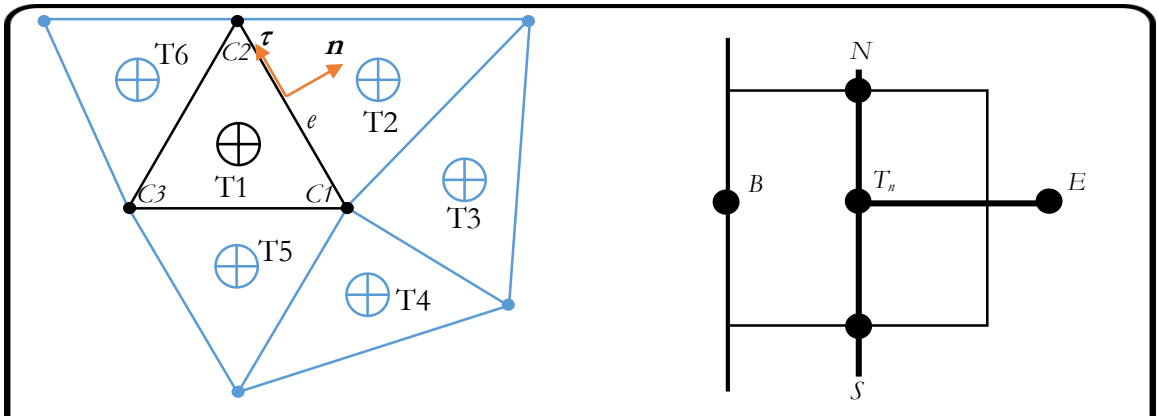

Figure A2. *(Left) Adjacent finite volumes (here 2D triangles T1-T6). The dependant variables and material properties are averaged over the cell volume and stored at the cell centre (⊕) for interpolation. (Right) Computational Boundary Cell.*

for which an expression can be obtained by subtracting Equation A1.19 from A1.18 and simultaneously assuming v_i' can be approximated by v_{Pi}' one may obtain:

$$\Psi_{T1} v_{T1}^{'} = \frac{-1}{\Psi_{T1} - \sum_i \Psi_i} \left(\sum_e p_e^* A_e \boldsymbol{n}_e \right)_{T1} \tag{A1.21}$$

the velocity correction at the face, v_e', is obtained by averaging the cell centre values from adjacent cells (T1 and T2):

$$v_e^{'} = \gamma_e v_{T1}^{'} + (1-\gamma_e) v_{T2}^{'} \tag{A1.22}$$

The conservation of mass equation was already integrated in A1.17, and if one defines the mass flux as:

$$C_e = \rho_e u_e^n A_e \tag{A1.23}$$

we then have:

$$\frac{\rho^k \Omega^k - \rho^{k-1} \Omega^{k-1}}{\Delta t} + \sum_e C_e = \dot{m}\, \Omega^k \tag{A1.24}$$

If v^* and p^* are used to calculate C_e, the resulting C_e^* will not satisfy (A1.24) and again a corrective term is introduced:

$$C_e = C_e^* + C_e^{'} \tag{A1.25}$$

Equation A1.24 can be recast by incorporating the corrective mass flux:

$$\frac{\rho_{T1}^{'} \Omega^k}{\Delta t} + \sum_e C_e^{'} = S_m \tag{A1.26}$$

In the above equation, S_m represents the mass correction within the control volume:

$$S_m = \frac{\rho_{T1}^{k-1} \Omega^{k-1} - \rho_{T1}^* \Omega^k}{\Delta t} + \dot{m}\, \Omega^k - \sum_e C_e^* \tag{A1.27}$$

With the face-normal velocity correction and the density correction expressed in terms of the pressure correction, substitutions can be made in Equation A1.27 and the pressure correction can be obtained from:

$$\Psi_{T1} v_{T1}^{'} = \left(\sum_i \Psi_i v_i^{'} \right) + S_m \tag{A1.28}$$

A summary of the SIMPLEC procedure is:

1. *Guess a pressure field P*;*
2. *Obtain the velocity field by solving Equation A1.19;*
3. *Evaluate C* from ρ* and v*;*
4. *Evaluate the mass source, S_m;*
5. *Obtain the pressure correction from Equation A1.28;*
6. *Correct the pressure and velocity fields using Equation A1.20a-b;*
7. *Solve the discretized equations for other flow variables such as enthalpy, turbulent quantities, scalars etc. and finally,*
8. *Go to step 2 and repeat the procedure until convergence is achieved.*

A3.3.1 Boundary Conditions

In CFD-ACE+ the boundary conditions are all implemented in the same manner. Specifically, a control cell adjacent to the west boundary of the calculation domain is shown in the right of Figure A2. A fictitious boundary node labelled *B* is shown. The finite-volume equation for node *Tn* is constructed as:

$$\omega_{Tn}\Phi_{Tn} = \omega_E\Phi_E + \omega_N\Phi_N + \omega_S\Phi_S + S \qquad \text{(A1.29)}$$

In the above equation, the coefficient $\omega_W = 0$ after the links to the boundary node *B* are incorporated into the linearized source term *S*:

$$S = S_U + S_{Tn}\Phi_{Tn} \qquad \text{(A1.30)}$$

Fixed boundary conditions at the boundary node B (Φ_B) require an augmentation of the source terms:

$$S_U = S_U + S_W\Phi_B \quad \& \quad S_{Tn} = S_{Tn} - \omega_W \qquad \text{(A1.31a-b)}$$

A4.1 Solving the Algebraic System

As was already shown, the SIMPLEC algorithm for the coupling of continuity and momentum equations is itself iterative. Hence, there is no need to obtain very accurate intermediate solutions, as long as the iteration process eventually converges to the true solution. Fortunately, CFD-ACE+ uses an iterative, segregated solution method wherein the equation sets for each variable are solved sequentially and repeatedly until a converged solution is obtained. The two iterative solvers implemented within the CFD-ACE+ platform are the Conjugate Gradient Squared (CGS) solver and the Algebraic Multigrid (*AMG*) solver [456]. *AMG* offers two significant advantages over the CGS solver in that:

1. *Increase in solver time is dependent only on the number of unknowns in the equations;*
2. *A faster convergence, particularly with fully unstructured meshes*

Multigrid methods are known to exploit the inherent differences in error behaviour and use iterations on meshes of different size. The short wavelength errors are effectively reduced on the finest meshes, whereas the long-wavelength errors rapidly decay on the coarsest meshes. There are two primary types of multi-grid methods, geometric and algebraic multi-grid, respectively. In CFD-ACE+, the latter method is chosen since it uses the equation matrix itself and not the geometry, in order to create the coarse grids.